MRI of Atherosclerosis

MRI of Atherosclerosis

Magnetische Resonantie Imaging van Atherosclerose

(met een samenvatting in het Nederlands)

Proefschrift

ter verkrijging van de graad van doctor aan de Universiteit Utrecht
op gezag van de rector magnificus, prof.dr. J.C. Stoof,
ingevolge het besluit van het college voor promoties in het openbaar
te verdedigen op dinsdag 11 mei 2010 des ochtend te 10.30u

door

Bernardus Cornelius Maria te Boekhorst

geboren op 18 februari 1972, te Tilburg

Promotoren:

Prof. dr. G. Pasterkamp
Prof. dr. C.J.A. van Echteld

Co-promotor:

Dr. M.J.M.Cramer

Contents

Chapter 1

Introduction

Introduction

Cardiovascular disease, particularly atherosclerosis, is the leading cause for morbidity and mortality in the United States, Europe and much of Asia, despite changes in lifestyle and new pharmacologic approaches to lower plasma cholesterol concentrations(1;2). Atherosclerosis is an inflammatory disease characterized by specific cellular and molecular responses of the vessel wall(1;2). Macrophages play a key role in this process. Atherosclerosis affects large and medium sized arteries like the aorta, carotid arteries, femoral arteries and coronary arteries(2;3).

Atherosclerotic lesions may be practically classified based on their histological composition and structure(4). Lesions may develop from one class to another through a person's lifetime. Initial lesions and fatty streaks are common in infants and young children(1). Advanced lesions are predominantly found in people at the age of 30 years and older, and are characterized by extra-cellular deposition of amorphous lipids, preceding the influx of macrophages and T lymphocytes(1). Acute coronary syndromes -unstable angina, myocardial infarction and sudden death- are often caused by disruption of a mildly to moderately obstructive coronary artery plaque with superimposed thrombosis(5;6).
The classical vulnerable plaque is characterized by a thin fibrous cap (<70 μm), a large lipid core (>40% of the plaque area) and many macrophages in the shoulder regions of the cap(5). The degree of inflammation is not only determined by the number of macrophages, but also the activity of these macrophages. Expression of molecular markers like matrix metalloproteinases(7) and scavenger receptors(8) could also reflect the vulnerability of the plaque.The clinical standard for diagnosis of coronary artery disease is coronary angiography. However, coronary angiography only visualizes luminal narrowing and not the arterial wall. Moreover arteries may accommodate plaque growth through outward displacement of the vessel wall, thereby preserving lumen cross-sectional area(9).

Diagnosis of early stages of atherosclerosis is important for tuning of preventive lifestyle changes and pharmacological interventions. Diagnosis of vulnerable plaque stages of atherosclerosis is important for screening of high-risk patients among patients with established coronary artery disease. MRI shows great promise as a diagnostic and prognostic tool for atherosclerosis owing to the provided anatomical detail, different MR contrast originating from the various plaque components and its noninvasive character(10;11). The massive number of studies regarding visualization of atherosclerotic plaque in the carotid arteries shows the success of MRI for visualization of plaque in large superficial arteries which are stable during cardiac action and respiratory motions(12-18). However, visualization of the coronary artery plaque is hindered by motion artifacts due to cardiac

and respiratory motion, which necessitates triggering on cardiac and respiratory motion, and limited size. For these reasons and because measurement time is practically limited, signal to noise ratio of clinical MR images of coronary arteries is limited. With MRI, there is a trade-off between signal to noise ratio and resolution, so high resolution means a low signal to noise ratio. Contrast agents high-lighting some pixels representing a specific component of the plaque could solve the problem of limited resolution. Moreover vehicles used as MR contrast agents can be coupled to antibodies or specific agonists directed to molecular markers which could be more relevant for characterization of vulnerable plaque than the classical morphologic features of vulnerability. For these reasons so-called cellular or molecular MRI with contrast agents has gained scientific interest.

Scope of this thesis

The following chapters will address MRI of atherosclerotic plaque. **Chapter 2** provides an overview of literature on MRI of atherosclerotic plaque without contrast agents and **Chapter 3** discusses MRI using contrast agents aimed at imaging molecular and cellular processes of atherosclerosis. In **Chapter 4** multi-contrast weighted MRI of carotid artery autopsy specimens at 9.4T is described using a panel of MR sequences including two novel sequences for visualization of intra-plaque hemorrhage and lipid core. A trained Mahalanobis Distance classifier was used for automatic classification of plaque components. **Chapter 5** describes an investigation into the routing and uptake of ultrasmall particles of iron oxide in plaque and the role of circulating monocytes. Also false positive observations of plaque uptake of USPIOs due to peri-aortic lymph node uptake are reported. **Chapter 6** reports the production, characterization, *in vitro* and first *in vivo* MRI results of peripheral cannabis receptor (CB2-R) targeted and neutrophil gelatinase associated lipocalin-2 (NGAL) targeted micelles in mouse atherosclerotic plaque. In **Chapter 7** the relation between transient ischemic attacks, cerebro-vascular accidents and NGAL expression in culprit lesions is assessed. Moreover in a severe atherosclerosis mouse model successful molecular MRI of 24p3 (mouse homologue of NGAL) is shown. **Chapter 8** studies the time window of MRI after administration of CB2-R targeted gadolinium containing micelles in mice and compares the efficiency of two MRI techniques for visualization of contrast-enhanced atherosclerotic plaque. **Chapter 9** compares a self-gated cardiac MRI method with a prospectively gated cardiac MRI method for evaluation of cardiac function parameters in mice after permanent occlusion of the left anterior descending artery. **Chapter 10** provides a general discussion of the results and conclusions reported in the previous chapters, and future implications. The final part of this chapter provides a summary in dutch.

Reference List

1   Ross R. Atherosclerosis is an inflammatory disease. Am Heart J 1999 November;138(5 Pt 2):S419-S420.

2   Libby P, Ridker PM, Hansson GK. Inflammation in atherosclerosis: from pathophysiology to practice. J Am Coll Cardiol 2009 December 1;54(23):2129-38.

3   Fayad ZA, Fuster V. The human high-risk plaque and its detection by magnetic resonance imaging. Am J Cardiol 2001 July;88(2A):42E-5E.

4   Stary HC, Chandler AB, Dinsmore RE, Fuster V, Glagov S, Insull W, Jr. et al. A definition of advanced types of atherosclerotic lesions and a histological classification of atherosclerosis. A report from the Committee on Vascular Lesions of the Council on Arteriosclerosis, American Heart Association. Arterioscler Thromb Vasc Biol 1995 September;15(9):1512-31.

5   Falk E, Shah PK, Fuster V. Coronary plaque disruption. Circulation 1995 August 1;92(3):657-71.

6   Fayad ZA, Fuster V, Fallon JT, Jayasundera T, Worthley SG, Helft G et al. Noninvasive in vivo human coronary artery lumen and wall imaging using black-blood magnetic resonance imaging. Circulation 2000 August 1;102(5):506-10.

7   Galis ZS, Khatri JJ. Matrix metalloproteinases in vascular remodeling and atherogenesis: the good, the bad, and the ugly. Circ Res 2002 February 22;90(3):251-62.

8   Lipinski MJ, Amirbekian V, Frias JC, Aguinaldo JG, Mani V, Briley-Saebo KC et al. MRI to detect atherosclerosis with gadolinium-containing immunomicelles targeting the macrophage scavenger receptor. Magn Reson Med 2006 September;56(3):601-10.

9   Pasterkamp G, Schoneveld AH, van der Wal AC, Haudenschild CC, Clarijs RJ, Becker AE et al. Relation of arterial geometry to luminal narrowing and histologic markers for plaque vulnerability: the remodeling paradox. J Am Coll Cardiol 1998 September;32(3):655-62.

10 Leiner T, Gerretsen S, Botnar R, Lutgens E, Cappendijk V, Kooi E et al. Magnetic resonance imaging of atherosclerosis. Eur Radiol 2005 June;15(6):1087-99.

11 Choudhury RP, Fuster V, Badimon JJ, Fisher EA, Fayad ZA. MRI and characterization of atherosclerotic plaque: emerging applications and molecular imaging. Arterioscler Thromb Vasc Biol 2002 July 1;22(7):1065-74.

12 Cai J, Hatsukami TS, Ferguson MS, Kerwin WS, Saam T, Chu B et al. In vivo quantitative measurement of intact fibrous cap and lipid-rich necrotic core size in atherosclerotic carotid plaque: comparison of high-resolution, contrast-enhanced magnetic resonance imaging and histology. Circulation 2005 November 29;112(22):3437-44.

13 Mitsumori LM, Hatsukami TS, Ferguson MS, Kerwin WS, Cai J, Yuan C. In vivo accuracy of multisequence MR imaging for identifying unstable fibrous caps in advanced human carotid plaques. J Magn Reson Imaging 2003 April;17(4):410-20.

14 Saam T, Yuan C, Chu B, Takaya N, Underhill H, Cai J et al. Predictors of carotid atherosclerotic plaque progression as measured by noninvasive magnetic resonance imaging. Atherosclerosis 2007 October;194(2):e34-e42.

15 Yuan C, Kerwin WS, Ferguson MS, Polissar N, Zhang S, Cai J et al. Contrast-enhanced high resolution MRI for atherosclerotic carotid artery tissue characterization. J Magn Reson Imaging 2002 January;15(1):62-7.

16 Cappendijk VC, Cleutjens KB, Kessels AG, Heeneman S, Schurink GW, Welten RJ et al. Assessment of human atherosclerotic carotid plaque components with multisequence MR imaging: initial experience. Radiology 2005 February;234(2):487-92.

17 Kampschulte A, Ferguson MS, Kerwin WS, Polissar NL, Chu B, Saam T et al. Differentiation of intraplaque versus juxtaluminal hemorrhage/thrombus in advanced human carotid atherosclerotic lesions by in vivo magnetic resonance imaging. Circulation 2004 November 16;110(20):3239-44.

18 Chu B, Kampschulte A, Ferguson MS, Kerwin WS, Yarnykh VL, O'Brien KD et al. Hemorrhage in the atherosclerotic carotid plaque: a high-resolution MRI study. Stroke 2004 May;35(5):1079-84.

Chapter 2

Recent developments and new perspectives on imaging of atherosclerotic plaque: Role of anatomical MRI

Bernard C.M. te Boekhorst[1,2], MD; Maarten-Jan M. Cramer[1], MD, PhD; Gerard Pasterkamp[1], MD, PhD; Cees J.A. van Echteld[1,3], PhD; Pieter A.F.M. Doevendans[1], MD, PhD

[1]Department of Cardiology, University Medical Center Utrecht; [2]Interuniversity Cardiology Institute of the Netherlands, [3]Present address: Novartis Institutes for BioMedical Research, Basel, Switzerland

Abstract

Atherosclerotic plaque disruption accounts for the major part of cardiovascular mortality and the risk of disruption appears to depend on plaque composition. Carotid plaques in patients, scheduled for endarterectomy, have been successfully characterised with MRI. MRI has the advantage of combining information about morphology and function. Unfortunately, the tortuosity and size of the coronary arteries, and the respiratory and cardiac motion hinder the *in vivo* characterisation of human coronary plaque. In addition to plaque composition several molecular markers of the different processes involved in atherosclerosis, such as integrins, matrix metalloproteinases (MMPs) and fibrin seem to correlate with risk of plaque rupture and clinical outcome. These molecular markers can be targeted with antibodies coupled to carriers, which are loaded with gadolinium for detection (molecular MRI). Several cellular/molecular MRI studies in animal models and some in human patients have been conducted with varying levels of success. The advent of clinical high field magnets, the development of contrast agent carriers with high relaxivity and the development of relatively new MR contrast techniques are promising in the field of plaque imaging. Future MRI studies will have to focus on the molecular target of the atherosclerotic process, which has the highest prognostic value with regard to acute coronary syndromes and on the most suitable contrast agent to visualize that target.

Part I

Imaging modalities for atherosclerotic plaque staging

Atherosclerosis is a systemic disease, which affects particularly the aorta, carotid arteries, iliofemoral arteries and the coronary arteries(1-4). Mortality from generalized vascular diseases is for 70% caused by myocardial ischemia or infarction, 10-20% by stroke and 10% by ruptured aneurysms or visceral infarctions(1,2). Most acute coronary syndromes (ACS) are the result from plaque disruption and consequent thrombosis(5). Many post-mortem examinations have revealed that the risk of plaque rupture (plaque vulnerability) depends mainly on plaque composition(1,5,7,8). Vulnerable plaques have thin or eroded fibrous caps that overlay large lipid cores and harbour an abundance of inflammatory cells(1,5). Coronary angiography is the gold standard technique for lumenography, but it is not apt for detection of vulnerable plaque, since in many cases growing plaque is associated with outward remodeling of the vessel(6). There is a need for a diagnostic technique, which is suitable for screening patients with coronary artery disease (CAD) for the presence of vulnerable plaques.

Table 1 lists an overview of techniques, which provide information about plaque morphology, chemical composition, inflammation or metabolic activity. A variety of techniques is available, which provide information about plaque morphology, such as intravascular ultrasound (IVUS)(9), optical coherence tomography (OCT)(10) and angioscopy. In addition, Raman spectroscopy (RS)(11) and near-infrared spectroscopy (NIRS)(12) provide information about chemical composition of the plaque. Thermography may provide indirect information about inflammatory activity in the plaque. However, heat was reported to be generated in non-culprit lesions both in patients with stable angina as well as in patients with ACS(13). All mentioned techniques share a major disadvantage of being invasive.

Among the non-invasive techniques are conventional ultrasound (US)(14), electron beam computed tomography (EBCT) or multi detector CT (MDCT)(15), positron emission tomography (PET) and single-photon-emission computed tomography (SPECT)(16) and magnetic resonance imaging (MRI)(1,17).

Conventional US is only applicable for imaging of vessels close to the skin, because of the low depth resolution(14). Moreover, only plaque size and, when used in combination with Doppler, arterial stenosis can be assessed(14).

Electron beam CT is suggested to be a good screening tool for risk prediction for CAD, better than traditional Framingham factors, by measuring coronary arterial calcium score. While coronary artery calcification burden appears to correlate with higher chance of significant coronary arterial narrowing, coronary calcification cannot be used to identify sites of stenoses(18) and may reflect a relatively dormant stage of atherosclerosis instead of current risk of an ACS. Of note, calcified plaque in aortic EBCT is overestimated by the so-called "blooming" effect, when compared to simultaneously performed MRI, especially for smaller plaques(19). Contrast-enhanced MDCT (16 slices) showed a statistically significant difference in attenuation between lipid-rich and fibrous plaques(20). However, the authors stated that in individual cases non-calcified plaque could not be characterized reliably, since the standard deviation of their results was high and the depiction of plaque micro-architecture was poor with MDCT, when compared with MRI(20). Contrast-enhanced MDCT (64 slices) allowed identification of proximal coronary lesions with reasonable accuracy, but even exact quantification of the degree of occlusion was not possible(21). Another important disadvantage of MDCT is the involvement of significantly higher radiation exposures as compared to single-slice and EBCT.

In PET and SPECT radiolabeled molecules are used to specifically target individual metabolic or enzymatic activities involved in a particular molecular process. For example, SPECT was applied for imaging of apoptosis in an atherosclerotic rabbit model(22). After rapid blood clearance, intense uptake of Tc-99m-annexin V in aortic plaque was observed 2 hours after injection. Another example of specifically targeting atherosclerotic plaque

Table 1. Comparison of Imaging Modalities for Identification of Atherosclerosis in Humans

Imaging modality	Physical basis	Spatial resolution	Penetration	Catheter	Invasive/Non-invasive/ radiation	Fibrous cap	Inflam-mation	Lipid core	Molec Imag feasible?	Sensitivity Molec Imag[A]
CAG	x-rays	±300 µm	No limit	+	Invasive, radiation	-	-	-	No	Not applicable
IVUS	reflection of HF sound	250-500 µm	Poor	+	Invasive	-	-	-	Yes	?
OCT	reflection of light	1-10 µm	1-2 mm	+	Invasive	+	+	+	Yes	?
PAT	reflection of light	15-45 µm	3 mm	+	Invasive	+	+	+	Yes	?
AS	visible light	Unknown	Very poor	+	Invasive	-	-	±	No	Not applicable
Thermo	temperature	0.5 mm	Unknown	+	Invasive	-	+	-	No	Not applicable
RS	energy exchange between light and molecules	Not applicable	1.0-1.5 mm	+	Invasive	-	+	+	Yes	"molecular fingerprint"
US	reflection of HF sound	>400 µm	Very poor	-	noninvasive	-	-	-	Yes	?
CT	x-rays	400-600 µm	No limit	-	radiation	-	-	-	Yes	?
Optical fluorescence techniques	visible light/NIR	2-5 mm	<1 cm	+	noninvasive	-	+	-	Yes	Not well characterized, likely 10^{-9}-10^{-12} mole/L
SPECT	low energy γ- rays	Several mms	No limit	-	radiation	-	+	-	Yes	10^{-10}-10^{-11} mole/L
PET	high energy γ- rays	Several mms	No limit	-	radiation	-	+	-	Yes	10^{-11}-10^{-12} mole/L
MRI	radiowaves	150-200 µm	No limit	-	noninvasive	+	+	+	Yes	10^{-3}-10^{-5} mole/L

CAG: Coronary Angiography; IVUS: Intravascular UltraSound, OCT: Optical Coherence Tomography; PAT: Photo-Acoustic Tomography; AS: Angioscopy; Thermo: Thermography; RS: Raman Spectroscopy; US: conventional UltraSound, CT: Computed Tomography; NIR: near infra-red, MRI: Magnetic Resonance Imaging Molec Imag: Molecular Imaging A: sensitivity of Molec Imag: the ability to detect a molecular probe, relative to the background, measured in moles/L. HF=high-frequency

markers is the use of 125-I-MDA2, which bound to the malondialdehyde epitope on ox-LDL, and showed significantly higher uptake in lipid-rich lesions of atherosclerotic mice and rabbits, when compared to the uptake in healthy arteries(23).

After intravenous administration of the PET-tracer F-18-fluorodeoxyglucose, metabolically active cells may take up this tracer, which has been shown useful for imaging in inflammatory conditions. For example, atherosclerotic plaque inflammation has been imaged with PET/CT and 18F-FDG in carotid, iliac and femoral arteries of patients(24). This study showed increased uptake of 18F-FDG particularly in the carotid arteries. However, the precise relationship between 18F-FDG, plaque macrophage activity and risk of plaque rupture cannot be determined yet, due to the small number of studied patients and the fact that 18F-FDG is not a macrophage-specific PET ligand.

Nevertheless, PET is a very sensitive technique allowing imaging of disease processes *in vivo* in the nanomolar/picomolar range(25). However, PET and SPECT lack definition of anatomic structure and have limited spatial resolution, so they are unable to precisely localize the site of increased tracer uptake. Combination of imaging modalities, which can define anatomic structure, like CT and MRI, avoids this problem, yet is more expensive. MRI has the ability to localize plaque and detect its constituents. As PET does, MRI also offers the possibility to image specific molecular targets with contrast enhancing targeted probes(17,25). In the scope of universal clinical applicability, MRI is the most versatile technique. MRI does not involve ionising radiation, is safe and non-invasive, apt as a screening tool, which can be repeated several times and provides high-resolution images of the plaque(26). Disadvantages of MRI are relatively long acquisition times and poor suitability for patients, who are claustrophobic. Sequences which have been most successfully used for coronary MRI differ from those used in current clinical practice for cardiac MRI. Motion artifacts caused by respiration and cardiac contractions pose an upper limit to the time-window of MRI signal acquisition during the cardiac cycle. However, development of high-field magnet systems and more efficient pulse sequence programs may lessen these problems in the near future.

Part II

MRI of atherosclerotic plaque: up to date

Ex-vivo MRI: recent developments
Nearly two decades ago a water suppression technique was applied in order to highlight plaque lipids(27). However, limited resolution hindered differentiation between peri-adventitial fat and plaque lipids. Another study compared *in vivo* fat suppression images

with water suppression images, both obtained with chemical shift imaging(28). Plaque was more clearly delineated in the *in vivo* images using fat suppression than in the images using water suppression, which may be due to the limited resolution of the Spin Echo (SE) image. Water suppression images were only useful for localising mobile lipid-containing areas, like peri-adventitial fat(28). More recently the lipid-water ratio in perivascular fat was reported to be 1.7, whereas the lipid-water ratio in the atheromatous core was 0.11 (29), which explains the clearer delineation of plaque using fat suppression when compared to water suppression(28). Further, the discriminative role of T2 weighting (T2w) with respect to identification of plaque constituents became evident[30]. Ten years ago, the value of a combination of various MRI weightings already was recognized for characterization of carotid artery plaque(31). Multi-contrast weighted MRI, including T1w, partially T2w, fully T2w and diffusion weighted (Dw) images, allowed full ex vivo classification of carotid atherosclerotic plaque components(31). The authors suggested that Dw imaging would be necessary for identification of thrombus(31). Water diffusion was reported to vary with the ageing process of thrombus, consistent with the degree of cross-linking of the fibrin strands occurring in the acute phase and the later phase of thrombus organisation(32). Water in recent (1 week old) thrombus, but also atheromatous core diffuses more isotropically due to absence or destruction of confining structures(32). Therefore, acute and late thrombus both had higher water diffusion coefficients, whereas atheromatous core and recent thrombus had lower diffusion coefficients. Water molecules bound to macromolecules such as collagen, fibronectin and elastin can be differentiated from free water molecules by their sensitivity to an off-resonance saturation pulse, a technique called magnetisation transfer. Magnetisation transfer has been shown to decrease signal from the fibrous cap in contrast to regions of lipid in human carotid endarterectomy specimens(33). However, another study failed to show a difference in sensitivity of lipid region and fibrous cap of ex vivo plaques from apoE knockout mouse aortic roots to magnetisation transfer pulses(34). Successful discrimination between thick fibrous and thin fibrous caps, based on the difference in water diffusion, was achieved with an intravascular self-contained MRI probe and Fast SE (FSE) with an extremely short inter-echo time (12 μs)(35). Table 2 lists MRI parameters and appearance of atherosclerotic plaque components of some *ex-vivo* studies. In contrast to ex vivo MRI, for *in vivo* MR studies many problems need to be solved. Laminar/pulsating flow and motion related to cardiac contraction and respiration produce artefacts, which need to be minimized.

Intravascular in vivo MRI

Intravascular *in vivo* MRI yields enhanced image quality and permits high-resolution MR images by virtue of the proximity of the MR detector coil to the arterial wall (Figure 1).

Catheters nowadays are typically 5 F in outer diameter and a close match between coil and arterial diameter is required to prevent motion of the coil, caused by pulsating flow. Loss of signal received from regions outside the loop (Figure 1) may lead to severe image degradation(36). However, a close match is difficult to achieve in atherosclerotic vessels with various degrees of obstruction. In addition, image quality is reduced significantly as the intra-vascular coil moves off axis from the external magnet field, a significant limitation for imaging tortuous coronary arteries(37). Nevertheless, intravascular MRI was successfully applied for characterisation of human iliac artery plaque *ex-vivo* and in-vivo(38,39). In comparative *in vivo* studies, IVUS images were inferior to MR images with regard to reliable identification of plaque constituents, due to acoustic shadowing in the presence of calcifications. However, an intravascular coil could cause plaque disruption and for this reason the invasive approach is not apt for screening.

Whole body in vivo MRI

Owing to its superficial position and the absence of respiratory motion, the constituents of atherosclerotic plaque in human carotid artery have been characterized successfully *in vivo* with MRI(4,40-45). Figure 2 shows an example of successful *in vivo* multi-contrast weighted MRI for detection of intra-plaque hemorrhage. Table 3 lists technical details of some studies conducted with respect to *in vivo* MRI of human atherosclerotic plaque. The readily available histo-pathological data for comparison of MRI images after carotid endarterectomy have made *in vivo* MRI studies of carotid artery plaque attractive.

Lipid core has traditionally been visualized with T2 weighted spin echo techniques(30). More recently, T1 weighted fast spin echo and time-of-flight (TOF) imaging have gained interest, because these sequences may lead to better visualization and bright depiction of lipid core(43,46-47). Multi-contrast weighted MRI at 3T showed nice depiction of large lipid cores and an association was reported between large lipid core and thin or ruptured fibrous cap(48), which is another marker of plaque vulnerability.

Time-of-flight images were used to investigate the state of the fibrous cap(49). Not only thick fibrous caps were distinguished from intact thin caps, but also intact caps could be distinguished from ruptured ones with support of T1w, proton density (PDw) and T2w images(49).

Intra-plaque hemorrhage (IPH) has also been accepted as a marker of plaque vulnerability and is caused by rupture of fragile neovasculature not supported with firm connective tissue(50). A follow-up MRI study in humans showed that hemorrhage into the carotid atherosclerotic plaque accelerated plaque progression in an 18 month period(50). Erythrocyte membranes contain more free cholesterol than any other cell in the body and macrophages surrounding the bleeding are activated and ingest more oxidized LDL(50). Classification of stages of IPH in carotid arteries of patients scheduled for carotid

Table 2. Ex-vivo MRI studies on atherosclerotic plaques: species, MRI parameters and appearance of plaque components

author	Species	Source of material	Field strength	Resolution: In plane x slice thickness	MR Technique	TR (ms)	TE (ms)	Appearance of Plaque Components				
								LC	Calc	SMC/FT	Thr	Haem
Shinnar[31]	Human carotid endarterectomy		9.4 T	48.3x48.3 μm x 0.5mm	SE PDW	2000	13	hyper	dark	hyper	hyper	NA
					SE T1w	300/700	13	hyper	dark	hyper	hyper	NA
					SE T2w	2000	30/50	dark	dark	hyper	variable	NA
					SE Dw	2000	30	dark	dark	dark	light	NA
Booth[27]	Rabbit	Aorta	2 T	547x273 μm x 10mm	total proton SE image	1000	28	no differentiation between plaque components				
					WS SE image			only lipids visible, both adventitial and plaque lipids				
Toussaint[29]	Human	Carotid, coronary, iliac artery and aorta	9.4 T	156x156 μm x 0.6mm	SE T1w	700	3	iso	dark	iso	NA	NA
					SE T2w	2000	50	hypo	dark	hyper	NA	NA
Itskovich[66]	Human	coronary artery	9.4 T	39x39x39 μm	3D FSE PDw	2000	9	hypo	dark	hyper	iso	NA
					3D FSE T1w	500	9	hypo	dark	iso	iso	NA
					3D FSE T2w	2000	25	hypo	dark	iso	hypo	NA
Worthley[67]	Mini-swine	coronary artery/aorta	1.5 T	156x156/234x 234 μm x 2/3 mm	FSE PDw	2300	19/16	iso	dark	hyper	NA	iso
					FSE T1w	600	13/14	iso	dark	hyper	NA	high
					FSE T2w	2300	55/80	hypo	dark	hyper	NA	low
Itskovich[59]	Mouse	aortic root	9.4 T	50 x 50 μm	SE PDw	2000	9	hypo	NA	hyper	NA	NA
					SE T1w	500	9	hyper	NA	hyper	NA	NA
					SE T2w	2000	30	hypo	NA	hyper	NA	NA
Schneider[34]	Mouse	aortic root	11.7 T	47x47x63 μm	3D multi-SE and FS	200	7/14/21/28	hypo	NA	hyper	NA	NA
				47x47x125 μm	MT	480	18	hypo	NA	hyper	NA	NA
				47x47x252 μm	WS	100	6.1	dark	NA	iso	NA	NA

TR = repetition time; TE = echo time; LC = Lipid Core; Calc = Calcification; SMC/FT = Smooth Muscle Cells/ Fibrous Tissue; Thr = Thrombus; Haem = Haemorrhage; (F)SE = (fast) spin echo; PDw = proton density weighting; intensity on MR images: hyper>iso>hypo>dark; NA = not available or not assessed; WS= water suppression; FS= fat suppression; IR= Inversion recovery; MT = Magnetisation Transfer; Dw= diffusion weighting; for other abbreviations, see Table 1.
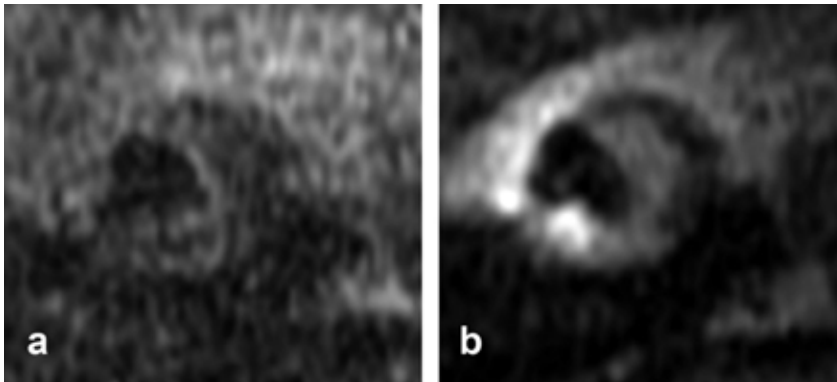
Figure 1. Printed with permission from Larose et al. [39]. Comparison of IVMRI and surface MRI. T1w surface MRI (a) and IVMRI (b) of a common iliac artery in a subject with an atheromatous plaque illustrates better image quality with IVMRI compared with surface MRI. Both images were produced by use of identical parameters (TR, 500 ms; TE, 13 ms; band width, 16 kHz; field of view, 9 cm; matrix, 256x256; no phase wrap) and in-plane resolution of 316 μm, but the relative SNR is superior for IVMRI. However, in case of a circumferential plaque the position of the catheter coil determines the local signal intensity of a plaque component, so homogeneity of the image SNR is impaired.
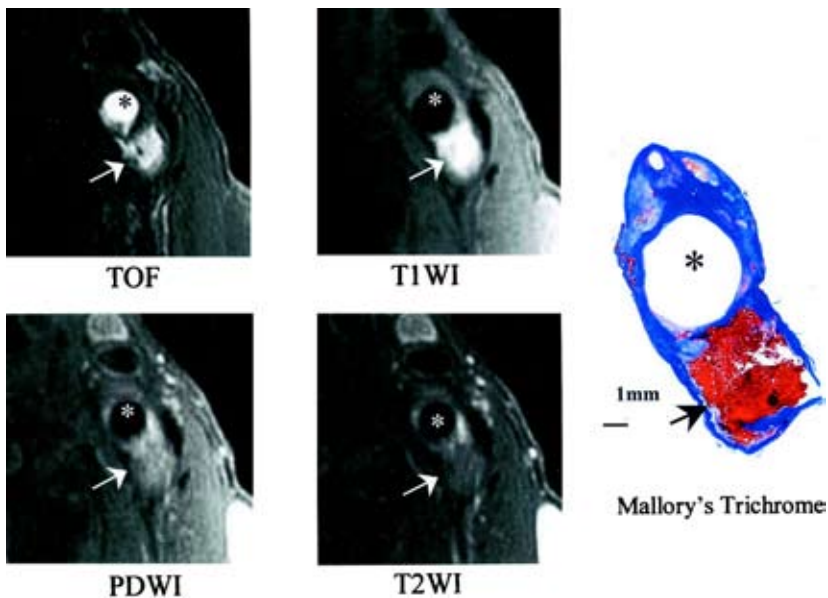

*Figure 2. Printed with permission from Cai et al. [44]. Example of type VI lesion just distal to carotid bifurcation (acute and subacute hemorrhages were detected by histology). On multicontrast-weighted MR images, acute and subacute hemorrhage had high SI on both TOF and T1WI images, iso-SI to slightly high SI on PDWI and T2WI images (arrow). * indicates lumen. Original magnification x10.*

Table 3 In vivo MRI studies on atherosclerotic plaques: MRI parameters and appearance of plaque components

Author	Species	Imaged vessel	Field strength	Technique	Resolution: In plane x slice thickness	TR (ms)	FA	TE (ms)	Appearance plaque components				
									LC	Calc	SMC/FT	Thr	Haem.
Vinitski [28]	rabbit/ human	abdominal aorta/ carotid artery	1.5 T	SE T1w	500x500 µm x 4mm	700 ms	90	12	no differentiation between plaque components				
				CSI FS			90	14	no differentiation between plaque components				
				CSI WS			90	14	only peri-adventitial lipid visible				
Toussaint [30]	Human	carotid artery	1.5 T	SE T2w	390x390 µm x 5mm	1 RR	90	20/55	hypo	dark	hyper	fresh: hyper organising: hypo	hypo
Cai[43]	Human	carotid artery	1.5 T	DIR FSE PDw	500x500 µm x 1/2 mm	3 RR	90	20	iso-hyper	dark	hyper	NA	(subacute: iso-hyper)
				DIR FSE T1w		800	90	9.3	iso	dark	hyper	NA	(sub)acute: hyper
				DIR FSE T2w		3 RR	90	40	iso-hyper	dark	iso	NA	(subacute: iso-hyper)
				3D TOF		23	25	3.8	iso	dark	hypo	NA	(sub)acute: hyper
Cappendijk [40]	Human	carotid artery	1.5 T	FSE PDw	390x390 µm x 2.5 mm	2 RR	90	20	hypo	dark	iso	NA	iso
				DIR FSE T1w		570	90	14	iso	dark	hyper	NA	hyper
				FSE T2w	390x490 µm x 3 mm	2 RR	90	30/50	hypo	dark	hyper	NA	iso
				3D EPI T1w with IR		10.3	15	4.0	hypo	dark	iso	NA	hyper
Chu [45]	Human	carotid artery	1.5 T		625x625 µm x 2 mm				fresh hem.		recent hem.		old hem.
				FSE PDw		3-4 RR	90	20	hypo/iso		hyper		hypo
				FSE T1w		800	90	9.3	hyper		hyper		hypo
				FSE T2w		3-4 RR	90	40	hypo/iso		hyper		hypo
				3D TOF		23	25	3.5	hyper		hyper		hypo

FA=flip angle of excitation pulse; DIR= double inversion recovery; EPI= echo planar imaging; RR= R-peak (ECG) to R-peak interval. For explanation of other abbreviations, see Table 2.

endarterectomy was performed using multi-contrast weighted MRI(45). The classification showed moderate agreement with the classification into fresh, recent and old categories according to histopathological criteria after carotid endarterectomy. Another study reported successful discrimination between IPH and luminal thrombus in human carotid artery lesions with four different MR weightings(51).

The ability of a non-invasive imaging technique to discriminate fresh from old luminal thrombus has obvious clinical relevance. Definitely, recent thrombosis has prognostic implications with regard to future acute coronary events(52). Carotid thrombi were induced in swine by arterial injury and could be differentiated in recent and old thrombi by assessment of signal intensity on T2w at 1.5 T(53).

In recent years, various mouse models have been developed in order to study the role of specific genes in cardiovascular pathophysiology. Several transgenic and knockout models to study vascular biology and atherosclerosis have been reported: e.g. apolipoprotein E deficient(54), apoE3-Leiden(55), low-density lipoprotein receptor deficient(26), and apoE/eNOS double knockout mice(56).

Successful MRI of aortic plaque in mice at high field may close the gap between successful *in vivo* MRI of human carotid plaque and thus far unsuccessful coronary plaque MRI at low field, because of similarity of size of human coronary artery and mouse aorta and the advent of clinical high field magnets. Wild-type mouse aortic wall thickness has been reported to measure ~ 50 μm at the abdominal level(57) and ~70 μm at the thoracic level(58). MRI measurements of abdominal aortic wall thickness of ApoE deficient mice revealed doubled wall thickness when compared to wild-type mice(57). At the thoracic and aortic root level the effect of the gene defect on the aortic wall thickness was even more conspicuous than at the abdominal level(58,59). Aortic wall area/thickness measurements in atherosclerotic mouse models and correlation coefficients between MRI and histopathology obtained from various mouse MR studies are listed in Table 4. MRI showed that increased wall area of the abdominal aorta of apoE deficient mice was completely compensated by outward remodeling, resulting in a constant lumen, as could be verified with histopathology(60). Aortic wall thickness was larger as assessed by MRI than when assessed by histopathology, which probably is caused by shrinkage through dehydration by the alcohol.

Imaging of the thoracic aorta in the mouse requires a nontrivial effort, because of small size and cardiac and respiratory motions. The heart in an awake mouse beats 600/min(61,62). *In vivo* assessment of plaque composition with MRI in the murine aorta has not been achieved thus far. Nevertheless, wall thickness/area and plaque area in the murine aortic root and brachiocephalic artery have been measured with MRI and compared with histopathology(26,59). A 3-dimensional MR technique was used, which offers the

Table 4 Mouse MRI studies on atherosclerotic vessel wall: MRI parameters and correlation with histology

Author	Mouse strain / Target of imaging	Field Strength	MRI technique	TR (ms)	TE (ms)	resolution	correlation between MR and histology	
							maximal wall thickness ± SD, μm	wall area, mm2
Fayad[55]	apoE-/-	9.4 T	SE PDw	2000	13	97x97x500μm/ 48x48x500μm	NA	MRI: 0.384±0.046 Hist.: 0.300±0.035 r=0.86
	abdominal aorta, iliac artery		SE T1w	1000	13	97x97x500μm/ 48x48x500μm		
			SE T2w	2000	30	97x97x500/ 48x48x500μm		
Choudhury[58]	apoE-/-, apoE-/-/apoA-I*	9.4 T	SE PDw	2000	9	109x109x500 μm	NA	MRI: 0.334† Hist.: 0.126† r=0.85
	abdominal aorta							
Itskovich[57]	apoE-/-(/apoA-I)	9.4 T	SE PDw	2000	9	156/78x156/78x 300 μm	MRI: 589±164 Hist.: 486±155 r>0.90	MRI: 2.09±1.04 Hist.: 1.74±0.92 r>0.90
	aortic root		SE T1w	500	9			
			SE T2w	2000	30			
Wiesmann[56]	apoE-/-	7T	SE T1w	1000	10	49x98x300 μm	MRI: 238±100 Hist.: ?	MRI: 1.19±0.19 Hist.: 0.96±? r=0.97
	thoracic aorta		3D FLASH	4.6	1.5	100x100x39 μm		
Hockings[26]	LDLR-/-§	7 T	3D FSE ± FS	800	13	140x187x187 μm	NA	MRI: 0.14±0.086 Hist.: 0.308±0.081 r=0.8
	innominate artery							

* human apolipoprotein A-I, Choudhury et al.: total study group has a wide range of severity of atherosclerosis † median value § Low-density lipoprotein receptor-deficient mice
For explanation of abbreviations, see Table 2.

advantage to reconstruct an image in any chosen orientation after the measurements have taken place(26). A very high correlation between MRI measurements and histopathology measurements of aortic wall area was demonstrated(58). Probably, the smaller difference between MRI and histopathology measurements of wall area in the latter study when compared to Choudhury et al.(60) can be explained by the smaller pixel dimensions of the images.

In vivo imaging of human coronary arteries requires cardiac and respiratory gating. Prospective gating increases measurement time, however retrospective gating and breath-hold techniques increase time efficiency tremendously. For use as a clinical screening tool, which scans the whole coronary artery tree, a sophisticated tracking strategy is required, to compensate for the motion and tortuosity of the coronary arteries(63). Wall thickness and remodelling of coronary arteries have been studied *in vivo* with MRI(64,65). Until now it has not been possible to identify different plaque constituents in the coronary arteries *in vivo* because of earlier mentioned problems.

Several research groups are involved in the solution of technical problems, while others are involved in contrast-enhanced MRI, which allows lower SNR because of increased contrast between targets of interest and their background. Equally important, the possibility to use vehicles carrying not only (super)paramagnetic agents but also antibodies, peptides or receptor agonists, provides a technique which is capable of targeting vulnerable plaque markers which are more specific and/or sensitive for prediction of plaque disruption than the classical morphologic features.

Reference List

1. Fayad ZA, Fuster V (2001), Clinical imaging of the high-risk or vulnerable atherosclerotic plaque, Circ. Res. 89: 305-316
2. Badimon L (2001), Atherosclerosis and thrombosis: lessons from animal models, Thromb.Haemost. 86: 356-365
3. Ross R (1999), Atherosclerosis is an inflammatory disease, Am.Heart J. 138: S419-S420
4. Mitsumori LM, Hatsukami TS, Ferguson MS, Kerwin WS, Cai J, Yuan C (2003), In vivo accuracy of multisequence MR imaging for identifying unstable fibrous caps in advanced human carotid plaques, J.Magn Reson.Imaging. 17: 410-420
5. Leiner T, Gerretsen S, Botnar R, Lutgens E, Cappendijk V, Kooi E, van EJ (2005), Magnetic resonance imaging of atherosclerosis, Eur.Radiol. 15: 1087-1099
6. Vink A, Pasterkamp G (2002), Atherosclerotic plaque burden, plaque vulnerability and arterial remodeling: the role of inflammation, Minerva Cardioangiol. 50: 75-83
7. Corti R, Fuster V (2003), New understanding, diagnosis, and prognosis of atherothrombosis and the role of imaging, Am.J.Cardiol. 91: 17A-26A
8. Ambrose JA, Tannenbaum MA, Alexopoulos D, Hjemdahl-Monsen CE, Leavy J, Weiss M, Borrico S, Gorlin R, Fuster V (1988), Angiographic progression of coronary artery disease and the development of myocardial infarction, J.Am.Coll.Cardiol. 12: 56-62
9. de Korte CL, Pasterkamp G, van der Steen AF, Woutman HA, Bom N (2000), Characterization of plaque components with intravascular ultrasound elastography in human femoral and coronary arteries in vitro, Circulation. 102: 617-623
10. Jang IK, Tearney GJ, MacNeill B, Takano M, Moselewski F, Iftima N, Shishkov M, Houser S, Aretz HT, Halpern EF, Bouma BE (2005), In vivo characterization of coronary atherosclerotic plaque by use of optical coherence tomography, Circulation. 111: 1551-1555
11. van de Poll SW, Kastelijn K, Bakker Schut TC, Strijder C, Pasterkamp G, Puppels GJ, van der LA (2003), On-line detection of cholesterol and calcification by catheter based Raman spectroscopy in human atherosclerotic plaque ex vivo, Heart. 89: 1078-1082
12. Wang J, Geng YJ, Guo B, Klima T, Lal BN, Willerson JT, Casscells W (2002), Near-infrared spectroscopic characterization of human advanced atherosclerotic plaques, J.Am.Coll.Cardiol. 39: 1305-1313
13. Toutouzas K, Drakopoulou M, Mitropoulos J, Tsiamis E, Vaina S, Vavuranakis M, Markou V, Bosinakou E, Stefanadis C (2006), Elevated plaque temperature in non-culprit de novo atheromatous lesions of patients with acute coronary syndromes, J.Am.Coll.Cardiol. 47: 301-306
14. Waki H, Masuyama T, Mori H, Maeda T, Kitade K, Moriyasu K, Tsujimoto M, Fujimoto K, Koshimae N, Matsuura N (2003), Ultrasonic tissue characterization of the atherosclerotic carotid artery: histological correlates or carotid integrated backscatter, Circ.J. 67: 1013-1016
15. Leber AW, Knez A, von ZF, Becker A, Nikolaou K, Paul S, Wintersperger B, Reiser M, Becker CR, Steinbeck G, Boekstegers P (2005), Quantification of obstructive and nonobstructive coronary lesions by 64-slice computed tomography: a comparative study with quantitative coronary angiography and intravascular ultrasound, J.Am.Coll.Cardiol. 46: 147-154
16. Ben-Haim S, Israel O (2006), PET/CT for atherosclerotic plaque imaging, J.Nucl.Med.Mol.Imaging. 50: 53-60
17. Choudhury RP, Fisher EA (2009), Molecular Imaging in Atherosclerosis, Thrombosis, and Vascular Inflammation, Arterioscler.Thromb.Vasc.Biol. 29: 983-991
18. Thompson BH, Stanford W (2005), Update on using coronary calcium screening by computed tomography to measure risk for coronary heart disease, Int.J.Cardiovasc.Imaging. 21: 39-53
19. Dey D, Slomka P, Chien D, Fieno D, Abidov A, Saouaf R, Thomson L, Friedman JD, Berman DS (2006), Direct quantitative in vivo comparison of calcified atherosclerotic plaque on vascular MRI and CT by multimodality image registration, J.Magn Reson.Imaging. 23: 345-354
20. Viles-Gonzalez JF, Poon M, Sanz J, Rius T, Nikolaou K, Fayad ZA, Fuster V, Badimon JJ (2004), In vivo 16-slice, multidetector-row computed tomography for the assessment of experimental atherosclerosis: comparison with magnetic resonance imaging and histopathology, Circulation. 110: 1467-1472
21. Leber AW, Becker A, Knez A, von ZF, Sirol M, Nikolaou K, Ohnesorge B, Fayad ZA, Becker CR, Reiser M, Steinbeck G, Boekstegers P (2006), Accuracy of 64-slice computed tomography to classify and quan-

tify plaque volumes in the proximal coronary system: a comparative study using intravascular ultrasound, J.Am.Coll.Cardiol. 47: 672-677

22. Kolodgie FD, Petrov A, Virmani R, Narula N, Verjans JW, Weber DK, Hartung D, Steinmetz N, Vander-heyden JL, Vannan MA, Gold HK, Reutelingsperger CP, Hofstra L, Narula J (2003), Targeting of apoptotic macrophages and experimental atheroma with radiolabeled annexin V: a technique with potential for non-invasive imaging of vulnerable plaque, Circulation. 108: 3134-3139

23. Tsimikas S, Shortal BP, Witztum JL, Palinski W (2000), In vivo uptake of radiolabeled MDA2, an oxida-tion-specific monoclonal antibody, provides an accurate measure of atherosclerotic lesions rich in oxidized LDL and is highly sensitive to their regression, Arterioscler.Thromb.Vasc.Biol. 20: 689-697

24. Rudd JH, Myers KS, Bansilal S, Machac J, Pinto CA, Tong C, Rafique A, Hargeaves R, Farkouh M, Fuster V, Fayad ZA (2008), Atherosclerosis inflammation imaging with 18F-FDG PET: carotid, iliac, and femoral uptake reproducibility, quantification methods, and recommendations, J.Nucl.Med. 49: 871-878

25. Massoud TF, Gambhir SS (2003), Molecular imaging in living subjects: seeing fundamental biological processes in a new light, Genes Dev. 17: 545-580

26. Hockings PD, Roberts T, Galloway GJ, Reid DG, Harris DA, Vidgeon-Hart M, Groot PH, Suckling KE, Benson GM (2002), Repeated three-dimensional magnetic resonance imaging of atherosclerosis develop-ment in innominate arteries of low-density lipoprotein receptor-knockout mice, Circulation. 106: 1716-1721

27. Booth RF, Honey AC, Martin JF, Lindon JC, Farrant RD, Carpenter TA, Hall LD (1990), Lipid charac-terization in an animal model of atherosclerosis using NMR spectroscopy and imaging, NMR Biomed. 3: 95-100

28. Vinitski S, Consigny PM, Shapiro MJ, Janes N, Smullens SN, Rifkin MD (1991), Magnetic resonance chemical shift imaging and spectroscopy of atherosclerotic plaque, Invest Radiol. 26: 703-714

29. Toussaint JF, Southern JF, Fuster V, Kantor HL (1995), T2-weighted contrast for NMR characterization of human atherosclerosis, Arterioscler.Thromb.Vasc.Biol. 15: 1533-1542

30. Toussaint JF, LaMuraglia GM, Southern JF, Fuster V, Kantor HL (1996), Magnetic resonance images lipid, fibrous, calcified, hemorrhagic, and thrombotic components of human atherosclerosis in vivo, Circulation. 94: 932-938

31. Shinnar M, Fallon JT, Wehrli S, Levin M, Dalmacy D, Fayad ZA, Badimon JJ, Harrington M, Harrington E, Fuster V (1999), The diagnostic accuracy of ex vivo MRI for human atherosclerotic plaque characteriza-tion, Arterioscler.Thromb.Vasc.Biol. 19: 2756-2761

32. Toussaint JF, Southern JF, Fuster V, Kantor HL (1997), Water diffusion properties of human atherosclerosis and thrombosis measured by pulse field gradient nuclear magnetic resonance, Arterioscler.Thromb.Vasc. Biol. 17: 542-546

33. Rogers WJ, Prichard JW, Hu YL, Olson PR, Benckart DH, Kramer CM, Vido DA, Reichek N (2000), Char-acterization of signal properties in atherosclerotic plaque components by intravascular MRI, Arterioscler. Thromb.Vasc.Biol. 20: 1824-1830

34. Schneider JE, McAteer MA, Tyler DJ, Clarke K, Channon KM, Choudhury RP, Neubauer S (2004), High-resolution, multicontrast three-dimensional-MRI characterizes atherosclerotic plaque composition in ApoE-/- mice ex vivo, J.Magn Reson.Imaging. 20: 981-989

35. Schneiderman J, Wilensky RL, Weiss A, Samouha E, Muchnik L, Chen-Zion M, Ilovitch M, Golan E, Blank A, Flugelman M, Rozenman Y, Virmani R (2005), Diagnosis of thin-cap fibroatheromas by a self-contained intravascular magnetic resonance imaging probe in ex vivo human aortas and in situ coronary arteries, J.Am.Coll.Cardiol. 45: 1961-1969

36. MacNeill BD, Lowe HC, Takano M, Fuster V, Jang IK (2003), Intravascular modalities for detection of vulnerable plaque: current status, Arterioscler.Thromb.Vasc.Biol. 23: 1333-1342

37. Correia LC, Atalar E, Kelemen MD, Ocali O, Hutchins GM, Fleg JL, Gerstenblith G, Zerhouni EA, Lima JA (1997), Intravascular magnetic resonance imaging of aortic atherosclerotic plaque composition, Arterio-scler.Thromb.Vasc.Biol. 17: 3626-3632

38. Larose E, Yeghiazarians Y, Libby P, Yucel EK, Aikawa M, Kacher DF, Aikawa E, Kinlay S, Schoen FJ, Selwyn AP, Ganz P (2005), Characterization of human atherosclerotic plaques by intravascular magnetic resonance imaging, Circulation. 112: 2324-2331

39. Larose E, Kinlay S, Selwyn AP, Yeghiazarians Y, Yucel EK, Kacher DF, Libby P, Ganz P (2008), Improved characterization of atherosclerotic plaques by gadolinium contrast during intravascular magnetic resonance

imaging of human arteries, Atherosclerosis. 196: 919-925

40. Cappendijk VC, Cleutjens KB, Kessels AG, Heeneman S, Schurink GW, Welten RJ, Mess WH, Daemen MJ, van Engelshoven JM, Kooi ME (2005), Assessment of human atherosclerotic carotid plaque components with multisequence MR imaging: initial experience, Radiology. 234: 487-492

41. Cappendijk VC, Heeneman S, Kessels AG, Cleutjens KB, Schurink GW, Welten RJ, Mess WH, van Suylen RJ, Leiner T, Daemen MJ, van Engelshoven JM, Kooi ME (2008), Comparison of single-sequence T1w TFE MRI with multisequence MRI for the quantification of lipid-rich necrotic core in atherosclerotic plaque, J.Magn Reson.Imaging. 27: 1347-1355

42. Luo Y, Polissar N, Han C, Yarnykh V, Kerwin WS, Hatsukami TS, Yuan C (2003), Accuracy and uniqueness of three in vivo measurements of atherosclerotic carotid plaque morphology with black blood MRI, Magn Reson.Med. 50: 75-82

43. Cai JM, Hatsukami TS, Ferguson MS, Small R, Polissar NL, Yuan C (2002), Classification of human carotid atherosclerotic lesions with in vivo multicontrast magnetic resonance imaging, Circulation. 106: 1368-1373

44. Cai J, Hatsukami TS, Ferguson MS, Kerwin WS, Saam T, Chu B, Takaya N, Polissar NL, Yuan C (2005), In vivo quantitative measurement of intact fibrous cap and lipid-rich necrotic core size in atherosclerotic carotid plaque: comparison of high-resolution, contrast-enhanced magnetic resonance imaging and histology, Circulation. 112: 3437-3444

45. Chu B, Kampschulte A, Ferguson MS, Kerwin WS, Yarnykh VL, O'Brien KD, Polissar NL, Hatsukami TS, Yuan C (2004), Hemorrhage in the atherosclerotic carotid plaque: a high-resolution MRI study, Stroke. 35: 1079-1084

46. Yuan C, Mitsumori LM, Ferguson MS, Polissar NL, Echelard D, Ortiz G, Small R, Davies JW, Kerwin WS, Hatsukami TS (2001), In vivo accuracy of multispectral magnetic resonance imaging for identifying lipid-rich necrotic cores and intraplaque hemorrhage in advanced human carotid plaques, Circulation. 104: 2051-6

47. Saam T, Hatsukami TS, Takaya N, Chu B, Underhill H, Kerwin WS, Cai J, Ferguson MS, Yuan C (2007), The vulnerable, or high-risk, atherosclerotic plaque: noninvasive MR imaging for characterization and assessment, Radiology. 244: 64-77

48. Ota H, Yu W, Underhill HR, Oikawa M, Dong L, Zhao X, Polissar NL, Neradilek B, Gao T, Zhang Z, Yan Z, Guo M, Zhang Z, Hatsukami TS, Yuan C (2009), Hemorrhage and large lipid-rich necrotic cores are independently associated with thin or ruptured fibrous caps: an in vivo 3T MRI study, Arterioscl.Thromb. Vasc.Biol. 29: 1696-1701.

49. Yuan C, Zhang SX, Polissar NL, Echelard D, Ortiz G, Davis JW, Ellington E, Ferguson MS, Hatsukami TS (2002), Identification of fibrous cap rupture with magnetic resonance imaging is highly associated with recent transient ischemic attack or stroke, Circulation. 105: 181-185

50. Takaya N, Yuan C, Chu B, Saam T, Polissar NL, Jarvik GP, Isaac C, McDonough J, Natiello C, Small R, Ferguson MS, Hatsukami TS (2005), Presence of intraplaque hemorrhage stimulates progression of carotid atherosclerotic plaques: a high-resolution magnetic resonance imaging study, Circulation. 111: 2768-2775

51. Kampschulte A, Ferguson MS, Kerwin WS, Polissar NL, Chu B, Saam T, Hatsukami TS, Yuan C (2004), Differentiation of intraplaque versus juxtaluminal hemorrhage/thrombus in advanced human carotid atherosclerotic lesions by in vivo magnetic resonance imaging, Circulation. 110: 3239-3244

52. Corti R, Fuster V (2003), New understanding, diagnosis, and prognosis of atherothrombosis and the role of imaging, Am.J.Cardiol. 91: 17A-26A

53. Corti R, Osende JI, Fayad ZA, Fallon JT, Fuster V, Mizsei G, Dickstein E, Drayer B, Badimon JJ (2002), In vivo noninvasive detection and age definition of arterial thrombus by MRI, J.Am.Coll.Cardiol. 39: 1366-1373

54. Zhang SH, Reddick RL, Piedrahita JA, Maeda N (1992), Spontaneous hypercholesterolemia and arterial lesions in mice lacking apolipoprotein E, Science. 258: 468-471

55. Lutgens E, Daemen M, Kockx M, Doevendans P, Hofker M, Havekes L, Wellens H, de Muinck ED (1999), Atherosclerosis in APOE*3-Leiden transgenic mice: from proliferative to atheromatous stage, Circulation. 99: 276-283

56. Kuhlencordt PJ, Gyurko R, Han F, Scherrer-Crosbie M, Aretz TH, Hajjar R, Picard MH, Huang PL (2001), Accelerated atherosclerosis, aortic aneurysm formation, and ischemic heart disease in apolipoprotein E/ endothelial nitric oxide synthase double-knockout mice, Circulation. 104: 448-454

57. Fayad ZA, Fallon JT, Shinnar M, Wehrli S, Dansky HM, Poon M, Badimon JJ, Charlton SA, Fisher EA,

Breslow JL, Fuster V (1998), Noninvasive In vivo high-resolution magnetic resonance imaging of athero-sclerotic lesions in genetically engineered mice, Circulation 98: 1541-1547

58. Wiesmann F, Szimtenings M, Frydrychowicz A, Illinger R, Hunecke A, Rommel E, Neubauer S, Haase A (2003), High-resolution MRI with cardiac and respiratory gating allows for accurate in vivo atherosclerotic plaque visualization in the murine aortic arch, Magn Reson.Med. 50: 69-74

59. Itskovich VV, Choudhury RP, Aguinaldo JG, Fallon JT, Omerhodzic S, Fisher EA, Fayad ZA (2003), Char-acterization of aortic root atherosclerosis in ApoE knockout mice: high-resolution in vivo and ex vivo MRM with histological correlation, Magn Reson.Med. 49: 381-385

60. Choudhury RP, Aguinaldo JG, Rong JX, Kulak JL, Kulak AR, Reis ED, Fallon JT, Fuster V, Fisher EA, Fayad ZA (2002), Atherosclerotic lesions in genetically modified mice quantified in vivo by non-invasive high-resolution magnetic resonance microscopy, Atherosclerosis. 162: 315-321

61. Weiss RG (2001), Imaging the murine cardiovascular system with magnetic resonance, Circ.Res. 88: 550-551

62. Wehrens XH, Kirchhoff S, Doevendans PA (2000), Mouse electrocardiography: An interval of thirty years, Cardiovasc Res. 45:231-7

63. Wendt M, Wacker FK (2000), Visualization, tracking, and navigation of instruments for magnetic reso-nance imaging-guided endovascular procedures, Top.Magn Reson.Imaging 11: 163-172

64. Kim WY, Stuber M, Bornert P, Kissinger KV, Manning WJ, Botnar RM (2002), Three-dimensional black-blood cardiac magnetic resonance coronary vessel wall imaging detects positive arterial remodeling in patients with nonsignificant coronary artery disease, Circulation 106: 296-299

65. Miao C, Chen S, Macedo R, Lai S, Liu K, Li D, Wasserman BA, Vogel-Claussen J, Lima JA, Bluemke DA (2009), Positive remodeling of the coronary arteries detected by magnetic resonance imaging in an asymp-tomatic population: MESA (Multi-Ethnic Study of Atherosclerosis), J Am.Coll.Cardiol. 53: 1708-1715

66. Itskovich VV, Samber DD, Mani V, Aguinaldo JG, Fallon JT, Tang CY, Fuster V, Fayad ZA. (2004), Quanti-fication of human atherosclerotic plaques using spatially enhanced cluster analysis of multicontrast-weight-ed magnetic resonance images, Magn Reson. Med. 52: 515-23

67. Worthley SG, Helft G, Fuster V, Fayad ZA, Fallon JT, Osende JI, Roqué M, Shinnar M, Zaman AG, Rod-riguez OJ, Verhallen P, Badimon JJ. (2000), High resolution ex vivo magnetic resonance imaging of in situ coronary and aortic atherosclerotic plaque in a porcine model, Atherosclerosis 150: 321-9.

Chapter 3

Recent developments and new perspectives on imaging of atherosclerotic plaque: Role of cellular and molecular MRI

Bernard C.M. te Boekhorst[1,2], MD; Maarten-Jan M. Cramer[1], MD, PhD; Gerard Pasterkamp[1], MD, PhD; Cees J.A. van Echteld[1,3], PhD; Pieter A.F.M. Doevendans[1], MD, PhD

[1]*Department of Cardiology, University Medical Center Utrecht;* [2]*Interuniversity Cardiology Institute of the Netherlands,* [3]*Present address: Novartis Institutes for BioMedical Research, Basel, Switzerland*

Abstract

Atherosclerotic plaque disruption accounts for the major part of cardiovascular mortality and the risk of disruption appears to depend on plaque composition. Carotid plaques in patients, scheduled for endarterectomy, have been succesfully characterised with MRI. MRI has the advantage of combining information about morphology and function. Unfortunately, the tortuosity and size of the coronary arteries, and the respiratory and cardiac motion hinder the *in vivo* characterisation of human coronary plaque. In addition to plaque composition several molecular markers of the different processes involved in atherosclerosis, such as integrins, matrix metalloproteinases (MMPs) and fibrin seem to correlate with risk of plaque rupture and clinical outcome. These molecular markers can be targeted with antibodies coupled to carriers, which are loaded with gadolinium for detection (molecular MRI). Several cellular/molecular MRI studies in animal models and some in human patients have been conducted with varying levels of success. The advent of clinical high field magnets, the development of contrast agent carriers with high relaxivity and the development of relatively new MR contrast techniques appear to be promising in the field of plaque imaging. Future MRI studies will have to focus on the molecular target of the atherosclerotic process, which has the highest prognostic value with regard to acute coronary syndromes and on the most suitable contrast agent to visualize that target.

Part III

Contrast-enhanced cellular and molecular MRI: up to date

Inflammation and endothelial dysfunction reinforce each other in the process of atherosclerotic plaque formation. It is not known why some plaques stay stable whereas others become vulnerable within a short term. More or less in the following time order various processes take place in the developing plaque from fatty streak to vulnerable and ruptured plaque. First, oxidized LDL uptake into the subintima stimulates endothelial cells to become dysfunctional, leading to inflammatory cell migration and activation, release of matrix degrading enzymes and other factors that eventually result in apoptosis of smooth muscle cells and macrophages. This may lead to fibrous cap thinning, lipid core growth, formation of fragile intraplaque neovasculature, IPH and finally fibrous cap rupture and thrombus formation, which may cause an acute thrombotic event. Figure 3 provides a graphical representation of the atherosclerotic process. For further information, some excellent reviews are available, which discuss in depth the process of atherosclerosis(1,2). Many elements in this figure represent targets for molecular or cellular MRI.

Macrophage Imaging with Iron Oxides

An important example of cellular MRI in atherosclerosis is visualisation of macrophage-rich plaques with iron-based contrast agents.

Iron-based contrast agents cause loss of signal on T2 weighted images, which is called "negative" contrast. Superparamagnetic particles of iron oxide (SPIOs) are particles with a size of 100-200 nm, ultrasmall particles of iron oxide (USPIOs) have a total hydrated particle size of only 18-30 nm. SPIOs are filtered from the blood by specific cells in the liver (Kupffer cells) and the reticulo-endothelial system (RES) of the spleen. Therefore, SPIOs were initally used in the context of lymph node imaging for tumor staging and detection of focal liver lesions(3). During a phase III trial, which investigated the use of USPIOs as a MRI contrast agent for staging of lymph node metastases, a focal subendothelial signal loss of the aortic and common iliac artery wall on T2*-weighted images at 24 and 36 hours after administration of 46 µmol/kg USPIOs suggested USPIO uptake in atherosclerotic plaque(4). This signal loss was associated with USPIO uptake by macrophages, which are believed to be an important hallmark of unstable plaques. Both SPIOs and USPIOs are made up of an iron crystalline core that consists primarily of superparamagnetic iron oxide, and a biocompatible coating such as dextran, carboxydextran, polyethylene glycol (PEG), or starch. USPIOs are not filtered from the blood by the RES of the spleen and liver at the fast rate of SPIOs, primarily due to their size.

Because of their long half-life in blood, USPIOs can be taken up by macrophages in the whole body. USPIOs have been used to study the *in vivo* presence of macrophage-rich plaques in the rabbit aorta(5). In Watanabe heritable hyperlipidemic rabbits, 3D MR angiography showed susceptibility effects of iron in the vessel wall, which represented USPIO uptake in plaque macrophages, 4 or 5 days after administration of 1 mmol Fe/kg (Figure 4). In the same study conventional 3D contrast-enhanced MRA with Gd-DOTA did not show irregularities of the aortic wall. Changes in T2*-contrast of human aortic atherosclerotic wall can be observed *in vivo* 24 hours after administration of USPIOs at a dose of 200 µmol/kg(6). *In vivo* MRI at 1.5 T of carotid atherosclerotic plaque in some patients, scheduled for surgery, showed a signal decrease on post-contrast T2*-weighted gradient echo images(6). Ruptured and rupture-prone lesions identified by histopathology (disrupted fibrous cap with thrombus and a very thin fibrous cap respectively) showed USPIO accumulation more frequently than stable lesions(6). A larger *in vivo* MRI study of human carotid artery plaque showed that focal signal loss corresponded to macrophage uptake in the fibrous cap(7). However, half of the patients showed diffuse signal loss, which corresponded to diffuse iron staining. Routing and exact destination of these USPIOs were not clear. Other patient studies confirmed these results(8-10). A recent MRI study of human carotid artery plaque showed differentiation between minor and major uptake of USPIOs by a signal increase on the T1 weighted image by a predominant T1

shortening effect and a signal decrease on the T2* weighted image, respectively(11).

Not only USPIOs, but also SPIOs have been found in aortic atherosclerotic plaque in mice after intravenous administration, despite earlier found gross filtering by the RES(12). The effect of cytokines on monocyte recruitment in mouse aortic atherosclerotic plaque after administration of SPIOs has been investigated. Various cytokines stimulated uptake of SPIOs into the plaque(12).

In the study of Ruehm et al., optimized MRI contrast was achieved with a conventional MR angiography sequence at 5-6 days after administration of 1 mmol/kg USPIOs(5). Earlier imaging led to increased "blooming" of the aortic wall because of increased blood levels of USPIOs(5). The word "blooming" is reserved for the effect that the
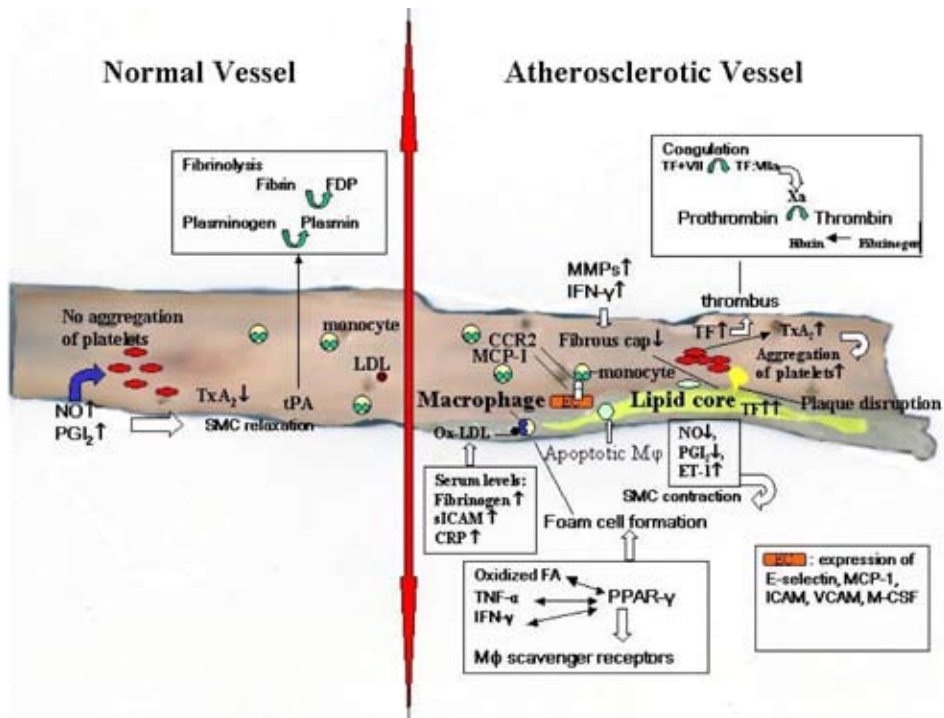

Figure 3. Pathogenesis of plaque development. White arrows, stimulation; black arrows, inhibition; green arrows, conversion; double arrows, ligand-receptor interaction. Abbreviations: FDP = fibrin degradation products; TF = tissue factor; MMPs= matrix metallo proteinases; IFN-γ= interferon gamma; NO= nitric oxide; PGI2= prostacycline; ET-1= endothelin 1; SMC= smooth muscle cell; TxA2= tromboxane A2; tPA= tissue plasminogen activator; (ox)LDL= (oxidised) low density lipoprotein; MCP-1= monocyte chemo-attractant protein 1; CCR2= receptor for MCP-1 (on monocytes); EC= endothelial cell; (s)ICAM= (soluble) intercellular adhesion molecule; CRP= C-reactive protein; FA= fatty acids; TNF-α= tumor necrosis factor alfa; MΦ= macrophage; PPAR-γ= peroxisome proliferator-activated receptor-gamma; VCAM= vascular cell adhesion molecule; M-CSF= macrophage colony-stimulating factor

USPIO-enhanced region may be much larger than, and not corresponding to the region of the USPIO uptake(3). This effect is due to extreme susceptibility effects of iron-based contrast agents, and creates an important disadvantage of these negative contrast agents. The dose of the contrast agent will be decisive in the extent of this effect. Furthermore, iron ingested by macrophages may appear in the subendothelium of existing plaques(13), at the edges of existing plaques and in areas free of lesions, which in the latter case could indicate fatty streaks(12). But iron may also be ingested by macrophages present at other inflammation sites or tumors(4), demonstrating limited specificity of (U)SPIOs. Moreover, because most MR techniques used for imaging of atherosclerotic plaque are dark-blood techniques, differentiation between blood and adjacent plaque constituents
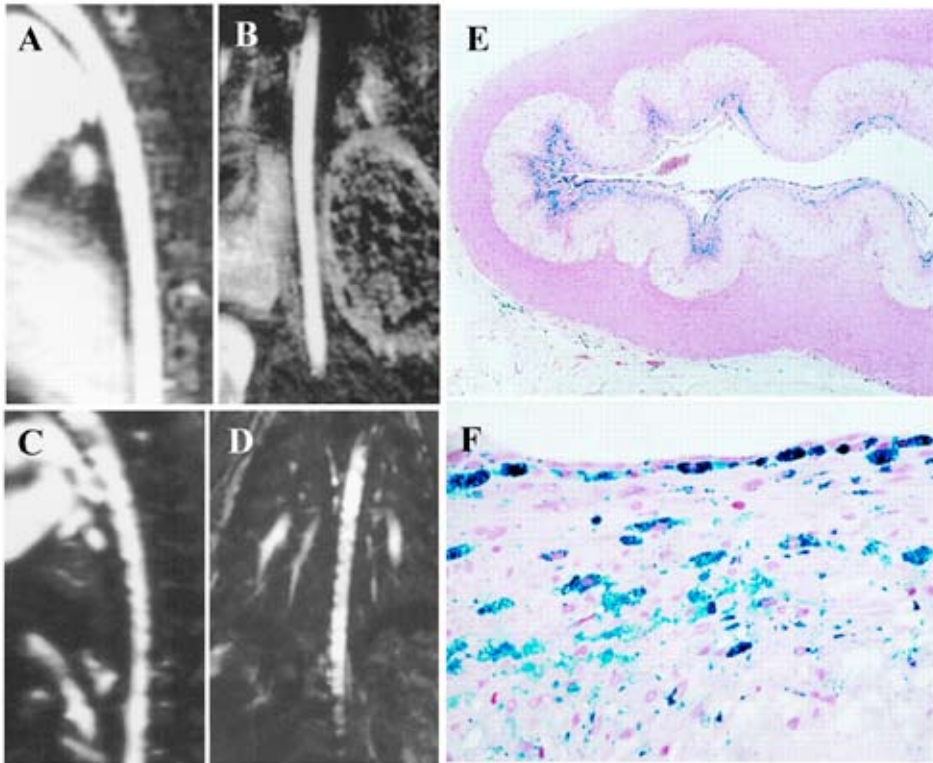

Figure 4. Printed with permission from Ruehm et al. [5]. Gd-DOTA enhanced 3D MRA of aorta of 7-month-old hyperlipidemic rabbit before, sagittal oblique (A) and coronal oblique (B) and 5 days after intravenous injection of USPIOs (1000 μmol/kg), sagittal oblique (C) and coronal oblique (D). Before injection of USPIOs, the aortic wall is smooth, without evidence of luminal narrowing. Note susceptibility effects originating within vessel wall and representing Fe uptake in macrophages embedded in plaque. Cross-sectional histopathological sections with Prussian blue (iron) staining of aorta (E and F) of same hyperlipidemic rabbit as depicted in A-D. Note thickening of intima with marked staining of Fe particles embedded in atherosclerotic plaque formations.

remains difficult with iron particle-based contrast agents. Recently, an MR technique using inversion recovery with on-resonance water suppression created off-resonance contrast enhancement of macrophage-rich atherosclerotic plaques instead of signal voids in rabbits(14). However, field inhomogeneities importantly limit the efficiency of this technique because of the small bandwidth of the water suppression pulse.

Imaging of the enhanced permeability and retention effect of atherosclerotic plaque
Positive contrast agents are advantageous because on T1-weighted images they create regions of increased signal, where the contrast agent prefers to concentrate. Most of these contrast agents are gadolinium (Gd^{3+})-based. Gd^{3+} is toxic and requires chelation to molecules, like diethylene triamine pentaacetic acid (DTPA). Dynamic contrast enhanced MRI was applied for quantitative assessment of neovasculature of carotid artery plaque(15). This study described the wash-in kinetics of a gadolinium-based contrast agent in carotid artery plaque after post-processing with an algorithm, which corrected noise and motion(15).

Due to the relatively low relaxivity of one Gd-DTPA molecule, a lot of Gd-DTPA molecules are required to enhance the region of interest. For unspecific targeting of the extra-cellular matrix of atherosclerotic plaque gadofluorine M was used(16,17). Gadofluorine M is a lipophilic, water-soluble gadolinium chelate complex (Gd-Do3A-derivative) with a perfluorinated side chain, which forces the monomers into micelles of ± 5 nm in hydrophilic solution. The exact mechanism of uptake and accumulation into the atherosclerotic plaque is still unknown, however gadofluorine M has been shown to bind to albumin and to enter the plaque (due to increased endothelial permeability)(18). It has affinity for extracellular matrix proteins(18).

Also non-targeted paramagnetic liposomes were injected in apoE-deficient mice in order to study intimal thickening in collared carotid artery with MRI(19). The observed accumulation of liposomes in the vessel wall occurred after 15 minutes and lasted for 24 hours. The earlier described "enhanced permeability and retention" effect(20) was held responsible for this uptake.

Imaging with targeted molecular contrast agents
Though mentioned agents are macrophage- or tissue-specific, those agents are not specifically targeted to a molecule or receptor. Abundance of specific molecular targets during different stages of atherosclerosis has pushed research in imaging of atherosclerosis from a pure morphological to a functional approach.

One MRI study reported selective *in vitro* uptake of immunomicelles, targeted to the mouse macrophage scavenger receptor (MSR) A types I and II, by mouse macrophages

and increase of signal intensity by 81% in *ex vivo* apoE^{-/-} mouse aortic wall(21). *In vivo* molecular MRI of macrophages has been performed using paramagnetic immunomicelles targeted to MSR A in atherosclerotic plaque of apoE^{-/-} mice(22). MSR-targeted micelles revealed at 24 hours postinjection a 79% increase in signal intensity of atherosclerotic aorta compared with only 34% using untargeted micelles(22). Not only macrophages but also the pro-atherogenic and pro-inflammatory oxidized low-density lipoprotein (Ox-LDL) has been visualized successfully with molecular MRI(23). Antibodies that bind unique oxidation-specific epitopes were attached to micelles by S-acetythioglycolic acid N-hydroxysuccinimide ester linking to a maleimide moiety(23). A radiotracer study showed that 125-I-MDA2, an iodinated form of a murine antibody that binds to malondialdehyde-lysine epitopes present on modified LDL accumulated in atherosclerotic plaques in proportion to the presence and extent of Ox-LDL(24).

The dysfunctional endothelium of atherosclerotic lesions expresses VCAM-1 after stimulation by minimally oxidized LDL in the subintima. VCAM-1 in endothelium of aorta in cholesterol-fed apoE-deficient mice has been successfully targeted and visualized with a bimodal (MRI and fluorescence imaging) cross-linked iron oxide nanoparticle(25). CLIO-Cy5.5 was conjugated to a specific sequence with homology to the α-chain of very late antigen (VLA4), which is a known ligand for VCAM-1(25).

Several MRI studies in different research areas have focused on imaging of apoptosis, which is also an important contributor to atherosclerosis. MRI of apoptosis was based on the expression of phosphatidylserine (PS) on the outer layer of the apoptotic cell membrane. The apoptotic process in transplanted subcutaneous tumours in mice has been successfully visualized with MRI using a small peptide coupled to SPIOs(26). However, an important limitation of PS-targeted imaging has become evident after publication of a SPECT study reporting visualization of apoptosis of cardiomyocytes in patients with acute myocardial infarction(27). This target may not be useful for imaging of vulnerable plaque in the coronary arteries, due to the possibly overwhelming background signal of enhanced cardiac muscle.

It is generally believed, that increased activity of matrix metalloproteinases (MMPs) –produced in SMCs and macrophages- contribute to plaque rupture(28,29). However, the MMP family is large and the exact molecular mechanisms are still being unravelled. It has been shown, that expression of MMP-2 and MMP-9 is upregulated in shoulder regions of human vulnerable plaques(29). Successful *in vivo* MRI of plaque MMPs has been performed with a small peptide covalently bound to a Gd-DOTA moiety with affinity for MMPs(30). Also with SPECT using a broad-spectrum MMP inhibitor, converted to a SPECT tracer by substitution with 123-I, MMP activity was visualized in murine carotid artery lesions after ligation and a cholesterol-rich diet(31). A threefold uptake in

atherosclerotic lesions was reported, when compared to the contralateral carotid artery, assessed *ex vivo* with the gamma counter. However, background signal that might be attributable to unspecific uptake in the scar surrounding the ligated artery in the *in vivo* imaging experiment was reported. The advent of specific inhibitors of MMP-9 and -2 may improve specificity of MMP targeted contrast agents. An important drawback of targeting MMPs could be the extracellular location, which increases the likelihood of early washout of MMPs to the blood, impairing visualization.

Whereas targets such as the extracellular matrix of atherosclerotic plaque or fibrin on thrombi are abundantly present, most of the intra-plaque molecular markers are scarcely present and the *in vivo* concentration of target molecules has to be in the micro-molar range for detection with molecular MRI with small Gd chelates(32). The nanomolar concentration of most of the molecular targets of interest in vulnerable plaques has shifted the attention from rather small Gd-chelates attached to antibodies or substrates to larger carriers, which can harbour larger payloads of gadolinium and so have larger relaxivity. Except for Gd payload, other important properties of the carrier, which define the probability to reach the intraplaque target of interest, are the size and charge. Atherosclerosis, being an inflammatory disorder, is characterized by an increased endothelial pore size (till 100 nm). So, micelles and small liposomes may be able to enter the plaque. To prevent phagocytosis of the carriers, polyethylene glycol (PEG) groups or polymers of vinyl pyrrolidone (PVP) are usually attached to the hydrophilic micellar corona or the outer layer of the liposome bilayer(33).

When the plaque does not need to be entered, as is the case with visualisation of diseased endothelium, large nanoparticles like Gd-perfluorocarbon nanoparticles (size ~250 nm) may be used(34). Advanced atherosclerotic plaque is characterized by an increase of the number of vasa vasorum, accompanied by an increased expression of integrins on the endothelial cell surface. Induced formation of neovasculature in the rabbit cornea after application of basic fibroblast growth factor has been visualized *in vivo* with MRI(35). Gd-perfluorocarbon nanoparticles were linked to an antibody directed to α(v)β(3) integrin, a molecular marker for angiogenic endothelium. Four hours after administration, *in vivo* MRI of the rabbit cornea with a surface coil revealed 25% increase in the average MR signal intensity of the neovasculature region. Also the feasibility of using 19-F signal from Gd-perfluorocarbon nanoparticles for visualization of angiogenesis has been shown in mice transfected with human papilloma virus and suffering from squamous carcinoma of the ears(36). They used diffusion weighted 19-F spectroscopy for selective suppression of background signal from nanoparticles in the blood(36). However, results obtained from *in vivo* atherosclerotic plaque MRI using these nanoparticles have to be awaited.

In order to investigate neovasculature in aortic plaques of apoE-deficient mice, fluorescent and radiolabeled human antibody against the extra-domain B of fibronectin (ED-B)

was applied(37). ED-B is inserted into the fibronectin molecule by alternative splicing during angiogenesis and tissue remodelling but is undetectable in normal adult tissues. Though only *ex vivo* experiments were performed, both with fluorescent imaging and autoradiography, selective targeting of plaques with neovasculature was demonstrated and the *in vivo* results are eagerly awaited.

Atherothrombotic events may lead to a total occlusion of an atherosclerotic vessel or multiple atherothrombotic events may gradually occlude the vessel. So, early recognition of frequent atherothrombosis has an important prognostic value. Many animal studies have been performed to visualize arterial thrombus. USPIOs attached to a cyclic arginine-glycine-aspartic acid (RGD) peptide specific for the αIIbβ3 integrin, which is expressed on activated platelets have been used(38). However, the achieved resolution with RGD-USPIO enhanced MRI was too low to detect thrombus *in vivo*. Further, small-molecule peptides with affinity to fibrin have been conjugated to Gd-DTPA and have been applied successfully *in vivo*(39,40). These studies demonstrated the feasibility of MRI, enhanced by this small molecular contrast agent, of acute coronary thrombus as well as subacute (1-3 days old) thrombus. They showed early signal enhancement at the clot surface followed by signal enhancement of the entire thrombus several hours after contrast administration. Fibrin was also targeted successfully with the relatively large Gd-perfluorocarbon nanoparticles(41-43).

Another approach is the use of HDL-like particles, which have the advantages of being endogenous and biodegradable, do not trigger immune reactions and are not recognized by the RES(44-46). The normalized signal intensity (calibrated to muscle intensity) of atherosclerotic mouse plaque was 135% at 24 hours after injection and at 48 hours the intensity was as low as the pre-injection value(44). Owing to the flexibility of the HDL platform, targeting molecules might be easily incorporated into these particles and may increase the retention of these particles into specific regions or types of plaques. A restriction to the translation of this strategy is the absence of a ready commercial source of apo A-I. Gadolinium containing HDL formulations interacting with macrophages and based on a synthetic lipid-binding apo A-I mimicking peptide (37pA) showed as much enhancement on *in vivo* MR images at 24 hours as HDL formulations based on a cheaper and easier synthesized apo A-I mimicking peptide (18A) (Figure 5)(46).

Future developments

Because the importance of increasing the sensitivity of contrast enhanced MRI is recognized, attention has been shifted from rather small Gd-chelates to carriers which can harbour larger payloads of gadolinium. Examples are: dendrimers (2-8 nm), micelles (5-50 nm), liposomes (80-400 nm), perfluorocarbon nanoparticles (250-500 nm), and gadonanotubes. The single-walled carbon gadonanotubes (20-80 nm long and 3-10
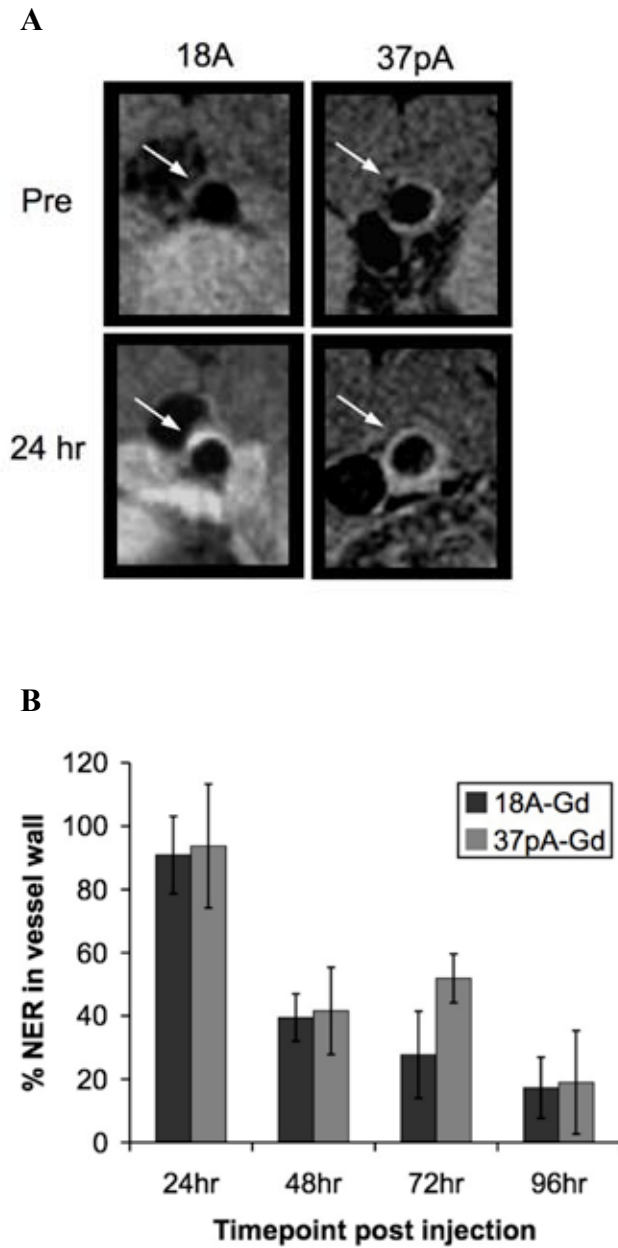
A

B

Figure 5. Printed with permission from Cormode et al. [45]. (A) MR images of the aorta of apoE$^{-/-}$ mice preinjection and 24 h postinjection with 18A-bound HDL formulation (left panels) and 37pA-bound HDL formulation (right panels). (B) Summary of the mean normalized enhancement ratio (% NER) at 24, 48, 72, and 96 h in the aortic walls of apoE$^{-/-}$ mice injected with 18A- or 37pA-bound formulations. Error bars are 1 standard deviation.

nm thick) have gained attention because of a tremendous relaxivity of the particle (40 times larger relaxivity than for any Gd^{3+}-based contrast agent in current clinical use) (47). Single-walled gadonanotubes contain internally-loaded Gd^{3+}nion clusters and superparamagnetic metal centers, which have access to many coordinated/exchanging water molecules per Gd^{3+} ion. It is believed that this is the reason for the extremely high relaxivity of these nanotubes. Even more important is that at high magnetic fields (>1.5 T) gadonanotubes have much higher discriminative power between enhanced and non-enhanced regions than the usual Gd^{3+} agents(48). The reason for this is not known and is under investigation. With the advent of clinical strong magnetic field systems (3.0 and 7.0T), the application of these carriers will become more and more appealing. Cyto-toxicity after internalization seems to be very low, but has to be investigated further. The first chemical report about functionalization of gadonanotubes with various amino acids and peptides has appeared in literature(49).

Another approach to visualise plaque targets is the use of chemical exchange saturation transfer (CEST) agents. CEST is a technique, which has been intensively employed by the group of Balaban et al.(50). CEST agents have exchangeable protons (–NH, –OH, etc.) that resonate at a chemical shift position that is distinguishable from the bulk water signal. When an RF pulse is applied at the resonance frequency of the exchangeable protons, these protons will be saturated. Transfer into the bulk water pool will lead to reduced equilibrium magnetization. This so-called saturation transfer effect can be switched "on" and "off" by simply changing the pulse sequence. The potential of the CEST technique has been demonstrated *in vitro* and *in vivo*. Many diamagnetic small organic molecules (amino acids, sugars, and heterocyclic compounds), as well as macromolecular systems (dendrimers and polymers), have been investigated(51). Perfluorocarbon nanoparticles that utilize a paramagnetic CEST chelate have been used for *in vitro* MRI of fibrin clots(43). CEST will possibly gain attention in the future with regard to *in vivo* MRI of atherosclerotic plaque markers. An activatable contrast agent is an agent, in which the access of water to the first coordination sphere of a chelated paramagnetic ion is blocked with a substrate that can be removed by enzymatic cleavage. Following cleavage, the paramagnetic ion can interact directly with water protons to increase the MR signal. Myeloperoxidase (MPO) secretion by activated neutrophils and macrophages in humans correlates well with plaque rupture in atherosclerotic disease(52). Covalent conjugates of Gd-DOTA and serotonin (3-(2-aminoethyl)-5-hydroxyindole) were efficiently polymerized in the presence of MPO(52). Following polymerization, the paramagnetic ion interacted directly with water protons to increase the MR signal by an increase in proton relaxivity of 70-100%(52). This MPO-activatable contrast agent has been used for *in vivo* MRI of atherosclerosis in rabbits(53). This approach could be translated to other blocking substrates for enzymes, which are active in atherosclerotic plaque, like MMPs.

Perspectives

Future MRI studies will have to focus on those molecular targets of the atherosclerotic process, which have the highest prognostic value with regard to acute coronary syndromes. Progressive cap thinning is an important sign of threatening plaque rupture and MMP-9 and 2 are important mediators of cap thinning(29). When more selective MMP inhibitors become available, which also serve a therapeutic purpose, research in this area will be facilitated. Another target in the extracellular matrix is fibronectin. As mentioned before, extra-domain B of fibronectin has been targeted with a radiolabeled antibody(37). The abundance of this target in remodeling atherosclerotic vessels may also allow for targeting with molecular MRI. The carrier should be small enough in order to invade the plaque and reach the target. The use of MPO-activatable contrast agent for visualization of atherosclerotic plaque in rabbit aorta has already been mentioned(53) and we are looking forward to activatable MR contrast agents using MMP-9 as activating enzyme. Successful molecular imaging of plasma-soluble cytokines or enzymes being released by activated macrophages and T-lymphocytes strongly depends on the concentration gradient of these substances between tissue and plasma.

Toxicity/costs: implications for clinical implementation

A major consideration in the design of new contrast agents is its potential toxicity. Though free Gd is toxic, this is not necessarily the case for bound Gd. However, it has been shown that gadolinium complexes of open-chain chelates like DTPA exhibit a higher susceptibility to transmetallation than other complexes like DOTA(54). Pharmacokinetics of the contrast agent complicates the toxicity issue even further. Immunogenicity created by the antibodies could be reduced with future use of Ab fragments, which are often cheaper and easier synthesized (46). However, the use of (partial) antibodies for targeted contrast agents still impairs large scale production for clinical use.

Conclusions

In conclusion: conventional MRI has proven its potential for *in vivo* plaque characterization of human carotid arteries. For imaging of coronary artery plaque, first motion artefacts have to be managed more successfully. Molecular MRI is one of the most promising non-invasive screening tools for identification of the CAD patient at risk. The MRI-visibility of targets, such as MMP-9, together with their sensitivity and specificity for association with vulnerable plaque will have to be investigated further. Future application of newly developed carriers like gadonanotubes in combination with high field MR systems and *in vivo* targeted imaging with an activatable contrast agent are promising.

Once MRI is successfully implemented as a clinical screening tool, treatment could be tailored to the individual patient. The vulnerability of the lesion and the number of lesions could determine whether the treatment should be interventional or pharmacological.

Reference List

1. Ross R (1999), Atherosclerosis--an inflammatory disease, N.Engl.J.Med. 340: 115-126
2. Lusis AJ (2000), Atherosclerosis, Nature 407: 233-241
3. Schmitz SA (2003), (Iron-oxide-enhanced MR imaging of inflammatory atherosclerotic lesions: overview of experimental and initial clinical results) Eisenoxidverstarkte MRT inflammatorischeratherosklerotischer Lasionen: Ubersichtexperimenteller und erster klinischer Ergebnisse, Rofo 175: 469-476
4. Schmitz SA, Taupitz M, Wagner S, Wolf KJ, Beyersdorff D, Hamm B (2001), Magnetic resonance imaging of atherosclerotic plaques using superparamagnetic iron oxide particles, J.Magn Reson.Imaging. 14: 355-361
5. Ruehm SG, Corot C, Vogt P, Kolb S, Debatin JF (2001), Magnetic resonance imaging of atherosclerotic plaque with ultrasmall superparamagnetic particles of iron oxide in hyperlipidemic rabbits, Circulation 103: 415-422
6. Kooi ME, Cappendijk VC, Cleutjens KB, Kessels AG, Kitslaar PJ, Borgers M, Frederik PM, Daemen MJ, van Engelshoven JM (2003), Accumulation of ultrasmall superparamagnetic particles of iron oxide in human atherosclerotic plaques can be detected by in vivo magnetic resonance imaging, Circulation 107: 2453-2458
7. Trivedi RA, Mallawarachi C, King-Im JM, Graves MJ, Horsley J, Goddard MJ, Brown A, Wang L, Kirkpatrick PJ, Brown J, Gillard JH (2006), Identifying inflamed carotid plaques using in vivo USPIO-enhanced MR imaging to label plaque macrophages, Arterioscler.Thromb.Vasc.Biol. 26: 1601-1606
8. Tang TY, Howarth SP, Li ZY, Miller SR, Graves MJ, King-Im JM, Trivedi RA, Walsh SR, Brown AP, Kirkpatrick PJ, Gaunt ME, Gillard JH (2008), Correlation of carotid atheromatous plaque inflammation with biomechanical stress: utility of USPIO enhanced MR imaging and finite element analysis, Atherosclerosis. 196: 879-887
9. Tang TY, Howarth SP, Miller SR, Graves MJ, King-Im JM, Li ZY, Walsh SR, Hayes PD, Varty K, Gillard JH (2008), Comparison of the inflammatory burden of truly asymptomatic carotid atheroma with atherosclerotic plaques in patients with asymptomatic carotid stenosis undergoing coronary artery bypass grafting: an ultrasmall superparamagnetic iron oxide enhanced magnetic resonance study, Eur.J Vasc.Endovasc. Surg. 35: 392-398
10. Kawahara I, Nakamoto M, Kitagawa N, Tsutsumi K, Nagata I, Morikawa M, Hayashi T (2008), Potential of magnetic resonance plaque imaging using superparamagnetic particles of iron oxide for the detection of carotid plaque, Neurol.Med.Chir (Tokyo). 48: 157-161
11. Tang TY, Howarth SP, Miller SR, Graves MJ, Patterson AJ, King-Im JM, Li ZY, Walsh SR, Brown AP, Kirkpatrick PJ, Warburton EA, Hayes PD, Varty K, Boyle JR, Gaunt ME, Zalewski A, Gillard JH (2009), The ATHEROMA (Atorvastatin Therapy: Effects on Reduction of Macrophage Activity) Study. Evaluation using ultrasmall superparamagnetic iron oxide-enhanced magnetic resonance imaging in carotid disease, J Am.Coll.Cardiol. 53: 2039-2050.
12. Litovsky S, Madjid M, Zarrabi A, Casscells SW, Willerson JT, Naghavi M (2003), Superparamagnetic iron oxide-based method for quantifying recruitment of monocytes to mouse atherosclerotic lesions in vivo: enhancement by tissue necrosis factor-alpha, interleukin-1beta, and interferon-gamma, Circulation. 107: 1545-1549
13. Klug G, Bauer L, Bauer WR (2008), Patterns of USPIO deposition in murine atherosclerosis, Arterioscler. Thromb.Vasc.Biol. 28: E157-E159
14. Korosoglou G, Weiss RG, Kedziorek DA, Walczak P, Gilson WD, Schar M, Sosnovik DE, Kraitchman DL, Boston RC, Bulte JW, Weissleder R, Stuber M (2008), Noninvasive detection of macrophage-rich atherosclerotic plaque in hyperlipidemic rabbits using "positive contrast" magnetic resonance imaging, J Am.Coll.Cardiol. 52: 483-491
15. Kerwin W, Hooker A, Spilker M, Vicini P, Ferguson M, Hatsukami T, Yuan C (2003), Quantitative magnetic resonance imaging analysis of neovasculature volume in carotid atherosclerotic plaque, Circulation. 107: 851-856
16. Zheng J, Ochoa E, Misselwitz B, Yang D, El N, I, Woodard PK, Abendschein D (2008), Targeted contrast agent helps to monitor advanced plaque during progression: a magnetic resonance imaging study in rabbits, Invest Radiol. 43: 49-55
17. Zheng J, Abendschein DR, Okamoto RJ, Yang D, McCommis KS, Misselwitz B, Gropler RJ, Tang D (2009), MRI-based biomechanical imaging: initial study on early plaque progression and vessel remodeling, Magn Reson.Imaging. doi:10.1016/j.mri.2009.05.032
18. Meding J, Urich M, Licha K, Reinhardt M, Misselwitz B, Fayad ZA, Weinmann HJ (2007), Magnetic resonance imaging of atherosclerosis by targeting extracellular matrix deposition with Gadofluorine M,

Contrast.Media Mol.Imaging. 2: 120-129

19. Mulder WJ, Douma K, Koning GA, van Zandvoort MA, Lutgens E, Daemen MJ, Nicolay K, Strijkers GJ (2006), Liposome-enhanced MRI of neointimal lesions in the ApoE-KO mouse, Magn Reson.Med. 55: 1170-1174

20. Lukyanov AN, Hartner WC, Torchilin VP (2004), Increased accumulation of PEG-PE micelles in the area of experimental myocardial infarction in rabbits, J.Control Release. 94: 187-193

21. Lipinski MJ, Amirbekian V, Frias JC, Aguinaldo JG, Mani V, Briley-Saebo KC, Fuster V, Fallon JT, Fisher EA, Fayad ZA (2006), MRI to detect atherosclerosis with gadolinium-containing immunomicelles targeting the macrophage scavenger receptor, Magn Reson.Med. 56: 601-610

22. Amirbekian V, Lipinski MJ, Briley-Saebo KC, Amirbekian S, Aguinaldo JG, Weinreb DB, Vucic E, Frias JC, Hyafil F, Mani V, Fisher EA, Fayad ZA (2007), Detecting and assessing macrophages in vivo to evaluate atherosclerosis noninvasively using molecular MRI, Proc.Natl.Acad.Sci.U.S.A. 104: 961-966

23. Briley-Saebo KC, Shaw PX, Mulder WJ, Choi SH, Vucic E, Aguinaldo JG, Witztum JL, Fuster V, Tsimikas S, Fayad ZA (2008), Targeted molecular probes for imaging atherosclerotic lesions with magnetic resonance using antibodies that recognize oxidation-specific epitopes, Circulation. 117: 3206-3215

24. Tsimikas S, Shortal BP, Witztum JL, Palinski W (2000), In vivo uptake of radiolabeled MDA2, an oxidation-specific monoclonal antibody, provides an accurate measure of atherosclerotic lesions rich in oxidized LDL and is highly sensitive to their regression, Arterioscler.Thromb.Vasc.Biol. 20: 689-697

25. Kelly KA, Allport JR, Tsourkas A, Shinde-Patil VR, Josephson L, Weissleder R (2005), Detection of vascular adhesion molecule-1 expression using a novel multimodal nanoparticle, Circ.Res. 96: 327-336

26. Zhao M, Beauregard DA, Loizou L, Davletov B, Brindle KM (2001), Non-invasive detection of apoptosis using magnetic resonance imaging and a targeted contrast agent, Nat.Med. 7: 1241-1244

27. Hofstra L, Liem IH, Dumont EA, Boersma HH, van Heerde WL, Doevendans PA, De Muinck E, Wellens HJ, Kemerink GJ, Reutelingsperger CP, Heidendal GA (2000), Visualisation of cell death in vivo in patients with acute myocardial infarction, Lancet. 356: 209-212

28. Vink A, Pasterkamp G (2002), Atherosclerotic plaque burden, plaque vulnerability and arterial remodeling: the role of inflammation, Minerva Cardioangiol. 50: 75-83

29. Galis ZS, Khatri JJ (2002), Matrix metalloproteinases in vascular remodeling and atherogenesis: the good, the bad, and the ugly, Circ.Res. 90: 251-262

30. Lancelot E, Amirbekian V, Brigger I, Raynaud JS, Ballet S, David C, Rousseaux O, Le GS, Port M, Lijnen HR, Bruneval P, Michel JB, Ouimet T, Roques B, Amirbekian S, Hyafil F, Vucic E, Aguinaldo JG, Corot C, Fayad ZA (2008), Evaluation of matrix metalloproteinases in atherosclerosis using a novel noninvasive imaging approach, Arterioscler.Thromb.Vasc.Biol. 28: 425-432

31. Schafers M, Riemann B, Kopka K, Breyholz HJ, Wagner S, Schafers KP, Law MP, Schober O, Levkau B (2004), Scintigraphic imaging of matrix metalloproteinase activity in the arterial wall in vivo, Circulation. 109: 2554-2559

32. Massoud TF, Gambhir SS (2003), Molecular imaging in living subjects: seeing fundamental biological processes in a new light, Genes Dev. 17: 545-580

33. Torchilin VP (2001), Structure and design of polymeric surfactant-based drug delivery systems, J.Control Release. 73: 137-172

34. Winter PM, Cai K, Caruthers SD, Wickline SA, Lanza GM (2007), Emerging nanomedicine opportunities with perfluorocarbon nanoparticles, Expert.Rev.Med.Devices. 4: 137-145

35. Anderson SA, Rader RK, Westlin WF, Null C, Jackson D, Lanza GM, Wickline SA, Kotyk JJ (2000), Magnetic resonance contrast enhancement of neovasculature with alpha(v)beta(3)-targeted nanoparticles, Magn Reson.Med. 44: 433-439

36. Waters EA, Chen J, Yang X, Zhang H, Neumann R, Santeford A, Arbeit J, Lanza GM, Wickline SA (2008), Detection of targeted perfluorocarbon nanoparticle binding using 19F diffusion weighted MR spectroscopy, Magn Reson.Med. 60: 1232-1236

37. Matter CM, Schuler PK, Alessi P, Meier P, Ricci R, Zhang D, Halin C, Castellani P, Zardi L, Hofer CK, Montani M, Neri D, Luscher TF (2004), Molecular imaging of atherosclerotic plaques using a human antibody against the extra-domain B of fibronectin, Circ.Res. 95: 1225-1233

38. Johansson LO, Bjornerud A, Ahlstrom HK, Ladd DL, Fujii DK (2001), A targeted contrast agent for magnetic resonance imaging of thrombus: implications of spatial resolution, J.Magn Reson.Imaging 13: 615-618

39. Botnar RM, Perez AS, Witte S, Wiethoff AJ, Laredo J, Hamilton J, Quist W, Parsons EC, Jr., Vaidya A, Kolodziej A, Barrett JA, Graham PB, Weisskoff RM, Manning WJ, Johnstone MT (2004), In vivo molecu-

lar imaging of acute and subacute thrombosis using a fibrin-binding magnetic resonance imaging contrast agent, Circulation 109: 2023-2029

40. Botnar RM, Buecker A, Wiethoff AJ, Parsons EC, Jr., Katoh M, Katsimaglis G, Weisskoff RM, Lauffer RB, Graham PB, Gunther RW, Manning WJ, Spuentrup E (2004), In vivo magnetic resonance imaging of coronary thrombosis using a fibrin-binding molecular magnetic resonance contrast agent, Circulation 110: 1463-1466

41. Morawski AM, Winter PM, Yu X, Fuhrhop RW, Scott MJ, Hockett F, Robertson JD, Gaffney PJ, Lanza GM, Wickline SA (2004), Quantitative "magnetic resonance immunohistochemistry" with ligand-targeted (19)F nanoparticles, Magn Reson.Med. 52: 1255-1262

42. Winter PM, Caruthers SD, Yu X, Song SK, Chen J, Miller B, Bulte JW, Robertson JD, Gaffney PJ, Wickline SA, Lanza GM (2003), Improved molecular imaging contrast agent for detection of human thrombus, Magn Reson.Med. 50: 411-416

43. Winter PM, Cai K, Chen J, Adair CR, Kiefer GE, Athey PS, Gaffney PJ, Buff CE, Robertson JD, Caruthers SD, Wickline SA, Lanza GM (2006), Targeted PARACEST nanoparticle contrast agent for the detection of fibrin, Magn Reson.Med. 56: 1384-1388

44. Frias JC, Ma Y, Williams KJ, Fayad ZA, Fisher EA (2006), Properties of a versatile nanoparticle platform contrast agent to image and characterize atherosclerotic plaques by magnetic resonance imaging, Nano. Lett. 6: 2220-2224

45. Cormode DP, Briley-Saebo KC, Mulder WJ, Aguinaldo JG, Barazza A, Ma Y, Fisher EA, Fayad ZA (2008), An ApoA-I mimetic peptide high-density-lipoprotein-based MRI contrast agent for atherosclerotic plaque composition detection, Small. 4: 1437-1444

46. Cormode DP, Chandrasekar R, Delshad A, Briley-Saebo KC, Calcagno C, Barazza A, Mulder WJ, Fisher EA, Fayad ZA (2009), Comparison of Synthetic High Density Lipoprotein (HDL) Contrast Agents for MR Imaging of Atherosclerosis, Bioconjug.Chem. 20: 937-943

47. Sitharaman B, Wilson LJ (2006), Gadonanotubes as new high-performance MRI contrast agents, Int.J Nanomedicine. 1: 291-295

48. Sitharaman B, Kissell KR, Hartman KB, Tran LA, Baikalov A, Rusakova I, Sun Y, Khant HA, Ludtke SJ, Chiu W, Laus S, Toth E, Helm L, Merbach AE, Wilson LJ (2005), Superparamagnetic gadonanotubes are high-performance MRI contrast agents, Chem.Commun.(Camb.). 3915-3917

49. Mackeyev Y, Hartman KB, Ananta JS, Lee AV, Wilson LJ (2009), Catalytic synthesis of amino acid and peptide derivatized gadonanotubes, J Am.Chem.Soc. 131: 8342-8343

50. Ward KM, Aletras AH, Balaban RS (2000), A new class of contrast agents for MRI based on proton chemical exchange dependent saturation transfer (CEST), J.Magn Reson. 143: 79-87

51. Aime S, Carrera C, Delli CD, Geninatti CS, Terreno E (2005), Tunable imaging of cells labeled with MRI-PARACEST agents, Angew.Chem.Int.Ed Engl. 44: 1813-1815

52. Chen JW, Pham W, Weissleder R, Bogdanov A, Jr. (2004), Human myeloperoxidase: a potential target for molecular MR imaging in atherosclerosis, Magn Reson.Med. 52: 1021-1028

53. Ronald JA, Chen JW, Chen Y, Hamilton AM, Rodriguez E, Reynolds F, Hegele RA, Rogers KA, Querol M, Bogdanov A, Weissleder R, and Rutt BK (2009), Enzyme-sensitive magnetic resonance imaging targeting myeloperoxidase identifies active inflammation in experimental rabbit atherosclerotic plaques, Circulation 120: 592-599.

54. Laurent S, Elst LV, Copoix F, Muller RN (2001), Stability of MRI paramagnetic contrast media: a proton relaxometric protocol for transmetallation assessment, Invest Radiol. 36: 115-122.

Chapter 4

Multi-spectral MRI including fat suppression and inversion recovery spin echo
allows for identification of intra-plaque hemorrhage and lipid core in human carotid plaque

Bernard C. te Boekhorst, MD[1], Ronald van 't Klooster, MS[2], Sandra M. Bovens, MS[1,3], Kees W. van de Kolk, MS[1], Maarten J. Cramer, MD, PhD[1], Matthijs F. van Oosterhout, MD, PhD[4], Pieter. A. Doevendans, MD, PhD[1], Rob J. van der Geest, PhD[2], Gerard Pasterkamp, MD, PhD[1], Cees J. van Echteld, PhD[1],[#]

[1]*Dept. of Cardiology, University Medical Center Utrecht, Utrecht, Netherlands, *[2]*Division of Image Processing, Dept. of Radiology, Leiden University Medical Center, Leiden, Netherlands, *[3]*Interuniversity Cardiology Institute of the Netherlands, Utrecht, Netherlands, *[4]*Dept. of Pathology, University Medical Center Utrecht, Utrecht, Netherlands, *[*]*Present address: Novartis Institutes for BioMedical Research, Basel, Switzerland*

Abstract

Purpose
Intra-plaque hemorrhage (IPH) and lipid core, characteristics of rupture prone carotid plaques, are often visualized *in vivo* with MRI using T1 weighted (T1w) gradient and spin echo, respectively. Increasing magnetic field strength may help to identify IPH and lipid core better. The added value of inversion recovery spin echo (IR-SE) and T1w imaging with fat suppression (FS) for discrimination between IPH or lipid core and stable plaque components with multi-spectral MRI was investigated.

Materials and Methods
After multi-spectral MRI (9.4T) of 9 formaldehyde-fixated autopsy specimens, the Mahalanobis Distances (MDs) between plaque component intensities were calculated for each MR weighting. Sensitivity, specificity and accuracy for correct labeling of pixels using a trained automated classifier were determined, validated by histology.

Results
MD between collagen/cell-rich area and IPH was largest with IR-SE , between collagen/cell-rich area/foam cells and lipid core with T1wFS. The sensitivity/specificity/accuracy of detection of lipid core in the presence of IPH was 60%/99%/93% when using T1w/T2w/PD(proton density)w and 75%/97%/94% when using T1wFS/T2w/PDw/IR-SE. The sensitivity/specificity/accuracy of detection of IPH was 85%/93%/92% when using T1w/T2w/PDw and 89%/99%/98% when IR-SE imaging was added.

Conclusion
The application of T1wFS and IR-SE leads to enhanced conspicuity of lipid core and IPH in human carotid artery plaque.

Keywords: MRI, rupture prone plaque, plaque components, intra-plaque hemorrhage, lipid core

Introduction

Clinically, the degree of stenosis, which is generally identified by angiography, is often used as a marker for plaques that may give rise to clinical symptoms. However, lumenography is regarded to be insufficient for identification of vulnerable plaques for two reasons. Outward remodeling with preservation of lumen size is a characteristic of vulnerable plaques but cannot be identified with lumenography (1). Secondly, plaque composition rather than lumen size appears to determine plaque vulnerability. For identification of high-risk carotid artery plaque not only the classical markers of plaque vulnerability -large lipid core, a thin fibrous cap (2) and abundance of macrophages (3)- but also intra-plaque hemorrhage (IPH) has been recognized as an important predictor of major clinical events, i.e. TIA or stroke (4-6). MRI is the most promising technique for visualization of these plaque markers, because each plaque component generates unique MR contrast, the technique is noninvasive and depicts the anatomy of the vessel. A substantial number of studies have been reported on carotid artery plaque MRI both *ex vivo* (7-11) and *in vivo* (4;5;12-15). In most studies, multi-spectral MRI is used for characterization of carotid atherosclerotic plaque. In particular, reports have stressed the importance of T2 weighted spin echo sequences for differentiation between lipid core and fibrous tissue (7). More recently, T1 weighted fast spin echo and gradient echo (time-of-flight (TOF)) imaging have gained interest, because these sequences may lead to better visualization and bright depiction of IPH (4-6) and lipid core(12;16;17).

With the advent of clinical high field magnets (7 T), interest in the possibilities for in-vivo carotid artery imaging at high field strength has grown. Higher field magnets bring the advantage of increased SNR or the possibility to increase resolution. Unfortunately, adjustments to MR sequences or development of novel methods are necessary, since T1 of a particular tissue increases with increasing field strength, while T2 decreases, necessitating adjustment of MR sequences in order to generate optimized contrast. Inversion Recovery Spin Echo (IR-SE) has a larger potential for visualization of T1 differences than non-prepared T1 weighted SE or TOF(18). Possibly, definition of IPH, characterized by short T1, and differentiation from adjacent stable plaque components at higher field will be better with IR-SE technique than with non-prepared SE or TOF technique.
Additionally, early studies have revealed that chemical shift imaging of lipid, aimed at the narrow frequency range of methylene protons within adipose tissue, could visualize lipid core(19;20). We found indications that at 9.4T lipid core was better delineated by a T1 weighted gradient echo technique, when chemically selective fat suppression, aimed at the same frequency range as in the mentioned studies, was applied, than without this fat suppression(21).

In order to objectively compare the image contrast between different plaque components amongst different MR sequences, techniques are needed that can quantify image contrast, based on absolute signal levels, which may vary across platforms and with coil configurations. Moreover, such statistical measures can be used in conjunction with pattern recognition techniques to enable automatic identification of plaque components based on their signal characteristics. In a number of studies the Euclidean Distance (ED) measure is used for identification of plaque components (9). The use of Mahalanobis Distance (MD) is preferred over ED because this measure is scale-invariant and takes into account the covariance in the data allowing comparison of multiple MR contrast weightings (22;23). The objective of this study is to investigate the added value of IR-SE and T1w FLASH with FS (T1wFS) to multi-spectral MRI for identification of unstable plaque components. Therefore, in this study we determine the MD between various plaque components on various MR weighted images, including IR-SE and T1wFS, of human carotid artery specimens. Subsequently we used the most promising combination of sequences to test the feasibility of automated plaque classification.

Materials & Methods

MRI
Nine carotid artery specimens (including bifurcation), obtained at autopsy, were 4% formaldehyde fixated and stored at 4 ˚C for at least 48 hours. Samples were re-warmed to 37 ˚C prior to and kept at 37 ˚C during imaging. This set of carotid artery specimens was used as the study set.
Artery samples were imaged in a vertical 9.4T, 89mm bore size magnet equipped with 1500 mT/m gradients and connected to an Avance 400 MR system (Bruker BioSpin, Germany) using a quadrature-driven birdcage coil with an inner diameter of 10 mm. Care was taken to remove any air bubbles. Six different MR weighted images were acquired: T1 weighted fast low angle shot (T1w FLASH) with and without fat suppression (T1wFS and T1w), proton density weighted fast spin echo (PDw FSE), T2 weighted FSE (T2w) with intermediate and long echo time (TE), and inversion recovery (IR)-SE. For all acquisition parameters, see Table 1.

T1 and T2 measurements of fresh and formaldehyde 4%-fixated femoral artery plaque
Three diseased femoral arteries were freshly obtained following surgery, immediately warmed to 37 ˚C and imaged. T1 was obtained from a series of IR images with increasing inversion times (TIs) (20 µs-8s) and a TR of 9.5 s. T2 was obtained from a series of images obtained with a single-slice multi-echo imaging sequence with incremented

TEs (4ms-100ms) and a TR of 5s. After T1 and T2 measurements, which took 2 hours, samples were formaldehyde 4% fixated, stored at 4 ˚C. Forty-eight hours later, T1 and T2 measurements were repeated at exactly the same slice position (macroscopic plaque morphology was used for adjustment of position).

Histology and image processing

Carotid and femoral artery specimens were decalcified by submersion in ethylenedia-minetetra-acetic acid for 24 hours and embedded in paraffin. Ten μm sections were cut at 0.5 mm intervals. Hematoxylin & eosin (HE) and collagen stainings with Picrosirius red

Table 1. MR acquisition parameters

MR weighting	T1w FLASH	T1wFS FLASH	PDw FSE	Partial T2w FSE	Full T2w FSE	IR-SE (TI= 400ms)	IR-SE (TI= 1000ms)	IR-SE (TI= 1300ms)
TR (ms)	300	300	3500	3500	3500	5000	5000	5000
TE (ms)	2.14	2.14	8.53	19.76	37.97	3.10	3.10	3.10
ETL[a]	-	-	8	16	16	-	-	-
Flip angle (˚)	60	60	90/180	90/180	90/180	90/180	90/180	90/180
Inversion time (ms)	-	-	-	-	-	400	1000	1300
FOV[b] (mmxmm)	10x10	10x10	10x10	10x10	10x10	10x10	10x10	10x10
matrix	256x256	256x256	256x256	256x256	256x256	256x256	256x256	256x256
resolution (μmxμm)	39x39	39x39	39x39	39x39	39x39	39x39	39x39	39x39
thickness (mm)	0.5	0.5	0.5	0.5	0.5	0.5	0.5	0.5
number of slices	20	20	20	20	20	1	1	1
Bw[c] (kHz)	152	152	152	152	152	200	200	200
Fat suppression	-	+	-	-	-	-	-	-
NEX[d]	50	50	50	50	50	6	6	6
AT[e] (h:mm:ss)	1:04:00	1:04:00	1:33:20	0:46:40	0:46:40	2:08:00	2:08:00	2:08:00

aETL, echo train length, bFOV, field of view, cBw, Bandwidth, dNEX, number of excitations, eAT, acquisition time

were performed. Photographs of stained slices (jpeg format) and MR data (ParaVision 4.0 (Bruker Biospin, Germany) converted to DICOM format) were manipulated with ImageJ software (W. Rasband, version 1.29, National Institutes of Health 2003). On every histological slice for each recognizable plaque component a ROI was traced. All histological slices were evaluated (B.t.B.), and regions of interest (ROIs) that represented the following plaque components unambiguously (truth regions), were delineated: lipid core, IPH, collagen, cell-rich area, foam cells, calcification. Necrotic areas with cholesterol crystals were identified as lipid core. Areas with (remnants of) erythrocytes and fibrin strands on HE staining were identified as IPH. Closely packed spindle-shaped cells and high densities of nuclei (both smooth muscle cells and fibroblasts) in the fibrous cap of plaque were identified as cell-rich areas. Closely packed purple/red strands on Picrosirius Red staining were identified as collagen. Lipid-laden round cells on HE staining were identified as foam cells. Histological slices were matched with MR slices by an independent observer (S.B.) on the basis of overall plaque morphology and, in case of the carotid artery samples, the known distance of each slice from the common carotid bifurcation. Twenty three histological carotid artery sections and six femoral artery sections could be matched to MR images. For both carotid and femoral artery specimens, ROIs were copied from histological sections to matching MRI slices. For MR images of femoral artery plaque, the mean absolute signal intensities of the ROIs were plotted against TI or TE. The T1 data sets were fit to a mono-exponential recovery curve and T2 data sets were fit to a bi-exponential decay curve.

Image segmentation
Image segmentation was performed using histology assisted tracing with VesselMass software (LKEB, Leiden, Netherlands) and subsequently statistical analysis was performed using Matlab (The Mathworks, Natick, USA).
The truth regions, which were drawn, serve as user input and represent the various "classes" or plaque components. For each MR sequence, the signal intensities of the various classes were determined and the MD was calculated between all available classes.

Calculation of Mahalanobis Distance (MD) and classification of plaque components
The Euclidean Distance (ED) is a metric (a rule for calculating the distance between two points) for settings involving spherically symmetric distributions:

$$(ED)^2 = \Sigma_i \, (x_i - \mu_i)^2.$$

with x = intensity coordinates of an individual pixel belonging to component 1; μ= intensity coordinates of the average of a cloud of pixels belonging to component 2.

The MD is a metric which is better adapted than the ED to settings involving non-spherically symmetric distributions:

$$(MD)^2 = (x - \mu)'S^{-1}(x - \mu)$$

with S the covariance matrix of the distribution. The MD takes into account the covariance among the variables in calculating distances. With the MD, the problems of scale and correlation inherent in the ED are no longer an issue. MDs of all selected ROIs were pooled per weighting and per pair of components. The MR weighting leading to the highest pooled MD for pairs of plaque components which we considered relevant for identification of vulnerable plaque (lipid core-cell rich area, lipid core-collagen, lipid core-foam cells, IPH-cell rich area, IPH-collagen, foam cells-cell rich area, foam cells-collagen) was determined. From two carotid artery samples, which included 2x4 matching slices, ROIs on 3 slices per sample were used as training set for a Mahalanobis classifier[22]. The trained classifier was then used for automatic classification of plaque components on a pixel-by-pixel basis in the fourth slice of the sample. For various relevant combinations of MR weightings this procedure was repeated. Also the clinically often used combination of T1w, T2w and PDw was compared with combinations using the novel weightings.

Sensitivity, Specificity, Accuracy
The results of the automatic classifier were compared on a pixel-by pixel basis to the truth regions in the fourth slice of the two carotid artery samples. Results from the two carotid artery samples were pooled to determine the overall sensitivity and specificity of the classifier for each plaque component. Sensitivity is defined as: number of pixels correctly labeled by the classifier as tissue x divided by total number of pixels labeled tissue x as determined by histological review. Specificity is defined as the number of pixels correctly excluded from tissue x by the classifier divided by the total number of pixels excluded from tissue x as determined by histological review. The accuracy was calculated: total number of pixels correctly labeled by the classifier divided by the total number of pixels analyzed.

Results

T1 and T2 measurements of fresh and 4% formaldehyde fixated plaque
In this article a novel combination of MRI sequences is presented which has been designed to optimize image contrast between components of interest inside the vessel wall. T1 and

T2 values measured in fresh and 4% formaldehyde fixated plaque are listed in Table 2. T2 values of all components in freshly obtained plaque were shorter when compared to 4% formaldehyde fixated plaque. T1 values of all components in freshly obtained plaque were longer when compared to 4% formaldehyde fixated plaque.

Table 2. T1 and T2 values (ms) of fresh and 4% formaldehyde-fixated atherosclerotic human femoral artery plaque components at 9.4 T and at 37 ˚C. Data are expressed as mean ± SD of three measurements of three sets of components from three plaques. Thrombus was only encountered in one of these plaques

Plaque component	Fresh in PBS	Fresh in PBS	4% formaldehyde-fixated	4% formaldehyde-fixated
	T1	T2	T1	T2
IPH (old)	827 ± 296	4.6 ± 0.11	793 ± 158	10.9 ± 2.30
IPH (recent)	982 ± 246	12.1 ± 1.05	833 ± 139	15.0 ± 2.15
Lipid core	1110 ± 171	10.6 ± 1.97	1035 ± 105	13.3 ± 2.40
Foam cells	1230 ± 300	12.4 ± 1.88	1150 ± 62	17.4 ± 2.91
Cell rich area	1538 ± 386	28.9 ± 3.81	1446 ± 41	33.4 ± 4.72
Collagen	1578 ± 440	25.6 ± 5.82	1548 ± 88	30.3 ± 3.12

Table 3. Sensitivity, specificity and accuracy of detection of various plaque components achieved with various sets of MR weightings.

Plaque component	Set of MR weightings	Sensitivity (%)	Specificity (%)	Accuracy (%)
Lipid core in presence of IPH	T1w/PDw/T2w	60	99	93
	T1wFS/PDw/T2w/IRSE	75	97	94
Large lipid core in absence of IPH	T1w/PDw/T2w	100	99	100
	T1wFS/PDw/T2w/IRSE	100	99	100
IPH	T1w/PDw/T2w	85	93	92
	T1w/PDw/T2w/IRSE	89	99	98
Cell-rich area	T1w/PDw/T2w	100	90	93
	T1wFS/PDw/T2w	100	91	93
Collagen	T1w/PDw/T2w	80	84	84
	T1wFS/PDw/T2w	86	86	86

Visual inspection of MRI of carotid plaque

Lipid core and IPH are visualized best with T1wFS and IR-SE respectively (Figure 1 and 2). T1wFS creates largest contrast between lipid core (dark) and other plaque components including foam cells (brighter). IR-SE shows largest contrast between IPH (bright) and other plaque components (darker).
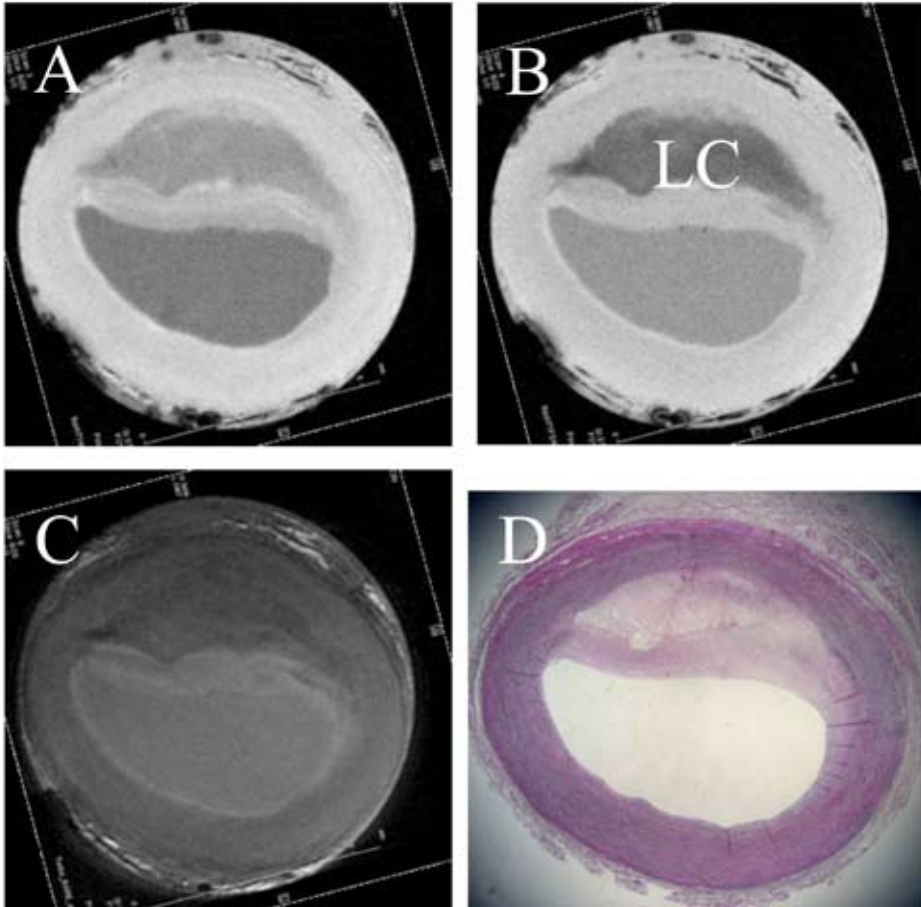

Figure 1. MRI and histology of carotid artery plaque with a large lipid core: A. T1w FLASH, B. T1w FLASH with FS, C. T2w, D. EVG staining. Conspicuity of lipid core is enhanced on T1w FLASH with FS when compared to T1w FLASH without FS. LC = lipid core.

Calculation of the MD

An example of discrimination between lipid, cell rich area and collagen using both the ED and the MD is shown in Figure 3. Clearly, the ED method does not take into account the variability of the values in all dimensions, and is therefore not an optimum discriminating analysis algorithm for multispectral MRI data.

Figure 4 shows the mean absolute signal intensities of the ROIs corresponding with plaque components for various carotid artery samples. Samples show large variations of intensities per plaque component and per MR weighting. Day-to-day differences of shim
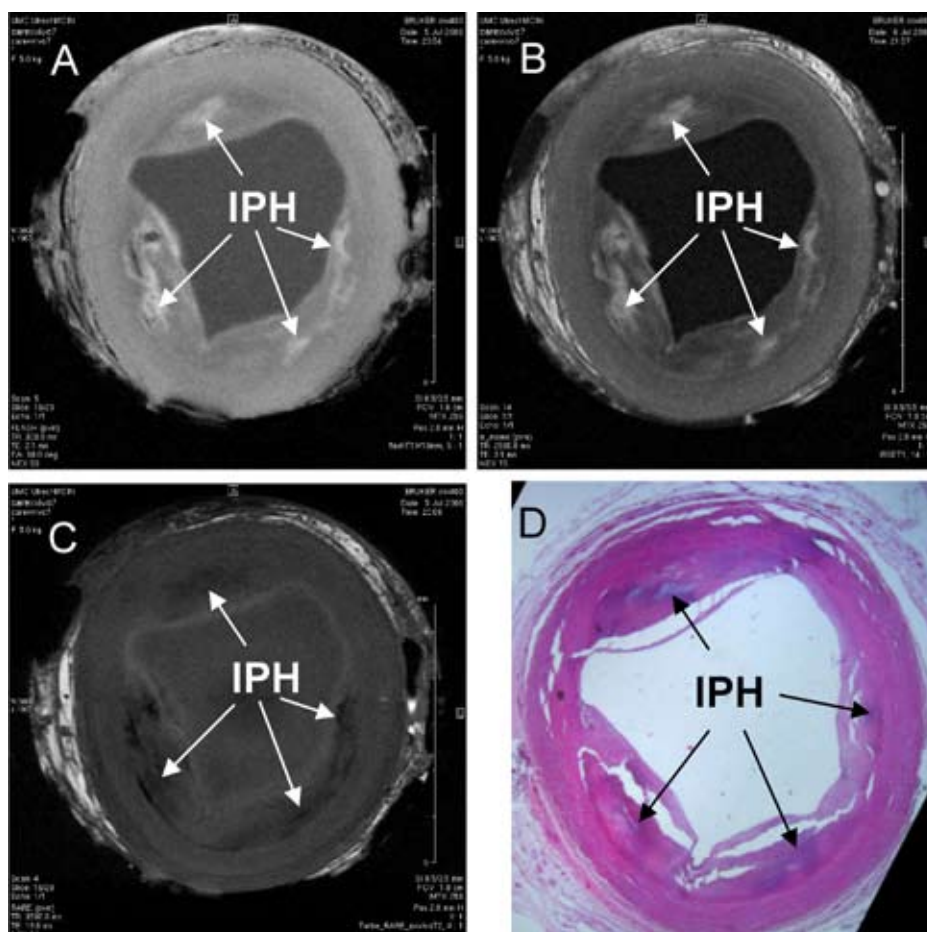
Figure 2. MRI and histology of human carotid atherosclerotic plaque with multiple regions of IPH: A. T1w, B. IRSE (TI=1000ms), C. T2w, D. HE staining. Arrows indicate IPH. T1w FLASH and IRSE image show bright regions in the plaque corresponding with IPH. IPH on T2w image is dark. IRSE image shows highest contrast of IPH.
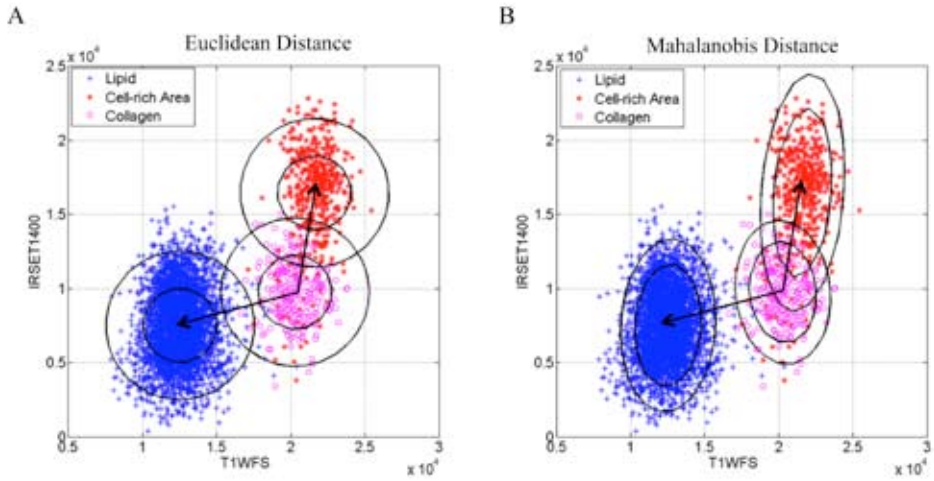
Figure 3: Euclidean distance versus MD of a cloud of data points representing collagen. Each data point represents a pixel. Obviously ED does not take into account the correlation of the data points according to the circular form of the iso-distance lines (A), whereas MD does take into account the correlation of the data points according to the ellipse form of the iso-distance lines (B). The distances between the group centers of collagen and cell rich area and between the group centers of collagen and lipid core (arrows) represent EDs (A and B). The two EDs measured from collagen to lipid core and from collagen to cell rich area are nearly similar (A). However, the MD between collagen and lipid core is larger than the MD between collagen and cell rich area as can be observed from the iso-distance lines in B.
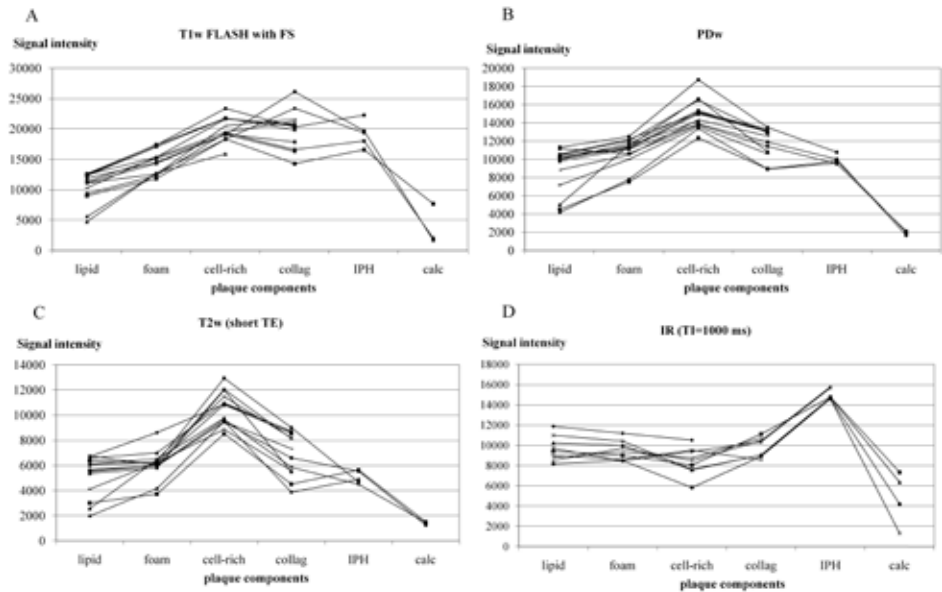
Figure 4. Absolute signal intensities (y-axis) of various components (x-axis) on T1wFS (A), PDw images (B), T2w (short TE) (C), and IR-SE (with TI=1000 ms) (D) images.
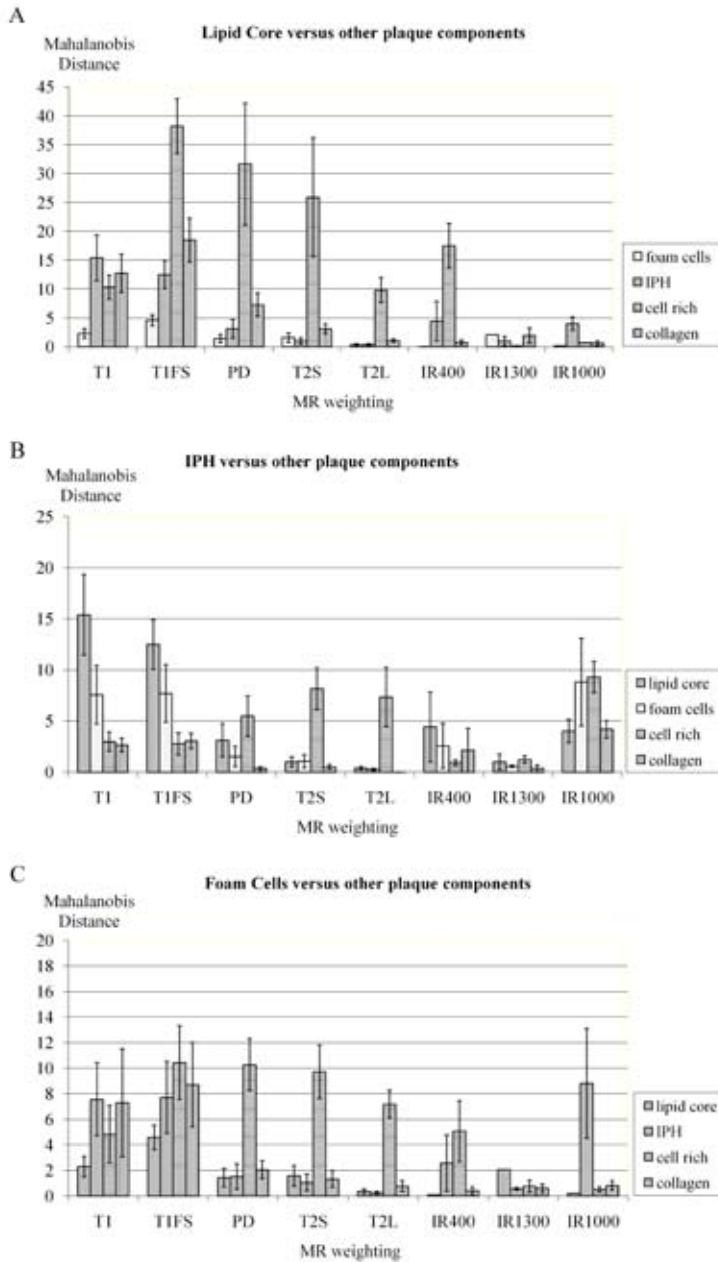
A

B

C

Figure 5. Mahalanobis distance between vulnerable carotid plaque components and stable plaque components. A. MD between lipid core and IPH, foam cells, cell rich areas, collagen; B. MD between IPH and lipid core, foam cells, cell rich areas, collagen; C. MD between foam cells and lipid core, IPH, cell rich areas, collagen.
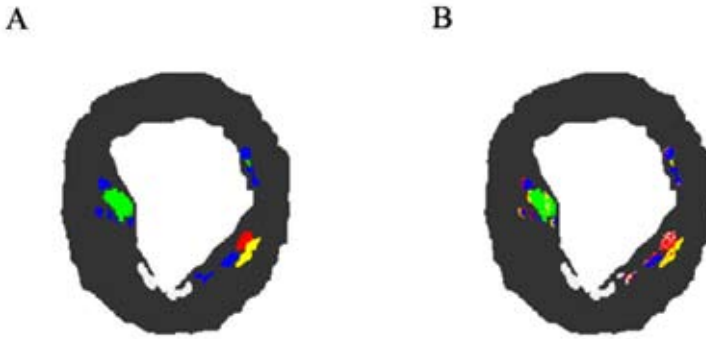
A   B

Figure 6: A. Truth regions drawn on histology and projected to the MR image at one slice level of a carotid artery sample, B. Plaque components assigned to same regions based on automatic classification on a pixel-by-pixel basis by a classifier trained on three different sections of the same carotid artery sample. Each color represents a different plaque component. Green: calcification; blue: IPH; red: collagen; white: cell rich area; yellow: lipid core.

settings and tuning/matching may cause these variations. However, the relative intensity differences between plaque components are similar per MR weighting (Figure 4).

Calcification has low signal intensity on all MR weightings. IPH has high signal intensity on IR-SE (TI=1000 ms) images, while other plaque components show lower signal intensities on these images. Cell-rich areas have high signal intensity on PDw images, while other plaque components have lower signal intensities on these images.

On every histological slice for each recognizable plaque component a ROI (truth region) was traced, and the mean signal intensities for the ROIs were calculated for each of the different MR contrast weightings. By calculating the MD for each pair of plaque components per MR weighting, a characteristic signature for each plaque component could be determined. Pooled MDs are shown in figure 5. IR-SE with TI=1000 ms increases the MD between collagen or cell-rich area and IPH when compared to other MR sequences. T1wFS appears to increase the MD between lipid core and foam cells or cell rich areas or collagen. T1w increases the MD between lipid core and IPH further when compared to T1wFS (Figure 5).

Figure 6 shows the correspondence of truth regions and automatically classified regions in one carotid artery sample after training on three adjacent slices. The sensitivity/specificity/accuracy of detection of various plaque components (lipid core, IPH, cell rich area, collagen) achieved with various sets of MR weightings is reported in Table 3. Large lipid core in the absence of IPH was easily distinguished with T1w, T2w and PDw imaging, while the sensitivity of the detection of lipid core in the absence of IPH was greatly improved by replacement of T1w with T1wFS and addition of IR-SE to the set of MR weightings. The sensitivity, specificity and accuracy of the detection of IPH were

improved by addition of IR-SE to the set of MR weightings (T1w, PDw, T2w). Sensitivity of the detection of collagen was improved by replacement of T1w by T1wFS within the set of MR weightings (T1w, PDw, T2w).

Discussion

This study shows that addition of IR-SE to a panel of MR weighted sequences (T1w FLASH, PDw FSE and T2w FSE) leads to better discrimination between IPH and stable plaque components of formaldehyde-fixated human carotid artery plaque. The addition of T1w FLASH with FS leads to better discrimination between lipid core and stable plaque components, including foam cells, when compared to T1w FLASH without FS. Comparison of T1 and T2 values of fresh and 4% formaldehyde-fixated plaque components indicates the feasibility to use this panel of sequences with only minor modifications to contrast parameters for *in vivo* high-field high-resolution MRI of human carotid atherosclerosis. Automated segmentation with a supervised classification algorithm, the "Mahalanobis distance-based classifier", which calculates the MD from multi-contrast weighted *ex vivo* MR images, provides the possibility to categorize characteristics of atherosclerotic plaques in six components.

Previous reports have shown that room temperature led to important T2 changes of fibrous plaque(23). Therefore and to allow direct translation to clinical high-field MRI, we have applied multi-contrast weighted MRI to *ex vivo* formaldehyde-fixated carotid artery specimens at 37˚C. The increase of T1 of tissues with increasing field strength increases the challenge to visualize T1 differences between plaque components at high field. Adjustment of MR sequences to increased field strengths should be based on T1 and T2 values of tissues of interest at those field strengths. However, there are some conflicting data from various reports on the T1 and T2 values of atherosclerotic plaque components at 9.4 T (7;24). The large range of T2 values found in literature for a particular plaque component may relate to differences in definition of plaque components on histology and the procedure of T1 and T2 measurement (spectroscopic or using MR imaging)(10;17;25;26).

Differentiation between IPH and stable plaque components, though feasible with T1 weighted spin echo, is difficult according to the moderate specificity of 74% for the in-vivo identification of recent IPH (4). At high field a T1 value for thrombus (=old IPH) at 9.4 T was reported to be 1180 ms, whereas T1 of fibrous tissue was reported to be ~ 1800 ms(24). Besides high field also application of a more powerful method to discriminate

between T1 of IPH and stable plaque components would be preferred. We achieved in this study clear identification of thrombus with IR-SE, most likely as a result of efficient suppression of stable plaque components. *In vivo* thrombus imaging has been reported before with a T1w inversion recovery 3D gradient echo sequence at 1.5 T(27;28). However, the TI in those studies was chosen to null the blood signal at 1.5 T (27;28), leaving suboptimal contrast between IPH and stable plaque components.

The second component of interest in this study was lipid core. MRI of lipid core has shifted from direct lipid imaging with spectroscopic techniques(19;20) to MRI of the water signal of lipid core(29). T1/T2w TOF (TR=35 ms) images at 1.5 T have been reported to show iso- to hyper-intensity of lipid core(16;30), but T1w FLASH images (TR=300 ms) at 9.4 T have been reported to show iso- to hypo-intensity of lipid core(21) as is shown in this study. The shortening of T2 of lipid core with increasing field, may explain the difference in signal intensity of lipid core on T1w images between low and high field. Lower signal intensity of lipid core, despite the chosen short TE (2.14 ms) is the result when compared to all other components but calcification. TE may be more signal limiting for T1w FLASH images, acquired at 9.4 T, than TR. The decrease of efficiency of T2w and PDw imaging for depiction of lipid core may be explained by an increase of T1 for both tissues with increasing field strength, resulting in more saturation of particularly the fibrous tissue. In carotid artery imaging, fat suppression is generally applied to remove strong signals from peri-adventitious fat which could lead to chemical shift artifacts. We showed that lipid core was visualized more accurately using FLASH including fat suppression, when compared to FLASH without fat suppression. Fat suppression is thought to have little impact on tissue contrast within atherosclerotic plaque, because lipids found in atherosclerotic plaque consist primarily of cholesteryl esters and free cholesterol and not triglycerides as in perivascular fat(31). Suppression of the small number of triglycerides in lipid core with a saturation pulse aimed at the resonant frequency of methylene protons, was surprisingly effective in increasing conspicuity of lipid core, suggesting an effect on relaxation of nearby water protons. Contrast-enhanced MRI using small gadolinium chelates has shown to differentiate lipid core and fibrous cap as good as or better compared with T2w imaging(15;32). However in these studies, difference in enhancement between fibrous tissue (~80%) and lipid core (~30%) occurred by virtue of presence of neovasculature in fibrous tissue(15), which may vary among plaques.

There is a relation between resolution of MRI and classification accuracy. Some plaque components use little space or are mixed up mostly with another component (area of lipid mingled with fibroblasts). At low field, due to the lower resolution these plaque components cannot be distinguished from each other due to partial volume effects.

However at higher resolution the partial volume effects will be smaller. So, differentiation between small foam cell areas, potentially evolving in lipid core in near future, and lipid core, and cell-rich areas may be possible at higher field strength.

One study reported that *in vivo* resolution of MRI of human carotid artery plaque would be not limiting for classification accuracy between 156 and 1250 μm in plane(33). However, the authors also stated that degradation in resolution is most detrimental to plaques with large numbers of components(33). The thicknesses of tissue layers should at least span one pixel, to differentiate them visually(25). To prevent over-estimation of the surface of spot-like plaque components the diameter should at least span 5 pixels(25). Most importantly, one should keep in mind that the classification accuracy depends also on the sizes of component areas delineated on histology.

In this study, classification of plaque components was done with a supervised classification algorithm, the "Mahalanobis Distance classifier". Validated automated classification algorithms help in achieving maximum reproducibility and reliability in longitudinal *in vivo* plaque characterization studies. Variation in shim settings and coil configuration may cause differences in raw signal intensity of the same plaque component between carotid artery samples and modify contrast between two plaque components. Further, display of the image data may vary due to variety of window level settings and will determine the size of the image contrast between two plaque components. Moreover, post-processing software often applies contrast stretching or normalization which prevents direct comparison of contrast between various MR weightings. Instead of visual assessment, statistics can be applied to the image data which provide a reproducible and quantitative assessment of the image contrast.

When using Euclidean Distance, the set of points equidistant from a given location is a sphere. The MD stretches this sphere to correct for the respective scales of the different variables, and to account for correlation among variables (Figure 3). If the ED was used, the measured distance would be largely influenced by contrast weightings with high average signal intensity instead of contrast weightings with highest image contrast (9). Because MD takes into account the covariance among the variables, it is invariant to scale and correlation. Therefore, it is an ideal measure for comparison of outcomes of various MR weightings and may compare the same MR weightings obtained at another MR laboratory without influencing classification results. MD is even suitable for comparison of different imaging modalities(34;35) and classification algorithms based on MD may be used for multi-center trials focused on longitudinal plaque characterization. Earlier reported automatic plaque segmentation methods like with a Gaussian classifier have been successfully applied, but used pre-processing which included re-scaling of all pixels values to a baseline "iso-intensity"(36), which was not needed in this study.

There are some limitations to this study. Clinical *in vivo* MRI of carotid arteries is complicated by decreased resolution, motion artifacts, signals from flowing blood and greater spatial variability in MR signal due to the use of surface coils. The automated classification method for detection of plaque components has not been applied to *in vivo* data in this study.

The acquisition time of the IR-SE sequence was very long and can possibly be shortened by a multi-slice FSE instead of a single-slice SE approach. Inclusion of a double IR module will lead to dark blood images. Performance of the classifier needs to be checked for signal intensities obtained with clinically realistic acquisition times.

Further, the sample size was limited and so was the number of carotid artery sections with IPH. Only old IPH and not fresh/recent IPH was found in this data set because the carotid artery samples were not obtained from surgery but from autopsy.

In conclusion, identification of lipid core and IPH in human carotid artery plaque was improved *ex vivo* at 9.4 T with two clinically not commonly used MRI techniques, T1w FLASH with FS and IR-SE (TI=1000 ms). Automatic plaque segmentation was performed using a supervised classification algorithm, which calculates the Mahalanobis Distance. Because this measure is scale-invariant and takes into account the covariance of the data, the MD is useful for classification of plaque components and suitable for multi-center trials focused on plaque characterization in follow-up studies.

Reference List

1. Pasterkamp G, Schoneveld AH, van der Wal AC, et al. Relation of arterial geometry to luminal narrowing and histologic markers for plaque vulnerability: the remodeling paradox. J Am Coll Cardiol 1998:32:655-662.
2. Falk E, Shah PK, Fuster V. Coronary plaque disruption. Circulation 1995:92:657-671.
3. Ross R. Atherosclerosis is an inflammatory disease. Am Heart J 1999:138:S419-S420.
4. Chu B, Kampschulte A, Ferguson MS, et al. Hemorrhage in the atherosclerotic carotid plaque: a high-resolution MRI study. Stroke 2004:35:1079-1084.
5. Kampschulte A, Ferguson MS, Kerwin WS, et al. Differentiation of intraplaque versus juxtaluminal hemorrhage/thrombus in advanced human carotid atherosclerotic lesions by in vivo magnetic resonance imaging. Circulation 2004:110:3239-3244.
6. Takaya N, Yuan C, Chu B, et al. Presence of intraplaque hemorrhage stimulates progression of carotid atherosclerotic plaques: a high-resolution magnetic resonance imaging study. Circulation 2005:111:2768-2775.
7. Toussaint JF, Southern JF, Fuster V, Kantor HL. T2-weighted contrast for NMR characterization of human atherosclerosis. Arterioscler Thromb Vasc Biol 1995:15:1533-1542.
8. Toussaint JF, Southern JF, Fuster V, Kantor HL. Water diffusion properties of human atherosclerosis and thrombosis measured by pulse field gradient nuclear magnetic resonance. Arterioscler Thromb Vasc Biol 1997:17:542-546.
9. Clarke SE, Hammond RR, Mitchell JR, Rutt BK. Quantitative assessment of carotid plaque composition using multicontrast MRI and registered histology. Magn Reson Med 2003:50:1199-1208.
10. Clarke SE, Beletsky V, Hammond RR, Hegele RA, Rutt BK. Validation of automatically classified magnetic resonance images for carotid plaque compositional analysis. Stroke 2006:37:93-97.
11. Rogers WJ, Prichard JW, Hu YL, et al. Characterization of signal properties in atherosclerotic plaque components by intravascular MRI. Arterioscler Thromb Vasc Biol 2000:20:1824-1830.
12. Cai JM, Hatsukami TS, Ferguson MS, Small R, Polissar NL, Yuan C. Classification of human carotid atherosclerotic lesions with in vivo multicontrast magnetic resonance imaging. Circulation 2002:106:1368-1373.
13. Cai J, Hatsukami TS, Ferguson MS, et al. In vivo quantitative measurement of intact fibrous cap and lipid-rich necrotic core size in atherosclerotic carotid plaque: comparison of high-resolution, contrast-enhanced magnetic resonance imaging and histology. Circulation 2005:112:3437-3444.
14. Mitsumori LM, Hatsukami TS, Ferguson MS, Kerwin WS, Cai J, Yuan C. In vivo accuracy of multisequence MR imaging for identifying unstable fibrous caps in advanced human carotid plaques. J Magn Reson Imaging 2003:17:410-420.
15. Yuan C, Kerwin WS, Ferguson MS, et al. Contrast-enhanced high resolution MRI for atherosclerotic carotid artery tissue characterization. J Magn Reson Imaging 2002:15:62-67.
16. Yuan C, Mitsumori LM, Ferguson MS, et al. In vivo accuracy of multispectral magnetic resonance imaging for identifying lipid-rich necrotic cores and intraplaque hemorrhage in advanced human carotid plaques. Circulation 2001:104:2051-2056.
17. Saam T, Hatsukami TS, Takaya N, et al. The vulnerable, or high-risk, atherosclerotic plaque: noninvasive MR imaging for characterization and assessment. Radiology 2007:244:64-77.
18. Mitchell DG. Preparatory Pulses, Including Fat Suppression. In: Mitchell DG, editor. MRI principles, 2nd edition. Philadelphia: Saunders; 2004. p 177-198.
19. Vinitski S, Consigny PM, Shapiro MJ, Janes N, Smullens SN, Rifkin MD. Magnetic resonance chemical shift imaging and spectroscopy of atherosclerotic plaque. Invest Radiol 1991:26:703-714.
20. Trouard TP, Altbach MI, Hunter GC, Eskelson CD, Gmitro AF. MRI and NMR spectroscopy of the lipids of atherosclerotic plaque in rabbits and humans. Magn Reson Med 1997:38:19-26.
21. Te Boekhorst BC, Cramer MJ, Van Oosterhout MF, Pasterkamp G, Doevendans PA, Van Echteld CJ. High-resolution MRI for identification of various components of human carotid artery plaque using different weightings and fat suppression. J Cardiovasc.Magn Reson. 9, 252-253. In: 6th Meeting of the Euro Cardiac MR Working Group; Rome, 2007.
22. Babiloni F, Bianchi L, Semeraro F, et al. Mahalanobis Distance-Based Classifiers Are Able to Recognize EEG Patterns by Using Few EEG Electrodes. In: Proceedings 23rd Annual Conference IEEE/EMBS Oct.25-28; Istanbul, 2001.
23. Dalager-Pedersen S, Falk E, Ringgaard S, Kristensen IB, Pedersen EM. Effects of temperature and his-

topathologic preparation on the size and morphology of atherosclerotic carotid arteries as imaged by MRI. J Magn Reson Imaging 1999:10:876-885.

24. Morrisett J, Vick W, Sharma R, et al. Discrimination of components in atherosclerotic plaques from human carotid endarterectomy specimens by magnetic resonance imaging ex vivo. Magn Reson Imaging 2003:21:465-474.

25. Schar M, Kim WY, Stuber M, Boesiger P, Manning WJ, Botnar RM. The impact of spatial resolution and respiratory motion on MR imaging of atherosclerotic plaque. J Magn Reson Imaging 2003:17:538-544.

26. Shinnar M, Fallon JT, Wehrli S, et al. The diagnostic accuracy of ex vivo MRI for human atherosclerotic plaque characterization. Arterioscler Thromb Vasc Biol 1999:19:2756-2761.

27. Moody AR, Murphy RE, Morgan PS, et al. Characterization of complicated carotid plaque with magnetic resonance direct thrombus imaging in patients with cerebral ischemia. Circulation 2003:107:3047-3052.

28. Murphy RE, Moody AR, Morgan PS, et al. Prevalence of complicated carotid atheroma as detected by magnetic resonance direct thrombus imaging in patients with suspected carotid artery stenosis and previous acute cerebral ischemia. Circulation 2003:107:3053-3058.

29. Toussaint JF, Pachot-Clouard M, Kantor HL. Tissue characterization of atherosclerotic plaque vulnerability by nuclear magnetic resonance. J Cardiovasc Magn Reson 2000:2:225-232.

30. Honda M, Kitagawa N, Tsutsumi K, Nagata I, Morikawa M, Hayashi T. High-resolution magnetic resonance imaging for detection of carotid plaques. Neurosurgery 2006:58:338-346.

31. Yuan C, Kerwin WS. MRI of atherosclerosis. J Magn Reson Imaging 2004:19:710-719.

32. Wasserman BA, Smith WI, Trout HH, Cannon RO, Balaban RS, Arai AE. Carotid artery atherosclerosis: in vivo morphologic characterization with gadolinium-enhanced double-oblique MR imaging initial results. Radiology 2002:223:566-573.

33. Ronen RR, Clarke SE, Hammond RR, Rutt BK. Resolution and SNR effects on carotid plaque classification. Magn Reson Med 2006:56:290-295.

34. Silveira L, Jr., Sathaiah S, Zangaro RA, Pacheco MT, Chavantes MC, Pasqualucci CA. Correlation between near-infrared Raman spectroscopy and the histopathological analysis of atherosclerosis in human coronary arteries. Lasers Surg Med 2002:30:290-297.

35. Nogueira GV, Silveira L, Martin AA, et al. Raman spectroscopy study of atherosclerosis in human carotid artery. J Biomed Opt 2005:10:031117.

36. Liu F, Xu D, Ferguson MS, et al. Automated in vivo segmentation of carotid plaque MRI with Morphology-Enhanced probability maps. Magn Reson Med 2006:55:659-668.

Negative MR contrast caused by USPIO uptake in lymph nodes may lead to false positive observations with *in vivo* visualization of murine atherosclerotic plaque

Bernard C.M. te Boekhorst[1,2], Sandra M. Bovens[1,2], Marcel G.J. Nederhoff[1,2], Kees W.A. van de Kolk[1], Maarten J.M. Cramer[1], Matthijs F.M. van Oosterhout[3,4], Michiel ten Hove[1], Pieter A. Doevendans[1], Gerard Pasterkamp[1], Cees J.A. van Echteld[1#]

Departments of [1]Cardiology and [3]Pathology, University Medical Center Utrecht, The Netherlands, [2]Interuniversity Cardiology Institute of the Netherlands, Utrecht, Netherlands, [4]Department of Pathology, Antonius Medical Center Nieuwegein, The Netherlands, [#]Present address: Novartis Institutes for BioMedical Research, Basel, Switzerland

Abstract

Objective

USPIO are used clinically as a contrast agent for magnetic resonance imaging (MRI) of lymph nodes, and in research settings for MRI of macrophages in atherosclerotic lesions. However, T2* weighted (T2*w) imaging can lead to "blooming" with overestimation of the area occupied by USPIO. In this study, plaque uptake of USPIO in atherosclerotic mice was investigated in the presence and absence of circulating monocytes. The influence of peri-aortic lymph node uptake on the interpretation of T2*w images of the aortic wall was studied.

Methods

Atherosclerotic mice were fed an atherogenic diet and were randomized to total body irradiation or non-irradiation. After 2 days, T2*w MRI of the abdominal aorta was performed, followed by intravenous administration of 100 μmol/kg USPIO (t=0). At t=3 and 5 days MRI of the abdominal aorta was repeated. Animals were sacrificed and histological evidence for iron uptake by aortic wall and lymph nodes was compared with the degree of focal signal loss on *in vivo* MR images.

Results

Aortic walls in irradiated and non-irradiated mice, but also in healthy wild-type mice, showed signal loss on T2*w MRI. Signal loss, however, did not correspond with histological evidence of USPIO uptake by aortic wall but by peri-aortic lymph nodes.

Conclusions

The versatility of USPIO as a negative MR contrast agent for both lymph node staging and atherosclerosis may limit the use for detection of atherosclerotic lesions in vessels where lymph nodes are highly prevalent.

Introduction

Atherosclerosis is an inflammatory disease, which affects mid-sized arteries including the coronary arteries(1, 2). Coronary angiography is the clinical diagnostic tool of choice, providing a silhouette of the lumen but it does not visualize the atherosclerotic plaque. Therefore, direct visualization of the atherosclerotic plaque using Magnetic resonance imaging (MRI) has gained interest. MRI offers both anatomic detail and the potential to image cellular and molecular tissue characteristics.

Ultra small superparamagnetic particles of iron oxide (USPIO) are used as a MR contrast agent with a strong T2* shortening effect. They have a diameter of 18-30 nm and are not immediately recognized by the hepatic and splenic mononuclear phagocytic system. The half-life of USPIO has been reported to be around 90 minutes which is comparable to that of small liposomes(3). Because of their long half-life in blood, USPIO can be digested by macrophages throughout the whole body. USPIO have been used for detection of macrophage-rich atherosclerotic lesions in rabbit studies(4, 5, 6), and in some clinical studies which focused on carotid artery plaque in patients scheduled for carotid arterectomy(7, 8, 9, 10, 11).

However, the use of USPIO as a contrast agent has some potential drawbacks. Firstly, the strong T2* effect can lead to focal signal loss of an area larger than corresponding with the location of the USPIO. This effect is called "blooming" and is concentration-dependent(12).

Secondly, USPIO are not tissue-specific: they target macrophages, which may be active in various infective diseases and in healthy lymph nodes. Lymph nodes are distributed along the vascular tree(13) and are often located close to arterial sites of interest like the aortic wall. Blooming may impair the discrimination between signal loss due to homing in atherosclerotic plaques and signal loss due to close proximity of peri-aortic lymph nodes. To our knowledge, it is unknown whether iron uptake in lymph nodes may lead to false positive observations in atherosclerotic plaque imaging procedures.

We studied to what extent blooming of lymph nodes following USPIO uptake occurs near to the murine aortic atherosclerotic wall, which could easily lead to false positive observations.

Materials & Methods

Animals and study setup:

Experimental protocols were reviewed and approved by the Institutional Animal Care and Use Committee at Utrecht University Medical Center.

All knockout mice were backcrossed for 10 generations to the C57BL/6J genetic background. eNOS knockout (eNOS^{-/-}) and apoE^{-/-} mice (Jackson Laboratories, Bar Harbor, Me) were crossed to generate double heterozygous mice. These mice were then crossed and the offspring genotyped for eNOS and for apoE by polymerase chain reaction. ApoE^{-/-}/eNOS^{-/-} animals (aged 5-7 months) were used for experiments. Mice were weaned at 21 days and fed a regular diet until entry in to the study protocol. In addition, old (age >1 year) apoE^{-/-} mice were used. Wild-type mice (balb-C) were used as controls.

Group A

male apoE^{-/-}/eNOS^{-/-} or apoE^{-/-} mice (n=15) were fed a high fat, high cholesterol diet (42% of total calories from fat; 0.15% cholesterol added; Harlan-Teklad) for 16 weeks. After this diet period (t=-2 days), depletion of circulating monocytes was achieved with total body irradiation (TBI) of the animals with 7.0 Gray, in order to study whether signals in the vascular wall would originate from circulating monocytes(14). Two days later, baseline (t=0) MRI of the abdominal aorta was performed at the region from the right renal artery branch up to 9 mm above this branch. Immediately after MRI, a bolus injection of 75 μL (=100 micromole/kg) USPIO (Sinerem (dextran-coated), Laboratoire Guerbet, Aulnay-Sous-Bois, France) was administered via the tail vein. MRI measurements were repeated at t=3 and 5 days. Six mice did not survive until t=3 days and were kept out of analysis because no follow-up MRI was available. Five mice were terminated after the imaging procedure at t=3 days because of ruptured abdominal aortic aneurysm or because of severe hind limping, caused by aortic dissection. Before termination or after the measurements at 5 days, aortas of animals were perfusion-fixed in 4% formaldehyde and histology was performed. Blood samples were obtained from the tail vein of 5 mice at baseline and at 3 days. Analysis of white blood cell count and differentiation was performed for 3 of these animals at 5 days after TBI.

Group B

male apoE^{-/-}/eNOS^{-/-} or apoE^{-/-} mice (n=7) were treated the same as the animals in group A, except that no TBI was applied. Two animals were sacrificed after the MRI examination at t=1 and 3 days respectively to study early plaque uptake. Ex-vivo MRI of the aorta of these animals was performed before histology. These animals were excluded from the statistical analysis.

Negative control

In one mouse, saline was administered instead of USPIO as a negative control for blooming of the aorta. Otherwise, the animal was treated as the animals in group B.

Wild-type controls

Three adult wild-type (Balb-c) mice were treated as animals in group B, except that they were fed a standard chow diet and MRI was performed only at t=5 days. MR images of the healthy aortas were acquired at aortic bifurcation, renal artery branches and aortic arch. These locations are known for the presence of peri-aortic lymph nodes(13).

Anaesthesia and MRI protocol: see on line supplement.

Histopathology and Immunohistochemistry

Aortas were perfusion-fixed, excised and stored in 4% formaldehyde. Transversely cut 5 μm sections were stained with hematoxylin/eosin and elastin von-Giesson (EvG). Prussian blue (PB) and MAC-3 stainings (R&D systems, Oxon, UK) were used for detection of iron particles and macrophages, respectively. The renal artery branches were used as landmarks for correspondence with MRI.

Comparison of MR images and histology

The degree of blooming on T2* weighted (T2*w) images was assessed semi-quantitatively using a "darkening index" (DI). Each MRI level was scored according to the degree of luminal signal loss of the aorta: 1. minimal (outside the lumen), 2. moderate (less than half the area), 3. severe (more than half the area) or 4. very severe (totally obscured lumen). The cumulative DI was defined as the sum of DI scores for the ten slice levels. Cumulative DI from group A was compared with cumulative DI from group B. The amount of iron uptake in the plaque and in the lymph node (PB-staining area) was quantified by measurement of the absolute area of positive PB-staining per slice level (software package Image J 1.41). PB-staining area was correlated to DI at the corresponding MRI level. The relative cumulative PB-staining area was defined as the cumulative PB-staining area divided by total lymph node area. The cumulative PB-staining area and relative cumulative PB-staining area were compared between groups. T2*w and T2w images acquired at t=3 days were compared with the corresponding images acquired at t=5 days. Plaque area and number of plaque macrophages were determined per slice level and cumulatively to obtain the total plaque area (mm^2) and total number of macrophages. The relative number of macrophages per mouse is calculated as the number of macrophages divided by the total plaque area.

Statistics

Descriptive statistics show mean ± standard error of the mean (SEM). Kendall's tau_b (τ) was calculated to test the correlation between the DI and PB-staining area of corresponding histology. Differences between groups A and B with regard to plaque area, number of macrophages in the plaque, cumulative DI and PB-staining area were analyzed by one-way analysis of variance (ANOVA) and Student's t-test where appropriate. If ANOVA revealed a significant difference or a strong tendency to a difference between the groups, post-hoc comparison of means was performed with a Bonferroni test (with 2-sided p value).

Results

Plaque area, number of macrophages, cumulative darkening index and PB-stained area
The irradiation protocol led to a significant depletion of white blood cells at 2 days after TBI. The number of all blood cell types further decreased from 2 days after TBI up to 7 days after TBI (Table 1).

No differences in plaque area and number of macrophages were observed between old apoE$^{-/-}$ and 5-7 month old apoE$^{-/-}$/eNOS$^{-/-}$ mice (p=0.54) and between group A and B (Table 2). Histology sections of both irradiated (group A) and non-irradiated mice (group B) showed extensive plaques around the renal artery branches.

Only minor PB-staining was detected in atherosclerotic plaques. PB stained macrophages were predominantly observed in lymph nodes (figure 1 and 2). No differences in cumulative DI were observed at t=3 days between groups A, B and controls. Interestingly, at t=5 days, PB stained macrophages were found in peri-aortic lymph nodes, but not in aortic plaque in the non-irradiated as well as the irradiated group (Figure 1 and 2 respectively). In all groups, one or two mice showed a few iron particles in the interstitium (around the

Table 1

Mouse	Before TBI (n=5)	Day 2 after TBI (n=5)	Day 7 after TBI (n=3)
WBC	12.1 ± 0.91*	1.16 ± 0.05*/**	0.57 ± 0.03*/**
Lymphocytes	8.94 ± 0.88*	0.84 ± 0.05*/**	0.37 ± 0.03*/**
Monocytes	1.64 ± 0.10*	0.10 ± 0.00*	0.10 ± 0.00*
Granulocytes	1.52 ± 0.08*	0.20 ± 0.03*	0.10 ± 0.00*

*The effect of TBI on depletion of white blood cells (WBC), lymphocytes, monocytes, and granulocytes (concentrations in 10^9/L). *p<0.001, differences between numbers of mentioned blood cell types before TBI and one of both time points after TBI.*

**p<0.001, differences between numbers of mentioned blood cell types at 2 days and 7 days after TBI.

Table 2:

Group	Plaque area (mm²)	Norm. Mφ (mm⁻²)	Cumulative DI (t=72h)	Cumulative DI (t=120h)	Cumulative PBSA (mm²)	Relative Cumulative PBSA (%)
A	1.74 ± 0.69	566 ± 100	10.67 ± 1.04	10.75 ± 1.11	0.26 ± 0.07	23.3 ± 4.7
B	2.46 ± 1.88	415.5 ± 95.1	11.40 ± 1.66	12.40 ± 1.97	0.39 ± 0.14	24.5 ± 4.7

Histology parameters and cumulative DI of all mice; mean ± SEM; Norm. Mφ= normalized number of macrophages, PBSA= PB-staining area (iron), Relative Cumulative PBSA= cumulative PBSA divided by total lymph node area.
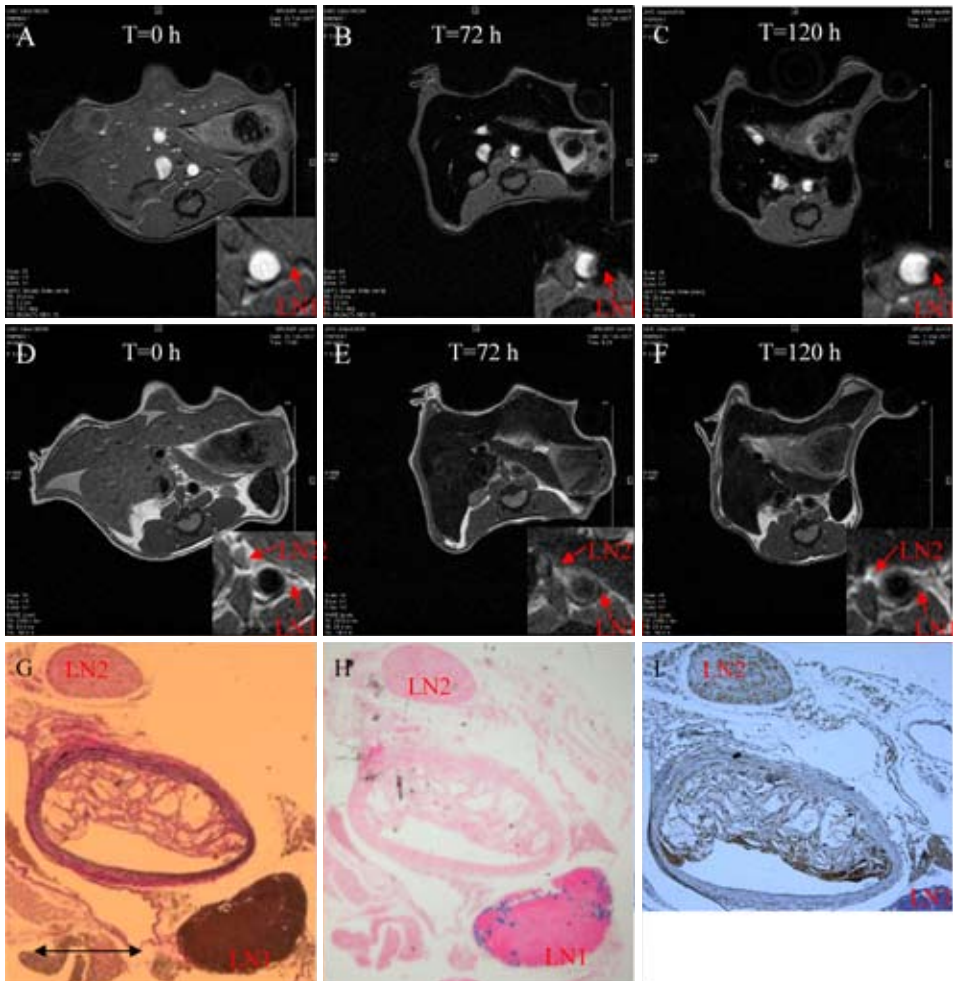
Figure 1. T2*w (A-C) and T2w (D-F) MR images of the aorta of an apoE⁻/⁻/eNOS⁻/⁻ mouse of group B at t=0 (A, D), t=3 days (B, E) and t=5 days (C, F); level: 3 mm above the right renal artery branch. Corresponding histology sections stained with EvG (G), for iron (PB) (H) and for macrophages (mac-3) (I). Inserted panels: magnification of peri-aortic region. Double arrow=500 μm. LN1 and LN2: lymph nodes.
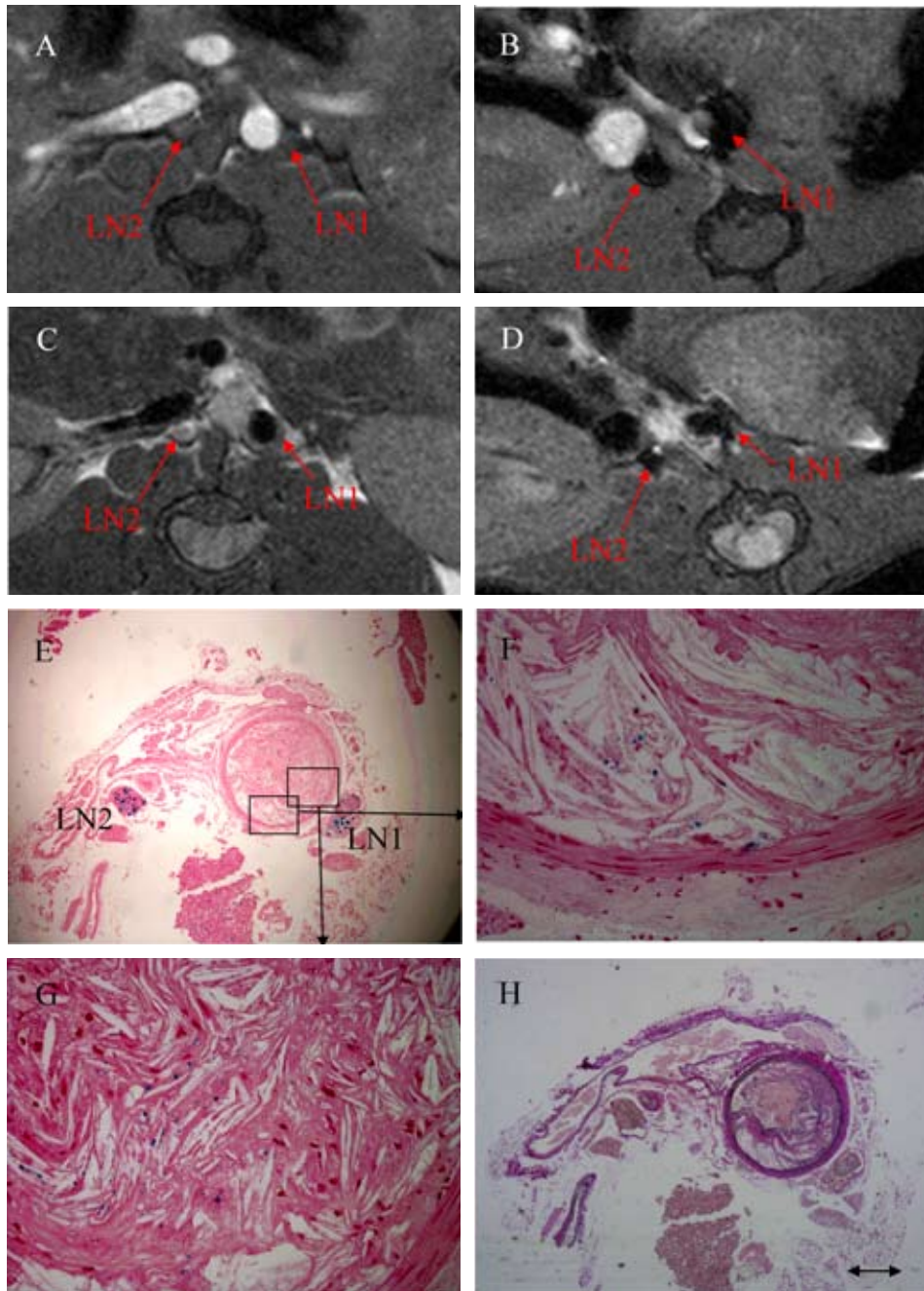
Figure 2. T2*w and T2w MR images of the aorta of an apoE⁻/⁻/eNOS⁻/⁻ mouse of group A at t=0 (A, C), and t=3 days (B, D); level: 1 mm above the right renal artery branch. Corresponding ex vivo sections are stained for iron (Prussian Blue) (E) and with EvG (H). Further magnification of two plaque regions (F,G) reveals intracellular uptake of USPIO in plaque macrophages at 3 days after administration. For further explanation: see text. Double arrow=500 μm.

vasa vasorum). In one mouse, from the irradiated group terminated at t=3 days, some PB-stained macrophages were found in the plaque. The amount of PB-staining of interstitium and plaque was negligible when compared to the amount of PB-staining of adjacent lymph nodes (Figure 2). The cumulative PB-staining area in group B was higher than in group A, but due to large variability this did not reach significance when compared to group A (Table 2; p=0.558). Importantly, despite the presence of strong focal signal loss, it was not possible to determine the exact location of iron uptake, *i.e.* in lymph nodes or plaque, based on the T2*w images. The T2w FSE images showed more confined signal loss. However, it was still not possible to locate this signal loss precisely. Retrospectively, it was often identified as a small lymph node, which approximated the outer aortic wall very closely (Figure 2).

To test whether MRI at higher resolution could better localize USPIO uptake, *in vivo* MRI of one mouse, treated as a non-irradiated mouse in group B and sacrificed at t=3 days instead of 5 days, was followed by *ex vivo* MRI. *In vivo* MRI showed a cumulative DI=11, which is similar to the mean cumulative DI in group A and B. High-resolution *ex vivo* MRI revealed that uptake of USPIO was confined to the peri-aortic lymph nodes, which was confirmed by histology (Figure 3). We treated another old apoE^{-/-} mouse as group B, but performed MRI and harvested the aorta at 14 hours after administration of USPIO. Also in this mouse plaque uptake of USPIO was not observed despite reasonable plaque area and number of macrophages (data not shown).

Correlation between MRI and histology

DI at t=5 days correlated positively with PB-staining area (τ=0.347, p<0.001). Therefore, the results of T2*w MRI correlated well with the abundant presence of USPIO in peri-aortic lymph nodes. DI at t=3 days also correlated well with PB-staining area in group A and B (τ=0.428, p<0.001). As expected, DI at t=3 days correlated closely with DI at t=5 days in irradiated and non-irradiated mice that were imaged at both time points (τ=0.821, p<0.001).

Control experiments

In one mouse, saline was administered instead of USPIO. At t=5 days, MRI showed no focal signal loss on T2*w images. Corresponding PB-stained sections did not reveal any iron in plaque, or in peri-aortic lymph nodes, indicating that endogenous iron did not explain the findings in groups A and B. The T2*w images of wild-type mice at t=5 days after injection of USPIO showed signal loss of the (peri-)aortic region. The extent of the signal loss was similar to the signal loss found on T2*w images of animals in all atherosclerotic mice groups (cumulative DI=11 ± 1). Histology revealed iron uptake in peri-aortic lymph nodes but not in the vessel wall (Figure 3).
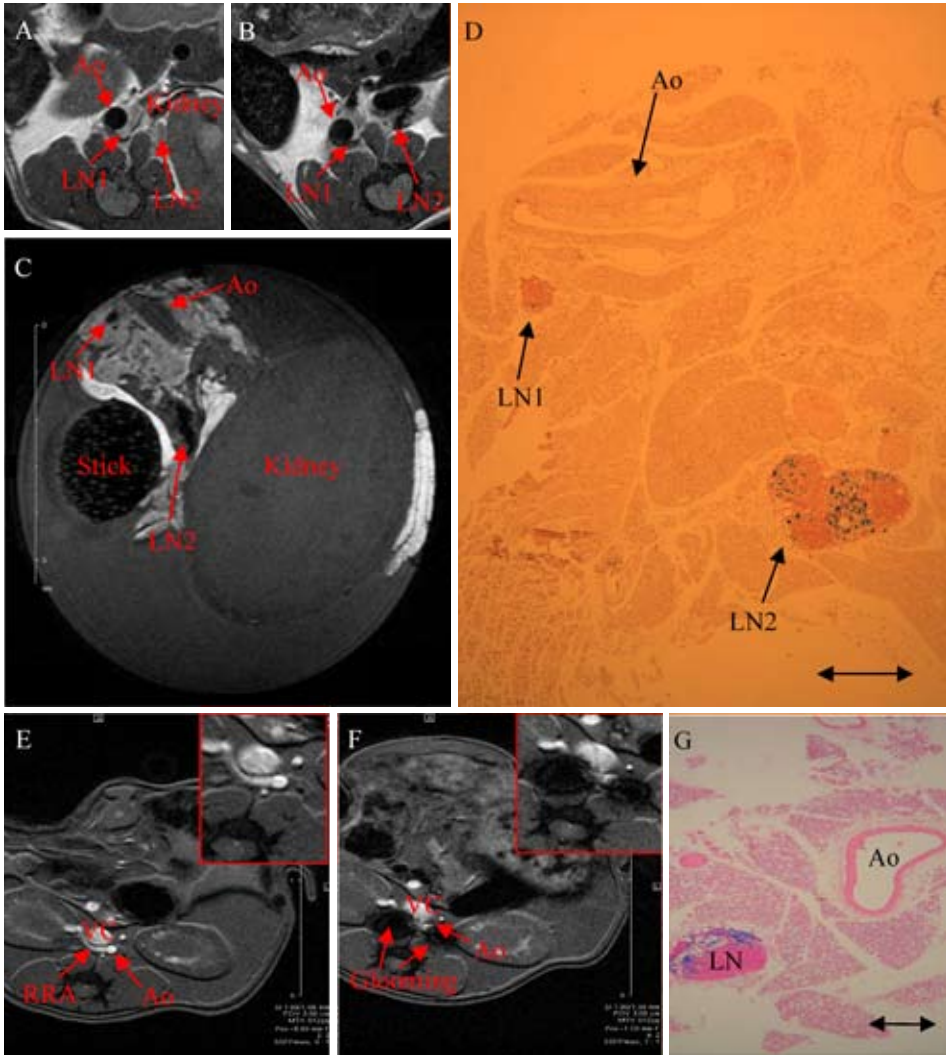
Figure 3. Comparison between in vivo/ex vivo MRI and histology in one apoE-/- mouse and between in vivo MRI and histology in a healthy wild-type mouse after administration of USPIO. In vivo T2w FSE images of the abdominal aorta of an old apoE-/- mouse at t=0 (A) and 3 days (B), and ex vivo high resolution T2w FSE image at 3 days (C). Corresponding histology section stained for iron (D). In vivo T2*w MRI at t=0 (E) and t=5 days (F) in a wild-type mouse. Corresponding histology section stained for iron (G). See text for explanation. Level: abdominal aorta, right renal artery branch. LN= lymph node; Ao= aorta; VC= vena cava; RRA= right renal artery. Double arrow=500 µm.

Discussion

We studied the effect of blooming of lymph nodes on *in vivo* MRI detection of USPIO uptake in murine aortic atherosclerotic wall. In addition, we studied plaque uptake of USPIO in plaque in the presence and absence of circulating monocytes. For this purpose, we used total body irradiation of apoE$^{-/-}$/eNOS$^{-/-}$ and apoE$^{-/-}$ mice, which are known to develop atherosclerotic lesions. Of five irradiated mice, only one (which died before t=5 days) had plaque stained minimally positive for iron. So, we were unable to draw any conclusions regarding the routing of USPIO into plaque. However, we did see blooming that originated from lymph nodes, in both irradiated and non-irradiated mice, suggesting that resident macrophages are responsible for uptake of the USPIO.

The main finding of our study was that focal signal loss of the aortic lumen on the T2*w images was exclusively caused by the accumulation of USPIO in peri-aortic lymph nodes. Therefore, we conclude that *in vivo* MRI of the murine aorta at the resolution used in this study (100 μm^2), may be impaired by the uptake of USPIO by peri-aortic lymph nodes. The latter may complicate the discrimination between aortic plaques and surrounding lymph nodes and could lead to false positive observations.

We found that focal signal loss of the aortic lumen on MR images, acquired at 3 and 5 days after USPIO administration, correlated with PB-staining. Endogenous iron did not cause positive iron staining. These results show that USPIO-enhanced MRI may differentiate between low and high uptake of exogenous iron.

In all mice, we found intense PB-staining of the lymph nodes, whereas only one irradiated mouse showed PB-stained plaque macrophages. However, in the latter, PB-staining of the lymph nodes was much more intense than PB-staining of the plaque. One may suggest that the time course of uptake and clearance of USPIO in mice is shorter than we anticipated and therefore t=5 days may be too late for histology assessment. This theory could explain why one mouse in the irradiated group, terminated at 3 days, showed some intracellular uptake by plaque macrophages, whereas none of the animals showed uptake at day 5. It could also account for the finding of some iron particles in the interstitial tissue at t=5 days. However, in old apoE mice (treated as group B) at t=1 and 3 days after administration of USPIO, we found no evidence for plaque uptake of USPIO, despite reasonable plaque area and number of macrophages.

In this study, USPIO were found particularly in macrophages. The avidity of macrophages for USPIO was shown by the fact that after ex-vivo incubation with USPIO, a reasonable amount of USPIO-loaded mouse peritoneal macrophages could be sorted with a magnetized column (data not shown). Other studies confirm in-vivo uptake of USPIO by macrophages(15). However, USPIO uptake in sub-intimal arterial wall layers and in media (via neovasculature) has also been reported(6, 16).

In contrast to our study, Litovsky *et al*. found SPIO in the plaque 5 days after administration(17). These particles, however, are substantially larger than USPIO which impairs comparisons. To our knowledge, only one other study has used MRI to visualise USPIO uptake in atherosclerotic plaque in mice was(15). Morris *et al*. showed the presence of USPIO in the plaque 48 hours after administration. However, in that study atherosclerotic plaque in the aortic arch of apoE$^{-/-}$ mice was visualized after stimulation of vascular inflammation with chronic angiotensin II infusion and not "spontaneously" (diet) induced plaque. Angiotension II could result in plaque microruptures, facilitating USPIO invasion into the plaque, rather than USPIO uptake in intact plaques. Ruehm *et al*. showed that in rabbits, MRI performed 120 hours after administration of USPIO showed plaque enhancement. Imaging at earlier time-points led to susceptibility artifacts caused by USPIO in the circulating blood(4). In patients who were scheduled for carotid atherectomy, USPIO were found in atherosclerotic plaque 24 hours after administration(8). Importantly, in all these studies, USPIO uptake in adjacent lymph nodes was not studied or at least not reported. Finally, the chosen animal model and patient condition could influence plaque uptake of USPIO by virtue of the density of macrophages in the plaque. However, this study shows that atherosclerotic plaques in these mouse models have a large number of macrophages. The number of macrophages in plaques is comparable to that in the large lymph nodes in close proximity, which showed abundant uptake of USPIO. The mechanisms which explain the difference in uptake of USPIO by macrophages between lymph nodes and plaque are unknown.

Focusing on the main finding of this study, local signal loss of the aortic lumen on the T2*w images was exclusively caused by the accumulation of USPIO in peri-aortic lymph nodes. Apparently, from the perspective of this study, the amount of iron uptake in the plaque is, at least at the assessed time-points, too low to overcome the signal from the lymph nodes. Schmitz *et al*. describe, in a review, that USPIO, need to occupy at least 5 adjacent layered cells to be visible as a local signal void(16). Indeed, in this study plaque uptake of USPIO did not span two or three adjacent cells ever, which could explain why intra-plaque USPIO was not detectable with MRI.

The ability to detect USPIO in atherosclerotic plaque is affected not only the number of adjacent cells occupied, but also by the MRI method of choice. As expected, T2*w images showed higher contrast between USPIO-containing regions and surrounding tissues, while T2w images showed more confined signal loss and less blooming. However, T2w *in vivo* images still did not discriminate between presence of USPIO in the plaque and the lymph node.

We hypothesized that resolution in relation to lymph node and plaque size is the main problem in accurate localization. Indeed, in this study, *ex vivo* high-resolution MRI showed that exact localization of USPIO is possible when the spatial resolution is increased (pixel

size 39x39 μm^2, slice thickness 0.25 mm). Based on these results, we can conclude that for discrimination between mouse aortic wall and peri-aortic lymph nodes with T2w USPIO-enhanced MRI, a pixel size much smaller than 100 μm^2 is required. Morris *et al*. also showed that *ex vivo* MRI with a spin echo sequence at a similar pixel size may accurately depict a confined area with signal loss caused by USPIO. As mentioned before, in that study the presence of USPIO in plaque in the aortic arch (using a non-spontaneous atherosclerotic plaque model) was demonstrated(15), in contrast to our results. In addition, they showed corresponding *in vivo* T2*w images with focal signal loss of the aortic wall expanding to the lumen with a pixel size of approximately 100μm^2, which is comparable to the *in vivo* pixel size in this study. Some human MRI studies(9, 10, 11) showed clear uptake of USPIO in carotid plaque. The local absence of lymph nodes, the large plaque size and relatively higher resolution could explain those results.

The lack of uptake of USPIO in this study could be due to the particle size in relation to the endothelial pore size. In an atherosclerotic rabbit model, fractionated SPIO (hydrodynamic diameter <15 nm) were observed in plaque whereas un-fractionated SPIO (hydrodynamic diameter ~120 nm) were not found in plaque(6). In this mouse study USPIO were slightly larger than the fractionated SPIO used in the mentioned rabbit study, while the average rabbit aortic diameter is approximately 4 times larger than the average murine aortic diameter(18, 19).

This study reveals some major limitations of dextran-coated USPIO, but PEG-lipid coated USPIO could avoid uptake by lymph node owing to lower immunogenicity. Also, antibodies or targeting peptides could be coupled to the PEG groups of these USPIO(20). Targeted USPIO could remain in atherosclerotic plaque for a longer time or at a higher concentration. To address the blooming effect, gradient echo techniques that create positive signal enhancement in areas containing USPIO may increase the confidence of USPIO localization(6).

Conclusions

Lymph node uptake may be misinterpreted as intra-plaque uptake of USPIO when visualized with MRI. Increased blooming on T2*w MR images may be prevented by T2w MR imaging at higher resolution because this strategy could lead to better discrimination between USPIO uptake in the plaque and the adjacent lymph nodes.

Acknowledgments

The authors thank Laboratoire Guerbet (Aulnay-Sous-Bois, France) for providing Sinerem.

References

1. Lusis AJ. Atherosclerosis Nature 2000; 407:233-41
2. Vink A, Pasterkamp G. Atherosclerotic plaque burden, plaque vulnerability and arterial remodeling: the role of inflammation Minerva Cardioangiol. 2002; 50:75-83
3. Weissleder R, Elizondo G, Wittenberg J, Rabito CA, Bengele HH, Josephson L. Ultrasmall superparamagnetic iron oxide: characterization of a new class of contrast agents for MR imaging Radiology. 1990; 175:489-93
4. Ruehm SG, Corot C, Vogt P, Kolb S, Debatin JF. Magnetic resonance imaging of atherosclerotic plaque with ultrasmall superparamagnetic particles of iron oxide in hyperlipidemic rabbits Circulation 2001; 103:415-22
5. Schmitz SA, Coupland SE, Gust R, Winterhalter S, Wagner S et al. Superparamagnetic iron oxide-enhanced MRI of atherosclerotic plaques in Watanabe hereditable hyperlipidemic rabbits Invest Radiol. 2000; 35:460-71
6. Briley-Saebo KC, Mani V, Hyafil F, Cornily JC, Fayad ZA. Fractionated Feridex and positive contrast: in vivo MR imaging of atherosclerosis Magn Reson. Med. 2008; 59:721-30
7. Trivedi RA, Mallawarachi C, King-Im JM, Graves MJ, Horsley J et al. Identifying inflamed carotid plaques using in vivo USPIO-enhanced MR imaging to label plaque macrophages Arterioscler. Thromb. Vasc. Biol. 2006; 26:1601-6
8. Kooi ME, Cappendijk VC, Cleutjens KB, Kessels AG, Kitslaar PJ et al. Accumulation of ultrasmall superparamagnetic particles of iron oxide in human atherosclerotic plaques can be detected by in vivo magnetic resonance imaging Circulation 2003; 107:2453-8
9. Kawahara I, Nakamoto M, Kitagawa N, Tsutsumi K, Nagata I et al. Potential of magnetic resonance plaque imaging using superparamagnetic particles of iron oxide for the detection of carotid plaque Neurol. Med. Chir (Tokyo). 2008; 48:157-61
10. Tang TY, Howarth SP, Li ZY, Miller SR, Graves MJ et al. Correlation of carotid atheromatous plaque inflammation with biomechanical stress: utility of USPIO enhanced MR imaging and finite element analysis Atherosclerosis 2008; 196:879-87
11. Tang TY, Howarth SP, Miller SR, Graves MJ, King-Im JM et al. Comparison of the inflammatory burden of truly asymptomatic carotid atheroma with atherosclerotic plaques in patients with asymptomatic carotid stenosis undergoing coronary artery bypass grafting: an ultrasmall superparamagnetic iron oxide enhanced magnetic resonance study Eur. J Vasc. Endovasc. Surg. 2008; 35:392-8
12. Qiu B, Gao F, Walczak P, Zhang J, Kar S et al. In vivo MR imaging of bone marrow cells trafficking to atherosclerotic plaques J Magn Reson. Imaging 2007; 26:339-43
13. Popesko P., Rajtova V., Horak J. colour atlas of Anatomy of Small Laboratory Animals, Saunders Ltd. 2003.
14. Harrington NP, Chambers KA, Ross WM, Filion LG. Radiation damage and immune suppression in splenic mononuclear cell populations Clin. Exp. Immunol. 1997; 107:417-24
15. Morris JB, Olzinski AR, Bernard RE, Aravindhan K, Mirabile RC et al. p38 MAPK inhibition reduces aortic ultrasmall superparamagnetic iron oxide uptake in a mouse model of atherosclerosis: MRI assessment Arterioscler. Thromb. Vasc. Biol. 2008; 28:265-71
16. Schmitz SA. [Iron-oxide-enhanced MR imaging of inflammatory atherosclerotic lesions: overview of experimental and initial clinical results] Rofo. 2003; 175:469-76
17. Litovsky S, Madjid M, Zarrabi A, Casscells SW, Willerson JT, Naghavi M. Superparamagnetic iron oxide-based method for quantifying recruitment of monocytes to mouse atherosclerotic lesions in vivo: enhancement by tissue necrosis factor-alpha, interleukin-1beta, and interferon-gamma Circulation 2003; 107:1545-9
18. Vernhet H, Demaria R, Perez-Martin A, Juan JM, Oliva-Lauraire MC et al. Wall mechanics of the stented rabbit aorta: long-term study and correlation with histological findings J. Endovasc. Ther. 2003; 10:577-84
19. Knipp BS, Ailawadi G, Sullivan VV, Roelofs KJ, Henke PK et al. Ultrasound measurement of aortic diameters in rodent models of aneurysm disease J. Surg. Res. 2003; 112:97-101
20. Li X, Du X, Huo T, Liu X, Zhang S, Yuan F. Specific Targeting of Breast Tumor by Octreotide-Conjugated Ultrasmall Superparamagnetic Iron Oxide Particles Using a Clinical 3.0-Tesla Magnetic Resonance Scanner Acta Radiol. 2009; 1-12

Supplement

Mice were imaged in a vertical 9.4T, 89mm bore size magnet equipped with 1500 mT/m gradients and connected to an Avance 400 MR system (Bruker BioSpin, Germany) using a quadrature-driven birdcage coil with an inner diameter of 3 cm. Monitoring of, and triggering on, respiratory and cardiac motion was performed with a respiratory pad connected to a trigger unit (Rapid, Würzburg, Germany). Inhalation anaesthesia was provided with isoflurane. In case of baseline measurements, an intravenous catheter was inserted into the tail vein. Coronal and saggital scout images of the suprarenal abdominal aorta were planned. Ten contiguous transverse slices, perpendicular to coronal and saggital scout images, were acquired from the right renal artery branch to 9 mm upwards. This slice package was used for planning anatomic T2 weighted dark-blood reference scans and T2* contrast weighted (T2*w) (most sensitive to negative contrast agents) bright-blood scans. These scans were acquired during maximal aortic flow velocity. Hereto, firstly, a T1w fast spin echo (FSE) scan (cardiac triggered and respiratory gated) of one transverse slice at the level of 5 mm above the right renal artery was repeatedly acquired while the trigger delay was varied. Images were checked for laminar flow artifacts (bright vessel rims: result of low flow velocity) and for maximal distension of the aortic lumen. The trigger delay that provided the image with no flow artifacts and the largest aortic diameter was chosen for anatomic reference scans and T2*w scans.

Parameters *in-vivo* MRI
T2w FSE anatomic reference scans: TR/TE=2800/29.3 ms, rare factor=20, sinc pulse 450 μs, excitation/refocusing flip angle=90°/180°, Spectral width=200000 Hz, FOV=30x30 mm^2, matrix=280x280 resulting in pixel dimension=107x107 μm^2, slice thickness=1 mm, NA=4. FOV=field of view, NA= number of averages. T2*w steady-state free precession (SSFP) scans: TR/TE=35/2.20 ms, sinc pulse 500 μs, flip angle=18°, Spectral width=166667 Hz, FOV=30x30 mm^2, matrix=280x280 resulting in pixel dimension=107x107 μm^2, slice thickness=1 mm, NA=15. Total scan time generally was 90 minutes. These measurements were repeated at t= 3 days and 5 days after administration of USPIOs, where appropriate. After the MRI measurements at 5 days, anaesthesia of mice was continued with a mixture of medetomidine (6%)/ketamine (5%) (0.1 mL per 10 gram), and aortas were harvested.

Ex-vivo **MRI**
The abdominal aorta of the mice in group B that were terminated at early timepoints, were fixed in formaldehyde 4% and subsequently immersed in fomblin. Coronal and saggital

scout MRI scans, described in the previous section, were acquired. Transverse T2w FSE scans were planned.

Parameters *ex-vivo* MRI

TR/TE=3500/17.8 ms, rare factor=4, sinc pulse 500 µs, excitation/refocusing flip angle =90˚/180˚, Spectral width=200000 Hz, FOV=10x10 mm^2, matrix=256x256 resulting in spatial resolution=39x39 µm^2, slice thickness=0.25 mm (20 slices, gap 0.25 mm), NA=128.

Characterization, *in vitro* and *in vivo* testing of CB2-receptor and NGAL-targeted paramagnetic micelles for molecular MRI of vulnerable atherosclerotic plaque

B.C.M. te Boekhorst[1,2], S.M.Bovens[1,2], J. Rodrigues-Feo[1], H.M.H.F. Sanders[3,4], C.W.A. van de Kolk[1], A.I.P.M. de Kroon[5], M.J.M. Cramer[1], P.A.F.M. Doevendans[1], M. ten Hove[1], G. Pasterkamp[1], C.J.A. van Echteld[1,#]

[1]*Department of Cardiology, University Medical Center Utrecht, The Netherlands,* [2]*Interuniversity Cardiology Institute of the Netherlands, Utrecht, The Netherlands,* [3]*Biomedical NMR, Department of Biomedical Engineering, Eindhoven University of Technology, Eindhoven, The Netherlands,* [4]*Soft Matter Cryo-TEM Research Unit, Eindhoven University of Technology, Eindhoven, The Netherlands,* [5]*Institute of Biomembranes, University of Utrecht, Netherlands,* [#]*Present address: Novartis Institutes for BioMedical Research, Basel, Switzerland*

Abstract

Purpose

Atherosclerotic plaque macrophages express the peripheral cannabinoid receptor (CB2-R) and promote fibrous cap degradation by secretion of Neutrophil Gelatinase Associated Lipocalin-2 (NGAL). In this study, we report the preparation, characterization, *in vitro* and *in vivo* testing of double-labeled (MR and fluorescent) CB2-R and NGAL targeted micelles.

Procedures/Results

Specific CB2-R agonists or antibodies directed to 24p3 (mouse homologue of NGAL) were incorporated into DOPE-PEG1000 micelles or DSPE-PEG2000 micelles. The hydrodynamic diameter, determined by dynamic light scattering, was 16.5 and 19.0 nm for CB2-R targeted DOPE-PEG1000 and DSPE-PEG2000 micelles respectively, and for Ab-conjugated DSPE-PEG2000 micelles 23.0 nm. *In vitro* and *in vivo* MRI and fluorescence microscopy showed specific binding of CB2-R targeted and 24p3 targeted micelles to *in vitro* systems and to aortic plaque in apoE$^{-/-}$/eNOS$^{-/-}$ mice, respectively.

Conclusions

CB2-R and NGAL targeted micelles show promise as tools for *in vivo* characterization of vulnerable plaque.

Introduction

Myocardial infarction and stroke are often the result of rupture or erosion of a vulnerable plaque. Classical vulnerable plaque characteristics are: a thin fibrous cap, large lipid core and many macrophages in the shoulder regions of the plaque(1). High-resolution MRI has been successfully used for *in vivo* visualization of various plaque constituents in the carotid arteries of patients scheduled for carotid endarterectomy(2). Identification of high-risk patients suffering from carotid atherosclerotic disease may become feasible in the future.

Molecular MRI with targeted contrast agents provides an attractive option to visualize vulnerable plaque characteristics in smaller arteries like coronary arteries for risk stratification of patients with coronary artery disease. The use of nanoparticle platforms which harbor both molecular probes with affinity for plaque or antibodies (Abs) directed against plaque antigens and a reasonable payload of gadolinium (Gd) as a T1 shortening agent has been reported in various animal studies(3-7). Some of these platforms have a large payload of Gd, which is imperative for MRI visualization of plaque markers, typically present at low *in vivo* concentrations (micromolar range). In various studies nanoparticles have been used for characterization of early stages of atherosclerotic disease(6-8) or for visualization of the sequelae of thrombosis(3,4). However, molecular MRI of the advanced rupture-prone plaque is clinically more relevant because clinical decision-making may be based on molecular imaging features of this plaque.

Inflammation is an important feature of atherosclerosis, and macrophages play a central role in the atherosclerotic process. Various anti-inflammatory negative feedback mechanisms that are protective during the atherosclerotic process are set into action, for example the upregulation of peripheral cannabinoid (CB2) receptor in the plaque(9). The peripheral CB2 receptor (CB2-R) is expressed on the cell membrane of macrophages and T lymphocytes only in advanced plaque(9) and has been thought to have a dampening effect on inflammation. Indeed, activation of this receptor via a very potent specific synthetic CB2-R agonist (HU-308) led to modification from an unstable plaque phenotype to a more stable plaque phenotype in mice(9,10).

Macrophages secrete matrix metalloproteinases (MMPs), which are enzymes thought to be causative in thinning of the fibrous cap of an atherosclerotic plaque(11,12). Although first discovered in neutrophils, it has been found recently that Neutrophil Gelatinase Associated Lipocalin (NGAL) is also released by macrophages, prolonging the activity of MMPs and destabilizing the plaque(13). Therefore, CB2-R and NGAL targeted contrast agents may help to identify vulnerable atherosclerotic plaques.

In this study, we report the preparation and characterization of micelle-based MR contrast

agents aimed at these targets. 24p3 (mouse homologue of NGAL) Abs are coupled after SATA (N-succinimidyl S-Acetylthioacetate) modification to maleimide-poly-ethylene-glycol (mal-PEG) present on the periphery of the micelles(14). The lipophilic synthetic specific CB2-R agonist (HU-308) can be conveniently mixed with the lipids making up the micelles. Because of the presumed location of the relatively lipophilic HU-308 at the interface of the lipophilic micelle core and the more hydrophilic corona and the anticipated rigidity of the micelle structure and steric hindrance caused by PEG groups, possibly masking HU-308, we make both DSPE-PEG2000 and DOPE-PEG1000 CB2-R targeted micelles.

We report on *in vitro* experiments performed with these contrast agents on CHO cells that express the CB2-R and on a phantom system consisting of a 24p3 coated Eppendorf tube. In addition, we show the first results of *in vivo* MRI on apoE$^{-/-}$/eNOS$^{-/-}$ mice, targeting plaque macrophages and 24p3 in the plaque with CB2-R targeted and 24p3 targeted micelles. The results demonstrate that these contrast agents have the potential to visualize vulnerable plaque *in vivo*.

Materials & Methods

Materials

Cells from the Chinese hamster ovary (CHO) cell line and CHO cells transfected with CB2-R (CHO-CB2), were cultured in Minimal Essential Medium Alpha (Gibco Life Technologies, Breda, the Netherlands) and supplements.

Monoclonal Phospho-p44/42 Mitogen-activated Protein Kinases (MAPK) (Thr202/Tyr204) (Erk1 and Erk2) rabbit antibody (Ab) was obtained from Cell Signaling Technology, Inc. (Boston, USA). Recombinant mouse 24p3, monoclonal rat anti-mouse 24p3 Ab, rat anti-mouse isotype Ab, biotinylated rabbit anti-mouse 24p3 polyclonal Ab and streptavidin-FITC were purchased from R&D Systems (Oxfordshire, UK). Rat anti-mouse mac-3 monoclonal Ab conjugated to AlexaFluor 647 was purchased from Biolegend (San Diego, USA).

Polyethylene glycol-di-oleoyl-phosphatidylethanolamine (DOPE-PEG) with a polyethylene glycol (PEG) residue of 1000 Da and di-stearoyl-PE-PEG with a PEG residue of 2000 Da (DSPE-PEG2000), Mal-PEG2000-di-stearoyl-phosphatidylethanolamine (Mal-PEG2000-DSPE), and Lissamine-rhodamine-phosphatidylethanolamine (Liss-rhod-PE) were purchased from Avanti Polar Lipids (Alabaster, AL, USA). Gd-DTPA-bisstearylamide was purchased from Gateway Chemical Technology Inc (St Louis, USA). A synthetic very potent selective CB2 agonist of CB2-R, 4-(4-(1,1-Dimethylheptyl)-2,6-dimethoxyphenyl)-6,6-dimethyl-bicyclo(3.1.1)hept-2-ene-2-methanol)) (HU-308)

was purchased from Alexis Biochemicals (San Diego, USA). SATA and hydroxylamine hydrochloride were purchased from Sigma-Aldrich (Schnelldorf, Germany). Bovine serum albumin was purchased from Mallinckrodt Baker (Deventer, The Netherlands). NaCl, Na2HPO4 and NaH2PO4 were purchased from Merck (Darmstadt, Germany). Phosphate buffered saline (PBS, containing 8.2 g/L NaCl and 3 g/L Na2HPO4 and 0.33 g/L NaH2PO4 (pH 7.4)) was prepared and passed through polycarbonate membrane filters with a pore diameter of 200 nm in order to remove dust particles.

Preparation of micelles

CB2 receptor targeted micelles
DOPE-PEG1000 (DOPE) micelles
A mixture of the appropriate amounts of lipids (DOPE-PEG1000, Gd-DTPA-bisstearylamide, Liss-rhod-PE and HU-308 in a molar ratio of 75:10:5:10), dissolved in chloroform, was dried by rotary evaporation at 40˚C during 3 min. The lipid film was subsequently hydrated in 1 ml PBS to a final lipid concentration of 10 mM.

DSPE-PEG2000 (DSPE) micelles
A mixture of the appropriate amounts of lipids (DSPE-PEG2000, Gd-DTPA-bisstearylamide, Liss-rhod-PE and HU-308 in a molar ratio of 35:50:5:10), dissolved in chloroform, was dried by rotary evaporation at 40˚C during 3 min. The lipid film was subsequently hydrated in 1 ml PBS at 40˚C during 5 min to a final lipid concentration of 10 mM.
Hydration of a lipid film of DOPE-PEG1000 including more than 10 mol% Gd-DTPA-bisstearylamide led to large lipid aggregates, whereas hydration of a lipid film of DSPE-PEG2000 including 50 mol% Gd-DTPA-bisstearylamide led to formation of micelles.

24p3 targeted and isotype Ab conjugated micelles
A mixture of the appropriate amounts of lipids (DSPE-PEG2000, Gd-DTPA-bisstearylamide, Liss-Rhod-PE and Mal-PEG2000-DSPE in a molar ratio of 43:50:5:2), dissolved in chloroform, was dried by rotary evaporation at 40 ˚C during 3 min. The lipid film was subsequently hydrated in 1 ml PBS during 5 min to a final lipid concentration of 10 mM and the suspension was kept under nitrogen. Rat anti-mouse Abs (molecular weight 140 kDa) targeted against 24p3 or rat anti-mouse isotype Abs were conjugated to the maleimide groups of the micelles by sulfhydryl-maleimide coupling(15). Sulfhydryl groups were added to rat anti-mouse 24p3 Abs or rat anti-mouse isotype Abs (10mg) by incubation for 30 min at room temperature with SATA. The modified Ab was added to the micelles and incubated for 14 hrs, at 4°C, while gently stirred. The ratio of Ab to

lipid (μmole:μmole) was 0.7:100. So, assuming an aggregation number of 100, nearly all micelles were occupied by Ab.

Micelles conjugated to SATA-modified Abs were separated from SATA-modified Abs and non-conjugated micelles by size exclusion chromatography using Sephacryl S-1000 Superfine with an exclusion diameter of ~3000 Å (Amersham Biosciences, Uppsala, Sweden). The length and diameter of the column was 65 cm and 1.1 cm, respectively. Fluorescence intensities of Liss-Rhod-PE ($\lambda_{excitation}$ 570 nm, $\lambda_{emission}$ 600 nm) and of tryptophan (from Abs) ($\lambda_{excitation}$ 280 nm, $\lambda_{emission}$ 350 nm) of eluted fraction volumes of 2 ml were measured. Simultaneous elution of protein and fluorophore was considered evidence of successful conjugation and the percentage of conjugated Abs was estimated from the fluorescence-elution volume plots. Additionally, the elution volume of non-conjugated micelles and non-modified Ab was checked after loading a mixture of them.

Moreover, the percentage of maleimide conjugated to Abs was assessed by sulfhydryl/ maleimide determination of micelles using a thiol and sulfide quantification kit (T6060, Molecular Probes Invitrogen, USA)(16).

Size measurements
Size measurements were performed on CB2-R targeted and on isotype Ab conjugated micelles but not on 24p3 targeted micelles, due to the high cost of these Abs.

DLS
The size and size distribution of the lipid dispersions (in PBS) were determined by dynamic light scattering (DLS) at 25 ˚C with a Malvern 4700 System.

Cryo-TEM
The cryo-TEM study was performed using a FEI Tecnai 20, type Sphera TEM instrument equipped with an LaB6 filament operating at 200 kV, in which the images were recorded with a bottom-mounted 1k x 1k Gatan CCD camera. A Gatan cryoholder operating at ~ -170 °C was used for the cryo-TEM measurements.

R2/2 Quantifoil Jena grids, were purchased from Aurion (Wageningen, the Netherlands). 300 mesh lacey carbon film grids were purchased from Agar Scientific (Essex, England). The TEM-grids were surface plasma treated using a Cressington 208 carbon coater operating at 5 mA for 40 s prior to the sample preparation. The lipid dispersions (in PBS) were brought into contact with a sample grid. The sample vitrification procedures were carried out using an automated vitrification robot (FEI Vitrobot Mark III) at 100% humidity.

Receptor activation

CHO cells, which over-expressed the CB2-R, and non-modified CHO cells were incubated with the HU-308-containing micelles at a lipid concentration of 25 µM for 15 min. Up-regulation of intracellular linked MAPK as a response to binding of CB2-R targeted micelles to CB2-R was tested by Western blotting. Negative and positive control experiments were performed with non-targeted micelles and free HU-308, respectively.

***In vitro* cell and phantom MRI experiments**

Qualitative assessment of binding/uptake of micelles by CHO cells and binding to 24p3: CHO cells, which over-expressed the CB2-R, and non-modified CHO cells were grown on glass capillaries. Glass capillaries were incubated with the CB2-R targeting micelles or control micelles at a lipid concentration of 1 mM for 1 h at 37˚C.

Poly-ethylene Eppendorf tubes were coated with mouse recombinant 24p3 (0.50 µg/mL) or bovine serum albumin (0.50 µg/mL) (the coating with 24p3 was confirmed by ELISA). These tubes were incubated for 1 h with 1 mM 24p3 targeted micelles or isotype-conjugated micelles.

Glass capillaries and Eppendorf tubes were subsequently washed three times with PBS to prevent nonspecific binding. T1-weighted MRI of these capillaries was performed (see MRI protocol).

Quantitative assessment of binding/uptake of micelles by CHO cells

CHO cells were cultured to a confluent layer in 25 ml flasks (10-12x106 cells). These flasks with CB2-R+ and CB2-R- CHO cells were incubated with CB2-R targeted and non-targeted DOPE and DSPE micelles at increasing lipid concentrations (0.2, 0.4, 0.6, 0.8, 1.0 mM) for 1 h. Cells were washed with PBS. Cells were trypsinized, centrifuged and 20 µl formaldehyde 4% (v/v) was added to the pellets (fixation for at least 24 h). Pellets were transferred to PCR tubes and T1 measurements of cell pellets were performed (see MRI protocol). CHO cells not incubated with micelles were treated the same way and various amounts of CB2-R targeted DOPE or DSPE micelles were added to the fixed cell pellets in order to make a calibration curve. These cell pellets were incubated for at least 45 min to allow binding. T1 measurements were performed and 1/T1 was plotted against Gd concentration. These calibration curves were used to determine quantitatively the dose-dependent uptake/binding of micelles by CHO cells.

***In vitro* cell fluorescence imaging**

Qualitative assessment of binding/uptake of micelles by CHO cells

CHO cells, which over-expressed CB2-R, and non-modified CHO cells were grown on cover glasses and incubated with CB2-R targeting micelles or control micelles at a

lipid concentration of 1mM for 20, 40, 60 or 80 min. Confocal microscope fluorescence imaging (excitation wavelength 543 nm, emission wavelength 600 nm) was done with a Zeiss LSM 510 meta microscope (lense: 63X, settings confocal pinhole 1.00 airy unit resulting in an optical slice thickness of 0.7 mm).

MRI protocol

T1 values of various micelle suspensions at various concentrations in PBS were measured at 37 ˚C with tabletop 0.47 T and 1.41 T NMR (Bruker Minispec spectrometers) and with a Bruker Avance 400 9.4 T NMR spectrometer, equipped with a vertical 8.9 cm bore size magnet and a 1500mT/m gradient insert (Bruker Biospin, Germany). Nanoparticles evaluated were: 1. CB2-R targeted DSPE-PEG2000 micelles with 50 mol% Gd, 2. CB2-R targeted DOPE-PEG1000 micelles with 10 mol% Gd, and 3. rat IgG isotype conjugated DSPE-PEG2000 micelles with 50 mol% Gd (same size and Gd content as 24p3 targeted micelles). Relaxivity of 24p3 targeted micelles was not evaluated because of the high cost of Abs.

For each micelle suspension measurements were performed 4 times. 1/T1 was plotted against Gd concentration. The relaxivities of the micelle suspensions were calculated by linear regression of these data. Correlation coefficient r of the fit was determined.

The 9.4T NMR spectrometer (Bruker Biospin, Germany) was also used for *in vitro* 1H MRI and 31P MRS. The 24p3 coated Eppendorf tubes were collectively imaged in a 1.0 cm diameter volume coil using quadrature detection as were capillaries with CHO cells. T1 measurements of cell pellets were performed in a 3.0 cm diameter volume coil.

A fast spin echo (FSE) sequence was used for producing transverse scout images. Inversion Recovery (IR)-FSE was the technique of choice for T1 weighted imaging of the CHO cells grown on capillaries and antibody-coated Eppendorf tubes (see table 1 for MRI parameters). T1 measurements were performed on cell pellets using IR-FSE images with increasing inversion time (TI) (70-100-200-400-1000-2000-3000-4000-8000ms (and TR=8500ms)).

The width at half height of the isotropic (narrow) phosphatidylethanolamine peak in the 31P NMR spectrum of DOPE and DSPE micelles was checked over a large temperature range (21.7 to 76.1 °C) to ensure, that over a clinically relevant temperature range no large lipid aggregates are formed in aqueous solution. 31P NMR measurements were performed at a spectrometer frequency of 161.975 MHz (parameters: hard (block) pulse, duration 25 μsec, flip angle 90°, spectral width 5000 Hz, number of scans 64).

In vivo **MRI experiments**

Feasibility to generate plaque enhancement *in vivo* was tested for both CB2-R targeted DSPE-PEG2000 and 24p3 targeted micelles in two apoE^{-/-}/eNOS^{-/-} mice, which were fed

an atherogenic diet for 4 weeks. This mouse model has been shown to create severe atherosclerosis in the abdominal aorta(17). Also non-conjugated micelles or rat isotype Ab conjugated micelles were injected via the tail vein in two apoE^{-/-}/eNOS^{-/-} mice as a control for CB2-R targeted and 24p3 targeted micelles. Plasma half lifes of similar non-conjugated micelles and CNA35-micelles (collagen binding bacterial protein) in apoE^{-/-} mice were found to be 22 hours and 17 hours, respectively (Van Bochove et al., unpublished results). Preliminary experiments in our lab showed higher uptake of CB2-R targeted micelles than control micelles at 48 hours post-injection, while a large difference in plaque uptake between 24p3-targeted micelles and isotype Ab conjugated micelles was observed at 72 hours post-injection. Therefore, post-injection MRI was timed according to these post-injection time-points, minimizing enhancement as a result of simple extravasation.

Animal preparation and anesthesia
Mice were imaged in the same 9.4 T NMR spectrometer using a quadrature-driven birdcage coil with an inner diameter of 3 cm. Monitoring of and triggering on respiratory and cardiac movements were performed with a respiratory pad connected to a trigger unit (Rapid Biomedical, Rimpar, Germany). Inhalation anesthesia was provided with isoflurane. An intravenous catheter for injection after the pre-injection measurement was inserted into the tail vein.

Scout images
An FSE technique was used for axial scout images. Subsequently, coronal and sagittal scout images of the abdominal aorta were acquired. The right renal artery branch was used as a landmark for matching of baseline, post-injection MRI and histology. Ten contiguous axial slices, perpendicular to coronal and sagittal scout images, were planned from 4 mm below the right renal artery branch till 5 mm above this branch.

Optimization of trigger delay
Signal acquisition was planned at the moment of maximal flow through the abdominal aorta. Hereto, axial T1 weighted FSE (cardiac and respiratory gated) at the level of 1 mm above the right renal artery was repeated with varying trigger delay. Images were checked for laminar flow artifacts (bright vessel rims as a result of slow flow) and the diameter of the aortic lumen. Trigger delay corresponding with the image, which lacked flow artifacts and had the largest aortic diameter, was chosen (optimized trigger delay) for other scans as described below.
IR-FSE was used for acquisition of T1 weighted images (for acquisition parameters: Table 1). The acquisition scheme was started with an inversion pulse. The chosen trigger

delay (TD) for IR-FSE was chosen in a way, that the equation (TI + TD)/(cardiac cycle duration) = integer number + optimized TD was satisfied.

Contrast injection and post-injection IR-FS

The cradle was removed from the magnet, contrast agent of choice (200 µL 10 mM lipid CB2-R targeted or non-targeted control micelles, or 200 µL 3 mM lipid 24p3 targeted or isotype Ab conjugated micelles) was injected via the intravenous catheter and subsequently the animal recovered from anesthesia. Forty-eight hours (CB2-R targeted

Table 1. MRI parameters T1 weighted imaging of phantom, CHO cells grown on glass capillaries and 24p3 coated Eppendorf tubes.

	In vitro		*In vivo*
	CHO cells	24p3	CB2-R/24p3 targeted micelles
TI (ms)	1000	1350	1300
TR (ms)	8500	5000	3500
ETL	1	8	16
TE (ms)	12.4	6.78	14.9
Exc. FA (°)	90	90	90
SW (kHz)	75	200	75.8
Matrix	132x256	96x128/48x64	192x256
FOV (mm x mm)	30x30	10x10	30x30
Zero filling factor	1.90	1.34	1.34
Resolution (µm x µm)	230x117	78x104/156x208	117x117
Slice thickness (mm)	0.25	0.5	0.50
Fat suppression	-	-	+
NA	2	1	20
AT (m:s)	38:32	0:30/ 1:00	13:20

TI=Inversion time, TR= repetition time, ETL=echo train length, TE=echo time, RF pulses: inversion, excitation and refocusing pulse, Exc. FA=excitation flip angle, SW=Spectral width, FOV=field of view, NA=number of averages, AT=acquisition time.

Table 2. Relaxivity per Gd concentration ($mM^{-1}s^{-1}$) at different field strengths (0.47, 1.41 and 9.4 T) at 37°C and size (hydrodynamic diameter (nm)), determined with DLS, of various contrast agents. Relaxivities are calculated from data in figure 1 by linear regression.

	Relaxivity			Size (DLS)
Contrast agent	0.47T	1.41T	9.4T	by volume
50 mol% Gd DSPE CB2-R targeted micelles	13.12	9.83	2.74	19.0±1.0
10 mol% Gd DOPE CB2-R targeted micelles	12.30	10.09	3.84	16.5±1.2
50 mol% Gd isotype-conjugated DSPE micelles	11.94	9.32	3.0	23.0±1.0

and control micelles) or 72 hours (24p3-targeted and isotype Ab conjugated micelles) later, the animal was anesthetized again and repositioned in the magnet. IR-FSE images were acquired as pre-injection.

Immunohistochemistry
Abdominal aortas were perfusion-fixed with formaldehyde 4%/PBS (1:10 v:v), excised, embedded in tissue-tek and stored at -20˚C until preparation of cryosections. Transversely cut 5 µm sections were stained with hematoxylin/eosin. Also sections were double-stained for macrophages and 24p3. Hereto rat anti-mouse mac-3 monoclonal antibody (macrophages) conjugated to AlexaFluor 647, biotinylated rabbit anti-mouse 24p3 polyclonal antibody and streptavidin-FITC were used. Fluorescence microscopy (laser excitation/emission wavelengths: 488/520 (FITC), 543/590 (lissamin-rhodamin), and 633/670 (AlexaFluor 647)) was performed. Co-localization of 24p3, macrophages and micelles was evaluated after merging of the three fluorescence images within ImageJ software (W. Rasband, version 1.29, National Institutes of Health 2003).

Results

Size, relaxivity
CB2-R targeted DOPE-PEG1000 and DSPE-PEG2000 micelles had a size of 16.5 ± 1.2 nm and 19.0 ± 1.0 nm, respectively (mean $\pm$ SD, n=6 measurements of one aliquot per preparation). Rat IgG-conjugated micelles had a size of 23.0 ± 1.0 nm (mean $\pm$ SD, n=6 measurements) (Table 2). All micelles had a narrow size distribution (Poly Dispersity Index = 0.160, 0.185 and 0.220, respectively). Cryo-TEM showed some disc-like aggregates in all micelle solutions, but overall confirmed the narrow size distribution (Figure 1). DLS showed that the antibody-conjugated micelles had the same size after storage for 6 weeks at 4 ˚C as freshly after preparation. Moreover, the antibody-conjugated micelles were shown by ELISA to still attach to mouse 24p3 after 6 weeks. The relaxivity of CB2-R targeted and antibody-conjugated micelles increased with decreasing field strength, as expected (see Figure 2 and Table 2). Relaxivities of various micelle preparations were comparable (Table 2).

Temperature stability
The linewidth of the phosphatidylethanolamine peak in the 31P NMR spectrum of the micelles ranged between 11.7 and 13.5 Hz within a temperature range of 21.7 to 76.1 °C (data not shown). This suggests that no large lipid aggregates are formed in an aqueous solution over a clinically relevant temperature range.
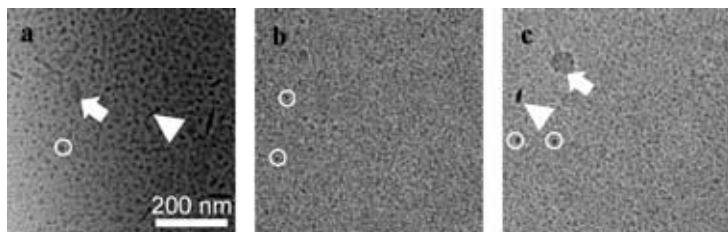
Figure 1. Cryo-TEM of 50M% Gd-DTPA-bisstearylamide DSPE-PEG2000 non-conjugated (a), isotype antibody-conjugated (b), and 10M% Gd-DTPA-bisstearylamide DOPE-PEG1000 non-conjugated (c) micelles. Panels show not only micelles but also some larger lipid aggregates (circles), discs (arrowhead) and a piece of ice (arrows).
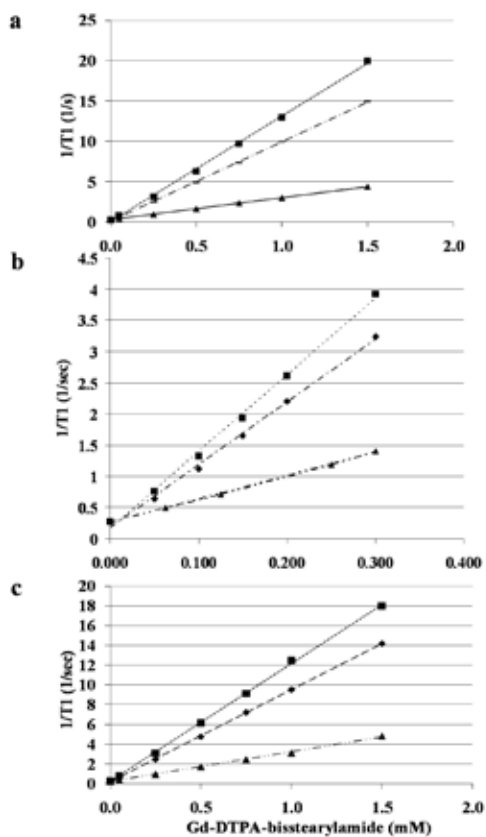

Figure 2. Relationship between 1/T1 (pooled from 4 T1 measurements) and Gd-DTPA-bisstearylamide concentration at different field strengths (0.47T (squares), 1.41T (diamonds) and 9.4 T (triangles) at 37˚C of 50 M% Gd-DTPA-bisstearylamide non-conjugated micelles (a), 10M% Gd-DTPA-bisstearylamide non-conjugated micelles (b) and 50M% Gd-DTPA-bisstearylamide antibody-conjugated micelles (c). Shown are the regression lines. Correlation coefficient r was at least 0.99 for all regression lines.

CB2 receptor targeted micelles

Biological activity of CB2-R targeted micelles

Up-regulation of intracellular linked MAPK after binding of CB2-R targeted micelles to CHO cells, which expressed the CB2-R, was tested by Western blotting. Indeed, in contrast to CHO cells without CB2-R, CHO cells with CB2-R showed significant upregulation of MAPK (p-ERK1 and p-ERK2) after incubation with HU-308 positive micelles for 15 min (Figure 3).

In vitro MRI and fluorescence microscopy of CHO cells incubated with micelles
Qualitative assessment of binding/uptake of micelles by CHO cells

In vitro MRI of CB2-R positive and CB2-R negative CHO cells, cultured on glass capillaries after 1 h incubation with CB2-R targeted and control DOPE and DSPE micelles, showed that glass capillaries with CB2-R positive CHO cells after incubation with CB2-R targeted DOPE and DSPE micelles were bright, whereas all control capillaries were dark (Figure 4A-B).

For fluorescence imaging of CHO cells, first incubation time (20, 40, 60, 80 min) was optimized. CB2-R positive CHO cells, which were incubated with CB2-R targeted micelles, showed evidently increased intracellular fluorescence intensity after an incubation time of 40, 60 and 80 min when compared to CB2-R negative CHO cells and both CHO cell types incubated with control micelles (Figure 5). After an incubation time of 20 min, hardly any uptake or binding of micelles was found. No difference in uptake behavior was observed between DOPE and DSPE CB2-R targeted micelles.
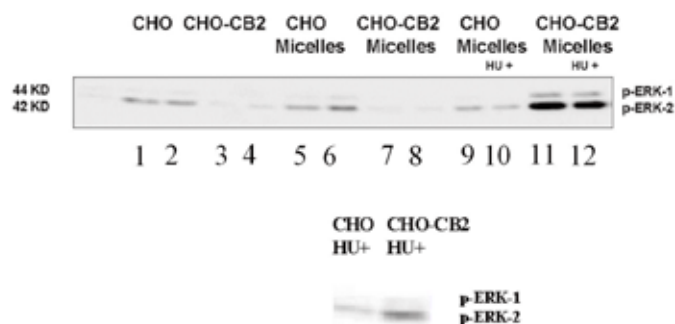

Figure 3. Western blot analysis: upregulation of intracellular MAP kinases (p-ERK-1 (44 kD) and p-ERK-2 (42 kD)) in Chinese Hamster Ovary cells with (CHO-CB2) or without (CHO) CB2-R after incubation with CB2-R targeted (HU+m) or control micelles (HU-m) (25 µM lipid) or without micelles. Experiments were performed in duplo. Upper panel: lane 1 and 2: CHO; lane 3 and 4: CHO-CB2; lane 5 and 6: CHO HU-m; lane 7 and 8: CHO-CB2 HU-m; lane 9 and 10: CHO HU+m; lane 11 and 12: CHO-CB2 HU+m. The upregulation of intracellular MAP kinases in these cells was also checked in the presence of free HU-308 (2.5 µM) (lower panel).

Quantitative assessment of binding/uptake of micelles by CHO cells

Cell pellet concentrations of bound and/or intracellular micelles were obtained from T1 measurements of cell pellets and comparison with calibration curves (figure 4C). Cell pellet concentrations increased almost linear with increasing incubation concentration only for the combination of CB2-R positive CHO cells and both types of CB2-R targeted
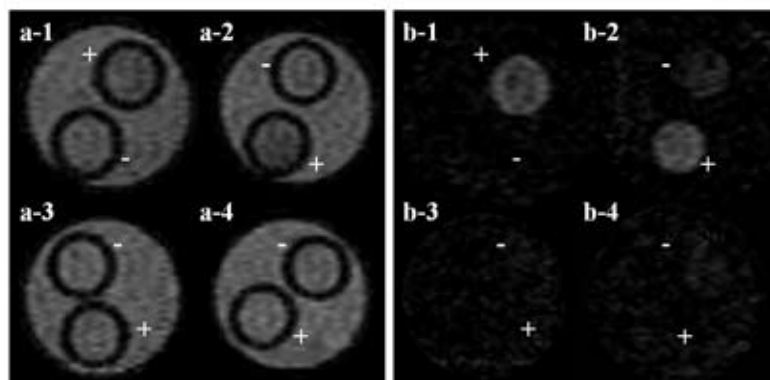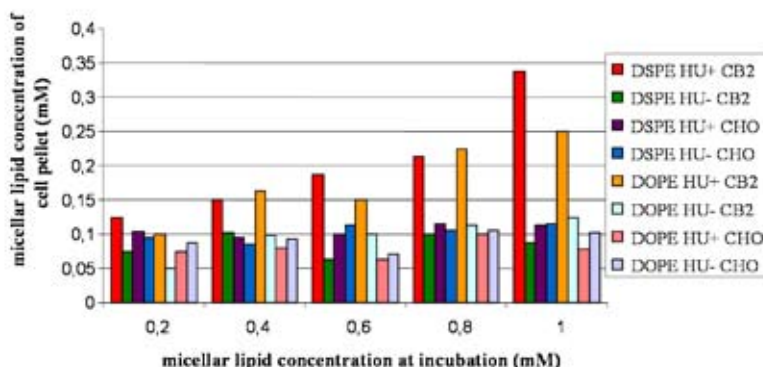

Dose dependence and specificity of binding of micelles to CHO cells

Figure 4. a and b. MR images of capillaries with CHO cells incubated with micelles. a: inversion recovery TI=250ms, which creates hardly any T1 contrast; b: inversion recovery TI=1000ms, which creates low signal of PBS and high signal of bound micelles. a-1/b-1: HU+ DSPE-PEG2000; a-2/b-2: HU+ DOPE-PEG1000; a-3/b-3: HU- DSPE-PEG2000; a-4/b-4: HU- DOPE-PEG1000; -: CB2-R negative CHO cell; +: CB2-R positive CHO cell. c. Dose-dependent CB2-R targeted micelle binding/uptake capacity of CB2-R positive CHO cells was quantified using T1 measurements of cell pellets. CB2-R positive (CB2) and CB2-R negative (CHO) cells grew confluent in 25 ml flashes and were incubated with increasing concentrations of CB2-R targeted and control micelles for 60 minutes. T1 values were measured with inversion recovery and concentrations were derived from calibration curves of 1/T1 values of CB2-R positive CHO cell pellets incubated with known concentrations of 50M% Gd-DTPA-bisstearylamide DSPE micelles or 10M% Gd-DTPA-bisstearylamide DOPE micelles.

micelles (peak concentrations with maximum incubation concentration (1mM): DSPE: 0.34 mM, DOPE: 0.25 mM). All other combinations showed a micelle concentration which did not exceed 0.12 mM. The difference between cell pellet concentrations after incubation with DOPE and DSPE CB2-R targeted micelles could be due to the difference in Gd content of the micelles.

24p3 targeted micelles
Antibody conjugation efficiency/occupation of maleimides by antibodies
A mixture of non-conjugated micelles and non-modified antibody was loaded on the Sephacryl column and the elution volume of non-conjugated micelles and non-modified antibody was 55 mL and 67 mL respectively. As expected, the elution volume of Ab conjugated micelles was smaller than that of free antibodies and also of bare micelles, so size exclusion chromatography could be used to determine the efficiency of the conjugation procedure (Figure 6). As can be observed from the areas under the antibody curves, conjugation was almost complete with more than 95% of the antibody added to the micelles becoming attached.

According to size exclusion chromatography >95% of antibodies was bound to mal-PEG (Figure 6). Given that the molar antibody to lipid ratio was 0.7:100 and the percentage of mal-PEG was 2%, it could be calculated that ~35% of mal-PEG was occupied by antibody. We found with the sulfhydryl/maleimide quantification method, that ~45% of mal-PEG2000-PE was occupied by thiol modified 24p3 antibody, in approximate agreement with our calculations.

***In vitro* MRI of 24p3 coated tubes incubated with micelles**
MR images of 24p3 coated tubes, which were incubated with 24p3 targeted micelles, showed a bright rim both at higher and lower resolution, in contrast to MR images of 24p3 coated tubes, which were incubated with isotype-conjugated micelles (Figure 7). MR images of bovine serum albumin coated tubes, incubated with isotype-conjugated or 24p3 targeted micelles did not show a bright rim either (data not shown).

***In vivo* MRI of plaque with CB2-R and 24p3 targeted micelles**
In apoE$^{-/-}$/eNOS$^{-/-}$ mice, at 48 h after injection of CB2-R DSPE and at 72 h after injection of 24p3 targeted micelles, signal intensity of plaque at 1-2 mm above the right renal artery was increased when compared to pre-injection images (Figure 8 and 9, panels A and B). Importantly, the lower and the upper part of the abdominal aorta showed lower plaque area and did not show increased signal intensity both after injection of CB2-R and 24p3 targeted micelles (Figure 10 and 11, panels A and B). Two mice injected with control
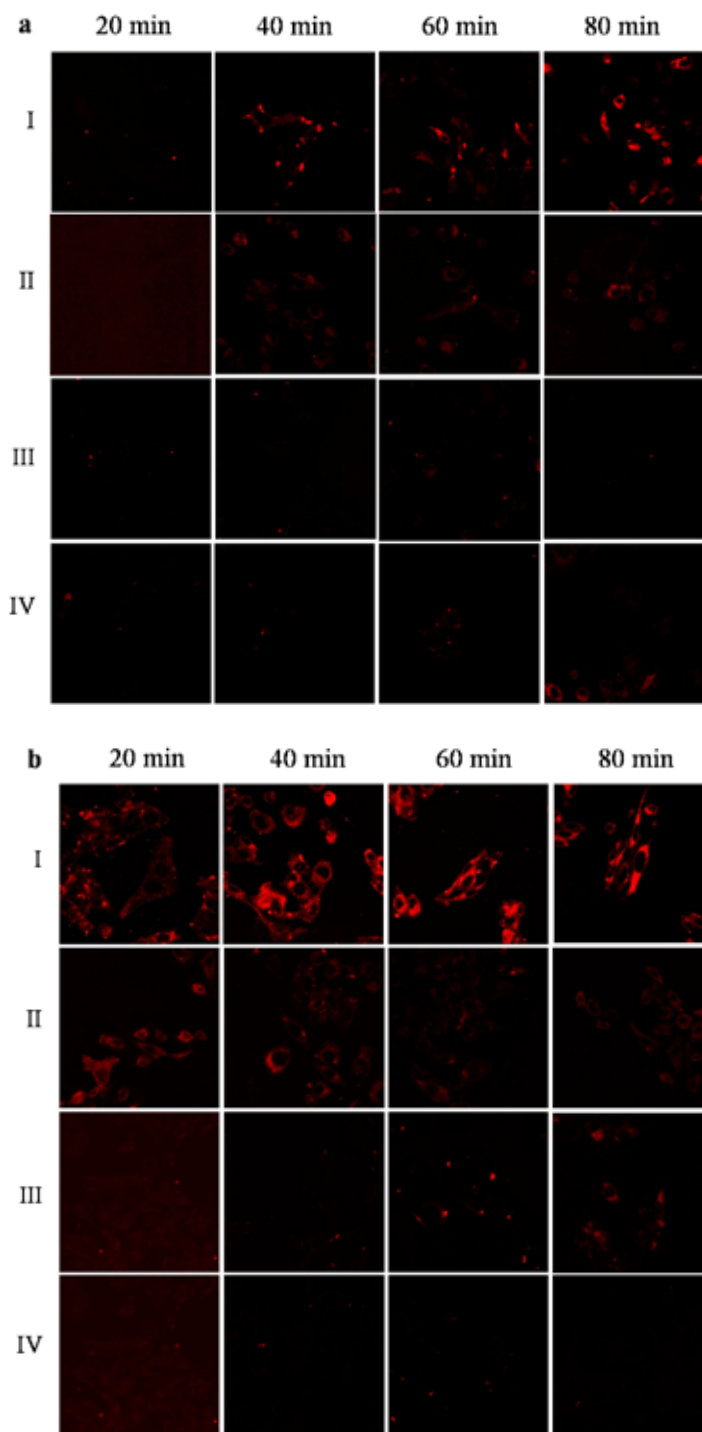
Figure 5.

Fluorescence imaging of CHO cells after incubation with (a) DOPE micelles or (b) DSPE micelles for 20, 40, 60 or 80 minutes. I: CB2-R positive CHO cells incubated with CB2-R targeted micelles. II: CB2-R negative CHO cells incubated with CB2-R targeted micelles. III: CB2-R positive CHO cells incubated with control micelles. IV: CB2-R negative CHO cells incubated with control micelles.
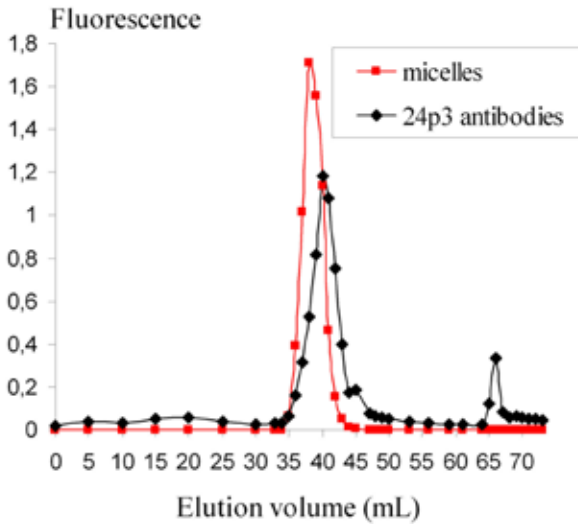
Figure 6. Fluorescence emission data of lissamin-rhodamin-PE and tryptophane of antibody-conjugated micelles and free antibody in sequential fractions (of 1 mL) collected during size exclusion chromatography. The elution volume of free antibodies (tryptophane=black line) is, as expected, larger (67 ml) than the elution volume of the larger antibody-conjugated micelles (35-40 ml). No non-conjugated micelles could be discerned.
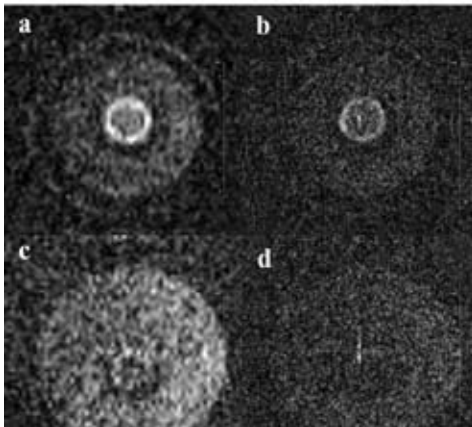

Figure 7. In vitro MRI of 24p3 coated Eppendorf tubes. The tubes coated with mouse recombinant lipocalin-2 and incubated with 24p3 targeted micelles showed a bright circular rim (a; in plane resolution 156 x 208 μm, slice thickness 0.5 mm and b; in plane resolution 78 x 104 μm, slice thickness 0.5 mm). The tubes coated with 24p3 and incubated with isotype-conjugated micelles (c; in plane resolution 156 x 208 μm, d; in plane resolution 78 x 104 μm) showed no rim.

micelles did not show any plaque enhancement (data not shown).

Histology on sections corresponding to levels of MR enhancement showed very large plaques with large lipid cores and many macrophages in the abdominal aorta immediately above the left and right renal artery (Figure 8, panel F, and Figure 9, panel G). Fluorescence
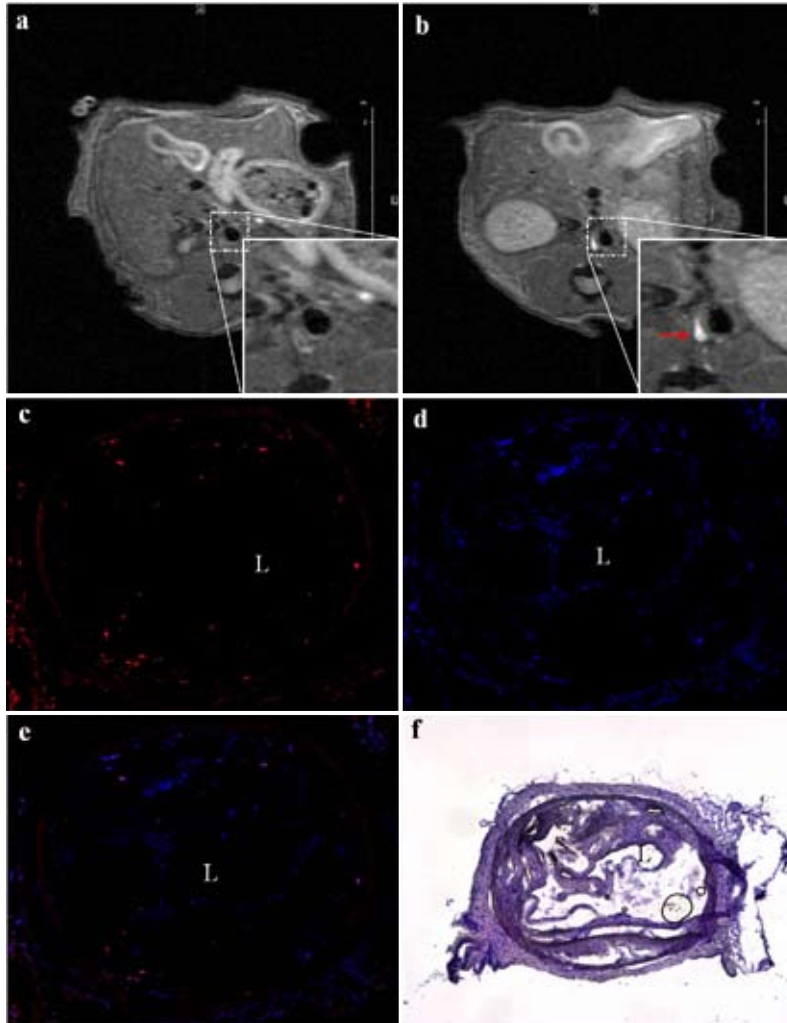

Figure 8. In vivo MRI of apoE$^{-/-}$/eNOS$^{-/-}$ mouse (a) before and (b) 48 hours after intravenous administration of CB2-R targeted micelles. Confocal fluorescence microscopy of corresponding histological slices for visualization of micelles (red) (c) and macrophages (blue) (d). Co-localization of macrophages and micelles (e) was observed after merging of the fluorescence images. Hematoxylin/eosin staining (f); L= aortic lumen.

microscopy showed that rhodamine of CB2-R targeted micelles co-localized with AlexaFluor 647 signal representing macrophages (Figure 8, panel C and D), while rhodamin of 24p3 targeted micelles co-localized with FITC signal representing 24p3 (Figure 9, panel C and E). Partial co-localization was observed for 24p3 and macrophages
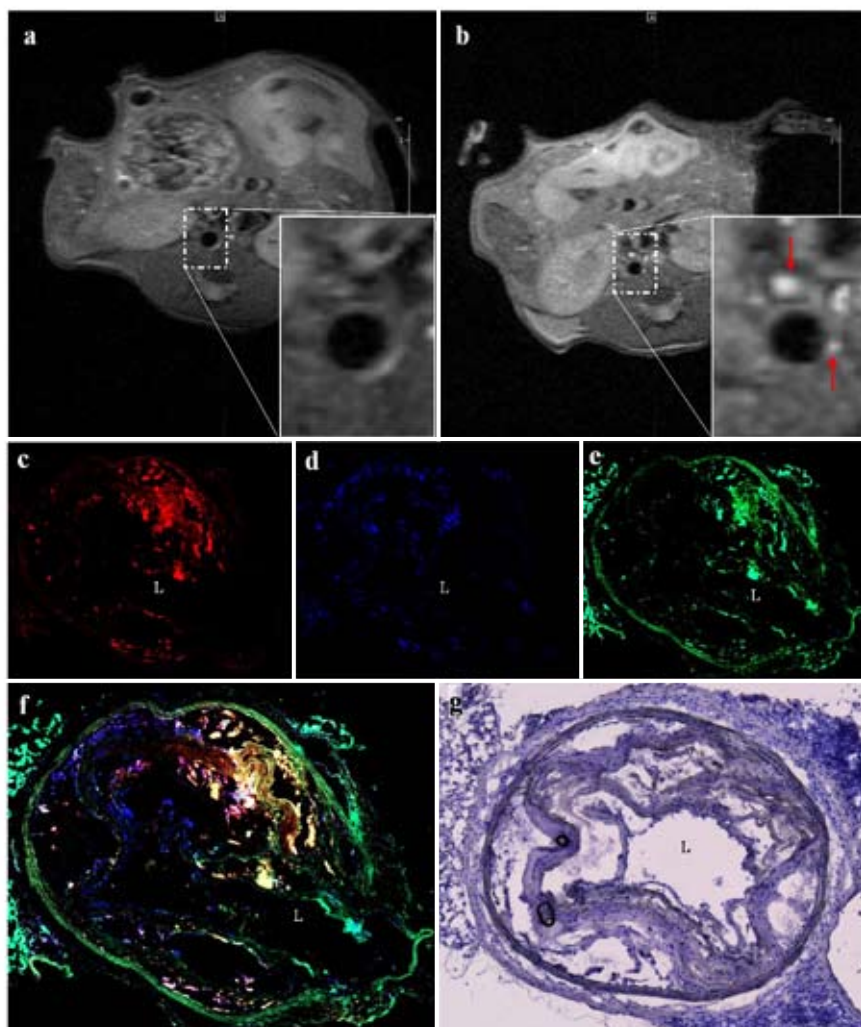

Figure 9. In vivo MRI of apoE$^{-/-}$/eNOS$^{-/-}$ mouse at (a) baseline and (b) 72 hours after intravenous administration of 24p3 targeted micelles. Confocal fluorescence microscopy of corresponding histological slices for visualization of micelles (red) (c), macrophages (blue) (d) and 24p3 (green) (e). Co-localization of macrophages or 24p3 and micelles (f) was observed after merging of the fluorescence images. Hematoxylin/eosin staining (g); L= aortic lumen.

(Figure 9, panel D and E). Plaques at distant levels from plaque MR enhancement showed not only lower plaque area, but also decreased numbers of macrophages and hardly any 24p3 staining (Figure 10, panels D and F, and Figure 11, panels D, E and G).

Discussion

Atherosclerosis is a chronic inflammatory disease, which can lead to acute thrombotic events following plaque rupture or erosion(18). This study shows the potential use of some micelle based contrast agents targeting two different inflammatory plaque markers.
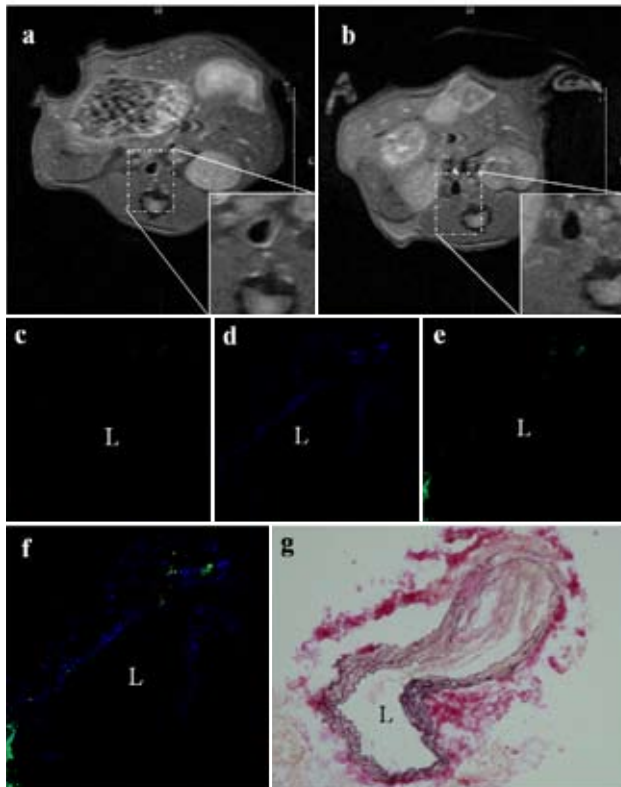One of these markers is the peripheral cannabinoid receptor, also called the CB2 receptor.

Figure 10. In vivo MRI of the same apoE$^{-/-}$/eNOS$^{-/-}$ mouse as in figure 8, but at a level 4 mm lower than in figure 8, (a) before and (b) 48 hours after intravenous administration of CB2-R targeted micelles. Confocal fluorescence microscopy of corresponding histological slices for visualization of micelles (c) and macrophages (d) and the merged image (e). EvG staining (f). In this small plaque fewer macrophages and micelles were observed. L= aortic lumen.

The immunosuppressive role of cannabinoids has been recognized for several years(19). CB2-R is expressed on immune cells, like B cells, T cells and monocytes in spleen and lymphoid tissues(19). CB2-R is reported to be expressed preferentially in advanced atherosclerotic plaques in both human and murine vessels(9). Stimulation of CB2-R led to significant inhibition of atherosclerosis progression in mice via pleiotropic effects on lymphoid and myeloid cells(9). In this study, we used a lipophilic synthetic CB2-R agonist (HU-308) for incorporation into micelles, which also contain gadolinium and a fluorophore. This study shows that this contrast agent can serve a diagnostic goal.

The other marker is 24p3, the mouse homologue of NGAL. MMPs, including MMP-9, have been found to play an important role in destabilization of the atherosclerotic plaque by degradation of the collagenous cap(11,20). NGAL has been shown to protect
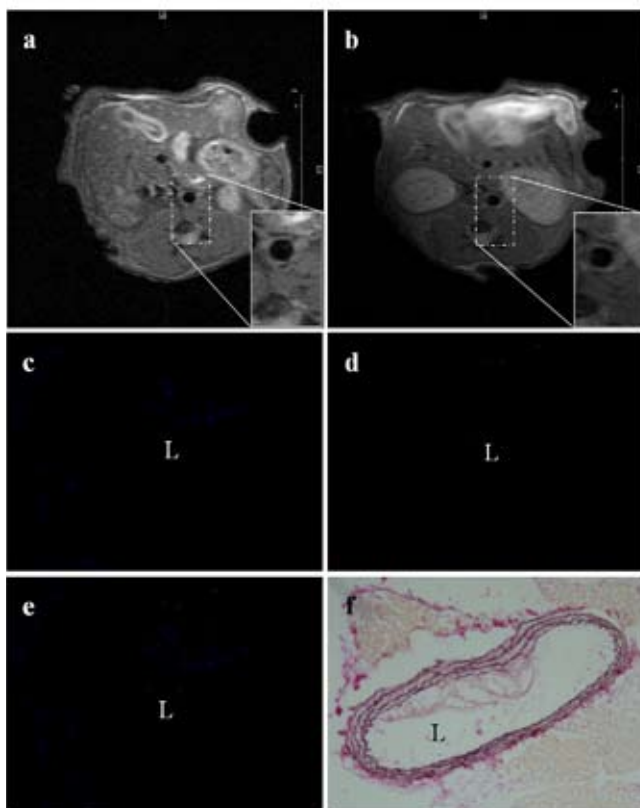

Figure 11. In vivo MRI of the same apoE-/-/eNOS-/- mouse as in figure 9, but at a higher (3 mm) level than in figure 9, (a) before and (b) 72 hours after intravenous administration of 24p3 targeted micelles. Confocal fluorescence microscopy of corresponding histological slices for visualization of micelles (c), macrophages (d), 24p3 (e) and the merged image (f). EvG staining (g). Hardly any 24p3 and micelles and fewer macrophages were found in this smaller plaque. L= aortic lumen.

MMP-9 by forming a stable dimeric complex, which renders MMP-9 less susceptible to inactivation(21). 24p3, the mouse homologue of human NGAL, has been found to colocalize with MMP-9 in murine atherosclerotic plaques(13). The complex of 24p3/MMP-9 was secreted from mouse macrophages according to Hemdahl et al.(13). Importantly, normal aortas of non-atherosclerotic C57BL/6J mice do not display 24p3 protein(13), which makes it an attractive target for imaging with targeted contrast agents. In this study we showed that targeted micelles targeted against 24p3 were visualized in plaque areas with a high macrophage content and large amount of 24p3. In contrast, smaller plaques with a lower number of macrophages were not enhanced with *in vivo* MRI. This result emphasizes a possible role of MRI using 24p3 targeted micelles in differentiation between stable and unstable plaques.

Choice of contrast agent

The contrast agent platform of choice was the micelle rather than the liposome because of the difference in size between these particles. A suitable molecular MR contrast agent would have both high relaxivity and free access to the marker. With regard to relaxivity, larger aggregates have higher relaxivity per aggregate(22). Therefore, in case of a limited number of target binding sites, it is highly efficient to use larger contrast agents in order to improve the sensitivity of detection. On the other hand, diffusion through fenestrations between endothelial cells is very important to get access to targets inside the plaque, which may be hampered by the size of the contrast agent. Vascular fenestration size is reported to vary between 5 and 100 nm, depending on the grade of inflammation. Targeted and non-targeted micelles have been reported to diffuse into infarcted myocardial tissue(23) and plaque(6-8,24) after intravenous administration in rabbit and mouse models. In order to prolong plasma life time, a large proportion of lipid monomers, which make up a micelle or liposome, can be coated with hydrophilic polymers, such as PEG(25).

Relaxivity and size

In this study, the relaxivity of the antibody-conjugated micelles, containing 50% Gd-bisstearylamide, at 1.41 T and 37 ˚C was 9.32 mM^{-1}s^{-1}. The relaxivity of MR contrast agents, like Gd-DTPA decreases with increasing field strength(26,27). At 9.4 T, we found that the relaxivity of antibody-conjugated micelles was 3.0 mM^{-1}s^{-1}, three times lower than at 1.41 T. However, the relaxivity of the micelles was still two times higher than that of Gd-DTPA at 9.4 T (1.8 mM^{-1}s^{-1}, measured in our lab). The larger relaxivity of the micelles could be due to a change of rotational dynamics, which allows for a longer rotational correlation time with inner shell water protons, or to faster water exchange(14,28). The sizes of the CB2-R targeted DOPE-PEG1000 (16.5 ± 1.2 nm) and DSPE-PEG2000 micelles (19.0 ± 1.0 nm) are in line with previous reports on micelles, composed of

PEG750-PE and PEG2000-PE(29,30). Our antibody-conjugated micelles had a size of 23.0 ± 1.0 nm.

In agreement with these size measurements, more than 95% of antibody added to the micelles was conjugated corresponding to approximately one antibody per micelle. This has an important advantage: this conjugation strategy does not cause a significant loss of antibody, and therefore, during routine procedures, removal of the free antibody in order to prevent competitive inhibition at the target site can be omitted. The procedure that we describe takes 3-4 hours, in contrast to earlier published methods(5,31,32), which take considerably longer.

For future clinical use, it is important to have a robust contrast agent preparation procedure, which allows the production of batches of contrast agent, which can be easily stored. The micelles in the antibody-conjugated contrast agent appeared to have the same size after storage for 6 weeks at 4 °C as freshly after preparation. The structural and functional stability of the specific binding site of mouse 24p3 antibody was confirmed after 6 weeks at 4 °C by ELISA.

Intracellular uptake of micelles

Fluorescence microscopy images show bright red spots in the cytosol of the CB2-R positive CHO cells, which indicates intracellular uptake of the micelle based contrast agent. Upon receptor phosphorylation and ß-arrestin binding, most G-protein-coupled receptors internalize into clathrin-coated vesicles(33). There is hardly any uptake of non-targeted micelles in the cytosol of CB2-R positive CHO cells and to an even lesser extent in the cytosol of CB2-R negative CHO cells after incubation with targeted micelles. Both DOPE-PEG1000 and DSPE-PEG2000 CB2-R targeted micelles were able to bind CB2-R and be ingested. So, a larger PEG size did not hamper HU-308 in specific binding. However, the difference in percentage of PEG groups available (due to different Gd-DTPA-bisstearylamide concentrations) nearly counterbalanced the difference in size of the PEG groups and will have led to a comparable micelle corona size. The relatively large PEG groups, when compared to HU-308, may best be considered as dynamic waving chains instead of massive blocks, intermittently allowing access and binding to the CB2-R binding region.

The cell binding assay, as done with the CB2-R targeted micelles, could not be done with regard to 24p3, because it is stored in intracellular granules or excreted by macrophages. Therefore, we coated polyethylene Eppendorf tubes with 24p3 and incubated these tubes with 24p3 targeted micelles. We performed T1-weighted MRI after some wash steps and showed enhancement at the border of the inner side of the tube.

Cell pellets incubated with contrast agent are often used for *in vitro* T1 weighted MRI(34) because it is easy to perform. The main advantage of incubation of cells adhering to a

surface over the use of cell pellets is that adequate washing is guaranteed. Inadequate washing steps in case of the cell pellets may lead to false positive results. Indeed, we found also a T1 shortening effect in CB2-R negative CHO cell pellets and in CB2-R positive CHO cell pellets after incubation with control micelles. However, in this study, specific binding/uptake could be distinguished from nonspecific binding/uptake. A T1~1850 ms corresponding to a cell pellet micelle lipid concentration of 0.15 mM, partially due to specific binding/uptake, could be distinguished from a T1~2000 ms corresponding to a cell pellet micelle lipid concentration of 0.10 mM, which was completely due to nonspecific uptake/binding. T1 of cell pellets without micelles was around 2200 ms. The detectable T1 difference of 150 ms corresponds to a difference in micelle Gd concentration of 25 micromole/L. This relation between T1 and Gd concentration underlines that molecular MRI has sensitivity in the micro- to millimolar range(35). Peak concentration was 0.34 mM for CB2-R targeted DSPE micelles, which led to a T1 of around 800ms. The large difference in T1 corresponding with a difference in concentration of only ~0.20 mM, shows the ability to quantify uptake of contrast agents based on T1 maps with inversion recovery.

However, quantification of intracellular paramagnetic contrast agents is complicated by the fact that after internalization in a cell, compartmentalization of Gd (vesicle compartments) could lead to quenching of relaxivity of the Gd containing contrast agent(36-38). Therefore, one should know the contribution of the quenching effect, as well as the cellular distribution (cytoplasm and/or vesicles) of the contrast agent after administration to calculate a concentration(36). In this study fluorescence microscopy of CHO cells showed internalization of CB2-R targeted micelles. However, the calibration curve was obtained from cell pellets, which are fixed before incubation with micelles, because we wanted to preserve cell structure after harvesting of the cells, same as the test pellets. So, only binding of micelles and no internalization of micelles was expected for the calibration curve. So concentration of Gd could be underestimated in this study.

In vivo **MRI of advanced plaque**

In this study, *in vivo* MRI in a severely atherosclerotic mouse model showed enhancement of abdominal aortic plaque at 48 hours after injection of CB2-R targeted and at 72 hours after injection of 24p3 targeted micelles via the tail vein. There was no enhancement of plaque after injection of control micelles. One may postulate that 24p3 targeted micelles bound to released 24p3 or unbound, will wash out to the blood stream. However, indications of (other) protein-binding to the subendothelial matrix have been found (39). Still, after release in the extracellular space, most proteins do not survive for a very long time. We found in this study, that micelles colocalized with 24p3 and macrophages. Presumably, micelles bound first to released 24p3 and could be subsequently, because

the protein-micelle complex is not washed immediately from the plaque as a result of binding of 24p3 to the matrix, ingested by macrophages. Apoptosis or necrosis of these macrophages just before 72 hours post-injection leaving 24p3-micelle complexes in the extracellular matrix could explain the finding of extracellular 24p3 targeted micelles at 72 hours after injection. Control micelles were likely not ingested or to a lower extent due to the earlier washout because there was no binding mechanism.

The degree of atherosclerosis was very profound when compared to atherosclerosis in the apoE$^{-/-}$ mouse model and even led to myocardial infarctions[17]. Many macrophage-related targets have been visualized with molecular MRI in apoE$^{-/-}$ mouse models with less advanced stages of atherosclerosis[7,24,40-42]. This study showed that mouse atherosclerotic plaque could be differentiated according to 24p3 and macrophage content in a mouse model suffering from profound atherosclerosis. For clinical risk stratification it is important to be able to differentiate between rupture-prone plaque, in which macrophage activity and MMP activity are believed to play an important role, and more stable plaques.

Toxicity

A major consideration in the design of new contrast agents is its potential toxicity. Though free Gd is toxic, this is not necessarily the case for bound Gd. Magnevist (Gd-DTPA), for example, is clinically used at a dose of 0.1.mmol/kg. The lipid monomer used in this study is Gd-DTPA-bisstearylamide. It has been shown that gadolinium complexes of open-chain chelates like DTPA exhibit a higher susceptibility to transmetallation than other complexes[43]. Moreover the bisamide derivatives exhibit the highest extent of transmetallation[43]. The finding that the CB2-R targeting micelles are taken up by the CHO cells complicates the pharmokinetics of the gadolinium and the toxicity issue even further. Use of macrocyclic complexes or bulky substituents present on the amide groups may be needed to decrease the susceptibility of Gd-DTPA to transmetallation. Alternatively, Gd-DOTA-DSPE exhibited no detectable transmetallation upon incubation with Zn2+[44]. It is still unknown whether Gd-DOTA-DSPE *in vivo* after internalization is stable or will be degraded in macrophage lysosomes. Whereas small gadolinium chelates like Magnevist are excreted by the kidney, there is accumulating evidence that gadolinium-containing micelles are excreted by the liver[24]. The degradation of the micelles in liver lysosomes, possibly releasing Gd from the chelates, may augment the toxicity problem. Immunogenicity created by the antibodies could be reduced with future use of Ab fragments. One may expect that the immunogenicity is less of an issue in the *in vivo* use of CB2-R targeted micelles, because they harbor only a small synthetic agonist. No adverse effects in mice were observed after administration of both CB2-R and 24p3 targeted micelles.

Conclusions

Two micelle-based contrast agents with high relaxivity were prepared. One contrast agent is aimed at the CB2-receptor, which is found in advanced mouse and human atherosclerotic plaques, and might serve both a diagnostic and therapeutic goal. The other contrast agent is aimed at NGAL, which has been found to co-localize with MMP-9 in murine and human atherosclerotic plaques and has a role in stabilizing MMP-9 leading to collagenous cap degradation and eventually plaque rupture. *In vitro* and *in vivo* experiments showed that both agents were capable to bind their targets and to provide MR contrast. Future animal studies are required to investigate their role in characterizing plaque vulnerability *in vivo*.

Reference List

1. Falk,E., Shah,P.K., and Fuster,V. Coronary plaque disruption. Circulation 92: 657-671, 1995.
2. Yuan, C., Oikawa, M., Miller, Z., and Hatsukami, T. MRI of carotid atherosclerosis. J.Nucl.Cardiol. 15: 266-275, 2008.
3. Botnar, R.M., Perez, A.S., Witte, S. et al. *In vivo* molecular imaging of acute and subacute thrombosis using a fibrin-binding magnetic resonance imaging contrast agent. Circulation 109: 2023-2029, 2004.
4. Botnar, R.M., Buecker, A., Wiethoff, A.J. et al. *In vivo* magnetic resonance imaging of coronary thrombosis using a fibrin-binding molecular magnetic resonance contrast agent. Circulation 110: 1463-1466, 2004.
5. Winter, P.M., Morawski, A.M., Caruthers, S.D. et al. Molecular imaging of angiogenesis in early-stage atherosclerosis with alpha(v)beta3-integrin-targeted nanoparticles. Circulation 108: 2270-2274, 2003.
6. Barkhausen, J., Ebert, W., Heyer, C., Debatin, J.F., Weinmann, H.J. Detection of atherosclerotic plaque with Gadofluorine-enhanced magnetic resonance imaging. Circulation 108: 605-609, 2003.
7. Lipinski, M.J., Amirbekian, V., Frias, J.C. et al. MRI to detect atherosclerosis with gadolinium-containing immunomicelles targeting the macrophage scavenger receptor. Magn Reson.Med. 56: 601-610, 2006.
8. Sirol, M., Itskovich, V.V., Mani, V. et al. Lipid-rich atherosclerotic plaques detected by gadofluorine-enhanced *in vivo* magnetic resonance imaging. Circulation 109: 2890-2896, 2004.
9. Steffens, S., Veillard, N.R., Arnaud, C. et al. Low dose oral cannabinoid therapy reduces progression of atherosclerosis in mice. Nature 434: 782-786, 2005.
10. Mach, F., Steffens, S. The role of the endocannabinoid system in atherosclerosis. J.Neuroendocrinol. 20 Suppl 1: 53-57, 2008.
11. Galis, Z.S., Khatri, J.J. Matrix metalloproteinases in vascular remodeling and atherogenesis: the good, the bad, and the ugly. Circ.Res. 90: 251-262, 2002.
12. Post, S., Peeters, W., Busser, E. et al. Balance between angiopoietin-1 and angiopoietin-2 is in favor of angiopoietin-2 in atherosclerotic plaques with high microvessel density. J.Vasc.Res. 45: 244-250, 2008.
13. Hemdahl, A.L., Gabrielsen, A., Zhu, C. et al. Expression of neutrophil gelatinase-associated lipocalin in atherosclerosis and myocardial infarction. Arterioscler.Thromb.Vasc.Biol. 26: 136-142, 2006.
14. Mulder, W.J., Strijkers, G.J., van Tilborg, G.A., Griffioen, A.W., Nicolay, K. Lipid-based nanoparticles for contrast-enhanced MRI and molecular imaging. NMR Biomed. 19: 142-164, 2006.
15. Duncan, R.J., Weston, P.D., Wrigglesworth, R. A new reagent which may be used to introduce sulfhydryl groups into proteins, and its use in the preparation of conjugates for immunoassay. Anal.Biochem. 132: 68-73, 1983.
16. Singh, R., Maloney, E.K. Labeling of antibodies by in situ modification of thiol groups generated from selenol-catalyzed reduction of native disulfide bonds. Anal.Biochem. 304: 147-156, 2002.
17. Kuhlencordt, P.J., Gyurko, R., Han, F. et al. Accelerated atherosclerosis, aortic aneurysm formation, and ischemic heart disease in apolipoprotein E/endothelial nitric oxide synthase double-knockout mice. Circulation 104: 448-454, 2001.
18. Naghavi, M., Libby, P., Falk, E. et al. From vulnerable plaque to vulnerable patient: a call for new definitions and risk assessment strategies: Part II. Circulation 108: 1772-1778, 2003.
19. Munro, S., Thomas, K.L., bu-Shaar, M. Molecular characterization of a peripheral receptor for cannabinoids. Nature 365: 61-65, 1993.
20. Schwartz, S.M., Hatsukami, T.S., Yuan, C. Molecular markers, fibrous cap rupture, and the vulnerable plaque: new experimental opportunities. Circ.Res. 89: 471-473, 2001.
21. Yan, L., Borregaard, N., Kjeldsen, L., Moses, M.A. The high molecular weight urinary matrix metalloproteinase (MMP) activity is a complex of gelatinase B/MMP-9 and neutrophil gelatinase-associated lipocalin (NGAL). Modulation of MMP-9 activity by NGAL. J.Biol.Chem. 276: 37258-37265, 2001.
22. Artemov, D. Molecular magnetic resonance imaging with targeted contrast agents. J.Cell Biochem. 90: 518-524, 2003.
23. Lukyanov, A.N., Hartner, W.C., Torchilin, V.P. Increased accumulation of PEG-PE micelles in the area of experimental myocardial infarction in rabbits. J.Control Release 94: 187-193, 2004.
24. Briley-Saebo, K.C., Shaw, P.X., Mulder, W.J. et al. Targeted molecular probes for imaging atherosclerotic lesions with magnetic resonance using antibodies that recognize oxidation-specific epitopes. Circulation 117: 3206-3215, 2008.

25. Oussoren, C., Storm, G. Lymphatic uptake and biodistribution of liposomes after subcutaneous injection: III. Influence of surface modification with poly(ethyleneglycol). Pharm.Res. 14: 1479-1484, 1997.

26. Pintaske, J., Martirosian, P., Graf, H. et al. Relaxivity of Gadopentetate Dimeglumine (Magnevist), Gadobutrol (Gadovist), and Gadobenate Dimeglumine (MultiHance) in human blood plasma at 0.2, 1.5, and 3 Tesla. Invest Radiol. 41: 213-221, 2006.

27. Parac-Vogt, T.N., Kimpe, K., Laurent, S. et al. Paramagnetic liposomes containing amphiphilic bisamide derivatives of Gd-DTPA with aromatic side chain groups as possible contrast agents for magnetic resonance imaging. Eur.Biophys.J. 35: 136-144, 2006.

28. Nicolle, G.M., Toth, E., Eisenwiener, K.P., Macke, H.R., Merbach, A.E. From monomers to micelles: investigation of the parameters influencing proton relaxivity. J.Biol.Inorg.Chem. 7: 757-769, 2002.

29. Lukyanov, A.N., Gao, Z., Torchilin, V.P. Micelles from polyethylene glycol/phosphatidylethanolamine conjugates for tumor drug delivery. J.Control Release. 91: 97-102, 2003.

30. Torchilin, V.P., Lukyanov, A.N., Gao, Z., Papahadjopoulos-Sternberg, B. Immunomicelles: targeted pharmaceutical carriers for poorly soluble drugs. Proc.Natl.Acad.Sci. (USA) 100: 6039-6044, 2003.

31. Anderson, S.A., Rader, R.K., Westlin, W.F. et al. Magnetic resonance contrast enhancement of neovasculature with alpha(v)beta(3)-targeted nanoparticles. Magn Reson.Med. 44: 433-439, 2000.

32. Gustafsson, B., Youens, S., Louie, A.Y. Development of contrast agents targeted to macrophage scavenger receptors for MRI of vascular inflammation. Bioconjug.Chem. 17: 538-547, 2006.

33. van Koppen, C.J., Jakobs, K.H. Arrestin-independent internalization of G protein-coupled receptors. Mol. Pharmacol. 66: 365-367, 2004.

34. van Tilborg, G.A., Mulder, W.J., Deckers, N. et al. Annexin A5-functionalized bimodal lipid-based contrast agents for the detection of apoptosis. Bioconjug.Chem. 17: 741-749, 2006.

35. Massoud, T.F., Gambhir, S.S. Molecular imaging in living subjects: seeing fundamental biological processes in a new light. Genes Dev. 17: 545-580, 2003.

36. Strijkers, G.J., Hak, S., Kok, M.B., Springer, C.S., Jr., Nicolay, K. Three-compartment T1 relaxation model for intracellular paramagnetic contrast agents. Magn Reson.Med. 61: 1049-1058, 2009.

37. Terreno, E., Geninatti, C.S., Belfiore, S. et al. Effect of the intracellular localization of a Gd-based imaging probe on the relaxation enhancement of water protons. Magn Reson.Med. 55: 491-497, 2006.

38. Kok, M.B., Hak, S., Mulder, W.J., van der Schaft, D.W., Strijkers, G.J., Nicolay, K. Cellular compartmentalization of internalized paramagnetic liposomes strongly influences both T1 and T2 relaxivity. Magn Reson.Med. 61: 1022-1032, 2009.

39. Zeng, X., Chen, J., Miller, Y.I., Javaherian, K., Moulton, K.S. Endostatin binds biglycan and LDL and interferes with LDL retention to the subendothelial matrix during atherosclerosis. J.Lipid Res. 46: 1849-1859, 2005.

40. Amirbekian, V., Lipinski, M.J., Briley-Saebo, K.C. et al. Detecting and assessing macrophages *in vivo* to evaluate atherosclerosis noninvasively using molecular MRI. Proc.Natl.Acad.Sci. (USA) 104: 961-966, 2007.

41. Mulder, W.J., Strijkers, G.J., Briley-Saboe, K.C. et al. Molecular imaging of macrophages in atherosclerotic plaques using bimodal PEG-micelles. Magn Reson.Med. 58: 1164-1170, 2007.

42. Cormode, D.P., Briley-Saebo, K.C., Mulder, W.J. et al. An ApoA-I mimetic peptide high-density-lipoprotein-based MRI contrast agent for atherosclerotic plaque composition detection. Small. 4: 1437-1444, 2008.

43. Laurent, S., Elst, L.V., Copoix, F., Muller, R.N. Stability of MRI paramagnetic contrast media: a proton relaxometric protocol for transmetallation assessment. Invest Radiol. 36: 115-122, 2001.

44. Hak, S., Sanders, H.M., Agrawal, P. et al. A high relaxivity Gd(III)DOTA-DSPE-based liposomal contrast agent for magnetic resonance imaging. Eur.J.Pharm.Biopharm. 72: 397-404, 2009.

Molecular MRI of murine atherosclerotic plaque targeting NGAL, a protein associated with human plaque vulnerability

Bernard C. te Boekhorst[1,2,3*] M.D.; Sandra M. Bovens[1,3*] M.Sc.; Willem E. Hellings[4] M.D.; Petra H. van der Kraak[5] B.Sc.; Kees W. van de Kolk[1] M.Sc; Aryan Vink[5] M.D. Ph.D.; Frans L. Moll[4] M.D. Ph.D.; Matthijs F. van Oosterhout[6] M.D. Ph.D.; Jean P. de Vries[7] M.D. Ph.D.; Pieter A. Doevendans[2,3] M.D. Ph.D.; Marie-José Goumans[8] Ph.D.; Dominique P. de Kleijn[1,3] Ph.D.; Cees J. van Echteld[1,9] Ph.D.; Gerard Pasterkamp[1] M.D. Ph.D.; Joost P. Sluijter[2,3] Ph.D.

*[1] Department of Cardiology, Experimental Cardiology Laboratory, University Medical Center, Utrecht, The Netherlands [2]Department of Cardiology, University Medical Center, Utrecht, The Netherlands [3]Interuniversity Cardiology Institute of the Netherlands (ICIN), The Netherlands [4]Department of Vascular Surgery, University Medical Center, Utrecht, The Netherlands [5]Department of Pathology, University Medical Center, Utrecht, The Netherlands [6]Department of Pathology, St. Antonius Hospital, Nieuwegein, The Netherlands [7]Department of Vascular Surgery, St. Antonius Hospital, Nieuwegein, The Netherlands [8]Department of Molecular Cell Biology, Leiden University Medical Center, Leiden, The Netherlands [9]Present address: Novartis Institutes for Biomedical Research, Basel, Switzerland *Authors contributed equally to this study*

Aims

Neutrophil Gelatinase-Associated Lipocalin (NGAL) is an effector molecule of the innate immune system. One of its actions is prolongation of MMP-9 activity by formation of a degradation resistant NGAL/MMP-9 complex. We studied the role of NGAL in human atherosclerotic lesions and we examined whether NGAL could act as a target for molecular imaging of atherosclerotic plaque.

Methods and Results

Increased levels of NGAL and the NGAL/MMP-9 complex were associated with human atheromatous atherosclerotic lesions, obtained during carotid endarterectomy (n=122). MMP-9 activity was strongly related with NGAL levels. In addition, in patients suffering from acute myocardial infarction (n=23), circulating levels of NGAL and NGAL/MMP-9 complex were increased compared to controls (n=10). After administration of NGAL/24p3-targeted micelles, enhancement on MR images was observed at 72 hours after injection of NGAL/24p3-targeted micelles in the abdominal aorta of ApoE$^{-/-}$/eNOS$^{-/-}$ mice. The specificity of these results was validated by histology, and colocalization of micelles, macrophages and NGAL/24p3 was observed.

Conclusions

NGAL is highly expressed in atheromatous human plaques and associated with increased MMP-9 activity. NGAL can be detected in mouse atherosclerotic arteries using targeted high resolution MRI. Therefore, we conclude that NGAL might serve as a novel imaging target for detection of vulnerable plaques.

Introduction

In vivo imaging of proteins which are associated with atherosclerotic disease progression and plaque destabilization is a major challenge. Magnetic resonance imaging (MRI) provides both a high anatomical detail and the option of molecular MRI of plaque proteins. Molecular MRI, using gadolinium (Gd) loaded nanoparticles, of macrophage and cholesterol metabolism related targets in early to intermediate plaques 1 has revealed promising results (2-5). Micelles are lipid-based nanoparticles, in the nm range, and may be coated with PEG (poly-ethylene-glycol), which extends blood circulation times (6). The possibility to bind antibodies to PEG and to incorporate Gd and fluorescent probes, makes these particles very suitable for targeted MRI of the vulnerable atherosclerotic plaque.

Neutrophil gelatinase-associated lipocalin (NGAL) is a 25 kD glycoprotein which was first discovered in human neutrophils (7, 8). NGAL is an effector molecule of the innate immune system through inhibition of bacterial iron uptake by binding bacterial siderophores (9). Moreover, it mediates inflammatory activity through binding to formyl-methionyl-leucyl-phenylalanine (fMLP; a chemotactic peptide), leukotriene B4 and platelet activating factor (10-12). Production of NGAL is induced via nuclear factor kappa B (NFκB) binding, and high levels are found in inflammatory conditions (11, 13). NGAL is able to form a stable, biologically active complex with matrix metalloproteinase 9 (MMP-9), preventing its degradation, and thereby prolonging MMP-9 activity(14). In addition, NGAL is involved in the allosteric activation of MMP-8 and MMP-9 (15).

MMPs are key players in atherosclerotic disease. They are capable of degrading a broad spectrum of extracellular matrix components and held responsible for vascular remodeling and breakdown of the fibrous cap of atherosclerotic lesions (16). Especially MMP-9 is implicated to play a crucial role in atherosclerotic plaque destabilization, both in human studies and experimental models (17-21). The mouse analogue of NGAL, called 24p3 (SIP24, lipocalin-2, uterocalin), was present in mouse atherosclerotic lesions, as demonstrated by Hemdahl et al. (22). Considering the function of NGAL in the innate immune system and its effect on MMP-9 activity, NGAL might play an important role in atherosclerotic plaque destabilization.

We studied whether NGAL is associated with unstable human atherosclerotic lesions and whether MRI of micelles, targeting NGAL, is feasible in the ApoE$^{-/-}$/eNOS$^{-/-}$ mouse model (23) and thereby could serve as a novel target to visualize unstable atherosclerotic lesions.

Methods

Human carotid atherosclerotic specimen

Carotid plaques were obtained from a consecutive series of patients undergoing carotid endarterectomy (N=122), participating in the Athero-Express biobank (24). This ongoing biobank is running in two Dutch Hospitals: The University Medical Center Utrecht and the St. Antonius Hospital Nieuwegein. These patients all suffered from high grade (>70%) carotid stenosis. Indications for carotid endarterectomy were based on recommendations from the NASCET, ECST, ACAS and ACST trials (25-28). In a subset of these patients, two blood samples were drawn during carotid endarterectomy: one directly from the carotid artery in the proximity of the atherosclerotic plaque and one from a peripheral catheter in the radial artery. Non-atherosclerotic mammary artery segments (n=10), obtained during coronary artery bypass grafting, served as arterial control tissues.

The investigations conformed with the principles outlined in the Declaration of Helsinki. The study was approved by the institutional review boards of both participating hospitals and all patients provided written informed consent.

Carotid plaque characterization

The carotid endarterectomy specimens were divided in segments of 5 mm thickness along the longitudinal axis of the vessel.

The segment with greatest plaque burden was embedded in paraffin for further histological characterization. Staining for macrophages, endothelial cells, smooth muscle cells and NGAL was performed. Semi-quantitative analysis of plaque for macrophages, smooth muscle cells, collagen, calcifications and overall phenotype followed.

The directly adjacent segment was used for protein extraction. Interleukin-6 (IL-6) and IL-8, MMP-2, -8 and -9 activities in the protein extracts were measured with ELISA. See online supplement for further details.

Detection of NGAL in carotid plaques

For immunohistochemical detection of NGAL/MMP-9 complex in carotid plaques, see online supplement. NGAL concentration in protein extracts of the tissue specimens was measured with a NGAL Enzyme-Linked Immunosorbent Assay (ELISA) kit, according to the manufacturer's protocol (Antibodyshop, Gentofte, Denmark). This assay has no cross-reactivity with NGAL/MMP-9 complexes. The measurements were standardized for total protein concentration of the protein extracts.

Gelatinolytic activity of the NGAL/MMP-9 complex was measured using gelatin zymography (see online supplement).

Release of NGAL and NGAL/MMP-9 complex from carotid plaques

To assess release of NGAL or NGAL/MMP-9 complexes from plaques into the systemic circulation, we applied a novel model comparable to the system applied by Maier et al (29). A blood sample obtained at the site of the plaque was compared to a peripheral blood sample for the concentration of NGAL and NGAL/MMP-9 complex in 9 consecutive patients undergoing carotid endarterectomy (CEA). The difference in concentration between the local and peripheral obtained samples is a measure of secretion of the protein by the plaque. During CEA, the blood sample at the plaque site ("plaque-related blood") was drawn directly from the already exposed common carotid artery (Figure 1C). This was done after the blood had been halted for 2 minutes at the plaque site during test-clamping, which is routinely performed in our hospital before incision of the carotid artery. At exactly the same time, a peripheral blood sample was drawn from the indwelling arterial line in the radial artery. NGAL was measured by ELISA as described above. Levels of the NGAL/MMP-9 complex were determined by ELISA (R&D Systems, Minneapolis, MN).

Murine aortic atherosclerosis

Animals

Animal experiments conformed with the Guide for the Care and Use of Laboratory Animals published by the US National Institutes of Health (NIH Publication No. 85-23, revised 1996) and were approved by the animal experimental committee of the Utrecht University. Old (between 9-12 months) male ApoE/eNOS double knockout mice (generated in our lab by crossing the offspring of ApoE$^{-/-}$ x eNOS$^{-/-}$ mice, genotype confirmed with RT-PCR) were fed a western type diet (Harlan) for 12 weeks. In group A1 (n=6), mice were injected with NGAL-targeted micelles and imaged at baseline and t=24 hours. In group A2 (n=8), mice were injected with NGAL targeted micelles and imaged at baseline, t=24 hours and t=72 hours. In group B1 (n=4) mice were injected with isotype-conjugated micelles (control) and imaged at baseline and t=24 hours. In group B2 (n=6) mice were injected with isotype-conjugated micelles (control) and imaged at baseline, t=24 hours and t=72 hours.

Micelles

A mixture of the appropriate amounts of lipids (DSPE-PEG2000 (43M%), Gd-DTPA-bisstearylamide (50M%), Liss-Rhod-PE (5M%) and Mal-PEG2000-DSPE (2M%); all purchased from Avanti Polar Lipids Inc., Alabaster, USA), dissolved in chloroform, was dried by rotary evaporation at 55 °C. The lipid film was subsequently hydrated in 1 ml PBS, yielding a total lipid concentration of 3 mM. Rat anti-mouse 24p3 antibodies (3mg/ml) (MAB1857, R&D systems, Minneapolis, USA) and rat IgG isotype antibodies

(Invitrogen, Carlsbad, USA) were conjugated via SATA-modification as described previously (30). The modified antibody was added to the micelles and incubated overnight at 4°C. According to size exclusion chromatography >95% of antibodies was bound to mal-PEG (data not shown). Given that the molar antibody to lipid ratio was 0.7:100 and the percentage of mal-PEG was 2%, ~35% of mal-PEG should be occupied by antibody. Assuming that these micelles are composed of ~100 lipid monomers, nearly all micelles were occupied by antibodies.

Rat isotype and 24p3 antibody-conjugated micelles had a size of ~23.0 nm determined by dynamic light scattering (data not shown).

Animal preparation and anesthesia:

Mice were imaged in a vertical 9.4T, 89mm bore size magnet equipped with a 1500 mT/m gradient set and connected to an Avance 400 MR system (Bruker BioSpin, Germany) in a quadrature-driven birdcage coil with an inner diameter of 3 cm. ParaVision 4.0 software was used for MR acquisition and reconstruction.

Mice were anesthetized with 5 vol% isoflurane in a 2:1 mixture of air (0.3 L/min) and oxygen (0.15 L/min). After the toe-pinch reflex had disappeared, the mouse was transferred to a cradle and anesthesia maintained with 1.5-2.5 vol% isoflurane to keep the respiratory rate stable. An intravenous catheter was inserted into the tail vein. The cardiac- and respiratory motion were monitored using a pad linked to an ECG/respiratory unit.

Baseline and follow-up MRI procedure

After scout imaging was performed, twenty contiguous axial slices were planned from 4 mm below the right renal artery branch up to 5 mm above this branch. Inversion Recovery-Fast Spin Echo (IR-FSE) images and anatomic reference images for lymph nodes and peri-aortic blood vessels were made.

See online supplement for further details.

Contrast injection, harvesting and preparation of aortas

After the baseline MRI procedure, 200 µL of contrast agent (3mM lipid 24p3-targeted or isotype-conjugated micelles) was injected via an intravenous catheter, the catheter was removed and the animal recovered from anesthesia until the next MRI procedure. After the last MRI procedure, anesthesia was continued with a mixture of medetomidine (6%)/ketamine (5%) (0.1 mL/10 gram). The imaged part of the aorta was harvested after perfusion with nitroglycerin /PBS (1:10). Part of the aortas was perfused with OCT compound/PBS (1:10) and embedded in OCT compound and stored at -20°C. The other part was perfusion-fixated with formaldehyde 4%/PBS (1:10) and embedded in paraffin.

Histology of murine atherosclerotic specimens

From 4mm caudal to 5mm cranial of the right renal artery branch, sections were made at every 0.5mm. Staining for lipids, macrophages, 24p3 and micelles was performed. See online supplement for further details.

MRI and Histological review

MRI data were reviewed independently (B.B. and S.B., both more than 3 years experience with evaluation of MR images), and regions of interest (ROIs) representing pre-vertebral (pv) muscle and plaque were drawn on pre- and post-injection images. The normalized enhancement ratio (NER) was derived from the signal intensity (SI) of plaque and pv muscle (SI_{plaque} and $SI_{pv\ muscle}$) using the next formula:

$(SI_{plaque} / SI_{pv\ muscle(post-injection)})/(SI_{plaque} / SI_{pv\ muscle\ (pre-injection)})$.

Data analysis

All measurements are presented as mean +/- SEM. Associations between variables were tested by Mann-Whitney U test or Spearman's non-parametric correlation where appropriate. Wilcoxon's signed rank test was used to test significance for the carotid plaque secretion experiments. To adjust the relation between MMP-9 and NGAL for the presence of macrophages, a linear regression model was constructed in which NGAL and number of plaque macrophages were entered as determinants and MMP-9 as the predicted variable.

Differences of NER between mouse groups were tested with the independent samples t-tests. P-values < 0.05 were considered statistically significant.

Results

NGAL expression in atherosclerotic carotid plaques

The carotid plaques (n=122) did not show significantly higher NGAL expression levels than the control arteries (n=10; 8.4+/- 0.79 and 7.1+/-1.74, respectively). However, in the atherosclerotic carotid plaques, a strong positive correlation was observed between total NGAL content and total MMP-9 (Figure 1A; R=0.528; p<0.001) and MMP-8 activity (R=0.654; p<0.001) as determined by activity ELISA. No association with MMP-2 activity could be observed (Figure 1B).

NGAL versus plaque composition

NGAL levels were higher in plaques with an unstable phenotype (Table 1). Atheromatous plaques, with larger necrotic core size, more macrophages and high levels of pro-

inflammatory cytokines IL-6 and IL-8 had higher NGAL content than stable plaques that are fibrous and have higher smooth muscle cell content. Together, these findings indicate an association of NGAL with unstable plaque characteristics. Immunohistochemical analysis for NGAL demonstrated expression of NGAL in smooth muscle cells, macrophages and endothelial cells (Figure 2A-D). High NGAL expression was mainly observed in macrophages, and although NGAL expression was observed in smooth muscle cells and endothelial cells in the carotid plaques, their number was limited. Figure 2B shows an example of luminal endothelium with absent staining for NGAL. Additionally, neutrophils were examined as a possible source of NGAL within the plaques, however, none or very few neutrophils could be observed. Therefore, neutrophils are probably not an important source of NGAL in carotid atherosclerotic plaques. The smooth muscle cells in the media of the mammary artery showed slight diffuse staining for NGAL (Figure 2E), whereas no staining was observed when an isotype control antibody was used (Figure 2F).

Table 1 Relation between plaque characterization and expression of NGAL

Plaque characteristics		NGAL (ng/mg)	P
n		122	
Overall	Fibrous	45 +/- 6	
	F- Atheromatous	101 +/- 14	0.007 A
	Atheromatous	80 +/- 9	
MO	Minor	80 +/- 10	0.9
	Heavy	89 +/- 12	
SMC	Minor	95 +/- 14	0.05
	Heavy	79 +/- 10	
MO/SMC	SMC dominant	92 +/- 11	0.8
	MO dominant	82 +/- 16	
Collagen	Minor	86 +/-12	0.2
	Heavy	84 +/- 10	
Calcifications	Minor	94+/- 14	0.7
	Heavy	74 +/- 8	
IL-6	Low B	69 +/- 9	0.003 A
	High C	101 +/- 13	
IL-8	Low B	49 +/- 4	<0.001A
	High C	128 +/- 15	

Abbreviations: F-Atheromatous, Fibro-Atheromatous; IL, interleukin; MO, macrophage infiltration; SMC, smooth muscle cell infiltration. All values are presented as mean +/- standard error of the mean. A Spearman's correlation B low: <median C high: >= median

Independence of the association between NGAL and MMP-9 levels

We investigated whether the strength of the association between NGAL and MMP-9 levels might be influenced by the number of macrophages in the plaque. Therefore, we rectified the relation between NGAL and MMP-9 levels for the extent of macrophage infiltration and put these variables in a linear regression model. This model showed that NGAL levels were associated with MMP-9 levels, independently on the presence of macrophages (β=0.43; p<0.001).
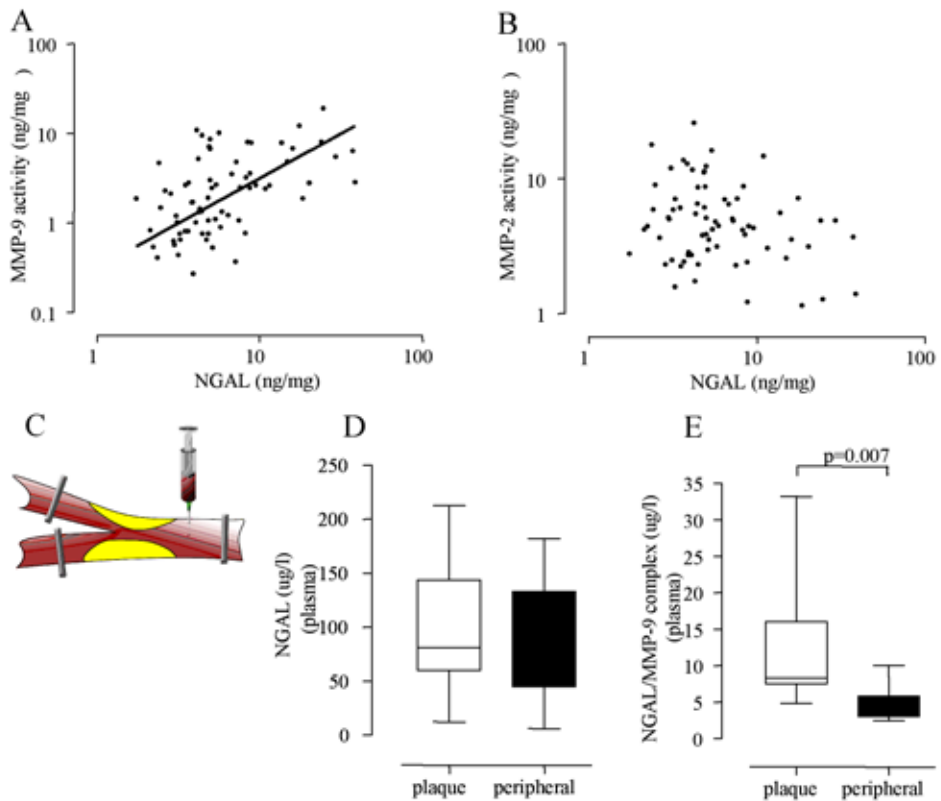

Figure 1: Association between NGAL and MMP activity; blood- and plaque levels of NGAL and NGAL/MMP-9 in humans
A: Association between plaque NGAL concentration and plaque MMP-9 activity (ELISA) (R=0.528; p<0.001). B: Association between plaque NGAL concentration and plaque MMP-2 activity (ELISA) (p=n.s.). C: Blood drawing procedure from the carotid artery. D: NGAL concentrations: local plaque-related blood vs. peripheral blood (n=9; p=0.06). E: NGAL/MMP-9 concentrations: local plaque-related blood vs. peripheral blood (n=9; p=0.007).
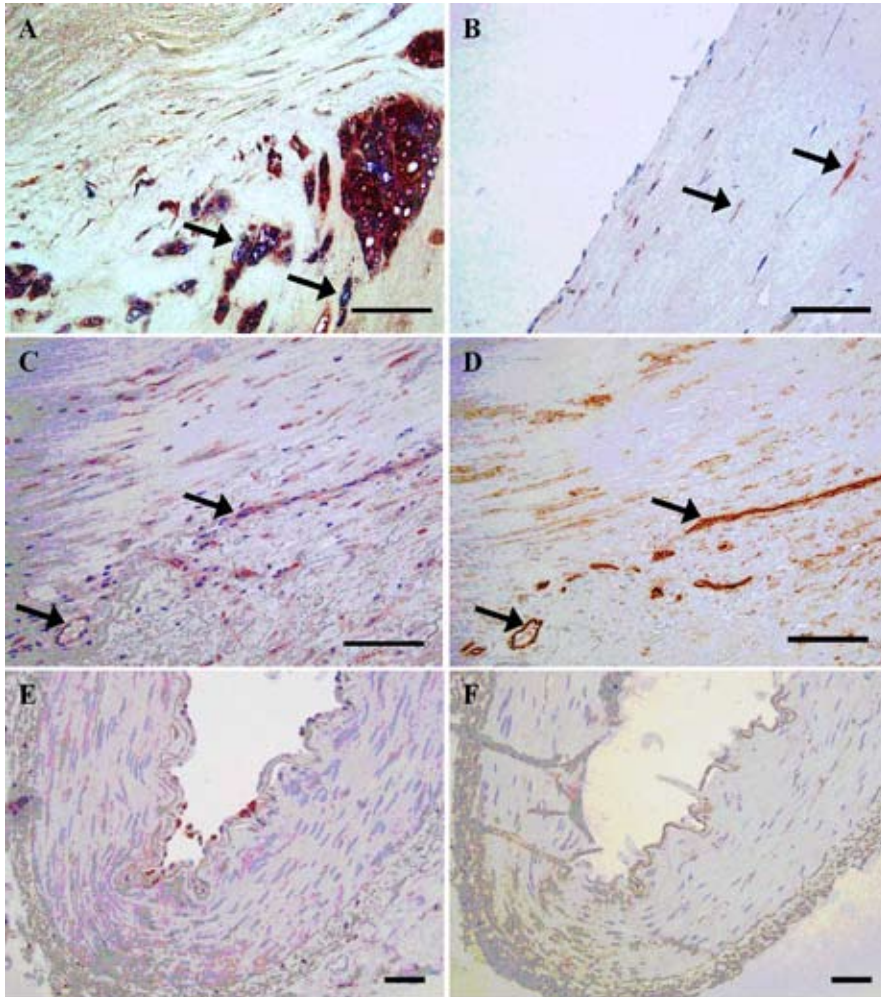
Figure 2: Histology of human atherosclerotic plaques
A: Double staining of NGAL (blue) and macrophages (CD68; red) reveals co-localization (purple). B: NGAL staining observed in smooth muscle cells (arrows) but not in inactive endothelium. C: NGAL staining observed in active endothelial cells aligning neovessels, and smooth muscle cells. D: CD34+ staining of the same endothelial cells aligning neovessels as in C. E: Mammary artery: smooth muscle cells reveal slight NGAL staining. Red blood cells adhering to endothelium contain much NGAL. F: Mammary artery: isotype control. Scale bar = 100µm.
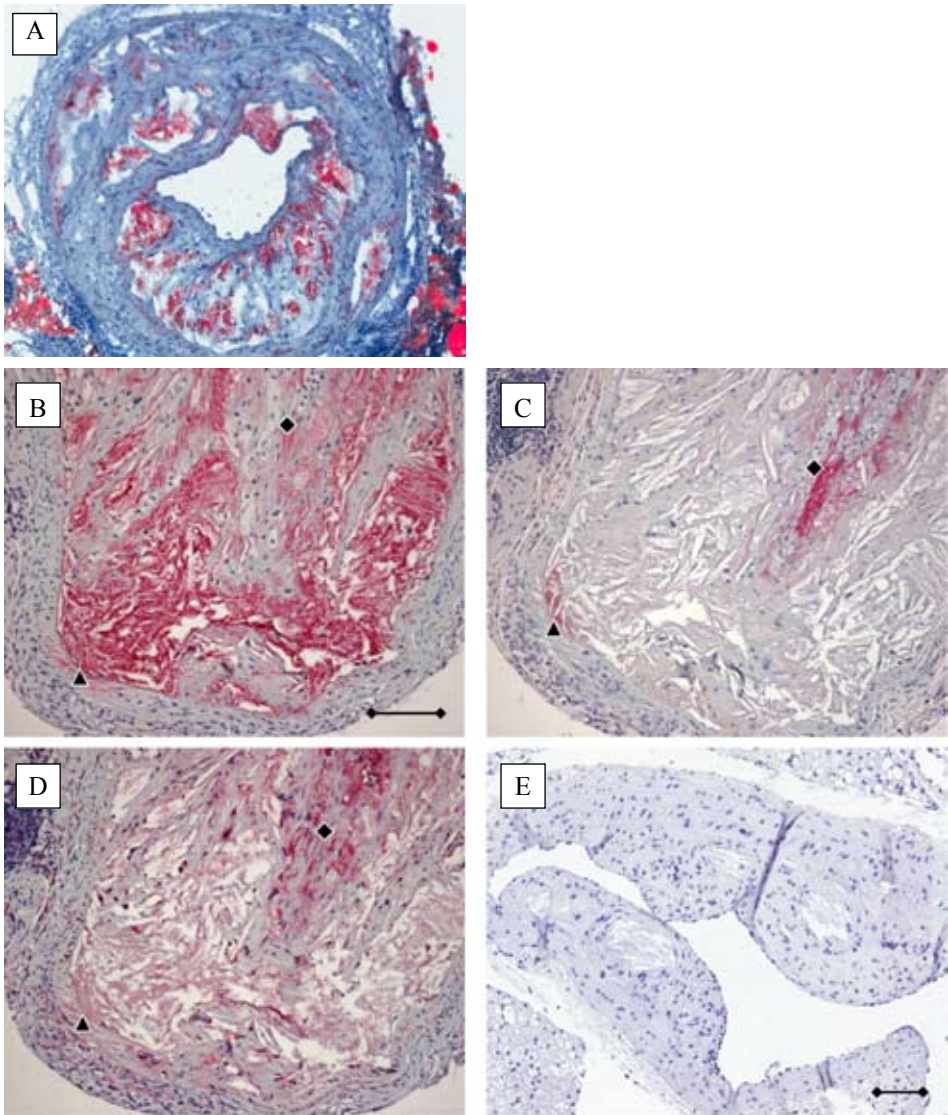
Figure 3: Histology of murine atherosclerotic plaques
A: Oil red O staining of a representative large aortic plaque with a large lipid core (cryo-section). B: NGAL/24p3 staining, C: staining of micelles, D: Staining of macrophages (mac-3) in a murine apoE$^{-/-}$/eNOS$^{-/-}$ aortic plaque after injection of NGAL/24p3-targeted micelles. Micelles co-localize partially with macrophages (black diamond) and partially with extracellular NGAL/24p3 (black triangle). E: micelle-staining in a control mouse, which is not injected. Scale bar = 100μm.
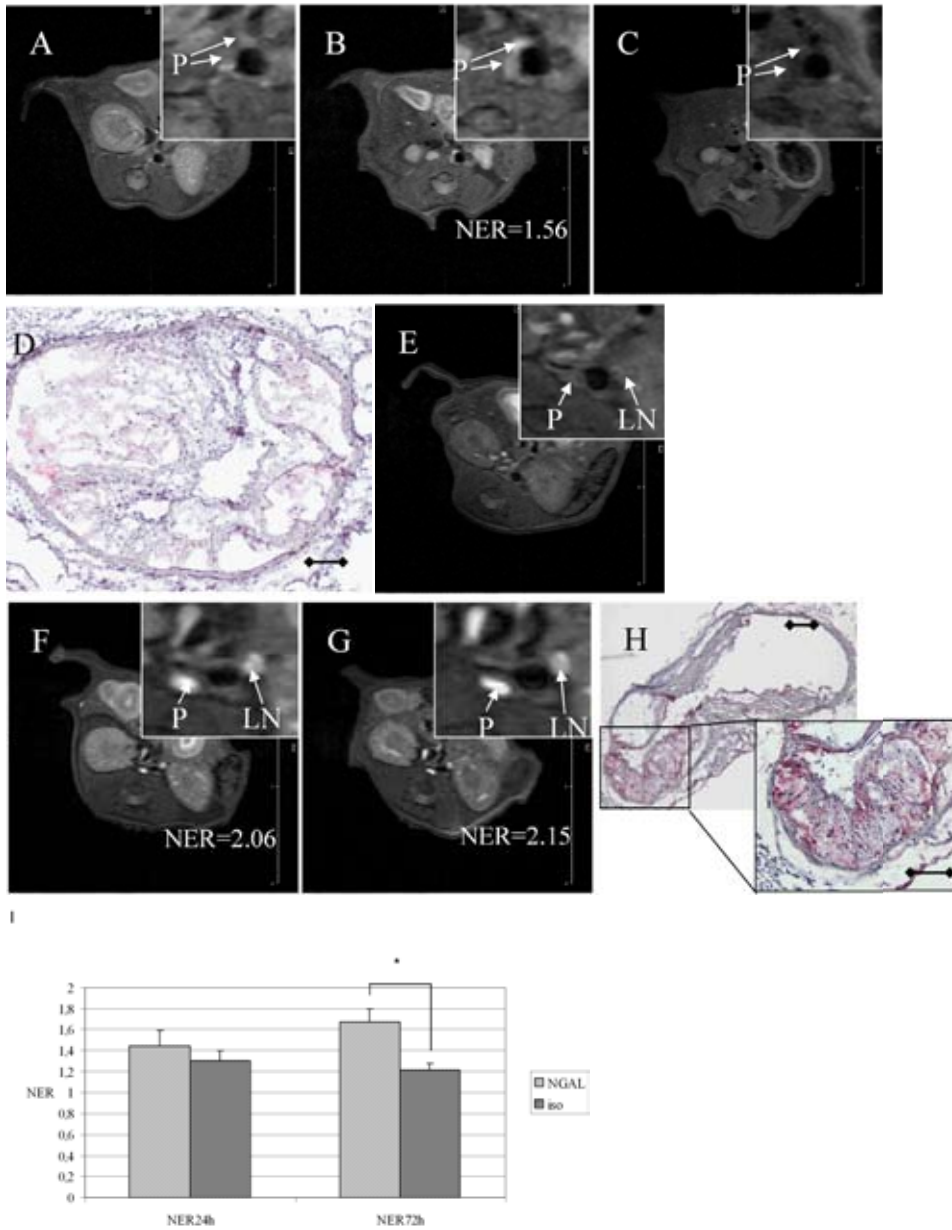
Figure 4: MR images and micelle-staining on corresponding levels
*Pre- and post-injection (0, 24 and 72 h) MR images of aortic wall in apoE$^{-/-}$/eNOS$^{-/-}$ mice injected with control (A-C) and NGAL/24p3-targeted (E-G) micelles. Histology on murine aorta showed no staining of micelles after injection with control micelles (D) and extensive red staining after injection of NGAL/24p3-targeted micelles (H). P=plaque, LN=lymph node. The post-injection MR images show enhancement of a lymph node, which was removed during harvesting of the aorta. Scale bar = 100µm. I: NER at 24 and 72 hours after injection of targeted and isotype-conjugated micelles. * p<0.05.*

Release of NGAL from atherosclerotic plaques
In blood, drawn directly from the carotid artery containing the atherosclerotic plaque (n=9), NGAL levels tended to increase when compared to NGAL levels in peripheral blood samples drawn at the same time (Figure 1D; p=0.06). Comparison of NGAL/MMP-9 complex levels (ELISA) in the plaque related to peripheral blood samples revealed a statistically significant increase of NGAL/MMP-9 complex level in the plaque related blood samples. (Figure 1E, p=0.007).

Mice/MRI
ApoE$^{-/-}$/eNOS$^{-/-}$ mice showed large atherosclerotic plaques in the abdominal aorta with large lipid cores and many macrophages (Figure 3A and D). Enhancement was seen at 24 hours post-injection both in mice injected with NGAL/24p3-targeted and isotype-conjugated control micelles (Figure 4: NER=1.45 ± 0.14 and 1.31 ± 0.10, respectively). However, at 72 hours post-injection we observed that mice injected with NGAL/24p3-targeted micelles showed more enhancement than mice injected with isotype-conjugated control micelles (Figure 4: NER=1.67 ± 0.12 and 1.21 ± 0.06, respectively (p<0.05)).
Via immunohistochemistry, we validated the specificity of the observed enhancement and detected micelles, macrophages and NGAL/24p3. The increase of NER at 72 hours in the NGAL/24p3-targeted mice was accompanied by micelle staining which co-localized with NGAL/24p3 expression and presence of macrophages (Figure 3B-D).
As expected, micelles were also found in the glomeruli of the kidneys (data not shown), possibly as a consequence of body clearance.

Discussion

MRI shows the most promise for imaging of atherosclerotic plaque vulnerability due to the combined information about anatomic detail and molecular expression. NGAL is a potential novel plaque target for visualization with molecular MRI. The current study reports several new findings regarding the expression of NGAL in human atherosclerotic lesions and its interaction with MMP-9, moreover a successful *in vivo* visualization of NGAL/24p3 within murine atherosclerotic plaques was achieved with molecular MRI.
Expression levels of NGAL are associated with unstable plaque characteristics, such as inflammation, and a large lipid core. Moreover, NGAL was associated with MMP-9 activity in plaques and is able to form a NGAL/MMP-9 complex thereby preserving MMP-9 activity (see supplementary methods and results). The established contribution of MMP-9 in plaque destabilization and the secretion of NGAL from plaques and

elevated circulating levels in patients suffering from myocardial infarction, suggests the involvement of NGAL in unstable atherosclerotic disease.

The role of NGAL in the plaque

Besides the interaction with MMPs, other functions of NGAL could be important in atherosclerotic plaques. NGAL is implicated to regulate inflammation, because it binds fMLP, leukotriene B4 and platelet activating factor (10-12). In addition, NGAL is proposed to be involved in cell survival, but it is disputed if its function is pro- or anti-apoptotic (31-33). In kidney ischemia, NGAL protects renal damage by preventing cell death via induction of haem-oxygenase (34). Since inflammation, cell death and ischemia are key processes in atherosclerosis, free NGAL could play a role in atherosclerotic lesions via these functions. However, these mechanisms were not addressed in the present study and warrant further investigation. Here, we focused on the interaction between NGAL and MMP-9 as an important effector mechanism of NGAL in atherosclerotic plaques. In atherosclerotic carotid lesions, NGAL/MMP-9 complex levels were below ELISA detection limits and therefore gelatinolytic activity of the NGAL/MMP-9 complex was measured (see supplementary methods and results). This demonstrated similar associations with plaque characteristics as NGAL individually. The current study is the first to show the coupling of NGAL and MMP-9 in human atherosclerotic plaques, as confirmed by gelatin zymography and western blotting (see supplementary methods and results), potentially leading to prolonged protease activity (see supplementary methods and results). The strong association between *in vivo* NGAL blood levels and MMP-8 activity is expected since NGAL was previously shown to be involved in activation of MMP-8 (15). The lack of difference between NGAL levels in healthy arteries and carotid atherosclerotic plaques was caused by some baseline expression of NGAL by smooth muscle cells, abundantly present in healthy arteries. The association between NGAL and an unstable plaque phenotype, suggested NGAL to be a potential candidate for molecular imaging of unstable atherosclerotic lesions. Some molecular atherosclerotic imaging studies have focused on targets available on macrophage membranes(35), while other studies have targeted ox-LDL, fibrin or MMPs(5, 36, 37), which have extra-cellular distributions. We may expect that a lot of extra-cellular targets in atherosclerotic plaque are also present in circulating blood. This could hamper the application of molecular MRI with micelles directed against these targets, because they could bind to the circulating marker before arrival in the plaque. Indeed, in this study NGAL concentrations in the plasma were 80 ng/ml, however NGAL concentrations in the plaque were ~120 times higher than in the blood. We generated gadolinium loaded micelles targeting NGAL specifically and observed an increased plaque NER after injection of NGAL/24p3-targeted micelles as

compared to isotype-conjugated micelles at 72 hours. At 24 hours, we could not observe a difference between the two types of micelles, suggesting an early and unspecific uptake of micelles due to the concentration gradient between blood and plaque. Although an earlier study revealed a difference in NER at 24 hours after injection of targeted versus non-conjugated micelles, their control micelles lacked an antibody and targeted the macrophage scavenger receptor (35). Also maximum uptake of micelles targeting oxidation-specific epitopes was reported at 72 hours after injection, but isotype-conjugated micelles did not show significant enhancement at any earlier time points (5). These findings plead for more extended investigation of the MRI timing window for each nanoparticle-target combination. Generally, fluorescence microscopy is used for ex vivo detection of fluorescently labeled paramagnetic micelles. Because of extensive auto-fluorescence of plaque lipids at various emission wavelengths, we used immunohistochemistry on micelle-conjugated rat antibodies. Via immunohistochemistry, we could not observe a difference after injection of targeted and isotype micelles at 24 hours, however, the observed enhancement at 72 hours post-injection was due to NGAL-targeted micelles since control targeted micelles could no longer be observed via histology. Micelles of isotype-conjugated and 24p3-targeted micelles were found in glomeruli, suggesting clearance by kidneys. This in contrast to earlier reported predominant clearance of immunomicelles by the liver (5).

Conclusions

The high expression levels of NGAL in atheromatous, inflammatory plaques, and the increased circulating levels in patients with acute myocardial infarction and large atherosclerotic lesions suggest the involvement of NGAL in unstable atherosclerotic disease. The high plaque to blood ratio of this target in patients and successful visualization of NGAL/24p3 in atherosclerotic plaque of apoE$^{-/-}$/eNOS$^{-/-}$ mice provides a basis for molecular MRI-based risk stratifications.

Reference List

1. Stary H, Chandler A, Dinsmore R, Fuster V, Glagov S, Insull W, Jr., et al. A definition of advanced types of atherosclerotic lesions and a histological classification of atherosclerosis. A report from the Committee on Vascular Lesions of the Council on Arteriosclerosis, American Heart Association. Circulation 1995;92:1355-1374.

2. Briley-Saebo K, Geninatti-Crich S, Cormode D, Barazza A, Mulder W, Chen W et al. High-relaxivity gadolinium-modified high-density lipoproteins as magnetic resonance imaging contrast agents. J Phys Chem B 2009;113:6283-6289.

3. Cormode D, Chandrasekar R, Delshad A, Briley-Saebo K, Calcagno C, Barazza A et al. Comparison of Synthetic High Density Lipoprotein (HDL) Contrast Agents for MR Imaging of Atherosclerosis. Bioconjug Chem 2009.

4. Mulder W, Strijkers G, Briley-Saboe K, Frias J, Aguinaldo J, Vucic E et al. Molecular imaging of macrophages in atherosclerotic plaques using bimodal PEG-micelles. Magn Reson Med 2007;58:1164-1170.

5. Briley-Saebo K, Shaw P, Mulder W, Choi S, Vucic E, Aguinaldo J et al. Targeted molecular probes for imaging atherosclerotic lesions with magnetic resonance using antibodies that recognize oxidation-specific epitopes. Circulation 2008;117:3206-3215.

6. Lukyanov A, Torchilin V. Micelles from lipid derivatives of water-soluble polymers as delivery systems for poorly soluble drugs. Adv Drug Deliv Rev 2004;56:1273-1289.

7. Kjeldsen L, Johnsen A, Sengelov H, Borregaard N. Isolation and primary structure of NGAL, a novel protein associated with human neutrophil gelatinase. J Biol Chem 1993;268:10425-10432.

8. Triebel S, Blaser J, Reinke H, Tschesche H. A 25 kDa alpha 2-microglobulin-related protein is a component of the 125 kDa form of human gelatinase. FEBS Lett 1992;314:386-388.

9. Goetz D, Holmes M, Borregaard N, Bluhm M, Raymond K, Strong R. The neutrophil lipocalin NGAL is a bacteriostatic agent that interferes with siderophore-mediated iron acquisition. Mol Cell 2002;10:1033-1043.

10. Sengelov H, Boulay F, Kjeldsen L, Borregaard N. Subcellular localization and translocation of the receptor for N-formylmethionyl-leucyl-phenylalanine in human neutrophils. Biochem J 1994;299:473-479.

11. Nielsen B, Borregaard N, Bundgaard J, Timshel S, Sehested M, Kjeldsen L. Induction of NGAL synthesis in epithelial cells of human colorectal neoplasia and inflammatory bowel diseases. Gut 1996;38:414-420.

12. Bratt T, Ohlson S, Borregaard N. Interactions between neutrophil gelatinase-associated lipocalin and natural lipophilic ligands. Biochim Biophys Acta 1999;1472:262-269.

13. Cowland J, Sorensen O, Sehested M, Borregaard N. Neutrophil gelatinase-associated lipocalin is up-regulated in human epithelial cells by IL-1 beta, but not by TNF-alpha. J Immunol 2003;171:6630-6639.

14. Yan L, Borregaard N, Kjeldsen L, Moses M. The high molecular weight urinary matrix metalloproteinase (MMP) activity is a complex of gelatinase B/MMP-9 and neutrophil gelatinase-associated lipocalin (NGAL). Modulation of MMP-9 activity by NGAL. J Biol Chem 2001;276:37258-37265.

15. Tschesche H, Zolzer V, Triebel S, Bartsch S. The human neutrophil lipocalin supports the allosteric activation of matrix metalloproteinases. Eur J Biochem 2001;268:1918-1928.

16. Galis Z, Khatri J. Matrix metalloproteinases in vascular remodeling and atherogenesis: the good, the bad, and the ugly. Circ Res 2002;90:251-262.

17. Galis Z, Sukhova G, Lark M, Libby P. Increased expression of matrix metalloproteinases and matrix degrading activity in vulnerable regions of human atherosclerotic plaques. J Clin Invest 1994;94:2493-2503.

18. Loftus I, Naylor A, Goodall S, Crowther M, Jones L, Bell P et al. Increased matrix metalloproteinase-9 activity in unstable carotid plaques. A potential role in acute plaque disruption. Stroke 2000;31:40-47.

19. Sluijter J, Pulskens W, Schoneveld A, Velema E, Strijder C, Moll F et al. Matrix metalloproteinase 2 is associated with stable and matrix metalloproteinases 8 and 9 with vulnerable carotid atherosclerotic lesions: a study in human endarterectomy specimen pointing to a role for different extracellular matrix metalloproteinase inducer glycosylation forms. Stroke 2006;37:235-239.

20. de Nooijer R, Verkleij C, der Thusen J, Jukema J, van der Wall E, van Berkel T et al. Lesional overexpression of matrix metalloproteinase-9 promotes intraplaque hemorrhage in advanced lesions but not at earlier stages of atherogenesis. Arterioscler Thromb Vasc Biol 2006;26:340-346.

21. Gough P, Gomez I, Wille P, Raines E. Macrophage expression of active MMP-9 induces acute plaque dis-

ruption in apoE-deficient mice. J Clin Invest 2006;116:59-69.

22. Hemdahl A, Gabrielsen A, Zhu C, Eriksson P, Hedin U, Kastrup J et al. Expression of neutrophil gelatinase-associated lipocalin in atherosclerosis and myocardial infarction. Arterioscler Thromb Vasc Biol 2006;26:136-142.

23. Kuhlencordt P, Gyurko R, Han F, Scherrer-Crosbie M, Aretz T, Hajjar R et al. Accelerated atherosclerosis, aortic aneurysm formation, and ischemic heart disease in apolipoprotein E/endothelial nitric oxide synthase double-knockout mice. Circulation 2001;104:448-454.

24. Verhoeven B, Velema E, Schoneveld A, de Vries J, de Bruin P, Seldenrijk C et al. Athero-express: differential atherosclerotic plaque expression of mRNA and protein in relation to cardiovascular events and patient characteristics. Rationale and design. Eur J Epidemiol 2004;19:1127-1133.

25. Beneficial effect of carotid endarterectomy in symptomatic patients with high-grade carotid stenosis. North American Symptomatic Carotid Endarterectomy Trial Collaborators. N Engl J Med 1991;325:445-453.

26. Endarterectomy for asymptomatic carotid artery stenosis. Executive Committee for the Asymptomatic Carotid Atherosclerosis Study. JAMA 1995;273:1421-1428.

27. Randomised trial of endarterectomy for recently symptomatic carotid stenosis: final results of the MRC European Carotid Surgery Trial (ECST). Lancet 1998;351:1379-1387.

28. Halliday A, Mansfield A, Marro J, Peto C, Peto R, Potter J et al. Prevention of disabling and fatal strokes by successful carotid endarterectomy in patients without recent neurological symptoms: randomised controlled trial. Lancet 2004;363:1491-1502.

29. Maier W, Altwegg L, Corti R, Gay S, Hersberger M, Maly F et al. Inflammatory markers at the site of ruptured plaque in acute myocardial infarction: locally increased interleukin-6 and serum amyloid A but decreased C-reactive protein. Circulation 2005;111:1355-1361.

30. Mulder W, Strijkers G, van Tilborg G, Griffioen A, Nicolay K. Lipid-based nanoparticles for contrast-enhanced MRI and molecular imaging. NMR Biomed 2006;19:142-164.

31. Tong Z, Wu X, Ovcharenko D, Zhu J, Chen C, Kehrer J. Neutrophil gelatinase-associated lipocalin as a survival factor. Biochem J 2005;391:2-8.

32. Tong Z, Wu X, Kehrer J. Increased expression of the lipocalin 24p3 as an apoptotic mechanism for MK886. Biochem J 2003;372:1-10.

33. Caramuta S, De Cecco L, Reid J, Zannini L, Gariboldi M, Kjeldsen L et al. Regulation of lipocalin-2 gene by the cancer chemopreventive retinoid 4-HPR. Int J Cancer 2006;119:1599-1606.

34. Mori K, Lee H, Rapoport D, Drexler I, Foster K, Yang J et al. Endocytic delivery of lipocalin-siderophore-iron complex rescues the kidney from ischemia-reperfusion injury. J Clin Invest 2005;115:610-621.

35. Amirbekian V, Lipinski M, Briley-Saebo K, Amirbekian S, Aguinaldo J, Weinreb D et al. Detecting and assessing macrophages *in vivo* to evaluate atherosclerosis noninvasively using molecular MRI. Proc Natl Acad Sci U S A 2007;104:961-966.

36. Botnar R, Perez A, Witte S, Wiethoff A, Laredo J, Hamilton J et al. *In vivo* molecular imaging of acute and subacute thrombosis using a fibrin-binding magnetic resonance imaging contrast agent. Circulation 2004;109:2023-2029.

37. Lancelot E, Amirbekian V, Brigger I, Raynaud J, Ballet S, David C et al. Evaluation of matrix metalloproteinases in atherosclerosis using a novel noninvasive imaging approach. Arterioscler Thromb Vasc Biol 2008;28:425-432.

38. Pasterkamp G, Schoneveld A, Hijnen D, de Kleijn D, Teepen H, van der Wal A et al. Atherosclerotic arterial remodeling and the localization of macrophages and matrix metalloproteases 1, 2 and 9 in the human coronary artery. Atherosclerosis 2000;150:245-253.

Online appendix

Methods

Carotid plaque characterization

The carotid endarterectomy specimens were divided in segments of 5 mm thickness along the longitudinal axis of the vessel. The segment with greatest plaque burden was embedded in paraffin for further histological characterization. The directly adjacent segment was used for protein extraction by dissolving in 40 mM Tris-HCl (pH=7.5) at 4°C as previously described.24

Histology of human atherosclerotic specimens

For NGAL staining, the following procedure was used: paraffin sections (5-µm thickness) were deparaffinized, blocked for 30 minutes in 1.5% hydrogen peroxide in methanol, and boiled for 12 minutes in 10 mM sodium citrate (pH 6.0). After pre-incubation with 10% normal rabbit serum in 1% PBSA for 1 hour, incubation with primary antibody was performed overnight (monoclonal rat-anti-NGAL, 10ug/mL; R&D Systems). Biotinylated rabbit-anti-rat IgG (0.4ug/mL; DAKO) was used as the secondary antibody, followed by horseradish peroxidase conjugated streptavidin, AEC substrate and counterstained with hematoxylin. Specificity of the staining was ascertained by absence of staining in isotype controls and increasing intensity of the staining with increasing concentrations of the primary antibody. Co-localization of NGAL with macrophages, smooth muscle cells and endothelial cells was assessed by double stainings. NGAL staining was performed under the same conditions as for the single NGAL staining, except Fast Blue substrate was used, followed by CD68 (macrophage) staining (KP-1, 3.3 µg/mL; DAKO), or Alpha-actin (1A4, 1:1500; Sigma, St. Louis, MO) or CD34 (Qbend10, 0.5 µg/mL; Beckman Coulter, Fullerton, CA) with AEC substrate. Neutrophil infiltration was assessed using myeloperoxidase staining (polyclonal rabbit anti-human, 1:10000; DAKO).

Paraffin sections of the plaques were stained and analyzed semi-quantitatively for macrophages (CD68), smooth muscle cells (Alpha-Actin), collagen (Picrosirius Red), calcifications (Hematoxylin and Eosin (H&E)) and overall phenotype, as described previously.24 Interleukin-6 (IL-6) and IL-8 were measured in plaque protein extracts with a multiplex suspension array system according to the manufacturer's protocol (Bio-Rad Laboratories, California, USA). MMP-2, -8 and -9 activities were measured by Biotrak RPN2631, RPN2635 and RPN2634, respectively (Amersham Biosciences, Buckinghamshire, UK). The measurements for MMPs and interleukins were standardized for total protein concentration of the protein extracts (DC protein assay, Bio-Rad).

Histology of murine atherosclerotic specimens

From 4mm caudal to 5mm cranial of the right renal artery branch, 5µm (cryo) or 3µm (paraffin) sections were made at every 0.5mm. Oil Red O (lipid) stainings were performed on cryo-sections.

Paraffin sections (For macrophage-, 24p3-, and micelle staining):

Because NGAL staining on cryo-sections was not successful, one murine aorta was perfusion-fixated with formaldehyde 4%/PBS (1:10) and the aorta was embedded in paraffin. 3µm thick sections were deparaffinized and washed with aqua-dest. For the 24p3 and MAC3 (macrophages) the sections were boiled for 20 minutes in citrate-buffer (pH=6), cooled (au bain Marie) and washed in PBS/Tween. After incubation for 60 minutes with the primary antibody, either 24p3 (1:100, Santa Cruz, sc-50351) or MAC3 (1:200, eBioscience, 11-5989), the sections were washed with PBS/Tween. The MAC3 stained sections were incubated for 60 minutes with a secondary rabbit anti-rat antibody (DAKO, p0450) in 10% normal mouse serum and washed in PBS/Tween. All sections were incubated for 30 minutes with PowerVision (biotin-free polyclonal-AP-anti rabbit, Immunologic, DPVR-110AP), and subsequently washed in PBS and TBS. Then, sections were incubated for 30 minutes in alkaline-phosphatase substrate, washed with aqua-dest and counterstained with hematoxylin. Finally, sections were washed with flowing tap water and air-dried. In case of the micelle-staining, sections were deparaffinized and washed with aqua-dest, incubated for 60 minutes with rabbit anti-rat (1:250, DAKO, p0450) in 10% normal mouse serum and washed with PBS/Tween. After incubation with Powervision (biotin-free polyclonal-AP-anti rabbit, Immunologic, DPVR-110AP) for 30 minutes, sections were washed with PBS and TBS. Sections were incubated for 30 minutes with alkaline-phosphatase substrate, washed with aqua-dest and counterstained with hematoxylin. Finally, sections were washed with flowing tap water and air-dried. All stainings were performed at room temperature.

Detection of NGAL/MMP-9 complex in carotid plaques

Gelatin zymography was performed as described before.[38] An equal amount of total protein extract was loaded for each sample[38]. The combined gelatinolytic activity of NGAL/MMP-9 (125 kD) and NGAL-dimer/MMP-9 (150 kD) was measured as the degradation of gelatin at 125 kD and 150 kD and is further referred to as NGAL/MMP-9 gelatinolytic activity.[14] Gelatinolytic activity of free MMP-9 (92kD) was measured and is further referred to as MMP-9 gelatinolytic activity. Western blotting for NGAL was additionally performed using monoclonal rat-anti-human NGAL antibody (5 µg/mL; R&D Systems) followed by biotinylated rabbit-anti-rat IgG (0.675 µg/mL; DAKO, Glostrup, Denmark) and horseradish peroxidase conjugated streptavidin. Levels of the

NGAL/MMP-9 complex were determined by ELISA (R&D Systems, Minneapolis, MN). An equal amount of protein extract was loaded for all samples. However, because the sensitivity of the ELISA was relatively limited (lower detection limit 312 ng/mL for NGAL/MMP-9 ELISA compared to 10 ng/mL for NGAL ELISA), only a limited subset of samples with high protein concentrations could be used for the analysis due to loading limitations.

Baseline and follow-up MRI procedure
Scout images
Fast Spin Echo (FSE) technique was used for axial scout images. Subsequently, coronal and saggital scout images of the suprarenal abdominal aorta using Fast Low Angle Shot (FLASH) were acquired. Twenty contiguous axial slices, perpendicular to coronal and saggital scout images, were planned from 4 mm below the right renal artery branch up to 5 mm above this branch.

Optimization of trigger delay
Signal acquisition was planned at the moment of maximal flow through the abdominal aorta. Hereto axial T1 weighted FSE (cardiac and respiratory gated) at the level of 1 mm above the right renal artery was repeated with varying trigger delay. Images were checked for laminar flow artifacts (bright vessel rims as a result of slow flow) and the diameter of the aortic lumen. Trigger delay corresponding with the image, which lacked flow artifacts and had the largest aortic diameter was chosen (optimized trigger delay) for other scans as described below.

IR-FSE images
IR-FSE axial images from 4 mm below the right renal artery branch up to 5 mm above were acquired. The acquisition scheme was started with an inversion pulse. The chosen trigger delay (TD) for IR-FSE was chosen in a way, that the equation "(inversion time + TD)/(cardiac cycle duration) = integer + optimized TD" was satisfied.

Reference images for recognition of anatomic landmarks: lymph nodes and small peri-aortic blood vessels
Diffusion weighted imaging sequence was used with diffusion gradient (b=400 s/mm2) and with the same acquisition modules but zero diffusion (b=0 s/mm2). These images were used for discrimination of peri-aortic lymph nodes (having low diffusion) usually found at 5 levels around the right renal artery branch (-1 up to +3 mm). A steady-state free precession technique was used for acquisition of non-triggered bright-blood images for depiction of small peri-aortic blood vessels.

MRI parameters:

IR-FSE images

TR/TE=3500/14 ms, inversion time=1300 ms, rare factor=10, excitation/refocusing pulse gauss 1 ms, flip angle=90˚/180˚, Spectral width=75757 Hz, FOV=30x30 mm^2, matrix=200x200 resulting in a pixel dimension=150x150 μm^2, 20 axial slices, thickness=0.5 mm, chemical shift selective fat suppression, 2 inflow saturation slices (1 cranial (saturation of arterial inflow) and 1 caudal (saturation of venous inflow)), thickness 10 mm, NA=10, zero fill acceleration factor 1.7, total acquisition time 7m20s.

Diffusion weighted images

TR/TE=2000/13.2 ms, hermite pulse 1.0 ms, excitation/refocusing flip angle=90˚/180˚, b value (longitudinal/z-axis) 0 or 400 s/mm^2, diffusion gradient duration 1.40 ms, separation 5.0 ms, Spectral width=50000 Hz, FOV=30x30 mm^2, matrix=256x256 resulting in a pixel dimension=117x117 μm^2, 1 axial slice, thickness=0.5 mm (at five levels around the right renal artery: -1 up to +3 mm), chemical shift selective fat suppression, NA=1, zero fill acceleration factor 1.9, total acquisition time 4m20s. Lymph nodes were discerned by calculation of the apparent diffusion coefficient: ADC=ln(S1-S2)/ΔB. S1 and S2 are the mean signal intensities on the image with b=0 and the image with b=400 s/mm^2, respectively, while Δb = 400-0=400 s/mm^2. If ADC was less than 1.8, the structure was identified as a lymph node.

Bright-blood images

TR/TE=150/1.75 ms, gauss pulse 500 μs, flip angle=90˚, Spectral width=166667 Hz, FOV=30x30 mm^2, Matrix =256x256 resulting in a pixel dimension=117x117 μm^2, 20 axial slices, thickness=0.5 mm, NA=5, zero fill acceleration factor 1.34, total acquisition time 2m24s.

Results

Interaction of NGAL and MMP-9 in atherosclerotic carotid plaques
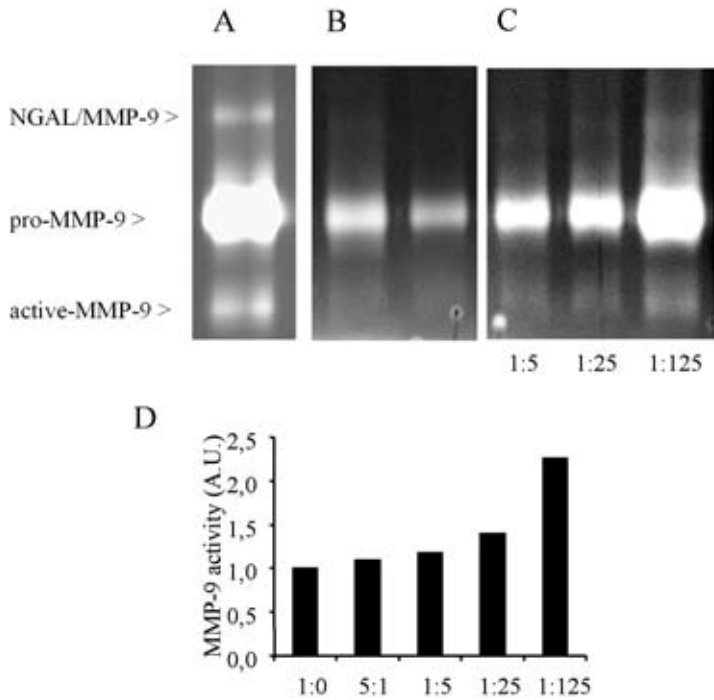
Gelatinolytic activity of NGAL/MMP-9 complexes (Suppl. Figure 1A) was detected at 125 kD (NGAL/MMP-9) and 150 kD (NGAL-dimer/MMP9) as previously described by Yan et al.14 This was confirmed via Western Blotting: specific NGAL bands were detected at 125 kD and 150 kD, corresponding to the two bands observed in zymography (Suppl. Figure 1A). In addition, free NGAL was detected by Western blotting at 25 kD (monomer) and 50 kD (dimer; data not shown). The NGAL/MMP-9 complexes could be reconstructed in vitro by incubation of MMP-9 and NGAL recombinants (Suppl.

Figure 2). Gelatinolytic activity of the NGAL/MMP-9 complex was significantly higher in carotid artery plaques compared to the control mammary arteries (Suppl. Figure 1B,C). Moreover, as can be appreciated in suppl. Figure 1B, an important part of total gelatinolytic activity in the plaques was attributable to the NGAL/MMP-9 complexes (6.75 A.U.) compared to free MMP-9 (15.3 A.U.), which was confirmed by quantification of the NGAL/MMP-9 complex levels via ELISA in a subset of samples (0.60ng/g vs. 2.51 ng/g, respectively). Gelatinolytic activity of the NGAL/MMP-9 complex was strongly related to NGAL concentration (R=0.310; p=0.001) and MMP-9 activity (Suppl. Figure 1D; R=0.315; p=0.005), whereas NGAL/MMP-9 gelatinolytic activity was not associated with MMP-8 or MMP-2 activity levels (data not shown).
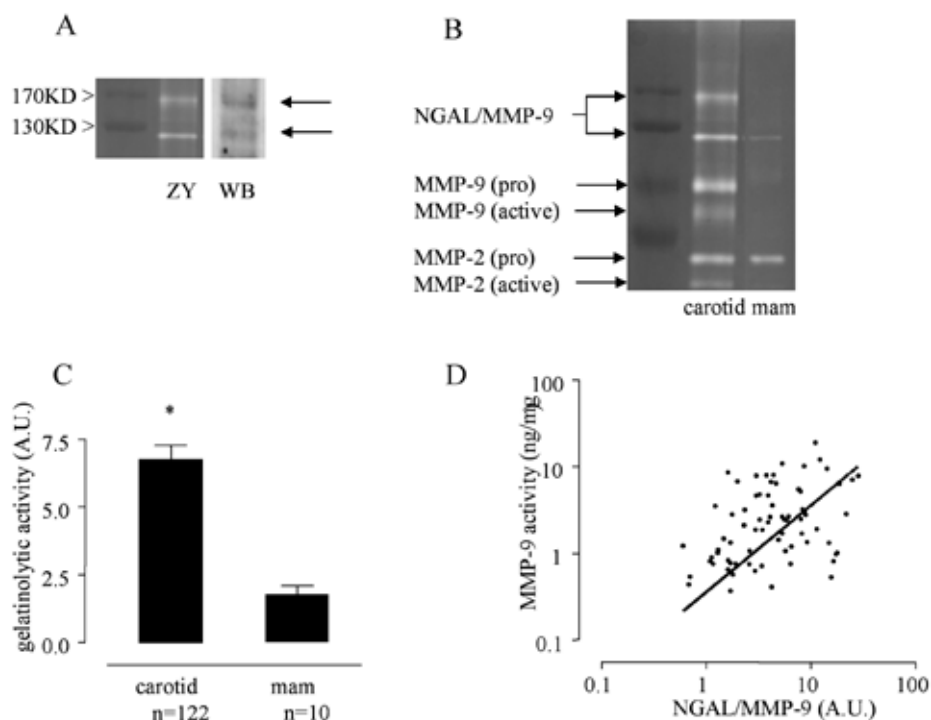
Supplement Figure 1: Association between NGAL and MMP activity
A: Representative zymogram (ZY) and NGAL Western Blot (WB), demonstrating that the gelatinolytic bands at 125 and 150 kD contain NGAL. B: representative zymogram detecting NGAL/MMP-9 complex at 125 kD and NGAL-dimer/ MMP-9 complex at 150 kD. C: Quantification of zymography among different tissues demonstrated that NGAL/MMP-9 activity is significantly higher expressed (p<0.01) in carotid plaques than in non-atherosclerotic mammary arteries. D: MMP-9 activity (Biotrak) is strongly related to gelatinolytic activity of the NGAL/MMP-9 complex (r=0.315; p=0.005) in carotid plaques.

Supplement Figure 2: NGAL preserves MMP-9 activity

Quantification of in vitro experiments by gelatin zymography. A: In vitro reconstruction of NGAL/MMP-9 complexes by combining recombinant NGAL and MMP-9. B: MMP-9 activity diminishes after 30 minutes incubation at 37℃ (left lane: no incubation, right lane: 30 minutes incubation). C: Increasing addition of NGAL prevents the autodegradation of MMP-9, (MMP-9:NGAL molar ratio 1:5 – 1:125). D: Quantification of C.

The time window of MRI of murine atherosclerotic plaques after administration of CB2 receptor targeted micelles

Inter-scan variability and relation between plaque signal intensity increase and gadolinium content of inversion recovery prepared versus non-prepared fast spin echo

*B.C.M. te Boekhorst[1,2], S.M. Bovens[2], C.W.A. van de Kolk[1], M.J.M. Cramer[1], P.A.F.M. Doevendans[1], M. ten Hove1, L. van de Weerdt[3], R. Poelmann[4], G.J. Strijkers[5], G. Pasterkamp[1], C.J.A. van Echteld[1,6]

[1]*Department of Cardiology, University Medical Center Utrecht, Utrecht, The Netherlands, [2]Interuniversity Cardiology Institute of the Netherlands, Utrecht, The Netherlands, [3]Department of Radiology, Leiden University Medical Center, Leiden, The Netherlands, [4]Department of Anatomy and Embryology, Leiden University Medical Center, Leiden, The Netherlands, [5]Biomedical NMR, Eindhoven University of Technology, Eindhoven, The Netherlands, [6]Present address: Novartis Institutes for BioMedical Research, Basel, Switzerland*

Abstract

Background

Single fast spin echo scans covering limited time frames are mostly used for contrast-enhanced MRI of atherosclerotic plaque biomarkers. Knowledge on inter-scan variability of the Normalized Enhancement Ratio (NER) of plaque and relation between the NER of plaque and gadolinium content for inversion-recovery fast spin echo is limited. Study aims were: evaluation of 1. timing of MRI after intravenous injection of Cannabis2 receptor (CB2-R) (expressed by human and mouse plaque macrophages) targeted micelles, 2. inter-scan variability of inversion-recovery fast spin echo and fast spin echo, 3. relation between the NER of plaque and gadolinium content for inversion-recovery fast spin echo and fast spin echo.

Methods/Results

Inversion-recovery fast spin echo/fast spin echo imaging was performed before and every 15 minutes up to 48 hours after injection of CB2-R targeted or control micelles using several groups of mice measured in an interleaved fashion. The NER of plaque (determined on inversion-recovery fast spin echo images) remained high (~2) until 48 hours after injection of CB2-R targeted micelles, whereas the NER of plaque decreased after 36 hours in the control group. The inter-scan variability and relation between the NER of plaque and gadolinium (assessed with Inductively Coupled Plasma- Mass Spectrometry) were compared between inversion-recovery fast spin echo and fast spin echo. Inter-scan variability was higher for inversion-recovery fast spin echo than for fast spin echo. Although gadolinium and the NER of plaque correlated well for both techniques, the NER of plaque was higher for inversion-recovery fast spin echo than for fast spin echo.

Conclusions

In mice injected with CB2-R targeted micelles, the NER of plaque can be best evaluated at 36-48 hours post-injection. Averaging values for the NER of plaque of consecutive inversion-recovery fast spin echo scans is recommended.

Introduction

Noninvasive imaging of atherosclerotic disease could facilitate serial studies to investigate the important issue of plaque stabilization and destabilization. There is an urgent need for surrogate measures of progression of the disease and new biomarkers are needed that can be applied to test drug efficacy with the objective to stabilize the atherosclerotic process. Magnetic Resonance Imaging (MRI) has important advantages in this perspective: it provides the possibility of contrast-enhanced molecular or cellular imaging combined with angiography and anatomic detail and it does not involve ionizing radiation.

Atherosclerotic plaques have been visualized using various carrier platforms of gadolinium (Gd) aimed at different molecular targets[1-15]. Pharmacokinetics of these carriers and the resultant concentration gradient between blood and plaque will determine the wash-in and washout kinetics and the time of maximum contrast enhancement of the plaque[16]. Clearance of untargeted agents from targeted tissues, e.g. vulnerable plaques, is likely to be faster when compared to specifically targeted agents. Contrast-enhanced MRI of mouse atherosclerotic plaque is performed typically at baseline, 24 and 48 hours after injection of micelles[1,5,6,9,17]. These time points are likely based on practical considerations related with the timing of the MRI procedure. However, it is largely unknown to what extent enhancement ratios remain stable over time.

In addition, molecular MR imaging of atherosclerotic plaques is often performed with single measurements and limited time frames. The knowledge on reproducibility of single measurements using targeted contrast is limited. Localization of contrast enhancement may suffer from inter-scan variability (ISV) when contrast-enhanced MRI is executed. Another complicating factor is that even with an in-plane spatial resolution of 100 μm^2 it is not straightforward to differentiate between peri-aortic lymph nodes and aortic wall in mice (Te Boekhorst et al. unpublished results). Lymph nodes may show uptake of contrast agent, which will challenge differentiation between lymph node and plaque enhancement.

The peripheral cannabis receptor (CB2-R) has been reported to be expressed in advanced human and murine atherosclerotic plaque[18]. CB2-R has an important immuno-modulatory function in atherosclerosis which is mediated by endogenous cannabinoids[19]. Activation of CB2-R by a synthetic agonist led to a decrease of the amount of atherosclerosis[18]. We have reported on the efficacy of T1 contrast generation after binding of CB2-R targeted micelles via this synthetic lipophilic CB2-R agonist (non-covalently bound to the outer micelle core) to the CB2 receptor to an *in vitro* cell system[20].

Additionally, in general, non-prepared T1-weighted sequences are used for visualization of the plaque with T1 contrast agents. However, theoretically, one would expect that inversion recovery (IR) prepared sequences are capable to generate larger T1 contrast than traditionally used non-prepared T1 weighted sequences[21].

In this study, we aim to optimize MRI procedures for detection of atherosclerotic plaque enhancement in mice. Hereto, we inject CB2-R targeting Gd containing micelles or control Gd containing micelles via the tail vein of apoE^{-/-}/eNOS^{-/-} mice, which are known to develop atherosclerotic plaque in the abdominal aorta(22). MRI data of murine atherosclerotic aorta are collected using an inversion recovery sequence every 15 minutes from pre- up to 48 hours after injection. We explore the time window after injection, in which only positive MR contrast, caused by plaque uptake of these atherosclerosis targeting micelles, can be observed. In a subset of animals both IR-Fast Spin Echo (IR-FSE) and FSE (modified from Briley-Saebo et al.(17)) are applied every 15 minutes and Gd-content will be measured *ex vivo* with Inductively Coupled Plasma-Mass Spectrometry (ICP-MS). We will evaluate the relation between increase of plaque signal intensity and Gd-content, for IR-FSE and FSE. Furthermore, we will examine the ISV for these scanning procedures.

Materials & Methods

Materials

Di-stearoyl-polyethylene glycol-phosphatidylethanolamine (DSPE) with a polyethylene glycol (PEG) residue of 2000 Da (DSPE-PEG2000), Lissamine-rhodamine-di-oleoyl-phosphatidylethanolamine (Liss-rhod-PE) were purchased from Avanti Polar Lipids (Alabaster, AL, USA). Gd-DTPA-bisstearylamide was purchased from Gateway chemical Technology Inc (St Louis, USA). A synthetic very potent selective agonist of the peripheral cannabisreceptor 2 (CB2-R), 4-(4-(1,1-Dimethylheptyl)-2,6-dimethoxyphenyl)-6,6-dimethyl-bicyclo(3.1.1)hept-2-ene-2-methanol)) (HU-308) was purchased from Alexis Biochemicals (San Diego, USA). NaCl, Na_2HPO_4 and NaH_2PO_4 were purchased from Merck (Darmstadt, Germany). Phosphate buffered saline (PBS, containing 8.2 g/L NaCl and 3 g/L Na_2HPO_4 and 0.33 g/L NaH_2PO_4 (pH 7.4)) was prepared. Magnevist (Gd-DTPA) (dimegluminegadopentetaat 469.01 mg/ml) was purchased from Schering Nederland B.V. (Weesp, Netherlands).

Preparation of micelles
CB2-R targeted and non-conjugated micelles
A mixture of the appropriate amounts of lipids (DSPE-PEG2000 (35M%), Gd-DTPA-bisstearylamide (50M%), Liss-rhod-PE (5M%) and HU-308 (10M%)), dissolved in chloroform, was dried by rotary evaporation at 55 ˚C. The lipid film was subsequently hydrated in 1 ml PBS, yielding a total lipid concentration of 10 mM, and Gd-DTPA-bisstearylamide concentration of 5 mM. HU-308 has a lipophilic chain of 7 carbon atoms

which has avidity for the micelle core, whereas the more hydrophilic methoxyphenyl and methanol groups will be located in the micelle corona. The more hydrophilic groups harbor the binding region for the CB2-R, however data published so far do not allow a detailed structure-activity relationship(23).

Control micelles were made similarly (DSPE-PEG2000 (45 M%)/Gd-DTPA-bisstearylamide (50 M%)/Liss-rhod-PE (5M%)).

Animal protocol and study setup
Experimental protocols were reviewed and approved by the Institutional Animal Care and Use Committee at Utrecht University Medical Center (Utrecht, the Netherlands) and were carried out in accordance with the standards established by the Dutch Animal Welfare Acts.

All knockout mice were backcrossed for 10 generations to the C57BL/6J genetic background. ApoE$^{-/-}$ and eNOS$^{-/-}$ mice (Jackson Laboratories, Bar Harbor, Me) were crossed to generate double heterozygous mice. These mice were then crossed and the offspring genotyped for eNOS and for apoE by polymerase chain reaction. Male apoE$^{-/-}$/eNOS$^{-/-}$ animals (aged 9-12 months) were used for experiments. After entry in the study protocol, they were fed for 4 weeks a high-fat high-cholesterol atherogenic diet containing 2.5% cholesterol (Arie Blok, Woerden, Netherlands).

Group 1 (4 teams of ~2 mice: n=9)
After positioning the mouse in a cradle, vital functions (heart rate and breathing frequency) were continuously recorded. Pre-injection MRI of the aorta was performed for team members, followed by injection of 200 μl CB2-R targeted micelles via the tail vein in the mouse which was measured last. MRI measurements were continued in this animal from t=8 minutes up to 24 hours, unless vital functions significantly deteriorated after which measurements were stopped. One hour after injection of this animal the team member in which pre-injection MRI was performed, was injected. Post-injection MRI measurements were executed from the time-point after injection of measurement stop in the team member till 48 hours post-injection. Finally, 4 episodes of 48 hours were covered with 4 teams. For a scheme of study setup, see figure 1. To fill the fourth episode of 48 hours in one team a third mouse was needed.

Group 2 (4 teams of ~2 mice: n=9)
Group 2 was treated similar to group 1, but instead of CB2-R targeted micelles control micelles were injected. Also in this group, in one team a third mouse was needed to complete the episode of 48 hours.

Group 3 (n=3)

Group3 was treated similar to groups 1 and 2, except for the facts that 60 μl Magnevist (Gd-DTPA, 4.69 mg/ml~ 5.0 mM) was injected and the follow-up MRI duration was up to 6 hours. This group served as a control group for the control micelles. So, the effect of the carrier itself, the micelle, on plaque uptake and residence time could be evaluated.

MRI protocol

Animal preparation and anesthesia

Mice were imaged in a vertical 9.4T, 89mm bore size magnet equipped with 1500 mT/m gradients and connected to an Avance 400 MR system (Bruker BioSpin, Germany) using a quadrature-driven birdcage coil with an inner diameter of 3 cm. Monitoring of and triggering on respiratory and cardiac movements were performed with a respiratory pad connected to a trigger unit (Rapid Biomedical, Rimpar, Germany). Inhalation anesthesia was provided with isoflurane. An intravenous catheter was inserted into the tail vein. A small eppendorf centrifuge tube filled with Magnevist (Gd-DTPA 5.0 mM) as an external reference was positioned left-sided to the mouse in the cradle (at the level of the right renal artery).
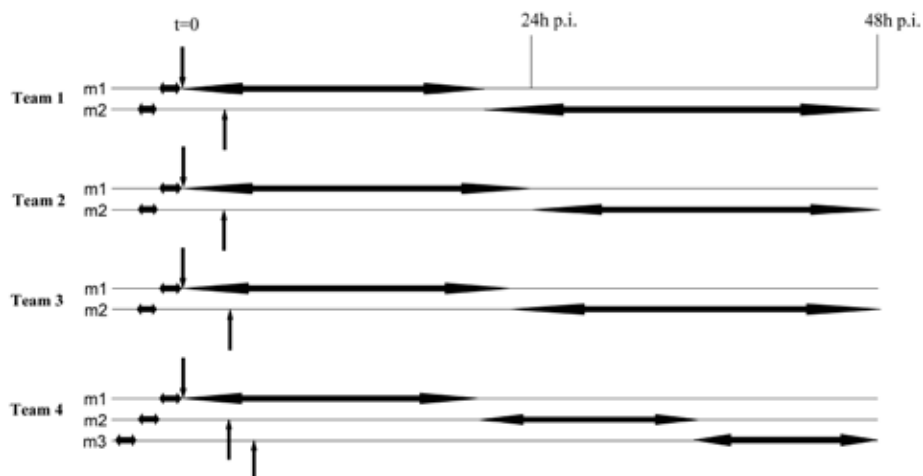

Figure 1. Scheme of study setup for group 1 or 2: 1 group contains 3 teams of 2 mice (m1 and m2) and 1 team of 3 mice, which cover 4 episodes of 48 hours per group. Horizontal arrows indicate start, duration and end of pre-and post-injection MRI measurements. Vertical arrows indicate injection of micelles at t=0 for mouse 1, t=1 hour for mouse 2 or t=2 hours for mouse 3.

Scout images

Fast Spin Echo (FSE) technique was used for axial scout images. Subsequently, coronal and saggital scout images of the suprarenal abdominal aorta were acquired. Twenty contiguous axial slices, perpendicular to coronal and saggital scout images, were planned from 4 mm below the right renal artery branch up to 5 mm above this branch.

Optimization of trigger delay

Signal acquisition was planned at the moment of maximal flow through the abdominal aorta. Hereto axial T1 weighted FSE (cardiac and respiratory gated) at the level of 1 mm above the right renal artery was repeated with varying trigger delay. Images were checked for laminar flow artifacts (bright vessel rims as a result of slow flow) and the diameter of the aortic lumen. Trigger delay corresponding with the image, which lacked flow artifacts and had the largest aortic diameter was chosen (optimized trigger delay) for other scans as described below.

Reference images for recognition of anatomic landmarks: small vessels, lymph nodes, delineation of plaque

Anatomic T2 weighted FSE axial reference images from 4 mm below the right renal artery branch up to 5 mm above were acquired. Diffusion weighted imaging sequence was used with diffusion gradient (b=400 s/mm^2) and with the same acquisition modules but zero diffusion (b=0 s/mm^2). These images were used for discrimination of peri-aortic lymph nodes (having low diffusion) usually found at 5 levels around the right renal artery branch (-1 up to +3 mm). A steady-state free precession technique was used for acquisition of non-triggered bright-blood images.

IR-FSE and FSE pre-injection images

For mice in which only IR-FSE was applied (group 1: n=4; group 2: n=6; group 3: n=3), this sequence was applied 5 times in order to define the standard deviation (SD) of the pre-injection signal intensity of plaque. For mice in which both IR-FSE and FSE were used (group 1: n=5; group 2: n=3), both sequences were applied 5 times in an interleaved fashion. For IR-FSE the acquisition scheme was started with an inversion pulse. The chosen trigger delay (TD) for IR-FSE was chosen in a way, that the equation (inversion time + TD)/(cardiac cycle duration) = integer + optimized TD was satisfied.

Contrast injection and post-injection IR-FSE and FSE

The cradle was removed from the magnet, contrast agent was injected via the intravenous catheter and the animal was repositioned in the magnet (or recovered from anesthesia). Scout scans were repeated to register a shift of the position of the aorta. An axial slice

package (20 slices) was oriented parallel to the transverse scout images of the aorta. T1 weighted scans were acquired every 15 minutes (interleaved IR-FSE and FSE or only IR-FSE). Duration of post-injection follow-up MRI has been mentioned before. The delay from injection of the contrast agent up to the start of post-injection MRI was 8-10 minutes.

MRI parameters

Anatomic T2 weighted FSE reference images

TR/TE=3500/28.9 ms, rare factor=8, sinc3 pulse 450 µs, excitation/refocusing flip angle=90˚/180˚, Spectral width=75757 Hz, Field of view (FOV)=30x30 mm^2, matrix=400x400 resulting in pixel dimension=75x75 µm^2, 20 axial slices, thickness=0.5 mm, chemical shift selective fat suppression, Number of Averages (NA)=15, zero fill acceleration factor 1.34, total acquisition time 32m22s.

Diffusion weighted images

TR/TE=2000/13.2 ms, hermite pulse 1.0 ms, excitation/refocusing flip angle=90˚/180˚, b value (longitudinal/z-axis) 0 or 400 s/mm^2, diffusion gradient duration 1.40 ms, separation 5.0 ms, Spectral width=50000 Hz, FOV=30x30 mm^2, matrix=256x256 resulting in a pixel dimension=117x117 µm^2, 1 axial slice, thickness=0.5 mm (at five levels around the right renal artery: -1 up to +3 mm), chemical shift selective fat suppression, NA=1, zero fill acceleration factor 1.9, total acquisition time 4m20s. Lymph nodes were discerned by calculation of the apparent diffusion coefficient: ADC=ln(S1-S2)/ΔB. S1 and S2 are the mean signal intensities on the image with b=0 and the image with b=400 s/mm^2, respectively, while Δb = 400-0=400 s/mm^2. If ADC was less than 1.8, the structure was identified as a lymph node.

Bright-blood images

TR/TE=150/1.75 ms, gauss pulse 500 µs, flip angle=90˚, Spectral width=166667 Hz, FOV=30x30 mm^2,
Matrix =256x256 resulting in a pixel dimension=117x117 µm^2, 20 axial slices, thickness=0.5 mm, NA=5, zero fill acceleration factor 1.34, total acquisition time 2m24s.

IR-FSE images

TR/TE=4000/15.14 ms, inversion time=1150 ms, rare factor=10, excitation/refocusing pulse gauss 1 ms, flip angle=90˚/180˚, Spectral width=75757 Hz, FOV=30x30 mm^2, matrix=200x200 resulting in a pixel dimension=150x150 µm^2, 20 axial slices, thickness=0.5 mm, chemical shift selective fat suppression, 2 inflow saturation slices (1

cranial (saturation of arterial inflow) and 1 caudal (saturation of venous inflow)), thickness 10 mm, NA=10, zero fill acceleration factor 1.7, total acquisition time 7m20s.

FSE images

TR/TE=1200/8.0 ms, rare factor=4, excitation/refocusing pulse hermite 1.2 ms, flip angle=90˚/180˚, Spectral width=200000 Hz, FOV=30x30 mm^2, matrix=256x256 resulting in a pixel dimension=117x117 μm^2, 20 axial slices, thickness=0.5 mm, chemical shift selective fat suppression, 2 inflow saturation slices (1 cranial (saturation of arterial inflow) and 1 caudal (saturation of venous inflow)), thickness 10 mm, NA=11, zero fill acceleration factor 1.92, total acquisition time 7m15s.

Harvesting and preparation of aortas

After 24 hours follow-up MRI or when vital functions deteriorated the animal was taken out of the magnet. Anesthesia was continued with a mixture of medetomidine (6%)/ ketamine (5%) (0.1 mL per 10 gram). The imaged part of the aorta was harvested after perfusion with PBS/formaldehyde 4% (9:1). The samples were stored in aluminium vials at -20 ºC until the ICP-MS procedure.

Quantification of Gd: ICP-MS

Gd-content was assessed in aortic samples (group1, n=8; group 2, n=8; group3, n=2). For technical reasons 3 aortic samples could not be analyzed. The samples were transferred to clean glass tubes. Tissue was digested in nitric acid. The amount of Gd was determined using ICP-MS (Philips Research, MiPlaza, Eindhoven, Netherlands). The amount of Gd present was determined by comparison with the intensities produced by standard solutions. The maximum inaccuracy in the amount of Gd is expected to be between 3-5%.

MRI data analysis

Aortic wall contours were manually traced on pre-injection T2 weighted images using software for data acquisition and processing (Paravision 4.0, Bruker-Biospin, Germany) (see figure 2 for example). Also circular regions of interest in representative areas of kidney, spleen, liver, lymph node and pre-vertebral skeletal muscle were drawn. These regions were copied to the five pre-injection and post-injection images and, when needed, slightly rotated and translated to fit relative distances to anatomic landmarks like right renal artery branch, vertebral spine, pre-vertebral muscle and peri-aortic lymph nodes. Relative signal intensities of plaque on pre- and post-injection images were defined as the signal intensity of plaque divided by the external reference. The values for the 5 baseline images were averaged. Normalized Enhancement Ratio (NER) was calculated as relative

signal intensity at a certain time point post-injection divided by averaged relative signal intensity pre-injection.

The plaques with highest NER were selected for further calculations. The NER after injection was averaged from 0 till 60 minutes, 60 till 120 minutes, and so on to obtain NER_{30min}, NER_{90min}, and so on for the whole covered time span. Graphs with NER (and standard deviation of measurements covering 1 hour) as a function of time were made in Excel Microsoft 2002. Visual inspection of these graphs revealed the plaque with highest NER per mouse. Plaques with highest NER were selected for further calculations as described in the next section.

Statistical Analysis

CB2-R targeted versus control micelles

For each team in group 1 and 2, NER_{plaque} determined from IR FSE images from 3 hour periods 4-6, 10-12, 16-18, 22-24, 28-30, 34-36, 40-42 and 46-48 hours post-injection were averaged. Team values were averaged per time-point and differences of averaged NER_{plaque} between group 1 and 2 for each of these time points were tested with an independent samples t-test. Also differences between NER of organs (kidney, spleen, liver, lymph node and skeletal muscle) were likewise tested at time points 4-6, 10-12, 22-24, 34-36 and 46-48 hours. Moreover differences between NER of organs and plaque at mentioned time points and pre-injection value (NER=1) were tested. For FSE images statistical tests for differences between groups were not executed, because less than 4 measurements were available per time point.

Relation between NER_{plaque} and Gd in aortic plaque

Correlation between final highest NER_{plaque} (averaged in 1 hour) and corresponding Gd-content, assessed by ICP-MS, was measured for IR-FSE and FSE. Pearson correlation coefficients were tested one-tailed. The higher the slope, the more sensitive the technique is to an increase in Gd-content. Secondly, for each mouse for which both IR-FSE and FSE were performed, the plaque with highest NER with IR-FSE and FSE was chosen and only the time point of 24 hours post-injection was analyzed. The pre-injection standard deviation (SD_0) was calculated as the standard deviation of the NER_{plaque} of the 5 pre-injection images. $NER_{24h}/(2xSD_0+1)$ was calculated for both imaging techniques. A value for the last ratio of more than one indicated that the NER at 24 hours was outside the 95% confidence interval of pre-injection NER ($p<0.05$). A higher averaged value for $NER_{24h}/(2xSD_0+1)$ for one of both techniques suggested also a higher sensitivity of this technique to a particular amount of Gd in that plaque. However, there was no external *ex vivo* validation. The number of plaques with $NER_{24h}/(2xSD_0+1)>1$ according to IR-FSE and FSE was assessed. A difference in this number suggested also a difference between the *in vivo* detection limits of Gd for these techniques.

Inter-Scan Variability (ISV)

Standard deviation of 4 consecutive measurements at 24 hours post-injection (SD_{24h}) was calculated. SD_{24h}/NER_{24h} is a measure of inter-scan variability (ISV) of NER_{plaque} scaled to the size of NER_{plaque}. A higher ratio indicated higher ISV.

Differences in $NER_{24h}/(2xSD_0+1)$, SD_{24h}/NER_{24h}, SD_0 and SD_{24h} were tested with a paired samples t-test. Significance was tested two-tailed. Moreover for each technique the number of mice with $NER_{24h}/(2xSD_0+1)>1$ was assessed.

Results

The contrast agent accumulated in plaque within 15 minutes after injection as validated by MRI. After a few hours lymph node and liver enhancement was observed, whereas kidney, spleen and pre-vertebral muscle did not show enhancement. Comparison of IR-FSE and FSE images with differences in NER, as a result of the difference in T1 contrast generating effect between the two techniques, is shown in Figure 2. Clearly seen is the lower overall plaque enhancement with the FSE technique when compared with the IR-FSE technique. Importantly, the FSE pre-injection images show higher signal than the IR-FSE pre-injection images (Figure 2, upper and third row).

Careful inspection of anatomic T2 weighted reference images suggested presence of peri-aortic lymph nodes at levels -1 up to +3 mm with respect to the right renal artery branch. Regions of interest drawn on this image were copied to the diffusion weighted image. For healthy lymph nodes an ADC of $1.15x10^{-3}$ mm^2/s has been reported[24]. In this study, we found ADC values of obvious mouse lymph nodes between $0.70x10^{-3}$ mm^2/s and $1.50x10^{-3}$ mm^2/s, whereas plaque regions had ADC higher than $2.5x10^{-3}$ mm^2/s. We think diffusion weighted imaging is a good technique for discrimination between aortic wall and peri-aortic lymph nodes.

CB2-R targeted versus control micelles

For IR-FSE images, differences of NER_{plaque} and NERorgan between groups 1 (CB2-R) and 2 (control) were tested. The NER_{plaque} in group1 remained stable around 1.9, whereas NER_{plaque} in group 2 decreased around 36 hours post-injection to achieve pre-injection values at t= 42 hours post-injection (42 hours: 1.95±0.29 versus 1.13±0.18 (p<0.05); 48 hours: 1.90±0.33 versus 1.22±0.15 (p<0.01), respectively) (Figure 3). NER_{plaque} in group 1 was higher than pre-injection values for all time points. NER_{plaque} in group 2 seemed to be higher than pre-injection values up to 36 hours, however with a large standard deviation. From 42 hours post-injection, NER_{plaque} in group 2 did not differ from the pre-injection

value. Group 3 (n=3) showed an increase of NER$_{plaque}$ post-injection to a peak level of 1.57±0.12 at 1.5 hours post-injection of Magnevist, returning to baseline level at 2.5 hours.
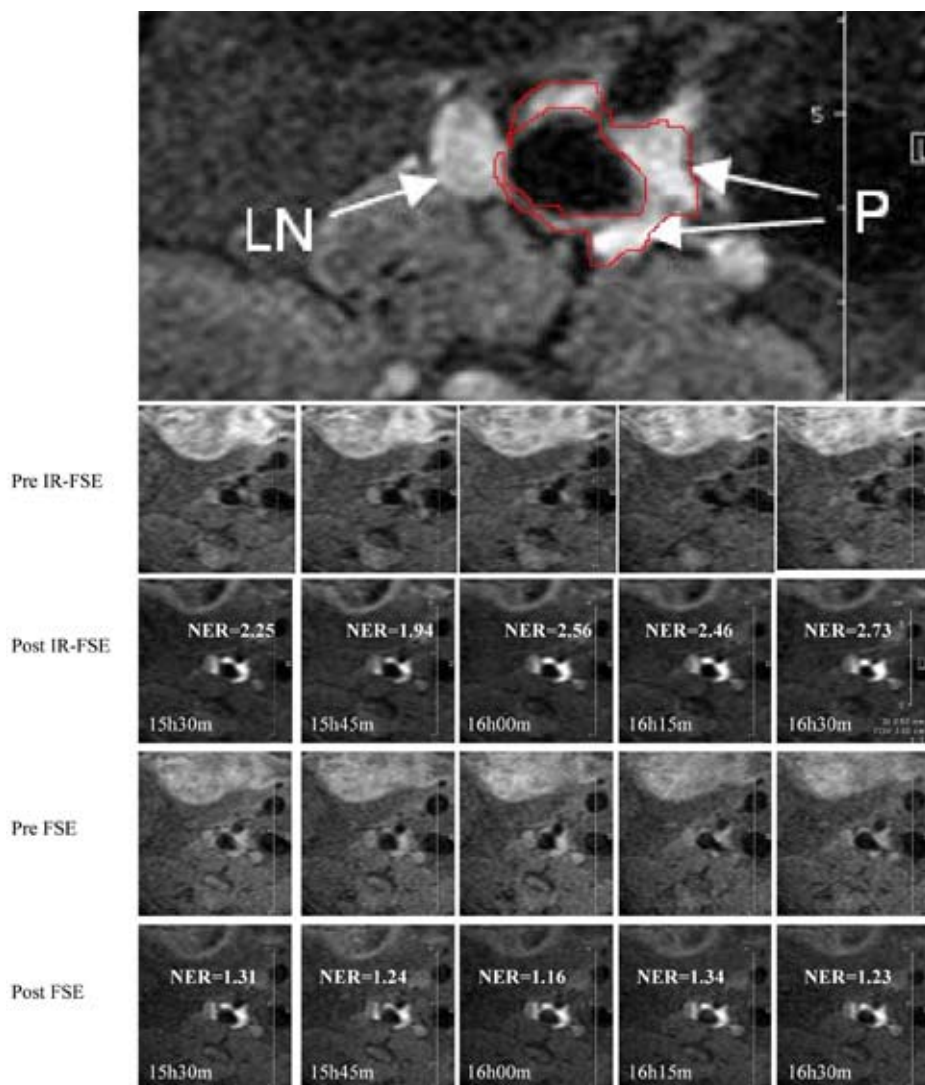

Figure 2. Variation in NER$_{plaque}$ around 16 hours after injection of CB2-R targeted micelles. The upper panel shows the anatomic T2 weighted reference image. The red line shows delineation of aortic wall/plaque. Five FSE and five IR-FSE images were acquired in an inter-leaved fashion. LN=lymph node; P=plaque.

NER$_{lymph\ node}$ increased after injection of CB2-R targeted micelles to ~1.3 at 12 hours post-injection and decreased to pre-injection values afterwards (Figure 4). NER$_{lymph\ node}$ did not increase after injection of control micelles. NER$_{liver}$ increased to ~1.5 at 24 hours after injection of CB2-R targeted micelles and decreased to pre-injection values later. Also after injection of control micelles NER$_{liver}$ seemed to increase a little bit with a peak level at 24 hours (~1.25). However, only at 12 and 24 hours after injection of CB2-R targeted micelles, NER$_{liver}$ was significantly higher than pre-injection. NER of kidney, spleen and pre-vertebral muscle did not show a change after injection of CB2-R targeted or control micelles (Figure 4).

Relation between NER$_{plaque}$ and Gd in aortic plaque

Correlation between Gd content and final highest NER$_{plaque}$ (averaged from 4 measurements) was highly significant for both IR-FSE images (Pearson correlation coefficient=0.837; $p<0.001$) and FSE images (Pearson correlation coefficient=0.663; $p<0.05$). The slope of the regression line was approximately 10 times higher for the IR-FSE technique when compared to the FSE technique (0.20 versus 0.022, with estimated standard errors of 0.03 and 0.015 respectively), indicating that the IR-FSE technique is more sensitive to an increased amount of Gd (Figure 5).
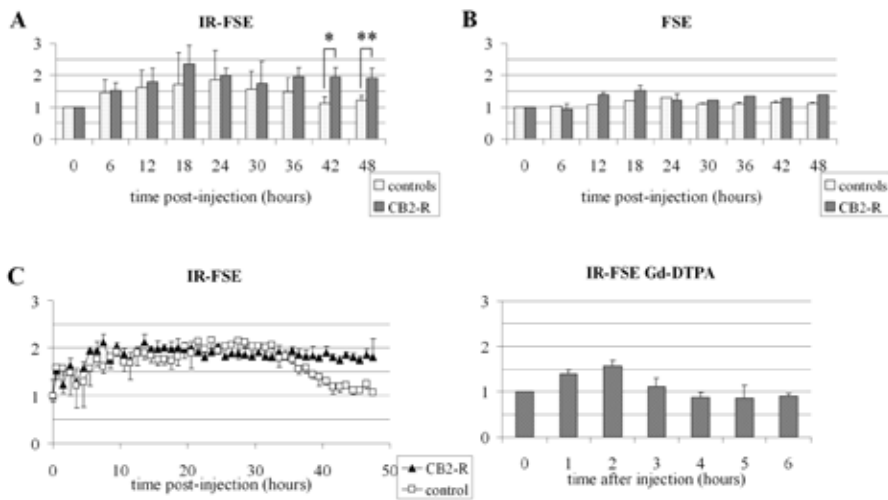

*Figure 3. NER of murine abdominal aortic plaque after injection of CB2-R targeted and control micelles determined on IR FSE images (A), and determined on FSE images (n=1 or n=2) (B). Also shown are typical examples of the course of NER determined on IR FSE images in a team of between 0 and 48 hours after injection of CB2-R targeted or control micelles (C). NER of murine abdominal aortic plaques during the first 6 hours after injection of Gd-DTPA (Magnevist) is also shown (n=3) (D). Whiskers show SD within each hour. *p<0.05; **p<0.01.*

Table 1. Sensitivity and ISV of IR-FSE and FSE for detection of enhancement of plaque

	IR FSE					SE				
Mouse	NER_{24h}	SD_0	SD_{24h}	Sens	ISV	NER_{24h}	SD_0	SD_{24h}	Sens	ISV
G1-1	1.72	0.26	0.26	1.13	0.15	1.03	0.11	0.06	0.85	0.06
G1-2	1.29	0.33	0.33	0.78	0.25	1.31	0.05	0.20	1.18	0.15
G1-3	1.63	0.15	0.11	1.25	0.07	1.18	0.14	0.02	0.92	0.02
G1-4	1.63	0.14	0.05	1.28	0.03	0.96	0.08	0.08	0.83	0.08
G1-5	2.11	0.15	0.12	1.63	0.05	1.36	0.02	0.08	1.31	0.06
G2-1	1.07	0.09	0.11	0.90	0.11	1.32	0.08	0.05	1.13	0.04
G2-2	1.93	0.08	0.13	1.65	0.07	1.61	0.04	0.05	1.50	0.03
G2-3	2.28	0.14	0.07	1.78	0.03	0.99	0.08	0.08	0.85	0.08
AVG±SD	1.71 ±0.39	0.17 ±0.08*	0.15 ±0.10*	1.30 ±0.36	0.09 ±0.07	1.22 ±0.22	0.08 ±0.04*	0.08 ±0.05*	1.07 ±0.25	0.06 ±0.04

*AVG=average; Sens=sensitivity of the technique to detect enhancement= $NER_{24h}/(2xSD_0+1)$. ISV= Inter-Scan Variability= SD_{24h}/NER_{24h}. *Differences between groups 1 and 2: p<0.05.*
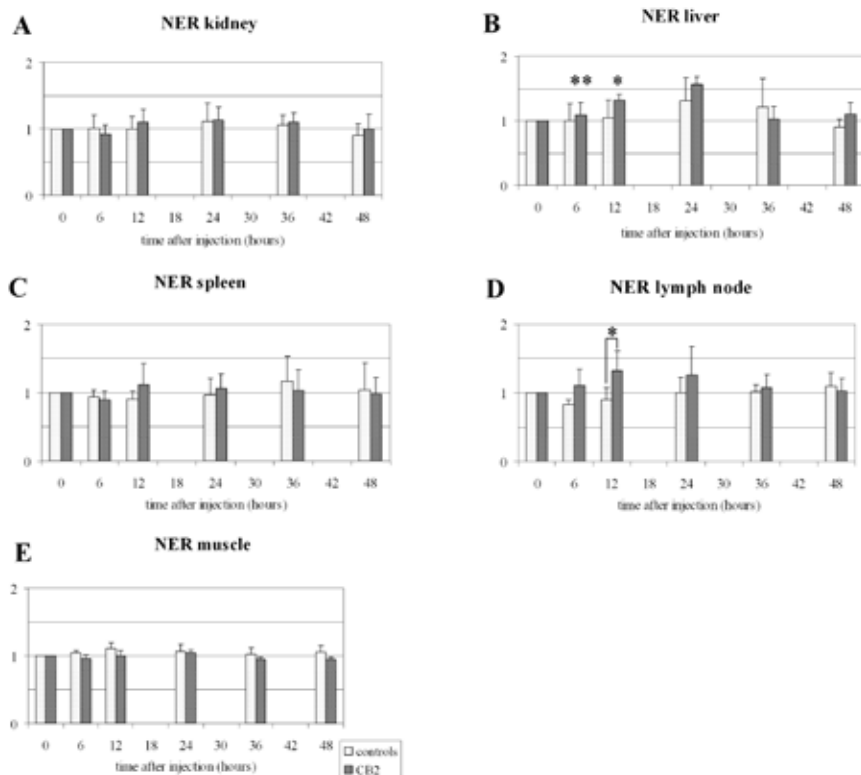

*Figure 4. NER determined on IR-FSE images of murine kidney (A), liver (B), spleen (C), lymph node (D) and pre-vertebral muscle (E) after injection of CB2-R targeted and control micelles. *p<0.05; **p<0.01 (B: one samples t-test (test value=1; D: independent samples t-test)*

This was supported by calculations of $NER_{24h}/(2 \times SD_0+1)$, which is only a surrogate measure of the sensitivity of the technique. IR-FSE showed higher ratios when compared to FSE, however differences were not significant (IR-FSE: 1.30±0.36; FSE: 1.07±0.25) (p=0.146) (Table 1). At 24 hours highest NER_{plaque} represented a significant increase of plaque signal intensity ($NER_{24h}/(2 \times SD_0+1) > 1$) in 6 of 8 mice with IR-FSE, while only in 4 of 8 mice highest NER_{plaque} with FSE represented a significant increase of plaque signal intensity. This observation supports the findings with *ex vivo* Gd measurements and point to a lower *in vivo* detection limit of gadolinium for IR-FSE when compared to FSE.

Inter-Scan Variability (ISV)

The ISV may be best examined by calculation of SD_{24h}/NER_{24h}. SD_0 and SD_{24h} were significantly lower with FSE technique than with IR-FSE (SD_0: 0.08±0.04 versus 0.17±0.08, respectively; SD_{24h}: 0.08±0.05 versus 0.15±0.10, respectively (p<0.05)). There

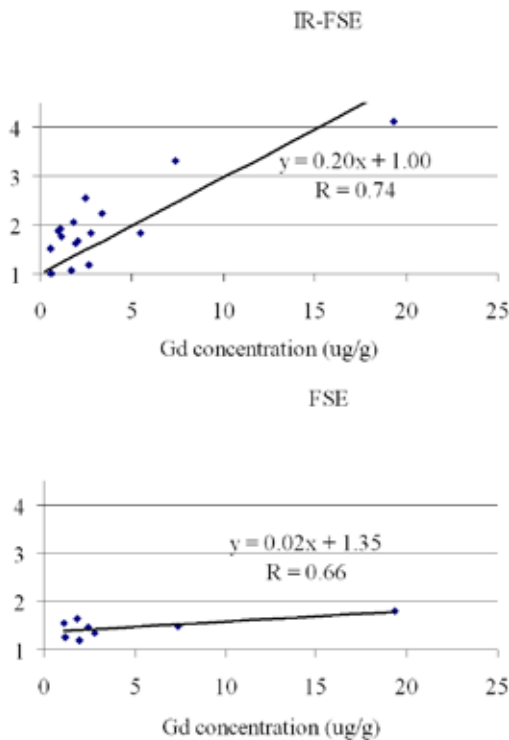*Figure 5. Correlation plot of Gd content of 18 mouse aortas (group 1, n=7; group 2, n=9; group 3, n=2) assessed with ICP-MS and corresponding highest NER_plaque on IR-FSE images (averaged from final 1 hour alive). The correlation was also executed on highest NER_plaque on FSE images when available (n=8).*

was a tendency to a lower SD_{24h}/NER_{24h} measured with FSE when compared to IR-FSE (9±7 % versus 6±4%) (p=0.169). An example of the large ISV of plaque enhancement with IR-FSE is shown in Figure 6. In this case the ISV of the FSE technique is lower, but NER_{plaque} is hardly increased when compared to the pre-injection value (Figure 6B). The large ISV, when IR-FSE is applied, is not observed in larger organs like liver, muscle and kidney (Figure 6D-E). On the other hand, peri-aortic lymph nodes also revealed large ISV (Figure 6C).

High ISV of NER_{plaque} is also visible on the IR-FSE images (Figure 2). A large difference between lowest NER_{plaque} and highest NER_{plaque} is observed for IR-FSE images (Figure 2, post IR-FSE row second panel and fifth panel, respectively).
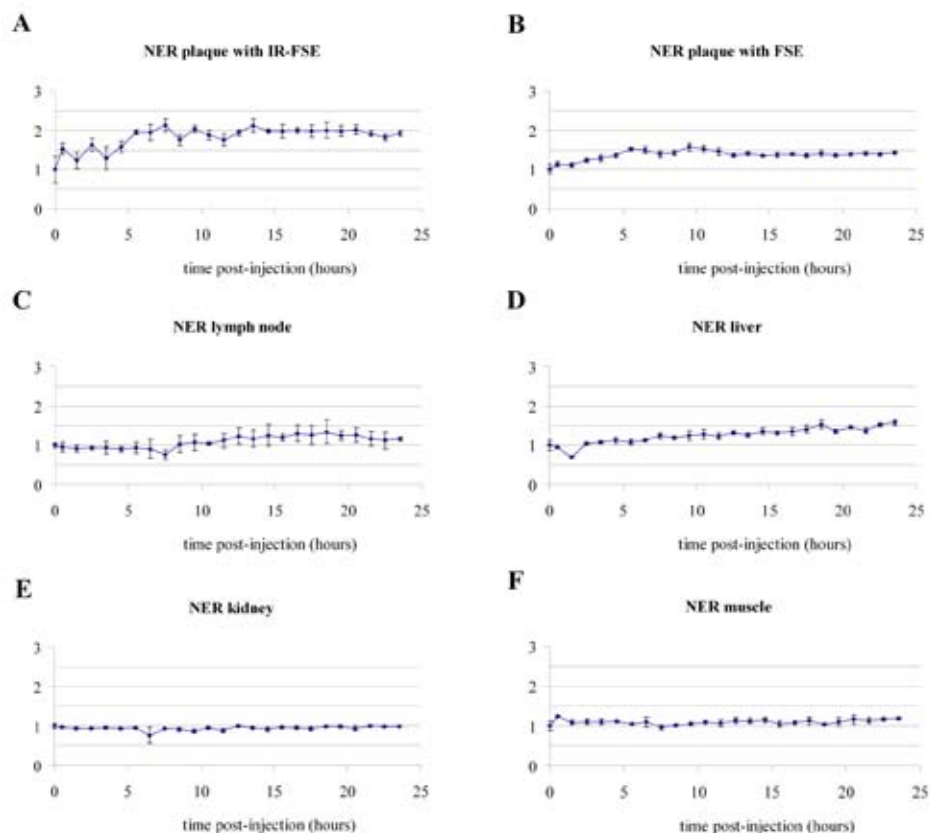
Figure 6. NER_{plaque} determined on IR-FSE and FSE as a function of time. A typical example (also shown in Figure 1C) of higher ISV of NER_{plaque} for IR-FSE (A) than for FSE (B) is shown. For IR-FSE images also NER of some organs during time after injection of CB2-R targeted micelles is shown. Notice the higher ISV of $NER_{lymph node}$ (C) when compared to ISV of NER_{liver} (D), NER_{kidney} (E) and $NER_{pre-vertebral muscle}$ (F).

Discussion

The main findings of this study are: 1. CB2-R targeted micelles show enhancement for a longer period in apoE$^{-/-}$/eNOS$^{-/-}$ mouse atherosclerotic plaque than control micelles, as shown by magnetic resonance IR-FSE imaging, 2. the increase of plaque signal intensity at similar increase of Gd content measured with IR-FSE is higher than the increase of plaque signal intensity measured with FSE, 3. the ISV was higher for IR-FSE than for FSE. The results of this study are highly relevant to the design of future studies concerning molecular MRI of atherosclerotic plaque in mice with targeted paramagnetic micelles.

Plaque enhancement did not differ between mice treated with atherosclerosis-targeted and control micelles until 36 hours post-injection. At 36 hours post-injection, plaque enhancement diverged between control and positive targeted micelles, and became more evident and consistent at 42 and 48 hours post-injection. However, at earlier time points, NER did not differ consistently between mice treated with CB2 targeted micelles and mice treated with control micelles. Another *in vivo* MRI study reported a higher NER$_{plaque}$ at 1 hour after injection of macrophage targeting micelles when compared to control micelles(1). Also 24 hours after injection of targeted molecular probes which recognize oxidation-specific epitopes, plaque enhancement was reported to be increased compared to non-targeted micelles(17). We used micelles which target another epitope on plaque macrophages. We cannot exclude that temporal signal enhancement may vary among molecular targets. In this study, the variability of NER$_{plaque}$ between mice within groups, treated with CB2-R targeted and control micelles, was remarkably large during the first 30 hours. An explanation for this variability could be large biological differences of inflammation within the group. This may lead to varying endothelial fenestration sizes leading to faster or slower wash-in kinetics of plaque. NER$_{plaque}$ in mice treated with control micelles apparently decreased 30 hours post-injection, accompanied by decreasing variability. The concentration of micelles in the blood decays and so does the concentration gradient of micelles between blood and plaque. Below a critical blood concentration, no more net plaque uptake will take place, whereas the wash-out process prevails. In mice treated with CB2-R targeted micelles, one would expect that NER$_{plaque}$ remains stable for a longer period when compared to mice treated with control micelles. Because highly variable wash-in kinetics does not contribute to the NER anymore, variability of NER$_{plaque}$ decreases after the blood concentration has decreased below a critical value. Further insights in general pharmacokinetics and biodistribution of nanoparticles are found in literature(16), however blood-clearance kinetics should still be evaluated for these CB2-R targeted and control micelles.

In our study, peak NER$_{plaque}$ in mice, treated with Magnevist (Gd-DTPA), was attained at

1.5 hours and returned to pre-injection values at 2.5 hours post-injection. In contrast with NER_{plaque} in mice treated with Magnevist, NER_{plaque} in mice treated with control micelles showed a prolonged stay up to 36 hours post-injection. The early drop to pre-injection value of NER_{plaque} in mice, treated with Magnevist, is in accordance with earlier reported results[1].

We found that plaque signal intensity increase accompanied by the same increase of aortic Gd content was higher for IR-FSE when compared to FSE. Approximately only 66% of the plaques with a NER value significantly higher than the pre-injection value according to IR-FSE images, had a NER value which was higher than pre-injection according to FSE images. The slope of the regression line of the correlation plot between aortic Gd content and NER_{plaque} was approximately ten times higher for IR-FSE images than for FSE images. Though data in this study fitted best to a linear function, relation between NER_{plaque} and Gd does not need to be linear. However, a linear relation is expected to exist between inverse T1 and Gd. Effective decrease of the MR signal of non-enhanced aortic wall by choosing a suitable inversion time determines the efficiency of IR-FSE for depiction of T1 contrast between tissues. In contrast to our results, Briley-Saebo et al. reported nice enhancement ratios with the FSE technique, similar to the FSE technique in this study, after injection of micelles targeting oxidation-specific epitopes[17]. The difference in injection dose could explain the different observations. Briley-Saebo et al. injected 0.075 mmol Gd/kg whereas we injected 0.033 mmol Gd/kg. The modification of the FSE technique in this study are: TR=1200 ms and FA=90° instead of TR=600 ms and FA=30°[17], but these differences will lead to approximately comparable T1 contrast. Another explanation could be a difference in quenching of the relaxation enhancement of contrast agent after internalization in the macrophage[25-27]. With *in vitro* fluorescence microscopy we showed that CB2-R targeted micelles were internalized by CB2-R over-expressing CHO cells[20]. Other studies have shown that intracellular compartmentalization of Gd (vesicle compartments) could lead to quenching of relaxivity of the Gd containing contrast agent[25-27]. However, the intracellular destiny of neither the CB2-R targeted nor the oxidation-specific epitope targeting micelles is known.

Molecular MRI is generally hampered by a low sensitivity for the presence of molecular markers[28]. Successful contrast-enhanced MRI needs μM-mM concentrations of the molecular marker of interest[28]. So, the most sensitive technique for visualization of a molecular plaque marker, often in the nM-μM range, is desirable. In this study, IR-FSE was more sensitive to an increase of Gd-content when compared to FSE.

In this study, the FSE technique tended to have lower ISV. An explanation for the tendency of a lower ISV for FSE when compared to IR-FSE could be complication of the "real trigger delay". The use of cardiac-gated MRI for visualization of abdominal aortic wall

has not been reported so far, to our knowledge. However, we think that triggering on vessel motion is important for better image quality and recognition of lymph nodes. The position and dilation of the aorta and small organs embedded together with the aorta in connective tissue (like peri-aortic lymph nodes) will be influenced by pulsating flow. Therefore, in this study not only NER_{plaque} but also $NER_{lymph\ node}$ values show larger inter-scan variability.

Further, we think that inadequacy in setting the real trigger delay for the IR-FSE technique could lead to higher ISV. The long inversion time could explain this inadequacy. For IR-FSE the inversion time was 1150ms. The next trigger is followed by this inversion time + echo time, which is much longer than 1 cardiac cycle. The cardiac cycle duration could vary during this long inversion time, which will lead to some shift of the acquisition within the cardiac cycle. For FSE the next trigger is followed by the echo time, which is much shorter than 1 cardiac cycle. So no shift of the acquisition within the cardiac cycle will occur. Actually, during the experiments we observed minor arrhythmias that caused variation of cardiac cycle duration. The IR-FSE images suffered more from these arrhythmias than FSE images, which is in support of the mentioned explanation. From this theory we can understand also that averaging IR-FSE images before calculation of NER_{plaque} will not solve the problem of the larger ISV. However, averaging NER_{plaque} calculated on repeated scans will decrease the chance of false positive and false negative results.

Immunomicelles are made by conjugation of specific antibodies to the micellar corona (of PEG for example)(2,29). We expect that biodistribution and pharmacokinetics of antibody-conjugated micelles highly depend on immunogenic response elucidated by the bound protein. Clearance of antibody-conjugated micelles from the blood is expected to be faster than for non-conjugated micelles. As a result of the prolonged circulation time, residence of non-conjugated micelles in micelle-excreting organs will be prolonged. However, the residence time of non-conjugated micelles in the plaque is expected to be lower due to lack of specific binding. We have used a small lipophilic agonist, which is non-covalently bound to the lipophilic core without modification of PEG groups forming the corona. Therefore, we believe that our micelles containing lipophilic agonist are similar in immunogenicity to non-conjugated micelles. We found a significant elevation of NER_{liver} at 12 and 24 hours after injection of CB2-R targeted micelles. Antibody-conjugated micelles, targeting oxidation-specific epitopes in plaque, and non-conjugated micelles were also found to be predominantly cleared by the liver, however with peak accumulation of gadolinium at 48 hours after injection(17). In the mentioned study, however, the concentration of gadolinium in the liver was measured with ICP-MS, whereas we measured NER_{liver} changes post-injection.

Study Limitations

We were only able to find a tendency to a larger ISV in IR-FSE images when compared to FSE images. Probably a statistic significant difference was found, when more animals would be studied with both techniques.

Conclusions

The present study shows *in vivo* aortic plaque enhancement after injection of specific plaque targeted and control Gd containing micelles in an atherosclerotic mouse model. In mice treated with CB2-R targeted micelles aortic plaque enhancement was significantly higher at 42 and 48 hours post-injection than in mice treated with control micelles. Plaque signal intensity increase accompanied by the same increase of aortic Gd content was higher for IR-FSE when compared to FSE. On the other hand, ISV tended to be higher with IR-FSE due to complication of triggered acquisition when compared to FSE. Therefore, we recommend the acquisition of repeated IR-FSE scans and averaging of NER_{plaque} for optimization of contrast enhancement of atherosclerotic plaque.

Reference List

1. Amirbekian V, Lipinski MJ, Briley-Saebo KC, Amirbekian S, Aguinaldo JG, Weinreb DB, Vucic E, Frias JC, Hyafil F, Mani V, Fisher EA, Fayad ZA. Detecting and assessing macrophages *in vivo* to evaluate atherosclerosis noninvasively using molecular MRI. Proc Natl Acad Sci U S A 2007; 104: 961-966.

2. Lipinski MJ, Amirbekian V, Frias JC, Aguinaldo JG, Mani V, Briley-Saebo KC, Fuster V, Fallon JT, Fisher EA, Fayad ZA. MRI to detect atherosclerosis with gadolinium-containing immunomicelles targeting the macrophage scavenger receptor. Magn Reson Med 2006; 56: 601-610.

3. Lancelot E, Amirbekian V, Brigger I, Raynaud JS, Ballet S, David C, Rousseaux O, Le GS, Port M, Lijnen HR, Bruneval P, Michel JB, Ouimet T, Roques B, Amirbekian S, Hyafil F, Vucic E, Aguinaldo JG, Corot C, Fayad ZA. Evaluation of matrix metalloproteinases in atherosclerosis using a novel noninvasive imaging approach. Arterioscler Thromb Vasc Biol 2008; 28: 425-432.

4. Cormode DP, Briley-Saebo KC, Mulder WJ, Aguinaldo JG, Barazza A, Ma Y, Fisher EA, Fayad ZA. An ApoA-I mimetic peptide high-density-lipoprotein-based MRI contrast agent for atherosclerotic plaque composition detection. Small 2008; 4: 1437-1444.

5. Mulder WJ, Strijkers GJ, Briley-Saboe KC, Frias JC, Aguinaldo JG, Vucic E, Amirbekian V, Tang C, Chin PT, Nicolay K, Fayad ZA. Molecular imaging of macrophages in atherosclerotic plaques using bimodal PEG-micelles. Magn Reson Med 2007; 58: 1164-1170.

6. Briley-Saebo KC, Amirbekian V, Mani V, Aguinaldo JG, Vucic E, Carpenter D, Amirbekian S, Fayad ZA. Gadolinium mixed-micelles: effect of the amphiphile on *in vitro* and *in vivo* efficacy in apolipoprotein E knockout mouse models of atherosclerosis. Magn Reson Med 2006; 56: 1336-1346.

7. Cornily JC, Hyafil F, Calcagno C, Briley-Saebo KC, Tunstead J, Aguinaldo JG, Mani V, Lorusso V, Cavagna FM, Fayad ZA. Evaluation of neovessels in atherosclerotic plaques of rabbits using an albumin-binding intravascular contrast agent and MRI. J Magn Reson Imaging 2008; 27: 1406-1411.

8. Winter PM, Morawski AM, Caruthers SD, Fuhrhop RW, Zhang H, Williams TA, Allen JS, Lacy EK, Robertson JD, Lanza GM, Wickline SA. Molecular imaging of angiogenesis in early-stage atherosclerosis with alpha(v)beta3-integrin-targeted nanoparticles. Circulation 2003; 108: 2270-2274.

9. Frias JC, Ma Y, Williams KJ, Fayad ZA, Fisher EA. Properties of a versatile nanoparticle platform contrast agent to image and characterize atherosclerotic plaques by magnetic resonance imaging. Nano Lett 2006; 6: 2220-2224.

10. Lobbes MB, Miserus RJ, Heeneman S, Passos VL, Mutsaers PH, Debernardi N, Misselwitz B, Post M, Daemen MJ, van Engelshoven JM, Leiner T, Kooi ME. Atherosclerosis: contrast-enhanced MR imaging of vessel wall in rabbit model--comparison of gadofosveset and gadopentetate dimeglumine. Radiology 2009; 250: 682-691.

11. Chen W, Vucic E, Leupold E, Mulder WJ, Cormode DP, Briley-Saebo KC, Barazza A, Fisher EA, Dathe M, Fayad ZA. Incorporation of an apoE-derived lipopeptide in high-density lipoprotein MRI contrast agents for enhanced imaging of macrophages in atherosclerosis. Contrast Media Mol Imaging 2008; 3: 233-242.

12. Zheng J, Ochoa E, Misselwitz B, Yang D, El N, I, Woodard PK, Abendschein D. Targeted contrast agent helps to monitor advanced plaque during progression: a magnetic resonance imaging study in rabbits. Invest Radiol 2008; 43: 49-55.

13. Kawahara I, Morikawa M, Honda M, Kitagawa N, Tsutsumi K, Nagata I, Hayashi T, Koji T. High-resolution magnetic resonance imaging using gadolinium-based contrast agent for atherosclerotic carotid plaque. Surg Neurol 2007; 68: 60-65.

14. Sirol M, Itskovich VV, Mani V, Aguinaldo JG, Fallon JT, Misselwitz B, Weinmann HJ, Fuster V, Toussaint JF, Fayad ZA. Lipid-rich atherosclerotic plaques detected by gadofluorine-enhanced *in vivo* magnetic resonance imaging. Circulation 2004; 109: 2890-2896.

15. Barkhausen J, Ebert W, Heyer C, Debatin JF, Weinmann HJ. Detection of atherosclerotic plaque with Gadofluorine-enhanced magnetic resonance imaging. Circulation 2003; 108: 605-609.

16. Neubauer AM, Sim H, Winter PM, Caruthers SD, Williams TA, Robertson JD, Sept D, Lanza GM, Wickline SA. Nanoparticle pharmacokinetic profiling *in vivo* using magnetic resonance imaging. Magn Reson Med 2008; 60: 1353-1361.

17. Briley-Saebo KC, Shaw PX, Mulder WJ, Choi SH, Vucic E, Aguinaldo JG, Witztum JL, Fuster V, Tsimikas S, Fayad ZA. Targeted molecular probes for imaging atherosclerotic lesions with magnetic resonance using

antibodies that recognize oxidation-specific epitopes. Circulation 2008; 117: 3206-3215.

18. Steffens S, Veillard NR, Arnaud C, Pelli G, Burger F, Staub C, Karsak M, Zimmer A, Frossard JL, Mach F. Low dose oral cannabinoid therapy reduces progression of atherosclerosis in mice. Nature 2005; 434: 782-786.

19. Mach F, Steffens S. The role of the endocannabinoid system in atherosclerosis. J Neuroendocrinol 2008; 20 Suppl 1:53-7.: 53-57.

20. Te Boekhorst, B. C., Rodriguez-Feo, J., Bovens, S. M. De Kroon T. I., Cramer, M. J., Pasterkamp, G., Doevendans, P. A., and Van Echteld, C. J. Characterization of micelle-based contrast agent targeting peripheral cannabis receptors and its potential use for atherosclerotic plaque visualization by MRI. 9 2, 256-257. 1-3-2007. Ref Type: Abstract

21. Mitchell DG. Preparatory Pulses, Including Fat Suppression. MRI principles. Philadelphia, Pennsylvania, USA: Saunders, 2004; 177-198.

22. Kuhlencordt PJ, Gyurko R, Han F, Scherrer-Crosbie M, Aretz TH, Hajjar R, Picard MH, Huang PL. Accelerated atherosclerosis, aortic aneurysm formation, and ischemic heart disease in apolipoprotein E/endothelial nitric oxide synthase double-knockout mice. Circulation 2001; 104: 448-454.

23. Hanus L, Breuer A, Tchilibon S, Shiloah S, Goldenberg D, Horowitz M, Pertwee RG, Ross RA, Mechoulam R, Fride E. HU-308: a specific agonist for CB(2), a peripheral cannabinoid receptor. Proc Natl Acad Sci U S A 1999; 96: 14228-14233.

24. Kwee TC, Takahara T, Luijten PR, Nievelstein RA. ADC measurements of lymph nodes: Inter- and intra-observer reproducibility study and an overview of the literature. Eur J Radiol 2009.

25. Terreno E, Geninatti CS, Belfiore S, Biancone L, Cabella C, Esposito G, Manazza AD, Aime S. Effect of the intracellular localization of a Gd-based imaging probe on the relaxation enhancement of water protons. Magn Reson Med 2006; 55: 491-497.

26. Strijkers GJ, Hak S, Kok MB, Springer CS, Jr., Nicolay K. Three-compartment T1 relaxation model for intracellular paramagnetic contrast agents. Magn Reson Med 2009; 61: 1049-1058.

27. Kok MB, Hak S, Mulder WJ, van der Schaft DW, Strijkers GJ, Nicolay K. Cellular compartmentalization of internalized paramagnetic liposomes strongly influences both T1 and T2 relaxivity. Magn Reson Med 2009; 61: 1022-1032.

28. Massoud TF, Gambhir SS. Molecular imaging in living subjects: seeing fundamental biological processes in a new light. Genes Dev 2003; 17: 545-580.

29. Mulder WJ, Strijkers GJ, van Tilborg GA, Griffioen AW, Nicolay K. Lipid-based nanoparticles for contrast-enhanced MRI and molecular imaging. NMR Biomed 2006; 19: 142-164.

Evaluation of infarcted murine heart function: Comparison of prospectively triggered with self-gated MRI

Sandra M. Bovens [1,2] [*], Bernard C.M. te Boekhorst [1*], Krista den Ouden [1], Kees W.A. van de Kolk [1], Arno Nauerth 3, Marcel G.J. Nederhoff [1,2], Gerard Pasterkamp [1], Michiel ten Hove [1] and Cees J.A. van Echteld [1#]

[1] Department of Cardiology, University Medical Center, Utrecht, The Netherlands, [2] Interuniversity Cardiology Institute of the Netherlands (ICIN), Utrecht, The Netherlands, [3] Bruker BioSpin MRI GmbH, Ettlingen, Germany, [#] Present address: Novartis Institutes for Biomedical Research, Translational Sciences, Biomarker Development, Basel, Switzerland, [*] Authors contributed equally to this study

Abstract

Background

Measurement of cardiac function is often performed in mice after, e.g., a myocardial infarction (MI). Cardiac magnetic resonance imaging (MRI) is often used, because it is noninvasive and provides high temporal and spatial resolution for the left- as well as the right ventricle. In animal cardiac MRI, the quality of the ECG signal is variable and sometimes deteriorates over time, especially with infarcted hearts or cardiac hypertrophy. Therefore we compared the self-gated IntraGateFLASH method with a prospectively triggered FLASH method in mice with myocardial infarcts (MI) (n=16) as well as control mice (n=21).

Methods

Mice with an MI and control mice were imaged in a vertical 9.4T MR system. Images of contiguous 1mm slices were acquired from apex to base with prospective- and self-gated methods. Data were processed to calculate cardiac function parameters for the left- and right ventricle. Signal-to-noise ratio (SNR) and contrast-to-noise ratio (CNR) were calculated in mid-ventricular slices.

Results

The SNR and CNR of the self-gated data were higher than the SNR and CNR of the prospectively gated data. Differences between the two gating methods in the cardiac function parameters for both left- and right ventricle (e.g. end-diastolic volumes) did not exceed the inter-observer variability in the control mice or in the MI mice. Using more than 10 cardiac frames improved intra-observer variability.

Conclusion

Both methods give comparable results with regard to the cardiac function parameters in both healthy control mice and mice with MIs. Moreover, the self-gated method provides better SNR and CNR when the acquisition time is equal. In conclusion, the self-gated method is suitable for routine use in cardiac magnetic resonance imaging in mice with an MI as well as in control mice, however in both gating methods the number of frames should be higher than 10 frames per cardiac cycle.

Introduction

Mice are widely used in models for cardiovascular diseases, due to the ability to knockout specific genes and the high reproduction rate(1-4). Assessment of cardiac function after a myocardial infarction (MI)(5) is often performed in mice with cardiac magnetic resonance imaging (CMR), because it is noninvasive and can provide high temporal and spatial resolution(2;6).

Electrodes attached to the (front) paws or tail of the animal, are used to record the ECG of the heart to obtain cardiac cine MR images without motion artifacts. In addition, a respiratory pad is placed under the chest to monitor the respiratory motion.

Prospective triggering is performed by synchronizing the image sampling with the cardiac cycle (cardiac triggering) and interrupting the image sampling during the respiratory period (respiratory gating), thus reducing motion artifacts(6;7). In animal CMR, the quality of the ECG signal is variable and sometimes deteriorates over time, especially in mice with an MI or cardiac hypertrophy.

Another method which can be used is retrospective gating, in which the ECG and respiratory data are stored together with the MRI data. During retrospective reconstruction of the images, data can be sorted to a particular cardiac phase and excluded when acquired during a specific respiratory phase(1). Recently, an alternative approach has been developed, which captures cardiac and respiratory motion measurements without sensors. The MR acquisition scheme of a FLASH sequence can be modified by postponing the read-out and phase-encoding gradients to the second echo; thus enabling the first echo for use as a navigator signal in the slice of interest. Due to cardiac and respiratory motion, different types of tissue move into the slice of interest, causing a change in MR signal(6). The duration of the navigator echo, which is determined by the number of navigator points, will affect the sampling time of motion information. However, this comes with an important trade-off: the signal intensity of the eventual image will decrease due to $T2^*$ decay with longer navigator echo duration.

This 'wireless' cardiac MRI, also called self-gated MRI, was first introduced by Spraggins(8) for human studies(9;10) and has been applied to studies using small rodents as well(4;6). The main benefit of this self-gated method is that electrodes or a respiratory pad are unnecessary for triggering purposes.

The goal of this study is to evaluate the quality of the self-gated method and whether this method can be used for routine cardiac cine MRI in healthy control mice and mice with an MI. Additionally, the influence of different navigator durations (number of navigator points) and number of cardiac frames will be evaluated.

Experimental

MRI method

Mice were imaged in a vertical 9.4T, 89mm bore size magnet equipped with 1500 mT/m gradients and connected to an Avance 400 MR system (Bruker BioSpin, Germany) using a quadrature-driven birdcage coil with an inner diameter of 3 cm. ParaVision 4.0 software (Bruker BioSpin, Germany) was used for cine MR acquisition and reconstruction. For the self-gated method, IntraGate software (Bruker BioSpin, Germany) linked to ParaVision 4.0 was used. All MR sequences started with a steady-state preparation using dummy scans for at least 5 seconds and all cine MR images were acquired using a cine Fast Low Angle SHot (FLASH) sequence. A navigator echo was added in the self-gated sequence (IntraGateFLASH).

IntraGateFLASH

For gathering information on the cardiac- and respiratory motion the read-out- and phase-dephase gradient were separated from the slice refocusing gradient in order to detect half an echo without phase encoding. The navigator is derived from the selectively excited slice. The number of navigator points collected during the first echo determines the duration of the navigator. If a low number of navigator points is chosen, the TE becomes shorter, but less information about the cardiac- and respiratory motion is derived. The MR scheme of the IntraGateFLASH sequence, with a short (A) and long (B) navigator (nav.), is shown in figure 1.
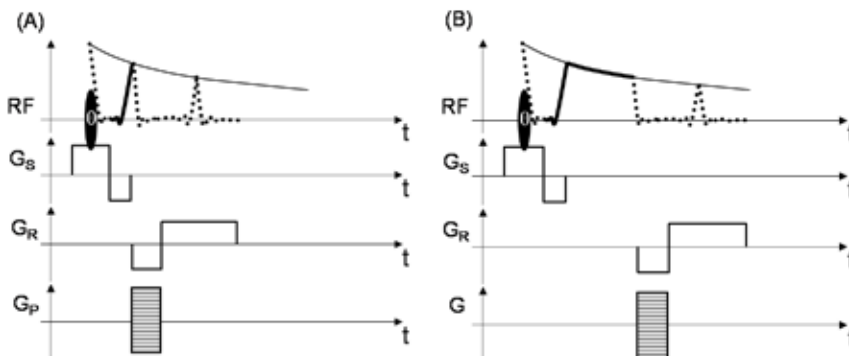

Figure 1: IntraGateFLASH sequence with a small number (A) or a large number (B) of navigator points. Black oval shape: RF pulse with flip angle θ; thick solid line: navigator; dotted line: echo; Gs: slice-selection gradient; Gr: read-out gradient; Gp: phase encoding gradient

There is one phase-encoding step per repetition time independent of the heart rate (Figure 2). Retrospectively, four primary signals are calculated from the navigator echo by the IntraGate program and subsequently analyzed and weighted according to their contribution to a respiratory and a cardiac signal(6). A mark is set on the minimum or maximum of the cardiac motion of every heart beat. The time between two marks is divided into the number of frames to reconstruct, for example 10 or 20. Data with different but contiguous k-space encodings are clustered and assigned to the correct frame (figure 2: for simplification only four cardiac frames are shown). The data acquired during respiratory motion are excluded and a cine MR image is reconstructed. The shared-phase option was also used. When using this option the time window per cardiac frame is chosen wider, resulting in a 50% overlap between each cardiac frame and the next, as well as an increase in number of averages.

MRI measurements

Mice were anesthetized with 5 vol% isoflurane in a 2:1 mixture of air (0.3 L/min) and oxygen (0.15 L/min). After the toe-pinch reflex had disappeared, the mouse was transferred to a home-build cradle and anesthesia was maintained with 1.5-2.5 vol% isoflurane. The cardiac and respiratory motion were monitored using a respiratory pad linked to an ECG/respiratory unit. When necessary the amount of isoflurane was adjusted during the experiment to keep the respiratory rate stable.

Healthy male BALB/c mice (Group A; n=11, weight 29.7 ± 2.0 gram) and male non-obese, diabetic, severe combined immunodeficient (NOD-SCID) mice with 90 (± 2) day old MIs

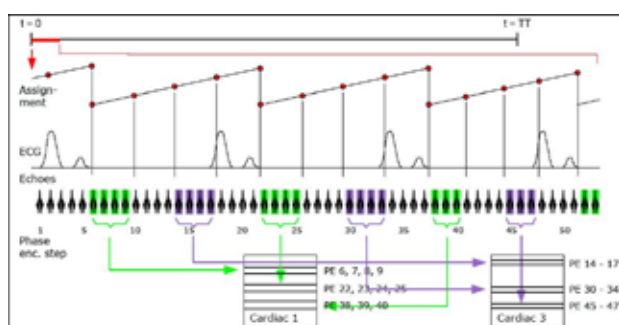*Figure 2: IntraGate reconstruction*
The start (t=0) of the total scan time (t=TT) is marked by a red line, and the assignment of the different phase encoding steps to the corresponding cardiac frame is shown. In this example 4 cardiac frames are reconstructed by IntraGate. The green phase encoding steps belong to the first cardiac frame; the purple phase encoding steps belong to the third cardiac frame.

(Group B; n=11, weight 30.4 ± 3.1 gram) were examined with both prospectively triggered and self-gated, using a long navigator, cardiac cine MRI. To evaluate the influence of a short navigator (a smaller number of navigator points) additional healthy male BALB/c mice (Group C; n=5, weight 30.7 ± 1.8 gram) were examined with both prospectively triggered and self-gated, using a short navigator, cardiac cine MRI. For the comparison of signal-to-noise ratio (SNR) and contrast-to-noise ratio (CNR), healthy male C57Bl/6 mice (Group D; n=5, weight 24.0 ± 1.7) and male haptoglobin knockout mice (C57Bl/6 background) with 90 (±3) day old MIs (Group E; n=5, weight 30.9 ± 2.8 gram) were examined with both prospectively triggered and self-gated cardiac cine MRI with similar parameters. Additionally, the influence of the number of cardiac frames was evaluated. Shared-phase reconstruction was used in the self-gated method of each group.

Due to unforeseen circumstances a different coil had to be used for the mice in group C.

Table 1: Acquisition parameters of the prospectively triggered and self-gated MR methods

	Prospective triggering	Self-gated	Self-gated (short nav)	Prospective triggering (group D/E)	Self-gated (group D/E)
TE (ms)	1,976	4,945	1,926	1,896	1,896
TR (ms)	Dependent on heart rate (HR) (~12-16ms)	8,258	5,239	6,754	6,754
RF pulse (ms)	1.0	0.300	0.300	0.300	0.300
Flip angle	22o	10o	10o	10o	10o
Spectr. Width (Hz)	101010.1	75757.6	75757.6	75757.6	75757.6
Echo position (%)	20	20	20	20	20
Acquisition matrix	256x128	256x128	256x128	256x128	256x128
Reconstructed matrix	256x256	256x256	256x256	256x256	256x256
In-plane resolution (μm)	117	117	117	117	117
Averages	4	~ 8	~ 17	8	Varying from 15-20 Depending on scan duration
Cardiac frames	10	10	10	Dependent on HR	Dependent on HR
Navigator points	NA	256	50	NA	50
Total acquisition time	Varying from 1m25s to 3m00s	2m20s	1m25s	Varying from 2m45s to 3m58s	Varying from 2m45s to 3m58s (per mouse equal to prospective)

The NOD-SCID mice and haptoglobin knockout mice were used in different studies as well, but these experiments did not influence the results of this study(11).

After orthogonal scout images, short axis (oriented roughly perpendicular to the septum) cardiac cine MR images were acquired using the parameters listed in table 1. For groups A, B, and C 10 cardiac frames were acquired per slice in the prospective method; the TR had to be adjusted according to the heart rate, to ensure that the 10 frames covered the entire cardiac cycle. In the self-gated method, also 10 cardiac frames were reconstructed per slice. The TR was equal in groups D and E and the number of frames (16-18 in group D and 18-24 in group E) was adjusted to the heart rate (prospective triggering) in these groups. Subsequently, when using the self-gated method, the same number of frames was reconstructed per slice and acquisition time was matched per mouse to the prospectively triggered experiment. In both methods the matrix was zero filled to 256x256. To cover the entire heart from apex to base, 8-9 slices (healthy mice) or 11-13 slices (mice with MI) were needed. The total experiment time, including mouse preparation and scout images was approximately 65-90 minutes and never exceeded two hours. At the end of the experiment the mice with MI were sacrificed and the hearts were excised for further analysis(11). The animal care committee of Utrecht University approved the experimental protocol.

Data Analysis

The SNR and CNR were calculated only in groups D and E, because relevant MRI parameters of the prospective and self-gated method were equal. The calculations were performed in the end-diastolic (ED) and end-systolic (ES) phase of mid-ventricular slices. For the SNR and CNR the following formulas were used:

$$SNR = \frac{SI \ (myocardium \ or \ blood)}{SD_{noise}}$$

$$CNR = \frac{SI_{blood} - SI_{myocardium}}{SD_{noise}}$$

Were SI is signal intensity and SD is standard deviation. The SD of the noise was determined in a square region of interest (ROI) outside the mouse and free from artifacts. The SI_{blood} was determined by drawing an ROI in the ES phase (consisting of the entire blood pool inside the LV) and copying to the ED phase. The $SI_{myocardium}$ was determined by drawing a circular ROI in a region of the myocardium minimally influenced by motion (typically near the septum).

Table 2: Global cardiac function parameters and prospectively triggered vs. self-gated data in mean ± SD.

A	Mean values Group A (Control) n=11	Differences Group A n=11	Mean values Group C (Control) n=5	Differences Group C n=5	Mean values Group B (MI) n=11	Differences Group B n=11
LVEDV (µl)	56.8 ± 12.8	1.9 ± 1.2 ns	64.0 ± 7.6	1.6 ± 1.1 ns	237.7 ± 89.9	7.9 ± 6.2*
LVESV (µl)	19.2 ± 7.5	1.8 ± 1.6 ns	28.2 ± 7.3	2.9 ± 1.4 ns	207.6 ± 93.2	6.1 ± 4.0*
LVSV (µl)	37.6 ± 6.6	2.8 ± 2.4	35.8 ± 3.0	1.3 ± 1.4	30.1 ± 5.1	4.1 ± 3.2
LVCO (ml/min)	16.6 ± 3.8	1.3 ± 1.2	13.8 ± 1.5	0.6 ± 0.1	11.6 ± 2.7	1.6 ± 2.1
LVEF (%)	67.1 ± 5.9	3.0 ± 2.6	56.5 ± 6.8	3.6 ± 1.8	14.9 ± 6.9	1.5 ± 1.6
RVEDV (µl)	42.6 ± 12.9	1.6 ± 1.3 ns	45.7 ± 6.7	2.1 ± 0.9 ns	51.3 ± 13.5	7.0 ± 5.3 ns
RVESV (µl)	13.4 ± 5.0	1.1 ± 1.6 ns	15.5 ± 2.8	4.2 ± 3.4 ns	30.4 ± 11.8	3.9 ± 2.7 ns
RVSV (µl)	29.2 ± 8.3	1.7 ± 0.7	30.2 ± 4.8	4.2 ± 2.2	21.0 ± 5.5	4.0 ± 3.0
RVCO (ml/min)	12.9 ± 3.9	0.7 ± 0.3	11.7 ± 1.9	2.0 ± 0.8	8.4 ± 3.1	1.6 ± 1.4
RVEF (%)	69.2 ± 4.5	2.4 ± 1.4	66.0 ± 3.4	8.6 ± 5.7	42.3 ± 11.7	4.1 ± 2.3

B	Mean values Group D (Control) n=5	Differences Group D n=5	Mean values Group E (MI) n=5	Differences Group E n=5
LVEDV (µl)	42.4 ± 5.2	2.8 ± 3.5 ns	111.6 ± 58.3	4.5 ± 3.2 ns
LVESV (µl)	17.1 ± 2.4	2.0 ± 0.8 ns	78.7 ± 60.5	4.5 ± 4.4 ns
LVSV (µl)	25.3 ± 3.4	2.7 ± 2.4	32.9 ± 5.1	4.5 ± 5.0
LVCO (ml/min)	12.7 ± 1.7	1.4 ± 1.2	14.5 ± 2.8	2.0 ± 2.2
LVEF (%)	59.6 ± 2.9	4.0 ± 1.1	35.0 ± 12.7	4.3 ± 4.9
RVEDV (µl)	30.1 ± 3.1	1.5 ± 1.6 ns	41.1 ± 7.1	1.4 ± 1.4 ns
RVESV (µl)	10.0 ± 1.6	0.7 ± 0.6 ns	15.6 ± 5.4	1.6 ± 1.4 ns
RVSV (µl)	20.1 ± 2.3	1.9 ± 1.8	25.5 ± 4.7	2.7 ± 1.1
RVCO (ml/min)	10.1 ± 1.3	1.0 ± 0.9	11.2 ± 2.3	1.2 ± 0.5
RVEF (%)	66.9 ± 3.7	3.5 ± 2.2	62.6 ± 9.2	4.8 ± 2.2

The global cardiac function parameters of the groups are averaged from the data of the two gating methods. (Table A: groups A, B, and C. Table B: groups D and E)

The difference between prospectively triggered data and self-gated data expressed in µl (EDV, ESV, and SV), ml/min (CO), and % (EF).Left ventricular (LV), right ventricular (RV), end-diastolic volume (EDV), end-systolic volume (ESV), stroke volume (SV), cardiac output (CO), ejection fraction (EF).

*Comparison per group between prospectively- and self-gated LVEDV, LVESV, RVEDV, and RVESV * p<0.05. ns = not significant.*

In all mice, dedicated, semi-automatic contour detection software (Qmass, MEDIS, Leiden, The Netherlands) was used for the determination of the end-diastolic volume (EDV) and end-systolic volume (ESV), in both the left and right ventricle. Stroke volume (SV), cardiac output (CO), and ejection fraction (EF) were calculated subsequently. The data set of group A was analyzed twice by the same observer. The data sets of groups B, C, D, and E were analyzed three times, twice by the same observer and once by a second observer. Between the first and second analysis there was at least a six week time interval to avoid memory effects.

Statistics

Data are expressed as means ± SD. Analysis of the differences between EDV and ESV measured with prospective triggering and self-gating was performed according to the technique of Bland and Altman(12). The differences of EDV and ESV were expressed against the mean. For all cardiac function parameters absolute values of both positive and negative differences were used since no offset bias is expected.

An independent t-test (SPSS 15.0, Chicago, USA) was used to test the intra- and inter-observer variability of EDV and ESV between prospectively triggered and self-gated data, between lower and higher temporal resolution data, and between self-gated data using a long and short navigator echo. When the Levene's test for equality of variances had a significance of >0.10, equal variances were assumed. To test the differences between the prospectively triggered and self-gated CNR, SNRblood, SNRmyocardium, EDV, and ESV a paired t-test was used. P-values of < 0.05 were considered significant.

Results

Cardiac Function

The average heart rates (HR) were (in beats per minute): 440 ± 52 in group A (healthy mice, long nav.), 390 ± 75 in group B (mice with MI, long nav.), 380 ± 33 in group C (healthy mice, short nav.), 503 ± 22 in group D (healthy mice, short nav., 16-18 frames), and 440 ± 47 in group E (mice with MI, short nav.,18-24 frames).

The results of the cardiac function analyses in the different groups are shown in table 2. The mean infarct size, as determined from the MR images (in %mass of total LV mass), was 31.7 ± 4.0 in group B and 19.7 ± 7.3 in group E.

Prospective- versus Self-gated

Figure 3 shows mid-ventricular slices of a control and a mouse with MI in both the end-diastolic and end-systolic phase. MR images acquired with the prospectively triggered
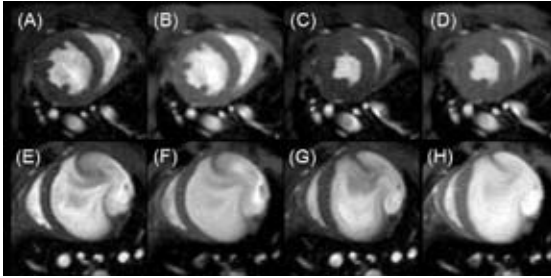
Figure 3: Mid-ventricular slice of a healthy murine heart (A-D) from group C, and a murine heart with an infarct (E-G) from group B; prospectively gated (A, C, E, G) and selfgated (B, D, F, H) in end-diastolic phase (A, B, E, F) and end-systolic phase (C, D, G, H).
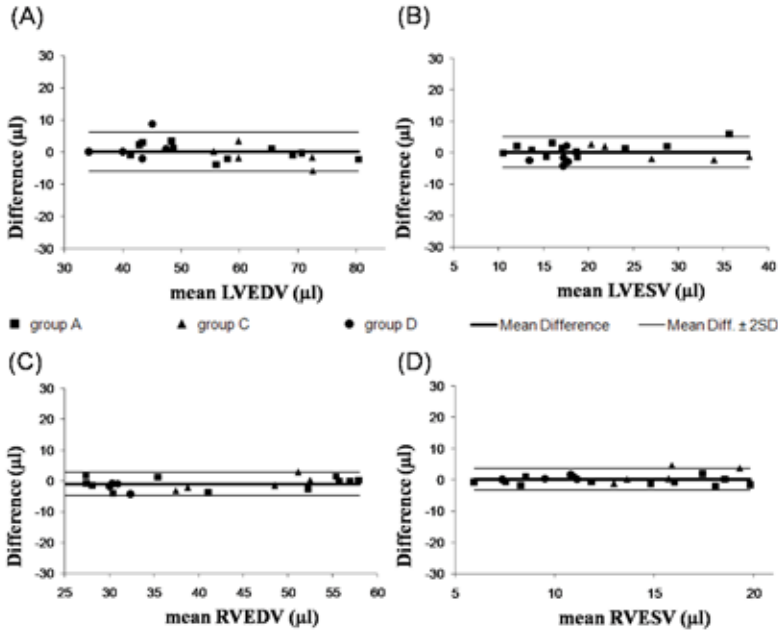

Figure 4: Bland Altman plots of prospectively triggered vs. self-gated data in healthy control mice. Left ventricular volumes (A+B) and right ventricular volumes (C+D). Prospective triggering vs. self-gated data is shown. The closed boxes indicate data from mice in group A. The closed triangles indicate data from mice in group C. The closed circles indicate data from mice in group D. The mean difference is indicated with the thick solid line; the 2SD lines are indicated as solid lines. All volumes are expressed in µl. A: Left ventricular end diastolic volume (LVEDV), B: Left ventricular end systolic volume (LVESV), C: Right ventricular end diastolic volume (RVEDV), D: Right ventricular end systolic volume (RVESV)

and self-gated method are shown. There were no significant differences in left and right ventricular volumes (LVV/RVV) between the prospective and self-gated method in either group as shown in figures 4 and 5. Also, no offset bias is observed for one of the methods. As seen in figure 5 (mice with MI) the infarction areas in group E are smaller than in group B, leading to smaller LVV.

In figure 6 all cardiac frames for both methods can be seen in a mid-ventricular slice. (group D).
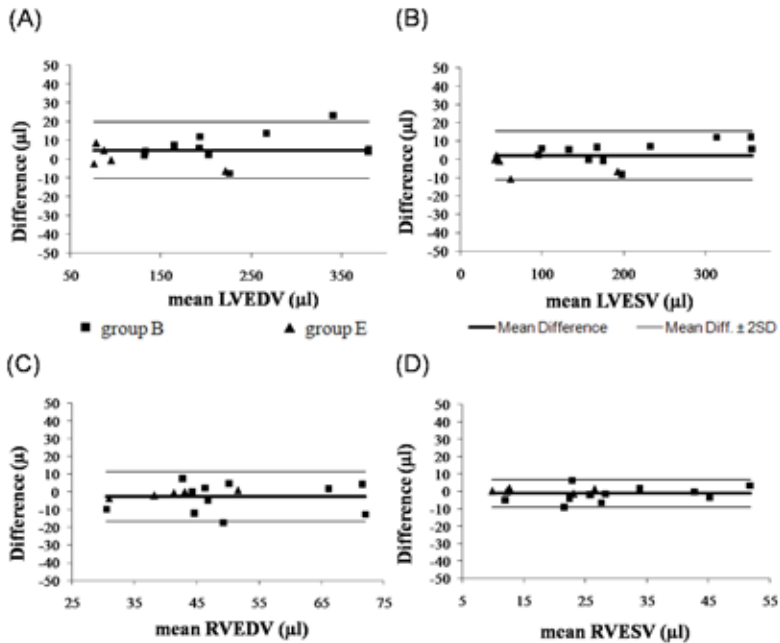

Figure 5: Bland Altman plots of prospectively triggered vs. self-gated data in mice with MIs. Left ventricular volumes (A+B) and right ventricular volumes (C+D). Prospective triggering vs. self-gated data is shown. The closed boxes indicate data from mice in group B. The closed triangles indicate data from mice in group E. The mean difference is indicated with the thick solid line; the 2SD lines are indicated as solid lines. All volumes are expressed in μl. A: Left ventricular end diastolic volume (LVEDV), B: Left ventricular end systolic volume (LVESV), C: Right ventricular end diastolic volume (RVEDV), D: Right ventricular end systolic volume (RVESV)
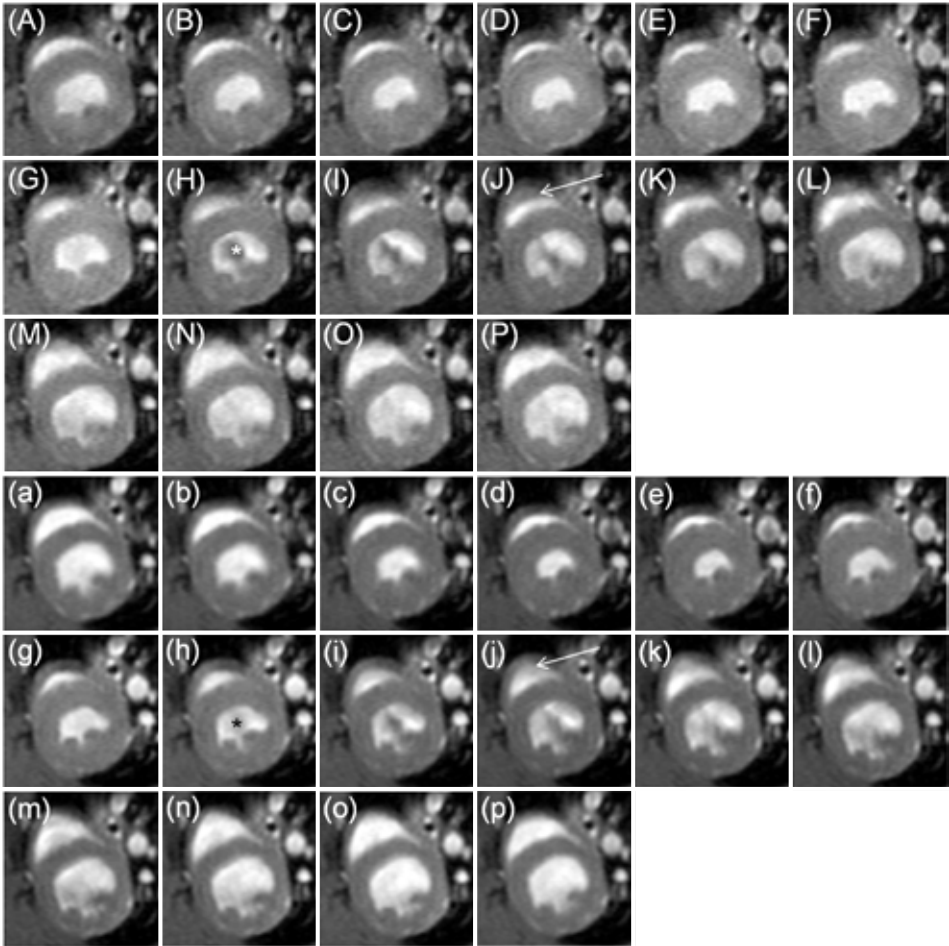
Figure 6: All 16 frames of prospectively triggered (A-P) and self-gated (a-p) images from a mid-ventricular slice of a healthy control mouse (group D) The white (H) and black (h) asterisks indicate flow artifacts, which are more conspicuous in the prospectively triggered image (H). In the right ventricle, white arrows (J and j) indicate the location of an artifact (in the RV) in the prospectively triggered image, which disappears in the self-gated method (j).
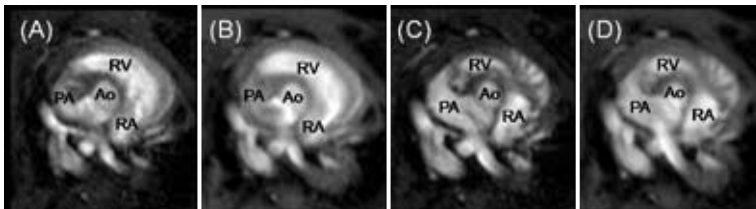

Figure 7: Slice of the right ventricular outflow tract of a healthy murine heart (group C); prospectively gated (A, C) and retrospectively gated with a short navigator (B, D) in end-diastolic phase (A-B) and end-systolic phase (C-D). Ao: aorta, RA: right atrium, RV: right ventricle, PA: pulmonary artery.

Visualization of the right ventricular outflow tract (RVOT) is needed for calculation of RVV. The ED and ES prospectively and self-gated frames of the RVOT of a healthy murine heart, are shown in figure 7. The prospectively triggered and self-gated images, acquired with a short navigator, provide similar depiction of the RVOT. RVOT image degradation occurred when the self-gated method, using a long navigator, was applied (images not shown).

Intra- and Inter-observer Variability
The intra-observer variability did not exceed 9 µl for LVV or RVV in healthy control mice.
In the healthy control mice the intra-observer variability decreased in the self-gated method when a short navigator was used. This decrease was not significantly different in the LVV, but both RVEDV and RVESV showed significant differences (p<0.05) between groups A (long nav.) and C (short nav.) using the self-gated method: EDV; 8.5 ± 8.1 µl and 1.3 ± 1.9 µl, resp., as well as ESV; 7.0 ± 5.1 µl and 2.6 ± 1.2 µl, resp. This suggest that the use of a short navigator improves intra-observer variability.
The inter-observer variability between the prospective method and the self-gated method is not significantly different in the healthy control mice.

The intra-observer variability in the mice with MI is not significantly different when using the prospective method compared to the self-gated method and does not exceed 4 µl for LVV and RVV when using either method.
The inter-observer variability for LVV and RVV in the MI mice is also not significantly different between the prospective and the self-gated method and did not exceed 26 µl. The higher inter-observer variability is in line with the larger mean volumes (ED and ES) due to post-MI LV dilatation.

Number of Cardiac Frames
The intra-observer variability of LVESV, prospectively triggered, decreases significantly (p=0.02), for the healthy control mice, when using more frames per heart cycle; 3.3 ± 1.8 µl (10 frames, group C) versus 0.5 ± 0.3 µl (16-18 frames, group D). The inter-observer variability of RVESV, prospectively triggered, decreases significantly (p=0.05) when using more frames per heart cycle; 5.0 ± 3.3 µl (10 frames, group C) versus 1.0 ± 0.4 µl (16-18 frames, group D).
Increasing the number of cardiac frames did not significantly change the LVV or RVV.
Between the groups B and E (mice with MI) no valid comparison of intra- and inter-observer variability is possible mainly due to different infarct sizes.

SNR and CNR

The results of the SNR and CNR analyses are shown in table 3. A gradual variation in the SI of the blood is seen during the cardiac cycle, this is caused by darkened areas due to blood inflow during diastole. This was observed in both methods, causing a variation in CNR. Significantly higher SNR and CNR ratios are seen in ED as well as ES for the self-gated method when compared to the prospective method. This might be explained by the higher number of averages in the self-gated method, even though the acquisition time is equal for both methods.

Table 3: SNR ± SD and CNR ± SD of the prospectively triggered and self-gated methods and groups. Comparisons of prospective vs. self-gated with * p<0.05 ** p<0.001.

	Group D Control ED	Group D Control ES	Group E MI ED	Group E MI ES
CNR prospectively triggered	33.4 ± 3.8	24.3 ± 3.9	28.3 ± 4.3	24.0 ± 3.3
CNR self-gated	63.2 ± 10.9*	44.2 ± 10.0*	63.0 ± 12.3*	56.1 ± 8.7**
SNR blood prospectively triggered	66.2 ± 3.8	59.3 ± 3.3	61.2 ± 6.3	58.6 ± 3.9
SNR blood self-gated	108.2 ± 9.7**	93.0 ± 10.2*	107.2 ± 16.6*	103.2 ± 13.8*
SNR myocardium prospectively triggered	32.8 ± 1.9	35.1 ± 2.7	32.9 ± 4.0	34.5 ± 4.2
SNR myocardium self-gated	45.0 ± 4.6*	48.8 ± 2.8*	44.2 ± 6.3*	47.1 ± 5.9*

Discussion

In this study we compared prospectively triggered to self-gated cardiac cine MRI in mice with MI and healthy control mice. We found that in control mice and mice with MI the cardiac function parameters were similar between both methods.

Cardiac Function

LV volumes in healthy mice found in this study are in line with values found in literature. For example Heijman et al (6) showed end-diastolic volumes in the range of 30-70μl when using healthy mice with a C57Bl/6 background, in our study the mice with a C57Bl/6 background showed volumes in the range of 30-50μl. For the end-systolic volumes their range is 8-22μl, which is similar to the range in our study (10-21μl). The BALB/c mice in our study show slightly higher volumes, this is probably related to the strain, since the weight of all mice is within a similar range.

In this study a systematic difference was found between LV and RV stroke volumes. This difference could be explained by the asymmetrical shape of the RV, in particular the RVOT, which complicates the perpendicular orientation of the short axis MR slices. In a human study Sheehan et al used a 3D method to circumvent this problem(13). This 3D method could be useful when studying diseases leading to RV dysfunction.

Schneider et al studied changes of cardiac function in mice during anesthesia, up to three hours(14). They showed a limited, but significant, decrease in LVESV over time. This decrease was even more pronounced in failing murine hearts. In our study prospectively triggered imaging was performed before self-gated imaging. We did not see any decrease in LVESV during a maximal examination time of two hours. However, we can not exclude that a true difference between the prospectively triggered and the self-gated method is masked by a small decrease in LVESV.

The image quality is determined by SNR of myocardium and blood and by CNR. The flip angle in groups A, B, and C using the prospective method was higher than the flip angle used in all other circumstances. The lower flip angle was chosen to optimize contrast between myocardium and blood, as well as myocardium and lung tissue. This can lead to better delineation of the epicardial contours, which is sometimes preferred in order to accurately determine ventricular mass.

The self-gated method has some distinct advantages over the prospectively triggered method. The self-gated cine shows a smoother transition from the last frame to the first, as seen in Figure 6, even when the heart rate varies during the experiment, because the cardiac frames are assigned retrospectively. Also, the flow-artifacts, caused by fast inflow of blood during diastole, are less conspicuous in the self-gated method (Figure 6). Additionally, the self-gated method leads to better delineation of the endocardial borders of the right ventricle (Figure 6).

Intra- and Inter-observer Variability
No significant differences were found in the inter-observer variability between the two methods in either the healthy control mice or the mice with MI. A short navigator resulted in a significantly improved intra-observer variability in healthy mice. This might be caused by a 3 ms decrease in TE, resulting in higher SNR and better image quality. No comparison of SNR was made between group A and C due to the use of a different RF coil in group C.

Our intra- and inter-observer variability is in line with other studies(2;3). Those studies provided intra- and inter-observer variability of LVV only, whereas we also determined intra- and inter-observer variability of RVV.

Number of Cardiac Frames

Mice with a different background had to be used in groups D and E when compared to groups A, B, and C (10 frames per cardiac cycle), due to limited availability of mice with MIs. This makes it difficult to study the influence of the number of cardiac frames on ED and ES volumes. However, we could evaluate this influence on intra- and inter-observer variability in healthy mice. The intra-observer variability of ESV, using the prospective method, decreased significantly when the number of frames was increased. This indicates that more than 10 frames per cardiac cycle are needed to produce accurate results for the assessment of cardiac function in mice. A tendency to a lower intra-observer variability was found when the self-gated method was used. Possibly, the difference would have reached significance when the number of mice per group had been increased.

Another explanation for the absence of a significant decrease could be that the ES phase is determined more accurately owing to the retrospective reconstruction, even with 10 frames.

The influence of the number of cardiac frames on intra- and inter-observer variability could not be evaluated in mice with MIs, since not only the mouse strain was different, but also the infarct size and group size were considerably smaller in group E. Additionally, shortening of navigator duration in group E when compared to group B could have contributed to a possible difference in intra- and inter-observer variability.

SNR and CNR

In our study we observed higher SNR for blood and myocardium and higher CNR when using the self-gated method. The relevant MR parameters (TE, TR, spectral width, flip angle, and acquisition time) were equal, leading to a higher number of averages for the self-gated method, when using the shared-phase reconstruction. If this shared-phase reconstruction was not used, the SNR and CNR were comparable to the SNR and CNR of the prospective method. However, the self-gated method can achieve a higher SNR and a higher quality of images in a similar time frame. When the number of averages would be lowered, resulting in an SNR equal to the SNR of prospectively triggered images, experiment time would be substantially shortened. On average $SNR_{myocardium}$ was 1.3 times higher for the self-gated method when compared to the prospectively triggered method, therefore the number of averages for the self-gated method could be $1.3^2 (=1.7)$ times lower to reach equal SNR.

As suspected the CNR varied slightly in the prospective method during cardiac cycle (as seen in Figure 6). The lowest CNR can be seen during the systolic phase. In the self-gated method there is also a lower CNR during the systolic phase, however no differences are found between the first and last reconstructed frame. This is most likely due to the steady state the self-gated method can maintain, since the data are continuously recorded without a breathing pause.

In our study an inslice-navigator was used. With the self-gated method it is also possible to use a separate saturation navigator slice, which can be positioned independently of the imaged slice. This creates the possibility to perform multi-slice experiments (with or without blood saturation to achieve black or bright blood images). Because a separate slice is used as a navigator the TE becomes shorter and TR longer, which will most likely result in an even higher SNR.

A comparable study has been performed solely in healthy mice at a lower field strength(6). The authors concluded that the SNR and CNR using the self-gated method were lower compared to the prospectively triggered method. This is in contrast with our findings, however they did not use the shared-phase reconstruction.

Conclusion

The self-gated method can be used in routine cardiac cine MR measurements in mice with an MI as well as in healthy control mice. The self-gated method is more time-efficient compared to the prospectively triggered method. However, it is important to use more than 10 cardiac frames per cardiac cycle, regardless of the gating method.

Abbreviations

CNR	=	contrast-to-noise ratio
CO	=	cardiac output
EDV	=	end diastolic volume(s)
EF	=	ejection fraction
ESV	=	end systolic volume(s)
HR	=	heart rate
LV	=	left ventricle/ventricular
LVV	=	left ventricular volume(s)
MI	=	myocardial infarction
Nav.	=	navigator
NOD-SCID	=	non-obese, diabetic, severe combined immunodeficient
RV	=	right ventricle/ventricular
RVOT	=	right ventricular outflow tract
RVV	=	right ventricular volume(s)
SD	=	standard deviation
SI	=	signal intensity
SNR	=	signal-to-noise ratio
SV	=	stroke volume
TT	=	total scan time

Reference List

1. Bishop J, Feintuch A, Bock NA, Nieman B, Dazai J, Davidson L, Henkelman RM. Retrospective gating for mouse cardiac MRI. Magn Reson.Med. 2006; 55: 472-477.

2. Ruff J, Wiesmann F, Hiller KH, Voll S, von Kienlin M, Bauer WR, Rommel E, Neubauer S, Haase A. Magnetic resonance microimaging for noninvasive quantification of myocardial function and mass in the mouse. Magn Reson.Med. 1998; 40: 43-48.

3. Schneider JE, Cassidy PJ, Lygate C, Tyler DJ, Wiesmann F, Grieve SM, Hulbert K, Clarke K, Neubauer S. Fast, high-resolution in vivo cine magnetic resonance imaging in normal and failing mouse hearts on a vertical 11.7 T system. J.Magn Reson.Imaging. 2003; 18: 691-701.

4. Hiba B, Richard N, Janier M, Croisille P. Cardiac and respiratory double self-gated cine MRI in the mouse at 7 T. Magn Reson.Med. 2006; 55: 506-513.

5. Timmers L, van Keulen JK, Hoefer IE, Meijs MF, van Middelaar B, den Ouden K, van Echteld CJ, Pasterkamp G, de Kleijn DP. Targeted deletion of nuclear factor kappaB p50 enhances cardiac remodeling and dysfunction following myocardial infarction. Circ.Res. 2009; 104: 699-706.

6. Heijman E, de Graaf W, Niessen P, Nauerth A, van Eys G, de Graaf L, Nicolay K, Strijkers GJ. Comparison between prospective and retrospective triggering for mouse cardiac MRI. NMR Biomed. 2006; 20: 439-447.

7. Rose SE, Wilson SJ, Zelaya FO, Crozier S, Doddrell DM. High resolution high field rodent cardiac imaging with flow enhancement suppression. Magn Reson.Imaging. 1994; 12: 1183-1190.

8. Spraggins TA. Wireless retrospective gating: application to cine cardiac imaging. Magn Reson.Imaging. 1990; 8: 675-681.

9. Crowe ME, Larson AC, Zhang Q, Carr J, White RD, Li D, Simonetti OP. Automated rectilinear self-gated cardiac cine imaging. Magn Reson.Med. 2004; 52: 782-788.

10. White RD, Paschal CB, Clampitt ME, Spraggins TA, Lenz GW. Electrocardiograph-independent, "wireless" cardiovascular cine MR imaging. J.Magn Reson.Imaging. 1991; 1: 347-355.

11. van Laake LW, Passier R, Monshouwer-Kloots J, Nederhoff MG, Ward-van Oostwaard D, Field LJ, van Echteld CJ, Doevendans PA, Mummery CL. Monitoring of cell therapy and assessment of cardiac function using magnetic resonance imaging in a mouse model of myocardial infarction. Nat.Protoc. 2007; 2: 2551-2567.

12. Bland JM, Altman DG. Statistical methods for assessing agreement between two methods of clinical mesurement. Lancet. 1986; 1: 307-310.

13. Sheehan FH, Ge S, Vick GW, Urnes K, Kerwin WS, Bolson EL, Chung T, Kovalchin JP, Sahn DJ, Jerosch-Herold M, Stolpen AH. Three-dimensional shape analysis of right ventricular remodeling in repaired tetralogy of Fallot. Am.J.Cardiol. 2008; 101: 107-113.

14. Schneider JE, Hulbert KJ, Lygate CA, Ten Hove M, Cassidy PJ, Clarke K, Neubauer S. Long-term stability of cardiac function in normal and chronically failing mouse hearts in a vertical-bore MR system. MAGMA. 2004; 17: 162-169.

General Discussion

Nederlandse Samenvatting

List of publications

Dankwoord

Curriculum Vitae

This thesis is aimed at better visualization of various stages of atherosclerotic plaques with MRI. Noninvasive screening for subclinical atherosclerosis as well as detection of high-risk atherosclerotic plaque in an established population of cardiovascular patients is important for patient management. Three MRI approaches, anatomical MRI utilizing intrinsic contrast based on different MR relaxation properties of plaque components, contrast-enhanced MRI using non-targeted ultra-small particles of iron oxide (USPIOs) and contrast enhanced MRI using micelles targeting novel targets of advanced atherosclerosis disease in plaque, were investigated.

Anatomical MRI of carotid atherosclerosis

Anatomical MRI of atherosclerosis has started nearly 20 years ago. Together with a thin fibrous cap and high macrophage density in the shoulder regions of the plaque, lipid core size had been recognized as an important vulnerable plaque feature(1). Later on, neovasculature and intra-plaque hemorrhage (IPH) have also been recognized as characteristics of a rupture-prone and fast-growing plaque(2).

Initially, human carotid plaque lipids have been detected with *ex vivo* chemical shift MR imaging of the fat signal(3;4). Because even in lipid core the lipid-water ratio was reported to be low (0.11) and the water resonance in lipid core has a short T2, the proton signal originating from plaque water exceeded by far the proton signal from plaque lipids(5).Therefore, water proton sequences benefit from a larger signal-to-noise ratio than techniques based on direct lipid analysis(6). Furthermore, water proton sequences allow simultaneous imaging of other plaque components such as collagen, fibroblasts/ smooth muscle cells and intra-plaque hemorrhage. Therefore, more recent studies have focused on ex-vivo proton MRI of carotid lesions.

With the advent of phased-array surface coils, stronger gradient systems and better flow suppression strategies, *in vivo* MRI of carotid plaque in patients scheduled for carotid endarterectomy showed the importance of multi-contrast weighted MRI(7). Lipid core and IPH were reported to be bright at T1 weighted FSE images and IPH was reported to be bright at TOF (time-of-flight) images(2;8). Foam cells found in early plaque stages are often the precursor of lipid core, an important component of a more vulnerable plaque stage. However, both components are not differentiated in existing carotid plaque MRI studies(7;9-11). So, better discrimination between lipid core and foam cells is important for better risk stratification of asymptomatic patients.

We succeeded in *ex vivo* discrimination between lipid core and foam cells and better discrimination between lipid core and stable plaque components in human carotid plaque using FLASH with fat suppression (FS) when compared to FLASH without FS (Chapter 4). Addition of Inversion Recovery Spin Echo (IRSE) to a panel of standard techniques (T1w/T2w/PDw) allowed for better identification of IPH. Improved detection of lipid

core and IPH is clinically important for prognostic assessment of patients with carotid atherosclerosis. Direct translation of these techniques to *in vivo* high-field clinical MRI is possible, when a flow suppression module is incorporated in these novel sequences.

Macrophage-targeted MRI of atherosclerosis using iron oxides
First, plaques in medium to small sized human arteries may be less suitable for imaging with anatomical MRI than carotid arteries or the aorta. Contrast-enhanced MRI may enhance conspicuity of a dangerous plaque without even showing anatomical detail. Secondly, instability does not depend only on plaque markers as lipid core and IPH but also on inflammatory state reflected by the presence and activity of macrophages. Detection of metastases of cancer using USPIO contrast-enhanced MRI is based on the uptake of iron in macrophages in healthy lymph node stations(12). This approach has been translated to atherosclerosis in animal and human studies by some research groups(12-18). The tremendous T2* contrast observed in these studies was also seen in our mouse study, however we were only able to relate the negative contrast caused by USPIOs to uptake in peri-aortic lymph nodes (Chapter 5). Blooming, the effect of spreading of negative contrast beyond the location of uptake of iron oxides, may account for mistaking uptake of USPIOs by peri-aortic lymph node macrophages for uptake by plaque macrophages. Use of T2 weighted high resolution images instead of T2* weighted lower resolution images can avoid this mistake (Chapter 5).

Molecular MRI of atherosclerotic plaque markers
Another avenue to contrast-enhanced MRI of atherosclerotic plaque is visualization of molecular processes involved in atherosclerosis. Molecular MRI of atherosclerotic plaque has been performed with contrast agents directed against a variety of targets. Some of these targets are macrophage membrane-bound receptors, like scavenger receptor A and B(19;20), or the CB2 receptor (Chapter 6 and 8). Other targets are intracellular proteins stored in macrophage granules and released from macrophages to the extracellular matrix, like MMPs(21;22) and NGAL (Chapter 6 and 7) or lipoproteins, which trigger macrophages to ingest them, like ox-LDL(23). The extracellular location of these proteins may pose a problem for visualization, because of early wash-out of these proteins bound or unbound to targeted contrast agents. On the other hand, respective studies showed specific uptake in the plaque at several time-points after injection of targeted agents. We also showed increased enhancement at 72 hours after injection of NGAL/24p3 targeted micelles when compared to isotype antibody conjugated micelles.

This long term enhancement could be explained by the fact that released proteins have affinity for extracellular matrix proteins, which prevents fast washout. Indications for binding of released proteins to the subendothelial matrix are found in literature. For

example, the aorta is an abundant tissue source of the heparan sulfate proteoglycan collagen XVIII and its proteolytically released endostatin (ES) fragment. Endostatin binds via biglycan to the subendothelial matrix(24) and interferes with LDL retention to the subendothelial matrix during atherosclerosis. However, generally, proteins do not show long survival after release in the extracellular space.

We found that micelles co-localized with NGAL/24p3 and macrophages in aortic plaque after intravenous injection. Presumably, micelles bind first to released NGAL/24p3, bound to the matrix in the plaque, and can be subsequently ingested by macrophages, because the protein-micelle complex is not washed immediately from the plaque. Apoptosis or necrosis of these macrophages just before 72 hours post-injection leaving NGAL-micelles in the extracellular matrix could explain the finding of extracellular 24p3 targeted micelles at 72 hours after injection. Control micelles were not ingested or to a lower extent due to the earlier washout because there was no binding mechanism.

Optimization of the timing of MRI after injection of these agents in order to observe the specific component of plaque uptake is not easy. Just from a practical point of view, in most studies post-injection MRI was planned at 24, 48 and 72 hours after injection. However, accurate definition of the timing window for visualization of specific uptake would be more appropriate in order to increase sensitivity and specificity of the test outcome. Though the unspecific extravasation time of micelles can be predicted more or less from their plasma half life, the result of the difference in binding properties of targeted and control micelles cannot be predicted. Knowledge about both the binding properties of both targeted and non targeted contrast agents to plaque components as well as the plasma half life of agents is important in this respect. Therefore, we performed continuous T1 weighted imaging of the aorta after injection of both CB2-R targeted and control micelles (Chapter 8). Moreover the relation between aortic normalized enhancement ratios (NER) and gadolinium content was calculated from standard T1 weighted images and from inversion-recovery prepared T1 weighted images (chapter 8). The relation was stronger when the NER was calculated from the inversion-recovery prepared T1 weighted image, however we advise averaging of several NER values calculated from sequential images, because of a substantial inter-scan variability (chapter 8). As a separate subject, performance of a self-gated cardiac MRI method has been shown comparable to a prospectively gated cardiac MRI method for evaluation of cardiac function parameters in mice after permanent occlusion of the left anterior descending artery (Chapter 9).

Role of MRI for visualization of atherosclerosis
Screening for early-stage asymptomatic cancer (like breast and colon) to prevent late-stage malignancies has been widely accepted. However, although atherosclerotic cardiovascular

disease (heart attack and stroke) accounts for more death and disability than all cancers combined, there are no national screening guidelines for asymptomatic (subclinical) atherosclerosis, and there is no government- or healthcare-sponsored reimbursement for atherosclerosis screening(25;26).

Costs-effectiveness analysis shows that intima-media thickness evaluated with ultrasound and calcium score evaluated with CT are most effective techniques for screening of large patient groups(27). This strategy has been shown to be more effective than traditional Framingham risk factors(27). Ultrasound and CT have been available longer than other modalities for direct visualization and determination of the extent of atherosclerosis. Naghavi et al. (SHAPE Task Force report Am J Cardiol 2006): "Other tests for the detection of atherosclerosis and abnormal arterial structure and function, such as MRI of the great arteries, are emerging and must be further validated"(27). So, the role of MRI in screening for subclinical atherosclerosis has to evolve further.

Screening results combined with risk factor assessment are used for risk stratification to identify the vulnerable patient and initiate appropriate therapy. The higher the risk, the more vulnerable a patient is to a near-term adverse event. Because <10% of the population who test positive for atherosclerosis will experience a near-term event, additional risk stratification based on reliable markers of disease activity is needed and is expected to further focus the search for the vulnerable patient in the future(27).

Concept of the vulnerable plaque and the vulnerable patient
Additional risk stratification could be based on molecular MRI. MRI could also have an important role in detection of high-risk/vulnerable plaques in an already established group of cardiovascular patients. Which factors determine the risk of local plaque rupture and which factors determine the general risk of an acute cardiovascular event? The classical vulnerable plaque markers (chapter 2) only predict to a certain extent plaque rupture. It has been suggested that in a patient a lot of plaques could be labeled vulnerable. Identification of intra-plaque molecular processes related to the inflammatory state of the plaque could be more important. Human carotid NGAL plaque levels in endarterectomy patients were related to the presence of thrombus in the same plaque (unpublished results Hellings et al). Importantly, it is not known whether the thrombus was the cause or the result of increased NGAL levels. However, NGAL could play a role in plaque erosion or rupture. However, vulnerable plaques are not the only culprit factors for the development of acute coronary syndromes, myocardial infarction, and sudden cardiac death. Vulnerable blood (prone to thrombosis) and vulnerable myocardium (prone to fatal arrhythmia) play an important role in the outcome(25;26).

Moreover, a vulnerable plaque at a particular location is not necessarily a culprit lesion but could also predict the rupture of a plaque elsewhere in the body. First, literature indeed

shows a relation between the presence of inflammatory plaque components in one of the carotid arteries and acute cardiovascular events(28). Secondly, the presence of NGAL in carotid plaque in endarterectomy patients is associated with cardiovascular symptoms at the time-point of surgery (chapter 7). Thirdly, carotid plaque NGAL levels in patients, achieving endpoints (acute cardiovascular events) during a 2-year follow-up after surgery, are significantly higher than in patients not achieving these end-points (chapter 7).

Importantly, blood NGAL levels did not show these associations (chapter 7). So, modalities for molecular imaging of plaque could be important candidates as techniques for screening of high-risk patients.

Molecular imaging modalities: molecular MRI and SPECT?

The ideal method for additional risk stratification on top of "calcium score" (CT) and "intima media thickness" (ultrasound) for screening vulnerable patients should be 1) inexpensive, 2) relatively noninvasive, 3) widely reproducible, 4) capable of adding predicted value to measurements of established risk factors, 5) avoiding repeated radiation exposure.

As we have shown in chapter 2 both SPECT and MRI show the most promise in this respect. An important advantage of MRI is combined information about anatomy and molecular processes (chapter 2). However, an important disadvantage is the relatively low sensitivity of molecular MRI when compared to SPECT or PET(29). Further, contrast agents used for molecular MRI are composed of carriers, like micelles(23;30), liposomes(31;32) or other nano-platforms(33-35), which still have to be approved by the FDA (US) and EMEA (Europe) for clinical application. In principle, most SPECT and PET tracers are approved after short (pre)clinical test procedures in contrast to the lengthy procedure required for MR contrast agents, because these tracers can be applied in nano- or even picomolar amounts, far below concentrations that could elicit any immune response or therapeutic or toxic effects. Therefore, high costs are involved in the clinical development of targeted MR contrast agents.

In conclusion, nowadays, because of the higher sensitivity of SPECT and PET, easy application of SPECT tracers in the clinic and the superior anatomical information provided by MRI, the ideal platform for molecular imaging appears to be combined MRI-SPECT(36). However, repeated screening with SPECT or PET tracers is limited by radiation exposure. Despite the higher development costs and longer development timelines, MRI based targeted contrast agent may still provide a valuable addition to the emerging repertoire of molecular imaging approaches to visualize vulnerable atherosclerotic plaques in patients.

USPIOs are the only MR contrast agents which have been approved for clinical use so far. The insecure destiny of micelle and liposomal lipids, possible exchange of lipid

monomers with cell membranes, and transmetallation (replacement of Gd with Zn)(37), further complicates the implementation of some lipid-based contrast agents. However, further research is needed for a full overview of the toxicity issues of these MR contrast agents. On the other hand, the clinical application of targeted functionalized USPIOs has already been reported in cancer research(38) and use of these USPIOs for clinical MRI of atherosclerosis may be anticipated earlier than lipid-based nanoparticles.

Both molecular MRI and SPECT require a baseline and post-injection measurement. However, in the case of molecular MRI this situation could be avoided by the use of PARACEST agents, for which the contrast effect can be tuned off(39;40). The availability and costs of both techniques are not optimal, and should be improved. High-field MRI and faster MR imaging techniques using k-SENSE and phased array coils with many elements may speed up MRI protocols(41).

In summary, in this thesis both anatomical MRI and targeted contrast-enhanced MRI for characterization of atherosclerotic plaques have been applied in *ex vivo* human arterial tissue and in *in vivo* mouse models. Pitfalls have been shown for *in vivo* cellular MRI using USPIOs, but on the other hand the feasibility of *in vivo* molecular MRI using NGAL and CB2-R targeted micelles for visualization of various stages of atherosclerosis was demonstrated. Implementation in human follow-up research for evaluation of the prognostic value of these molecular MRI methods will have to be preceded by further biodistribution, excretion and safety studies of lipid-based MR contrast agents.

Reference List

1   Falk E, Shah PK, Fuster V. Coronary plaque disruption. Circulation 1995 August 1;92(3):657-71.

2   Takaya N, Yuan C, Chu B, Saam T, Polissar NL, Jarvik GP et al. Presence of intraplaque hemorrhage stimulates progression of carotid atherosclerotic plaques: a high-resolution magnetic resonance imaging study. Circulation 2005 May 31;111(21):2768-75.

3   Booth RF, Honey AC, Martin JF, Lindon JC, Farrant RD, Carpenter TA et al. Lipid characterization in an animal model of atherosclerosis using NMR spectroscopy and imaging. NMR Biomed 1990 April;3(2):95-100.

4   Vinitski S, Consigny PM, Shapiro MJ, Janes N, Smullens SN, Rifkin MD. Magnetic resonance chemical shift imaging and spectroscopy of atherosclerotic plaque. Invest Radiol 1991 August;26(8):703-14.

5   Toussaint JF, Southern JF, Fuster V, Kantor HL. T2-weighted contrast for NMR characterization of human atherosclerosis. Arterioscler Thromb Vasc Biol 1995 October;15(10):1533-42.

6   Toussaint JF, LaMuraglia GM, Southern JF, Fuster V, Kantor HL. Magnetic resonance images lipid, fibrous, calcified, hemorrhagic, and thrombotic components of human atherosclerosis in vivo. Circulation 1996 September 1;94(5):932-8.

7   Cai JM, Hatsukami TS, Ferguson MS, Small R, Polissar NL, Yuan C. Classification of human carotid atherosclerotic lesions with in vivo multicontrast magnetic resonance imaging. Circulation 2002 September 10;106(11):1368-73.

8   Chu B, Kampschulte A, Ferguson MS, Kerwin WS, Yarnykh VL, O'Brien KD et al. Hemorrhage in the atherosclerotic carotid plaque: a high-resolution MRI study. Stroke 2004 May;35(5):1079-84.

9   Cai J, Hatsukami TS, Ferguson MS, Kerwin WS, Saam T, Chu B et al. In vivo quantitative measurement of intact fibrous cap and lipid-rich necrotic core size in atherosclerotic carotid plaque: comparison of high-resolution, contrast-enhanced magnetic resonance imaging and histology. Circulation 2005 November 29;112(22):3437-44.

10 Yuan C, Kerwin WS, Ferguson MS, Polissar N, Zhang S, Cai J et al. Contrast-enhanced high resolution MRI for atherosclerotic carotid artery tissue characterization. J Magn Reson Imaging 2002 January;15(1):62-7.

11 Mitsumori LM, Hatsukami TS, Ferguson MS, Kerwin WS, Cai J, Yuan C. In vivo accuracy of multisequence MR imaging for identifying unstable fibrous caps in advanced human carotid plaques. J Magn Reson Imaging 2003 April;17(4):410-20.

12 Schmitz SA, Taupitz M, Wagner S, Wolf KJ, Beyersdorff D, Hamm B. Magnetic resonance imaging of atherosclerotic plaques using superparamagnetic iron oxide particles. J Magn Reson Imaging 2001 October;14(4):355-61.

13 Schmitz SA, Coupland SE, Gust R, Winterhalter S, Wagner S, Kresse M et al. Superparamagnetic iron oxide-enhanced MRI of atherosclerotic plaques in Watanabe hereditable hyperlipidemic rabbits. Invest Radiol 2000 August;35(8):460-71.

14 Schmitz SA. [Iron-oxide-enhanced MR imaging of inflammatory atherosclerotic lesions: overview of experimental and initial clinical results]. Rofo 2003 April;175(4):469-76.

15 Ruehm SG, Corot C, Vogt P, Kolb S, Debatin JF. Magnetic resonance imaging of atherosclerotic plaque with ultrasmall superparamagnetic particles of iron oxide in hyperlipidemic rabbits. Circulation 2001 January 23;103(3):415-22.

16 Trivedi RA, Mallawarachi C, King-Im JM, Graves MJ, Horsley J, Goddard MJ et al. Identifying inflamed carotid plaques using in vivo USPIO-enhanced MR imaging to label plaque macrophages. Arterioscler Thromb Vasc Biol 2006 July;26(7):1601-6.

17 Kooi ME, Cappendijk VC, Cleutjens KB, Kessels AG, Kitslaar PJ, Borgers M et al. Accumulation of ultrasmall superparamagnetic particles of iron oxide in human atherosclerotic plaques can be detected by in vivo magnetic resonance imaging. Circulation 2003 May;107(19):2453-8.

18 Tang TY, Howarth SP, Li ZY, Miller SR, Graves MJ, King-Im JM et al. Correlation of carotid atheromatous plaque inflammation with biomechanical stress: utility of USPIO enhanced MR imaging and finite element analysis. Atherosclerosis 2008 February;196(2):879-87.

19 Lipinski MJ, Amirbekian V, Frias JC, Aguinaldo JG, Mani V, Briley-Saebo KC et al. MRI to detect atherosclerosis with gadolinium-containing immunomicelles targeting the macrophage scavenger receptor. Magn Reson Med 2006 September;56(3):601-10.

20   Amirbekian V, Lipinski MJ, Briley-Saebo KC, Amirbekian S, Aguinaldo JG, Weinreb DB et al. Detecting and assessing macrophages in vivo to evaluate atherosclerosis noninvasively using molecular MRI. Proc Natl Acad Sci U S A 2007 January 16;104(3):961-6.

21   Aguinaldo JG, Amirbekian V, Mani V, Sirol M, Hyafil F, Lancelot E. A novel imaging agent P947, a marker that molecularly targets matrix metalloproteinases in atherosclerotic plaque using in-vivo MR imaging. Molecular Imaging 4[3], 343-344. 7-9-2005. Ref Type: Abstract

(22 Amirbekian V, Aguinaldo JG, Amirbekian S, Hyafil F, Vucic E, Sirol M et al. Atherosclerosis and Matrix Metalloproteinases: Experimental Molecular MR Imaging in Vivo. Radiology 2009 February 12.

23   Briley-Saebo KC, Shaw PX, Mulder WJ, Choi SH, Vucic E, Aguinaldo JG et al. Targeted molecular probes for imaging atherosclerotic lesions with magnetic resonance using antibodies that recognize oxidation-specific epitopes. Circulation 2008 June 24;117(25):3206-15.

24   Zeng X, Chen J, Miller YI, Javaherian K, Moulton KS. Endostatin binds biglycan and LDL and interferes with LDL retention to the subendothelial matrix during atherosclerosis. J Lipid Res 2005 September;46(9):1849-59.

25   Naghavi M, Libby P, Falk E, Casscells SW, Litovsky S, Rumberger J et al. From vulnerable plaque to vulnerable patient: a call for new definitions and risk assessment strategies: Part I. Circulation 2003 October 7;108(14):1664-72.

26   Naghavi M, Libby P, Falk E, Casscells SW, Litovsky S, Rumberger J et al. From vulnerable plaque to vulnerable patient: a call for new definitions and risk assessment strategies: Part II. Circulation 2003 October 14;108(15):1772-8.

27   Naghavi M, Falk E, Hecht HS, Jamieson MJ, Kaul S, Berman D et al. From vulnerable plaque to vulnerable patient--Part III: Executive summary of the Screening for Heart Attack Prevention and Education (SHAPE) Task Force report. Am J Cardiol 2006 July 17;98(2A):2H-15H.

28   Verhoeven B, Hellings WE, Moll FL, de Vries JP, de Kleijn DP, de BP et al. Carotid atherosclerotic plaques in patients with transient ischemic attacks and stroke have unstable characteristics compared with plaques in asymptomatic and amaurosis fugax patients. J Vasc Surg 2005 December;42(6):1075-81.

29   Massoud TF, Gambhir SS. Molecular imaging in living subjects: seeing fundamental biological processes in a new light. Genes Dev 2003 March 1;17(5):545-80.

30   Mulder WJ, Strijkers GJ, Briley-Saboe KC, Frias JC, Aguinaldo JG, Vucic E et al. Molecular imaging of macrophages in atherosclerotic plaques using bimodal PEG-micelles. Magn Reson Med 2007 December;58(6):1164-70.

31   Mulder WJ, Douma K, Koning GA, van Zandvoort MA, Lutgens E, Daemen MJ et al. Liposome-enhanced MRI of neointimal lesions in the ApoE-KO mouse. Magn Reson Med 2006 May;55(5):1170-4.

32   Mulder WJ, Strijkers GJ, Griffioen AW, van BL, Molema G, Storm G et al. A liposomal system for contrast-enhanced magnetic resonance imaging of molecular targets. Bioconjug Chem 2004 July;15(4):799-806.

33   Cormode DP, Briley-Saebo KC, Mulder WJ, Aguinaldo JG, Barazza A, Ma Y et al. An ApoA-I mimetic peptide high-density-lipoprotein-based MRI contrast agent for atherosclerotic plaque composition detection. Small 2008 September;4(9):1437-44.

34   Cormode DP, Chandrasekar R, Delshad A, Briley-Saebo KC, Calcagno C, Barazza A et al. Comparison of Synthetic High Density Lipoprotein (HDL) Contrast Agents for MR Imaging of Atherosclerosis. Bioconjug Chem 2009 April;%20.

35   Mulder WJ, Koole R, Brandwijk RJ, Storm G, Chin PT, Strijkers GJ et al. Quantum dots with a paramagnetic coating as a bimodal molecular imaging probe. Nano Lett 2006 January;6(1):1-6.

36   Wallis d, V, van Dam GM, Tio RA, Hillebrands JL, Slart RH, Zeebregts CJ. Current imaging modalities to visualize vulnerability within the atherosclerotic carotid plaque. J Vasc Surg 2008 December;48(6):1620-9.

37   Hak S, Sanders HM, Agrawal P, Langereis S, Grull H, Keizer HM et al. A high relaxivity Gd(III)DOTA-DSPE-based liposomal contrast agent for magnetic resonance imaging. Eur J Pharm Biopharm 2009 June;72(2):397-404.

38   Zhang C, Jugold M, Woenne EC, Lammers T, Morgenstern B, Mueller MM et al. Specific targeting of tumor angiogenesis by RGD-conjugated ultrasmall superparamagnetic iron oxide particles using a clinical 1.5-T magnetic resonance scanner. Cancer Res 2007 February 15;67(4):1555-62.

39   Aime S, Carrera C, Delli CD, Geninatti CS, Terreno E. Tunable imaging of cells labeled with MRIPA-RACEST agents. Angew Chem Int Ed Engl 2005 March 11;44(12):1813-5.

40   Winter PM, Cai K, Chen J, Adair CR, Kiefer GE, Athey PS et al. Targeted PARACEST nanoparticle con-

trast agent for the detection of fibrin. Magn Reson Med 2006 December;56(6):1384-8.

41 Niendorf T, Sodickson DK. Highly accelerated cardiovascular MR imaging using many channel technology: concepts and clinical applications. Eur Radiol 2008 January;18(1):87-102.

Nederlandse Samenvatting

(voor de geïnteresseerde leek)

Atherosclerose (aderverkalking) is doodsoorzaak nummer 1 in de westerse wereld. Diagnose van diverse stadia van atherosclerose is van belang voor adequate behandeling (Figuur 1). De samenstelling van de vetafzetting (plaque) blijkt het risico op scheuring van de plaque te bepalen. Een groot vetmeer, een dunne bedekkende bindweefsellaag, veel macrofagen (alles etende cellen van belang voor de afweer) in de schouderregio van de plaque en bloeding uit vaatjes in de plaque zijn karakteristieken van een hoog-risico plaque. Met MRI is bepaling van de samenstelling van de plaque mogelijk, hetgeen met de meest gebruikte klinische methode, catheterisatie van de kransslagaders, niet mogelijk is. Bovendien kunnen met behulp van MR contrastmiddelen die specifiek hechten aan moleculen, moleculaire processen die te maken hebben met destabilisatie van de plaque in beeld gebracht worden (moleculaire MRI).

Een overzicht van de beschikbare literatuur op het gebied van MRI van atherosclerose zonder en met deze contrastmiddelen wordt geboden in hoofdstuk 2 en 3, respectievelijk.

### MRI zonder contrastmiddelen van de halsslagader in de mens

Bepaling van de samenstelling van plaques in de halsslagader met MRI zoals dat in de literatuur beschreven is, lijkt verbeterd te kunnen worden met behulp van 2 MRI technieken, "inversion recovery spin echo" en "T1 gewogen FLASH met vetsuppressie" (hoofdstuk 4). Twee bestanddelen van plaques die samenhangen met instabiliteit van die plaques, vet en bloeding uit vaatjes in de plaque, worden beter zichtbaar met T1w met vetsuppressie en IR-SE, respectievelijk.

MRI van muizenaorta met behulp van USPIOs

Macrofaagrijke plaques blijken een hoger risico op scheuring te hebben dan macrofaagarme. Deze worden in experimentele situaties zichtbaar gemaakt met USPIOs (minuscule ijzerbolletjes) die na inspuiting in een ader opgegeten worden door macrofagen in plaques en op speciale MRI opnames zwart worden. Het succes van deze USPIOs is wat afgezwakt door ons vanwege de bevinding, dat vooral lymfknopen rondom de plaque deze USPIOs opnemen en dit op MRI plaatjes verward kan worden met opname in de plaque (hoofdstuk 5).

Produktie en karakterisatie van micellen als moleculair MR contrastmiddel

We laten de productie en karakterisering van twee MRI contrastmiddelen zien waarmee gevorderde plaques zichtbaar gemaakt kunnen worden, doordat ze hechten aan eiwitten die alleen in gevorderde plaques zitten (hoofdstuk 6). De contrastmiddelen zijn gebaseerd
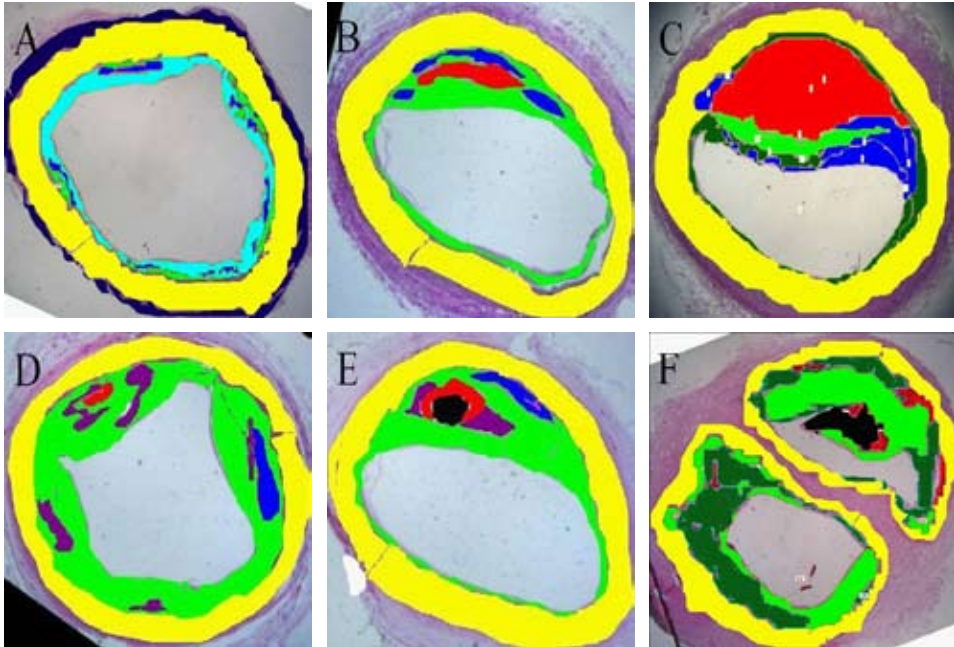
Figuur 1. Progressie van atherosclerotische plaques van intima hypertrofie (A), via vorming van schuimcellen (blauw), na opname van slechte vorm van cholesterol door macrofagen, en beginnende vorming van een vetmeer met weefselversterf (red) (B), tot een hoog-risico plaque met een groot vetmeer met weefselversterf (C) of een hoog-risico plaque met bloeding (paars) (D). Vetmeren in plaques kunnen verkalkt raken (zwart) (E en F, bovenste doorsnede), waardoor de plaques een minder hoog risico op scheuring hebben. Plaques kunnen ook met name collageen (lichtgroen) en bindweefselcellen (donkergroen) (F, onderste doorsnede) bevatten waardoor ze een lager risico op scheuring hebben. Lichtblauw: losmazig bindweefsel.

op wateroplosbare vetbolletjes, die micellen genoemd worden. Een van deze middelen bindt aan NGAL, een eiwit dat de afbraak van collageenafbrekende eiwitten remt en zo zou leiden tot eerdere scheuring van die plaque. Het andere middel bindt en activeert de zogenaamde cannabinoid receptor type 2 (CB2-receptor), een eiwit op de buitenzijde van macrofagen, dat via onderdrukking van het afweersysteem het risico van scheuring van de plaque tracht te verminderen.

Moleculaire MRI van plaques in de muis gericht op NGAL, een molecuul geassocieerd met humane hoog-risico plaques

In hoofdstuk 7 laten we zien dat patiënten die na operatie aan de halsslagader een TIA, beroerte of hartinfarct krijgen een hogere hoeveelheid NGAL in de veroorzakende plaque in de halsslagader hebben dan patiënten die een dergelijke aandoening niet krijgen. In een muizenmodel laten we met MRI vervolgens zien, dat contrastmiddelen waaraan antistoffen gericht tegen dit eiwit gekoppeld zijn, versterkt opgenomen worden in de

plaque 72 uur na injectie in de bloedbaan vergeleken met contrastmiddelen waaraan controle antistoffen gekoppeld zijn.

Moleculaire MRI van plaques in de muis gericht op de CB2-receptor; gevoeligheid en reproduceerbaarheid van het contrast van 2 technieken

MRI van de plaque in muizen met behulp van contrastmiddel, gericht tegen de CB2-receptor, laat voor het eerst 42 uur en op zijn minst tot 48 uur na injectie hoger contrast zien dan met behulp van het controle contrastmiddel. Het MR contrast bij gelijke hoeveelheid contrastmiddel in de plaque is groter met "T1 gewogen inversion recovery fast spin echo" dan met de in de literatuur meest gebruikte techniek, "T1 gewogen spin echo" (hoofdstuk 8). De reproduceerbaarheid van de meting van het contrast lijkt iets beter te zijn in geval van "T1 gewogen spin echo" dan in geval van "T1 gewogen inversion recovery fast spin echo". De aanbeveling wordt gedaan de contrastmetingen van meerdere scans te middelen ten behoeve van verbetering van de reproduceerbaarheid.

Self-gated MRI

Resterende pompfunctie van het hart kan na een hartinfarct zeer nauwkeurig met behulp van MRI bepaald worden. De ejectiefractie is het percentage van het bloedvolume in de kamer tijdens de volledig ontspannen fase dat de kamer verlaat tijdens de samentrekking van het hart. De ejectiefractie wordt in de kliniek gebruikt als maat voor de pompfunctie van het hart. Bij meting van de pompfunctie van het hart met MRI wordt er een hartfilmpje gemaakt door het MR signaal te verzamelen op gezette tijden na een afgesproken ijkpunt op de registratie van een tegelijkertijd opgenomen elektrocardiogram (elektrische signaal van de hartspier) en tijdens inademing geen signaal te verzamelen. Dit heet ook wel "prospective triggering". Bij onregelmatig hartactie, een ritmestoornis, welke vaak voorkomt na een hartinfarct wordt informatie van delen van de contractiecyclus van het hart gemist. Zo kan bij een vertraging van de hartactie een cyclus onvolledig gesampled zijn of, bij versnelling van de hartactie, kunnen twee cycli als een gezien worden. Als gevolg hiervan kan de volledig samengeknepen toestand van de linker kamer en/of de volledig verwijde toestand gemist worden. Dit heeft een onjuiste berekening van de ejectiefractie tot gevolg.

Zogenaamde "self-gating" is een methode waarbij het MR signaal zelf gebruikt wordt om te bepalen hoe ver in de hart- en ademhalingscyclus de meting zich bevindt en geen electrocardiografische en ademhalingsregistratie nodig zijn. Door alternerend het MR signaal voor bewegingsinformatie en voor het MRI plaatje te gebruiken is het na afloop van de gehele meting mogelijk MR signaal bestemd voor de MRI plaatjes aan de juiste hart- en ademhalingsfase toe te wijzen zonder informatie weg te gooien. Hoofdstuk 9 laat zien dat deze "self-gated" methode leidt tot een zelfde berekening van

de hartfunctieparameters als de "prospectively triggered" methode, en hogere signaal/ruis en contrast/ruis verhoudingen bij gelijke meettijden.

Rol van MRI bij visualisatie van atherosclerose

Screening op kanker (zoals borstkanker en dikke darmkanker) in een vroeg stadium zonder symptomen ter preventie van late onbehandelbare stadia is alom geaccepteerd. Hoewel hart- en vaatziekten op basis van atherosclerose (zoals een hartinfarct en beroerte) voor meer sterfte en invaliditeit zorgen dan alle vormen van kanker bij elkaar, zijn er geen nationale screening richtlijnen voor vroege stadia van atherosclerose zonder symptomen en is er ook geen door de overheid of gezondheidszorg gesponsorde vergoeding van screening op atherosclerose. Analyse van de kosten effectiviteit laat zien dat de "intima-media thickness" (som van de dikte van binnenbekleding van het bloedvat en de gladde spiercellaag er naast), gemeten met echo en calcium scores gemeten met CT de meest effectieve technieken zijn met betrekking tot screening van grote groepen patiënten. Een strategie van screening op basis van deze 2 technieken is effectiever gebleken dan traditionele Framingham risicofactoren. Echo en CT hebben al een veel langere periode tot het diagnostische arsenaal, voor directe beeldvorming en bepaling van de ernst van atherosclerose, behoord dan andere technieken. Naghavi et al. (SHAPE Task Force report Am J Cardiol 2006): "Other tests for the detection of atherosclerosis and abnormal arterial structure and function, such as MRI of the great arteries, are emerging and must be further validated". De rol van MRI met betrekking tot screening van vroege atherosclerose zonder symptomen moet zich dus nog uit kristalliseren.

Resultaten van de screening gecombineerd met het in kaart brengen van risicofactoren wordt gebruikt voor indeling van patiënten naar risico om de geschikte therapie te starten. Hoe hoger het risico, des te hoger is de kans op een acuut "cardiovasculair event" (hartinfarct, beroerte, of perifere vaatafsluiting) op korte termijn. Omdat minder dan 10% van de mensen, die positief getest worden op atherosclerose, een acuut "cardiovasculair event" op korte termijn zal ondergaan, zal additionele indeling van patiënten naar risico gebaseerd op betrouwbare markers van ziekte-activiteit nodig zijn. Met behulp van deze betrouwbare markers zal de hoog-risico patiënt in de toekomst mogelijk beter gekarakteriseerd kunnen worden.

Concept van de hoog-risico plaque en de hoog-risico patiënt

Moleculaire MRI zou voor additionele indeling van patiënten naar risico kunnen zorgen. MRI zou ook een belangrijke rol kunnen hebben bij de identificatie van hoog-risico plaques in een groep patiënten met reeds bewezen atherosclerose. Welke factoren bepalen het risico van scheuring van een specifieke plaque en welke factoren bepalen het algemene risico op een "acuut cardiovasculair event"?

De klassieke kenmerken van een hoog-risico plaque (chapter 2) voorspellen alleen tot op zekere hoogte scheuring van die plaque. De suggestie wordt gedaan dat in een patiënt een heleboel plaques als hoog-risico plaque benoemd kunnen worden. Karakterisering van moleculaire processen die zich in de plaque afspelen en gerelateerd zijn aan ontsteking, zou belangrijker kunnen zijn dan de klassieke kenmerken van een hoog-risico plaque. Concentraties NGAL in plaques in de halsslagaders van patiënten, waarbij die plaques operatief verwijderd werden, waren hoger als er ook stolsels in diezelfde plaques aanwezig waren dan als er geen stolsels aanwezig waren (niet-gepubliceerde resultaten Hellings e.a.). Van groot belang is het echter te melden dat het hierbij niet bekend was of het stolsel de oorzaak of het gevolg van de toegenomen NGAL concentratie was. Hoe dan ook, NGAL zou een rol kunnen spelen bij erosie of scheuring van een plaque.

Echter, een hoog-risico plaque in de kransslagaderen blijkt niet de enige factor te zijn van belang voor het krijgen van een (bijna) hartinfarct, en plotse hartdood. "Hoog-risico bloed" (verhoogde neiging tot stolling) en "hoog-risico myocard" (hartspier met verhoogde neiging tot gevaarlijke ritmestoornissen) spelen een belangrijke rol met betrekking tot de prognose.

Bovendien, een hoog-risico plaque op een bepaalde locatie hoeft niet de veroorzakende plaque voor een acuut "cardiovasculair event" te zijn, maar kan ook een voorspeller zijn voor scheuring van een plaque ergens anders in het lichaam. Ten eerste, de literatuur laat inderdaad een relatie zien tussen de aanwezigheid van plaque componenten gerelateerd aan ontsteking in een van de halsslagaders en "acute cardiovasculaire events". Ten tweede wordt de aanwezigheid van NGAL in plaques in de halsslagader van patiënten, waarbij die plaques operatief verwijderd werden, geassocieerd met cardiovasculaire symptomen op het moment van operatie (chapter 7). Ten derde zijn NGAL concentraties in plaques in de halsslagader van patienten, die gedurende een follow-up van 2 jaar na operatie een "acuut cardiovascular event" kregen, duidelijk hoger dan in vergelijkbare patienten, die geen "acuut cardiovasculair event" kregen (chapter 7).

Van belang is dat NGAL concentraties in het bloed niet gerelateerd was aan het krijgen van een "acuutcardiovasculair event" (chapter 7). Hieruit kunnen we concluderen, dat technieken gericht op visualisatie van moleculaire processen in atherosclerotische plaques van belang zouden kunnen zijn voor screening van hoog-risico patiënten.

Moleculaire beeldvormende technieken voor plaques: MRI and SPECT?

De ideale methode voor additionele inschatting van het risico van patiënten bovenop calcium score (CT) en de "intima media thickness" (echo) zou moeten zijn: 1) goedkoop, 2) relatief noninvasief, 3) reproduceerbaar, 4) in staat om voorspellende waarde toe te voegen aan erkende risicofactoren, 5) niet gepaard gaand met herhaalde blootstelling aan straling.

Zoals we hebben laten zien in hoofdstuk 2, zijn zowel SPECT (single photon emission computed tomography) als MRI veelbelovend wat deze aspecten aangaat. Een belangrijk voordeel van MRI is gecombineerde informatie met betrekking tot anatomie en moleculaire processen (chapter 2). Een belangrijk nadeel is echter de relatief lage gevoeligheid van MRI zodra deze techniek ingezet wordt voor moleculaire beeldvorming vergeleken met SPECT of PET. Een ander nadeel is het feit, dat contrastmiddelen welke gebruikt worden voor moleculaire MRI vaak bestaan uit dragers als micellen, liposomen (grotere vetbolletjes) of andere platforms, welke nog goedgekeurd dienen te worden door de FDA (VS) en EMEA (Europa) voordat klinische toepassing kan plaatsvinden. In principe worden de meeste SPECT en PET contrastmiddelen goed gekeurd na korte (pre) klinische test procedures in tegenstelling tot de langdurige procedure welke benodigd is voor MR contrastmiddelen. Deze SPECT en PET contrastmiddelen kunnen namelijk toegepast worden in veel lagere concentraties dan benodigd zijn om een immunologische reactie uit te lokken of toxische effecten op te wekken. Daarom zijn er veel hogere kosten verbonden aan de ontwikkeling van klinische moleculaire MR contrastmiddelen.

Concluderend kunnen we stellen, dat op dit moment, gezien de hogere gevoeligheid van SPECT, gemakkelijke toepassing van SPECT contrastmiddelen in de kliniek en de superieure anatomische beeldinformatie van MRI, het ideale platform voor moleculaire beeldvorming MRI-SPECT lijkt te zijn. Herhaalde screening met SPECT of PET contrastmiddelen is echter niet wenselijk wegens blootstelling aan straling. Ondanks de minder kosten- en tijdsefficiënte ontwikkeling kunnen moleculaire MR contrastmiddelen een waardevolle bijdrage leveren aan het arsenaal van moleculaire beeldvormende technieken met betrekking tot de visualisatie van hoog-risico plaques in patiënten.

USPIOs zijn tot dusver de enige moleculaire MR contrastmiddelen, die zijn goed gekeurd voor klinische toepassing. De onduidelijke bestemming van lipiden (bouwstenen van vetten) van micellen en liposomen, mogelijke uitwisseling met lipiden in celmembraan, en mogelijke uitwisseling van gadolinium (metaal in MR contrastmiddel, dat voor MR contrast zorgt maar in vrije vorm toxisch is) met zink in het lichaam, compliceert de implementatie van een aantal MR contrastmiddelen gebaseerd op lipiden in de kliniek. Meer onderzoek is echter benodigd voor een volledig begrip van de toxiciteit van deze MR contrast middelen. Van de andere kant zijn met een eiwit gemodificeerde USPIOs als moleculair MR contrastmiddel reeds klinisch toegepast voor kankeronderzoek en gebruik van deze USPIOs voor beeldvorming van atherosclerose kan waarschijnlijk eerder verwacht worden dan MR contrastmiddelen gebaseerd op lipiden.

Zowel moleculaire MRI als SPECT vereist een voorafmeting en een meting na toediening van het contrastmiddel. In het geval van moleculaire MRI kan deze situatie vermeden worden door het gebruik van zogenaamde PARACEST middelen. Het contrast effect kan bij gebruik van deze middelen uit en aan gezet worden. De beschikbaarheid en kosten van

beide technieken zijn niet optimaal en verdienen verbetering. Hoog-veld MRI en snellere MRI technieken gebruik makend van specifieke hardware verbeteringen kunnen MRI protocollen aanmerkelijk verkorten.

Samenvattend: in dit proefschrift worden zowel anatomische MRI van plaques in halsslagaders van humaan autopsiemateriaal als moleculaire MRI van plaques in een muizenmodel in leven beschreven. Enerzijds werden valkuilen wat betreft beeldvorming van macrofagen met USPIOs en MRI, anderzijds de mogelijkheid om met moleculaire MRI, gericht op NGAL en de CB2-receptor met behulp van micellen, verscheidene stadia van atherosclerose zichtbaar te maken, gedemonstreerd. Implementatie in klinische follow-up studies ten behoeve van evaluatie van de prognostische waarde van deze moleculaire MRI technieken kan pas volgen na verdere studies naar verdeling van het MR contrastmiddel gebaseerd op lipiden in het menselijk lichaam na injectie via de bloedbaan, uitwassing uit de bloedbaan en toxiciteit.

List of publications

1 **Te Boekhorst BC**, Cramer MJ, Pasterkamp G, van Echteld CJ, Doevendans PA.
   Recent developments and new perspectives on imaging of atherosclerotic plaque: role of anatomical, cellular and molecular MRI Part I and II.
   Int J Cardiovasc Imaging, 2010 Jan 29. Epub ahead of print..

2 **Te Boekhorst BC**, Cramer MJ, Pasterkamp G, van Echteld CJ, Doevendans PA.
   Recent developments and new perspectives on imaging of atherosclerotic plaque: role of anatomical, cellular and molecular MRI part III.
   Int J Cardiovasc Imaging, 2010 Jan 8. Epub ahead of print.

3 **Te Boekhorst BC**, Bovens SM, Nederhoff MG, van de Kolk KW, Cramer MJ, van Oosterhout MF et al.
   Negative MR contrast caused by USPIO uptake in lymph nodes may lead to false positive observations with in vivo visualization of murine atherosclerotic plaque.
   Atherosclerosis, 2009 Nov 3. Epub ahead of print..

4 **Te Boekhorst BC**, Bovens SM, Rodrigues-Feo J, Sanders HM, Van de Kolk CW, De Kroon AI, Cramer MJ, Doevendans PA, Ten Hove M, Pasterkamp G, Van Echteld CJ.
   Characterization, In Vitro and In Vivo Testing of CB2-Receptor and NGAL-Targeted Paramagnetic Micelles for Molecular MRI of Vulnerable Atherosclerotic Plaque.
   Molecular Imaging and Biology 2010. In press.

5 **Te Boekhorst BC**, Bovens SM, Van de Kolk CW, Cramer MJ, Doevendans PA, Ten Hove M, Van der Weerd L, Poelmann RE, Strijkers GJ, Pasterkamp G, Van Echteld CJ.
   The Time Window of MRI of Murine Atherosclerotic Plaques after Administration of CB2 Receptor Targeted Micelles. Inter-Scan Variability and Relation between Plaque Signal Intensity Increase and Gadolinium Content of Inversion Recovery Prepared Versus Non-Prepared Fast Spin Echo.
   NMR in Biomed 2010. In press.

6   **Te Boekhorst BC**, Bovens SM, Hellings WE, Van der Kraak PH, Van de Kolk CW, Vink A, Moll FL, Van Oosterhout MF, De Vries JP, Doevendans PA, Goumans MJ, De Kleijn DP, Van Echteld CJ, Pasterkamp G, Sluijter JP.
    Molecular MRI of murine atherosclerotic plaque targeting NGAL, a protein associated with high-risk human plaque.
    Submitted. Te Boekhorst and Bovens contributed equally to this manuscript.

7   **Te Boekhorst BC**, Van 't Klooster R, Bovens SM, Van de Kolk CW, Cramer MJ, Van Oosterhout MF, Doevendans PA, Van der Geest RJ, Pasterkamp G., Van Echteld CJ. *Multi-spectral MRI Including Fat Suppression and Inversion Recovery Spin Echo Allows for Identification of Intra-Plaque Hemorrhage and Lipid Core in Human Carotid Plaque*.
    Submitted.

8   Bovens SM, **Te Boekhorst BC**, Den Ouden K, Van de Kolk CW, Nauerth A, Nederhoff MG, Pasterkamp G, Ten Hove M, Van Echteld CJ.
    Evaluation of infarcted murine heart function: Comparison of prospectively triggered with self-gated MRI.
    Submitted. Bovens and Te Boekhorst contributed equally to this manuscript.

9   Brandon Bravo Bruinsma GJ, Nederhoff MG, **Te Boekhorst BC**, Bredee JJ, Ruigrok TJ, van Echteld CJ.
    Brain death-induced alterations in myocardial workload and high-energy phosphates: a phosphorus 31 magnetic resonance spectroscopy study in the cat.
    J Heart Lung Transplant 1998 October;17(10):984-90.

10 Reijneveld JC, **Te Boekhorst BC**, Zonderland ML, Kalmijn S, Notermans NC.
    Response to exercise of patients with idiopathic hyper-CK-emia.
    Muscle Nerve 2002 December;26(6):832-7.

11 Sabelis LW, Senden PJ, **Te Boekhorst BC**, Hulzebos HJ, Van De Wiel A, Van Haeften TW, Zonderland ML, Mosterd WL.
    Does physical training increase insulin sensitivity in chronic heart failure patients?
    Clin Sci (Lond) 2004 May;106(5):459-66.

12 **Te Boekhorst BC**.
    Report 49th Annual Meeting of the ACSM.
    Geneeskunde en Sport, 2002, 4: 25-26.

13 **Te Boekhorst BC**, Senden PJ.

Myocardial ischemia caused by myocardial bridging in an endurance sportsman.
Geneeskunde en Sport, 2003, 3: 67-70. Dutch.

Oral presentations

Te Boekhorst BC, Sabelis LW, Senden PJ, Hulzebos E, Mosterd WL, University Medical Center Utrecht, Meander Medical Center Amersfoort. Training and muscle O2 uptake at exercise onset in chronic heart failure, 49th Annual Meeting American College of Sports Medicine, St.Louis (VS), 2002, May 28- June 1.

Te Boekhorst BC, Sabelis LW, Senden PJ, Hulzebos E, Zonderland ML, Mosterd WL, University Medical Center Utrecht, Meander Medical Center Amersfoort. VO2 kinetics at exercise onset and training in chronic heart failure patients, XXVII FIMS World Congress of Sports Medicine, Boedapest, 2002, June 5-9.

Poster awards

3d poster award, XIVth Annual Scientific WCN Meeting, Amsterdam, 2001, December 15, Te Boekhorst BC, Sabelis LW, Senden PJ, Hulzebos E, Zonderland ML, Mosterd WL, Meander Medical Center Amersfoort, University Medical Center Utrecht. Effect of Physical Training on VO2 Kinetics at Exercise Onset in Chronic Heart Failure.

3d poster award, Scientific Day Netherlands Heart Foundation, Amsterdam, 2002, October 18, Te Boekhorst BC, Sabelis LW, Senden PJ, Hulzebos E, Zonderland ML, Mosterd WL, University Medical Center Utrecht, Meander Medical Center Amersfoort, Physical training improves oxygen uptake kinetics at exercise onset in patients with chronic heart failure.

1st poster award, Congress NVVC, 2006, Te Boekhorst BC, Cramer MJ, Van Oosterhout MF, Pasterkamp G, Doevendans PA, Van Echteld CJ, High-resolution MRI for identification of various components of human carotid artery plaque using different weightings and fat suppression.

Abstracts

Te Boekhorst BC, Sabelis LW, Senden PJ, Hulzebos E, Zonderland ML, Mosterd WL.
Effect of Physical Training on VO2 Kinetics at Exercise Onset in Chronic Heart Failure.
XIVth Annual Scientific WCN Meeting, Amsterdam, 2001, December 15.

Te Boekhorst BC, Sabelis LW, Senden PJ, Hulzebos E, Zonderland ML, Mosterd WL.
Physical training improves oxygen uptake kinetics at exercise onset in patients with chronic heart failure.
Scientific Day Netherlands Heart Foundation, Amsterdam, 2002, October 18.

Te Boekhorst BC, Cramer MJ, Van Oosterhout MF, Pasterkamp G, Doevendans PA, Van Echteld CJ.
High-resolution MRI for identification of various components of human carotid artery plaque using different weightings and fat suppression.
Congress NVVC, 2006.

Brandon Bravo Bruinsma GJ, **Te Boekhorst BC**, Nederhoff MG, Ruigrok TJ, Van Echteld CJ, Bredée JJ.
Brain Death-Induced Deterioration of Myocardial Workload Is Not Caused by Reduced Phosphocreatine/ATP ratio.
J Am Coll Cardiol 1998; 31: 59A, 805-6.

Brandon Bravo Bruinsma GJ, **Te Boekhorst BC**, Nederhoff MG, Bredée JJ, Ruigrok TJ, Van Echteld CJ.
Myocardial Energetics Following Induction of Brain Death in the Cat.
Proc Internat Soc Magn Reson Med 1997; Vol II: 1286.

Brandon Bravo Bruinsma GJ, Nederhoff MG, **Te Boekhorst BC**, Bredée JJ, Ruigrok TJ, Van Echteld CJ.
Brain death means Heart death?
Ned Tijdschr Geneesk 1999; 143 (6);325. Dutch.

Te Boekhorst BC, Rodriguez-Feo J, Bovens SM, De Kroon AI, Cramer MJ, Pasterkamp G, Doevendans PA, Van Echteld CJ.
A micelle-based MR contrast agent for targeting the peripheral CB2 receptor in atherosclerotic plaque.
Mol Imag 2006; 5 (3):391-392.

Te Boekhorst BC, Rodriguez-Feo J, Bovens SM, De Kroon AI, Cramer MJ, Pasterkamp G, Doevendans PA, Van Echteld CJ.
Characterization of micelle-based contrast agent targeting peripheral cannabis receptors and its potential use for atherosclerotic plaque visualization by MRI.
J Cardiovasc Magn Res 2007; 9 (2):256-257.

Te Boekhorst BC, Cramer MJ, Van Oosterhout MF, Pasterkamp G, Doevendans PA, Van Echteld CJ.
High-resolution MRI for carotid artery plaque characterization using different weightings and fat suppression.
J of Mol and Cell Cardiol 2007; 42: S238–S246.

Te Boekhorst BC, Cramer MJ, Van Oosterhout MF, Pasterkamp G, Van Echteld CJ.
High-resolution MRI for identification of various components of human carotid artery plaque using multicontrast-weighting and fat suppression.
Neth.Heart J 2006; 14, supplement 1:25.

Te Boekhorst BC, Cramer MJ, Van Oosterhout MF, Pasterkamp G, Van Echteld CJ.
High-resolution MRI for identification of various components of human carotid artery plaque using different weightings and fat suppression.
Eur Heart J 2006; 27:366-367.

Te Boekhorst BC, Cramer MJ, Van Oosterhout MF, Pasterkamp G, Doevendans PA, Van Echteld CJ. *High-resolution MRI for identification of various components of human carotid artery plaque using different weightings and fat suppression.*
J Cardiovasc Magn Res 2007; 9 (2):252-253.

Van Echteld CJ, Nederhoff MG, **Te Boekhorst BC**, Van de Kolk CW, Jansen MA, Nauerth A. *Self-gated, wireless cine-MRI allows accurate and time-efficient analysis of mouse heart function when conventional ECG- and respirator gated cine MRI fails.*
Proc.ISMRM.2006; 14:17.

Van Echteld CJ, **Te Boekhorst BC**, Nederhoff MG, Van de Kolk CW, Nauerth A.
Wireless, self-gated multislice cine MR of mouse hearts in vivo.
J Cardiovasc Magn Res 2007; 9 (2):373-374.

Te Boekhorst BC, Bovens SM, Den Ouden K, Nederhoff MG, Van de Kolk CW, Cramer

MJ, Ten Hove M, Doevendans PA, Poelmann RE, Pasterkamp G, Van Echteld CJ, *Identification of advanced atherosclerotic plaque in abdominal aorta in a murine atherosclerotic model with 24p3 (mouse homologue of neutrophil gelatinase-associated lipocalin)-targeted micelles and MRI.*
ISMRM, 17th Scientific Meeting & Exhibition, 18-24 April 2009.

Te Boekhorst BC, Bovens SM, Den Ouden K, Nederhoff MG, Van de Kolk CW, Cramer MJ, Ten Hove M, Doevendans PA, Poelmann RE, Pasterkamp G, Van Echteld CJ. *Characterization of MR contrast enhancement in murine advanced atherosclerotic plaque after administration of 24p3 (NGAL)-targeted micelles*.
ISMRM, 17th Scientific Meeting & Exhibition, 18-24 April 2009.

Te Boekhorst BC, Bovens SM, Nederhoff MG, Van de Kolk CW, Cramer MJ, Van Oosterhout MF, Ten Hove M, Doevendans PA, Pasterkamp G, Van Echteld CJ.
Negative Magnetic Resonance Contrast of Peri-Aortic Lymph Nodes created by Uptake of Ultrasmall Superparamagnetic Particles of Iron Oxide (USPIOs) May Mask the Aortic Lumen and Lead to False Positive Results with Regard to the Diagnosis of Atherosclerosis.
ISMRM, 17th Scientific Meeting & Exhibition, 18-24 April 2009.

Dankwoord

Een aantal mensen wil ik speciaal bedanken voor het tot stand komen van dit proefschrift. Uiteraard probeer ik volledig te zijn, maar vergeef het me als ik toch mensen vergeet.

Prof. G. Pasterkamp, beste Gerard,
Bijzonder bedankt voor je begeleiding bij het schrijven tijdens de afrondende fase van mijn promotie. Ik waardeer je openheid en enthousiasme zeer en dit maakte het mogelijk om goede discussies te voeren. Je heldere blik, en praktische inslag droegen mede bij tot het welslagen van het project.

Prof. Dr. C.J.A. van Echteld, beste Cees, erg veel dank voor de mogelijkheden die ik gekregen heb om op jouw lab dit project te starten. Je bespiegelingen op het gebied van biomembranen en je kennis van NMR hebben me veel inspiratie geboden om de micellen op een handige manier te produceren en MRI technieken voor beeldvorming van atherosclerotische plaques in de muis te verbeteren, ook toen je naar Zwitserland vertrokken was.

Dr. M.J.M. Cramer, beste Maarten-Jan, bedankt voor de enthousiaste wijze waarop je me begeleidde. Dank ook voor het meedenken bij moeilijke beslissingen. Je wist altijd de positieve dingen wat extra uit te vergroten.

Prof. Dr. P.A.F.M. Doevendans, beste Pieter, ontzettend bedankt voor je hulp op diverse gebieden tijdens belangrijke fases van mijn promotie-traject. Bedankt voor de logistieke en financiële mogelijkheden die je me geboden hebt om mijn onderzoek te doen. Bedankt voor de doelmatige overlegmomenten.

Prof. K. Nicolaij, beste Klaas, prof. R.P.E. Poelmann, beste Rob, en de medewerkers binnen het NELU project uit Leiden en Eindhoven, dank voor jullie constructieve opmerkingen en ideeën tijdens de bijeenkomsten gedurende de afgelopen jaren.

Dan het Cardio MR lab:

beste Michiel, toen Cees net vertrokken was naar Zwitserland, werd jij hoofd van het lab. Je enthousiasme in het onderzoek en onze scherpe discussies zullen me bijblijven. Dank voor je hulp bij het schrijven van enkele artikelen. Beste Kees, Marcel, Eissa, Sandra en Krista. Dank voor de hulp tijdens en rondom diverse experimenten. Vooral Sandra wil ik speciaal bedanken. Gelukkig voor mij koos je destijds als student voor mijn project. We hebben erg veel werk verzet en ook erg veel plezier beleefd binnen en buiten het werk. Heel veel dank daarvoor. Veel succes met de afronding van jouw promotie, dat gaat zeker lukken!

Beste Toon, Eef-Jan en Rutger, bedankt voor jullie bijdrage aan het welslagen van de productie van getargete micellen door het beschikbaar stellen van apparatuur in het Kruytgebouw en het advies. Even checken of de micel size en fluorescenties wel klopten en erover door filosoferen bleek zeer nuttig.

Beste Gustav, Willem, Erik, bedankt voor jullie nuttige tips met betrekking tot lipid-gebaseerde contrastmiddelen en de geboden faciliteiten op de TUE wat betreft NMR relaxometrie. Erik, bedankt voor de erg waardevolle enthousiaste discussie op de ISMRM op Hawaii en over de mail. Gustav, ik hoop op een vruchtbare samenwerking in de nabije toekomst. Jullie kritische blikken op de artikelen behorend bij hoofdstukken 6 en 8 waren voor mij erg belangrijk.

Beste Rob en Ronald, dank voor de prettige samenwerking. Ik maakte dankbaar gebruik van jullie expertise op het gebied van beeldverwerking. Ronald, succes met jouw project voor de komende 4 jaar!

Beste Marijn, aan het einde van mijn project gekomen, leek me verder onderzoek naar MRA van muize-coronairen erg leuk en ik vond jou bereid 3D reconstructies van mijn plaatjes te maken. Niet meer voor het boekje weliswaar, maar ik denk dat we in de nabije toekomst mooie resultaten kunnen laten zien. De kaft laat vast een voorproefje zien!

Beste Margo, bedankt voor je onmisbare administratieve activiteiten in de eerste jaren van mijn promotie-traject. Beste Ineke, erg veel dank voor het vele werk op allerhande gebied dat je voor me gedaan hebt, en je snelle interventies als ik op administratief niveau af en toe eens tekort schoot.

Mijn dank gaat ook uit naar de mensen in het moleculaire lab. Vooral Arjan, met je heldere no-nonsense antwoorden op mijn vele vragen. Hoewel ik moet bekennen soms met knikkende knieën en het zweet in de oksels vragen aan je gesteld te hebben, heb ik veel praktische hulp en een fors aantal waardevolle ideeën van jou gekregen. Speciale dank hiervoor. Ook veel dank aan de vele AIOs in de vroege jaren en latere jaren, voor het meeleven en de gezelligheid. Ben en Evelyn, dank voor jullie hulp bij diverse dierexperimenten.

Ook moet ik vooral denken aan de pathologie-afdeling: bedankt Matthijs: er leek niet veel uit de studie met de "ijzerbolletjes" te komen, maar zoals zo vaak blijken sommige negatieve resultaten later erg belangrijk. Later Aryan: bedankt voor je kritische blik, en het grote enthousiasme dat je uitstraalt richting ons onderzoek. Ik hoop binnenkort verder met je te kunnen samenwerken. Ook Petra wil ik speciaal bedanken: zonder jouw tomeloze inzet en vaardigheden op immunohistochemisch gebied was het allemaal een stuk lastiger, zo niet onmogelijk, geworden om het NGAL verhaal af te ronden. Ook hoop ik op jouw hulp te kunnen rekenen in de nabije toekomst.

Het GDL-team wil ik bedanken, vooral Tamara en Jeroen, voor de goede verzorging van de muizen en konijnen.

Lia, Herman, mede-atlete en trainer, en vooral vrienden, fijn dat jullie mijn paranimfen willen zijn (succes!). Een aantal jaren geleden mocht ik bij jou, Lia, de kunst afkijken. Overige vrienden en mede-atleten van Phoenix en andere verenigingen, bedankt voor het meeleven gedurende de afgelopen jaren.

Tot slot wil ik mijn vader en moeder bedanken, dat ze het mij mogelijk maakten te gaan studeren. Mam, bedankt voor je hulp, steun en interesse. Op zulke momenten is het zwaar mijn vader te moeten missen. Mijn broer en zussen, Hans, Conny en Els, bedankt voor jullie interesse en enthousiasme.

Curriculum Vitae

Bernard te Boekhorst werd op 18 februari 1972 geboren te Tilburg. Hij behaalde in 1990 het VWO diploma aan het Sint Odulphus Lyceum te Tilburg. In hetzelfde jaar startte hij de studie Medische Biologie aan de Universiteit van Utrecht. Na twee jaar werd ook aangevangen met de studie Geneeskunde aan dezelfde universiteit. Een van de afstudeerstages voor Medische Biologie werd gevolgd op het Cardio Magnetic Resonance laboratorium destijds nog geleid door prof. dr. T.J.C. Ruigrok, waar zijn interesse voor NMR gewekt werd. In 1996 werden de doctoraalbullen van zowel Medische Biologie als Geneeskunde verkregen. In 1999 nam hij zijn artsenbul in ontvangst.

Aansluitend werkte hij als AGNIO Cardiologie in het Meander Medisch Centrum te Amersfoort, waarna hij als fervent hardloper de opleiding tot sportarts startte. In 2003 schreef hij, samen met prof. dr. C.J.A. Van Echteld, een subsidie-aanvraag ten behoeve van een promotie-project, welke gehonoreerd werd tijdens de jaarlijkse subsidie-ronde van de Nederlandse Hart Stichting van dat jaar. Hij staakte de opleiding tot sportarts om in oktober 2004 als arts-onderzoeker op de Cardio MR afdeling van het laboratorium voor Experimentele Cardiologie in het Universitair Medisch Centrum Utrecht te beginnen met het promotie-project onder begeleiding van prof. dr. C.J.A. van Echteld, prof. dr. G. Pasterkamp en dr. M.J.M. Cramer. Vanaf januari 2010 continueert hij de opleiding tot sportarts in het Maxima Medisch Centrum te Veldhoven (opleider dr. G. Schep).